

EDDIES AND CURRENTS OF THE HAWAIIAN ISLANDS

A DISSERTATION SUBMITTED TO THE GRADUATE DIVISION OF THE  
UNIVERSITY OF HAWAII IN PARTIAL FULFILLMENT OF THE  
REQUIREMENTS FOR THE DEGREE OF

DOCTOR OF PHILOSOPHY

IN

OCEANOGRAPHY

DECEMBER 1998

By

Claude Frederick Lumpkin

Dissertation Committee:

Pierre Flament, Chairperson

John Learned

Doug Luther

Mark Merrifield

Bill Patzert

Bo Qiu

We certify that we have read this dissertation and that, in our opinion, it is satisfactory in scope and quality as a dissertation for the degree of Doctor of Philosophy in Oceanography.

DISSERTATION COMMITTEE

---

Chairperson

©Copyright 1998

by

Claude Frederick Lumpkin

## ACKNOWLEDGEMENTS

I would like to thank my advisor, Pierre Flament, and the other members of my Ph.D. committee, John Learned, Doug Luther, Mark Merrifield, Bill Patzert, and Bo Qiu, for all their feedback.

I was fortunate to work closely with Rudolf Kloosterziel, Jean Tournadre and Larry Armi, who gave me much of their time.

While visiting France in January 1998, I had invaluable conversations on the subjects of vortex merging and dynamics with Jacques Verron, Emil Hopfinger, G. J. F. van Heijst, Bernard Le Cann, Jérôme Paillet, Yves Morel and Xavier Carton. I would also like to thank Tom Rossby for valuable advice on handling the large drifter data set (“don’t get so buried in statistics that you stop looking at individual tracks”).

Thanks to Tom Daniels of NELHA, who helped us locate a grounded drifter and supervised the deployment of two drifters in April 1996. Several drifters grounded on Maui, and their recover was assisted by Glenn James. Thanks to Cristina Lumpkin, who helped me carry a grounded drifter across the mud flats of southern Moloka’i as the tide came in and the sun boiled the air around us, then through a mangrove swamp filled with banana spiders best described in *The Hobbit*.

I received an enormous amount of help gathering archived data from Pat Caldwell and Myra Pazos. ALACE data appears courtesy of Russ Davis. ADCP data from the HOT cruises appear courtesy of Eric Firing. The ERS-1/TOPEX altimetry data were compiled by Jean Tournadre.

Technical assistance, ranging from data processing to programming help, was provided by Michael Sawyer, Derek Young and June Firing. Navigation, SST processing and compilation of the AVHRR imagery was performed by Cristina Lumpkin, June Firing

and Heidi Jackson.

I would like to thank the graduate students and ex-students of UH for their feedback throughout the development of this dissertation, particularly Schuiming Chen and Sean Kennan.

I owe an enormous amount of gratitude to Pierre, my family and Cristina for encouragement and support throughout this project.

This dissertation was supported by the Office of Naval Research under grant #N000149710147. The drifters deployed for this project, and the technical support for the ensuing data management, were supported by NOAA's Pelagic Fisheries Research Program under grant #NA67RJ0154.

## ABSTRACT

Hawaiian lee eddies are examined in WOCE drifter trajectories, ADCP measurements, in-situ sea level records, satellite altimetry and AVHRR imagery. The mean currents, temperature, and their variance in the Hawaiian region are mapped from the surface drifter data and the historical hydrography. A regression analysis is used to identify the Ekman component of the drifter speed.

It is shown that the islands have a profound effect on the downstream flow: the island wake is composed of counter-rotating gyres over 800 km long. Eddy energy is greatly magnified in this region, and the mean propagation paths of cyclonic and anticyclonic eddies correspond to the vorticity of the gyres. These gyres are separated by a narrow countercurrent, the Hawaiian Lee Countercurrent. The northern edge of the cyclonic gyre is delineated by a westward current, which flows along the southwest shores of the islands. This current has not previously been identified, and is named the Hawaiian Lee Current (HLC) in this study. Once passing Kaua‘i, the HLC joins with the North Hawaiian Ridge Current to form a westward jet extending to  $180^\circ$ .

Hawaiian lee eddies are generated at  $\sim 50$ – $70$  day intervals, and can be clearly identified in satellite altimetry. A generalized form of the Rankine vortex structure is described, which allows for nonzero vorticity in the vortex shell. This model is used to characterize the observed lee eddies, which range from quasigeostrophic to nonlinear length and velocity scales. A synthesis of the drifter data, altimetry and AVHRR imagery provides a description of the eddies’ life cycle from birth to downstream propagation and spin-down. The maximum core vorticity of several newly-formed anticyclonic eddies may have been limited by centrifugal instability; possible azimuthal mode 2 instability leading to the production of a tripolar vortex is also noted for two cyclonic

eddies. The eddies' propagation speeds compare favorably to existing theory, with deviations possibly due to advection and eddy-eddy interaction. The spin-down of the eddies is modeled by a simple entrainment model. Drifter observations suggest that anticyclonic eddies may occasionally merge as they drift west-southwest from Hawai'i, producing rapid jumps in their core vorticity and size.

Lagrangian statistics of individual drifters are calculated in several subregions, demonstrating an increase of 1.3-1.6 times in diffusivity due to the lee eddies. The zonal diffusivity is larger than the meridional diffusivity by an amount consistent with the background shear of the mean currents.

## TABLE OF CONTENTS

<b>Acknowledgements</b> . . . . .	<b>iv</b>
<b>Abstract</b> . . . . .	<b>vi</b>
<b>List of Tables</b> . . . . .	<b>x</b>
<b>List of Figures</b> . . . . .	<b>xi</b>
<b>Chapter 1 Introduction</b> . . . . .	<b>1</b>
<b>Chapter 2 Data</b> . . . . .	<b>11</b>
2.1 Satellite-tracked drifting buoys . . . . .	11
2.2 Hydrography . . . . .	18
2.2.1 Calculating density for bathythermograph casts . . . . .	18
2.2.2 The dynamic height field . . . . .	19
2.3 Winds . . . . .	21
2.4 Altimetry . . . . .	22
2.5 In-situ sea level . . . . .	23
2.6 Sea surface temperature . . . . .	23
2.7 Shipboard ADCP . . . . .	24
2.8 Mixed-layer depth . . . . .	24
<b>Chapter 3 Eddies</b> . . . . .	<b>42</b>
3.1 The cyclogeostrophic balance . . . . .	43
3.2 Centrifugal instability . . . . .	46
3.2.1 Stability of a solid-body eddy . . . . .	48
3.2.2 Stability of the core/shell model . . . . .	48
3.3 Eddy birth . . . . .	49
3.3.1 Cyclones . . . . .	50
3.4 Anticyclones . . . . .	52
3.5 Propagation . . . . .	54
3.5.1 Observations of eddy propagation . . . . .	55
3.5.2 Linear theory: $\beta$ -induced drift . . . . .	56
3.5.3 Other processes affecting eddy speed . . . . .	59
3.6 Eddy observations: a descriptive view of the lee eddy field . . . . .	60
3.6.1 1989 ADCP transect . . . . .	61
3.6.2 Eddy AC94a . . . . .	62
3.6.3 Eddy AC94b . . . . .	63
3.6.4 October 1994 to September 1996 deployments . . . . .	65
3.7 Discussion . . . . .	67
3.7.1 Half-inertial lee eddies . . . . .	68
3.7.2 Spin-down . . . . .	68
3.7.3 Eddy merging . . . . .	70
3.8 Conclusions . . . . .	75

<b>Chapter 4 Mean currents</b>	<b>104</b>
4.1 Deep geostrophic currents	105
4.2 Ekman drift	106
4.3 Calculating means and variances	108
4.4 Energy fluxes	110
4.5 Observations of the mean currents and eddy field	112
4.5.1 North Equatorial Current	114
4.5.2 North Hawaiian Ridge Current	116
4.5.3 Currents in the Island Lee	118
4.5.4 Flow through the channels separating the major islands	124
4.6 Conclusions	128
<b>Chapter 5 Dispersion and eddy diffusivity</b>	<b>166</b>
5.1 Classical theory: Taylor's Theorem and eddy diffusivity	167
5.2 Direct calculation of Lagrangian properties	169
5.3 Asymptotic behavior of the dispersion	171
5.4 Lagrangian spectra	172
5.5 Discussion	173
<b>Chapter 6 Discussion</b>	<b>185</b>
<b>Appendix A Kriging</b>	<b>193</b>
<b>Appendix B Models for the radial structure of reduced gravity eddies</b>	<b>196</b>
B.1 Solid-body eddy	196
B.2 Vortices with finite-shear edges	197
B.2.1 Gaussian eddies	197
B.2.2 Rankine eddies	198
B.2.3 The core/shell eddy model	198
<b>Appendix C Observations of lee eddies, 1994–1996</b>	<b>200</b>
C.1 August and October 1994 cruises	200
C.2 July–August 1995 cruise	205
C.3 April 1996 cruise	210
<b>Appendix D Eddy dissipation</b>	<b>242</b>
<b>Appendix E Vortex merging in a <math>1\frac{1}{2}</math>-layer fluid on an <math>f</math>-plane</b>	<b>244</b>
E.1 Introduction	244
E.2 Development of the model	245
E.2.1 Mass and angular momentum of an isolated vortex	245
E.2.2 Angular momentum of vortices immersed in quiescent fluid	246
E.2.3 Energy of vortices	247
E.3 Vortex merging	248
E.3.1 Solid-body vortices	249
E.3.2 Vortices with finite-shear edges	251
E.4 Discussion	253
<b>Appendix F Dispersion magnification by the mean current shear</b>	<b>267</b>
<b>References</b>	<b>270</b>

## LIST OF TABLES

<u>Table</u>		<u>Page</u>
2.1	Number of dynamic height estimates . . . . .	20
3.1	Structure of AC94b from altimetry . . . . .	65
5.1	Lagrangian properties in the Hawaiian subregions . . . . .	170
C.1	Structure of AC94c from altimetry . . . . .	203

## LIST OF FIGURES

Figure		Page
1	Map of the Hawaiian Islands . . . . .	8
2	Levitus94 dynamic height . . . . .	9
3	Mean currents at moorings in the Hawaiian Islands . . . . .	10
4	Raw fixes of a grounded drifter . . . . .	25
5	Number of fixes per day and submergence of drifters . . . . .	26
6	Interpolated drifter tracks . . . . .	27
7	Density of drifter coverage . . . . .	28
8	Number of observations in mean current maps . . . . .	29
9	Mean currents . . . . .	30
10	Mean currents (closeup) . . . . .	31
11	Variance of currents and dynamic height . . . . .	32
12	Variance ellipses . . . . .	33
13	Mean divergence and curl . . . . .	34
14	Annual signal in the temperature data . . . . .	35
15	Mean temperature and its variance . . . . .	36
16	Locations of CTD and XBT casts . . . . .	37
17	T-S profiles . . . . .	38
18	Wind stress . . . . .	39
19	Wind around Hawai'i . . . . .	40
20	Mean altimetric sea surface height and sea level anomaly . . . . .	41
21	Cyclogeostrophy applied to a solid-body eddy . . . . .	78
22	Sea level anomaly in the lee of Hawai'i . . . . .	79
23	Birth of a cyclonic eddy . . . . .	80
24	Birth of an anticyclonic eddy . . . . .	81
25	ADCP profile of the NEC passing the south point of Hawai'i . . . . .	82
26	ADCP profile of the NEC passing the island of Hawai'i . . . . .	83
27	Paths of eddies and distribution of rotary variance . . . . .	84
28	Mean CCW/CW variance of drifter trajectories . . . . .	85
29	Longitude vs. time plots of sea level anomaly, Pt. I . . . . .	86
30	Longitude vs. time plots of sea level anomaly, Pt. II . . . . .	87
31	Longitude vs. time plots of sea level anomaly, Pt. III . . . . .	88
32	Sea level at Johnston Atoll and Wake Island . . . . .	89
33	Spectrum of sea level at Johnston and Wake . . . . .	90
34	Propagation speeds of eddies . . . . .	91
35	The $\beta$ -drift of core/shell eddies . . . . .	92
36	Eddy AC89 . . . . .	93
37	Orbital characteristics of a drifter in AC94a . . . . .	94
38	Orbital characteristics of a drifter in AC94b . . . . .	95
39	ERS-1 scatterometer winds concurrent with AC94b . . . . .	96
40	Altimetry in frame of reference moving with AC94b . . . . .	97
41	Modeling the decay of an eddy's core vorticity . . . . .	98
42	Energy of the eddy in the spin-down model . . . . .	99
43	Modeling AC94b, Pt. I: entrainment only . . . . .	100
44	Modeling AC94b, Pt. II: merging only . . . . .	101
45	Modeling AC94b, Pt. III: merging + entrainment . . . . .	102

46	Modeling AC94b, Pt. IV: tuning the model . . . . .	103
47	Dynamic height anomaly at 400 dbar relative to 1000 dbar . . . . .	131
48	Speeds of ALACE buoys . . . . .	132
49	Mean wind and mixed layer depth . . . . .	133
50	Ekman drift (regression model) . . . . .	134
51	Mean drifter-derived currents and dynamic topography . . . . .	135
52	Mean currents and SST east of the Hawaiian Islands . . . . .	136
53	Mean turbulent quantities east of the Hawaiian Islands . . . . .	137
54	Mean eddy energy and fluxes east of the Hawaiian Islands . . . . .	138
55	Mean dynamic height east of the Hawaiian Islands, Pt. I . . . . .	139
56	Mean dynamic height east of the Hawaiian Islands, Pt. II . . . . .	140
57	Zonal speed from drifters and hydrography . . . . .	141
58	Mean currents and SST, 156.5–160° W . . . . .	142
59	Mean turbulent quantities, 156.5–160° W . . . . .	143
60	Mean eddy energy and fluxes, 156.5–160° W . . . . .	144
61	Mean dynamic height, 156.5–160° W . . . . .	145
62	Mean currents and SST, 160–168° W . . . . .	146
63	Mean turbulent quantities, 160–168° W . . . . .	147
64	Mean eddy energy and fluxes, 160–168° W . . . . .	148
65	Mean dynamic height, 160–168° W . . . . .	149
66	Mean currents and SST, 170–180° W . . . . .	150
67	Mean turbulent quantities, 170–180° W . . . . .	151
68	Mean eddy energy and fluxes, 170–180° W . . . . .	152
69	Mean dynamic height, 170–180° W . . . . .	153
70	Mean currents and SST along the Hawaiian Ridge . . . . .	154
71	Mean turbulent quantities along the Hawaiian Ridge . . . . .	155
72	Mean eddy energy and fluxes along the Hawaiian Ridge . . . . .	156
73	Mean dynamic height along the Hawaiian ridge . . . . .	157
74	Variability of the North Hawaiian Ridge Current . . . . .	158
75	The Hawaiian Lee Current . . . . .	159
76	Time series of the HLC and HLCC . . . . .	160
77	The HLCC in eddy-trapped and non-eddy-trapped drifters . . . . .	161
78	Mean dynamic height across the ‘Alenuihaha Channel . . . . .	162
79	Trajectories of drifters near the ‘Alenuihaha Channel . . . . .	163
80	Near-surface flow through the ‘Alenuihaha Channel . . . . .	164
81	AVHRR images on 3 February 1993 . . . . .	165
82	Diffusivity and Lagrangian scales . . . . .	176
83	Lagrangian properties as a function of rms speed . . . . .	177
84	Rms displacement . . . . .	178
85	Initial rms displacement . . . . .	179
86	Energy-preserving plots of the Lagrangian spectra of $u$ and $v$ . . . . .	180
87	Energy-preserving plots of the Lagrangian rotary spectra . . . . .	181
88	Rotary spectra in the island lee . . . . .	182
89	Log-log plots of the Lagrangian spectra of $u$ and $v$ . . . . .	183
90	Log-log plots of the Lagrangian rotary spectra . . . . .	184
91	Summary flowchart . . . . .	191
92	Summary schematic . . . . .	192
93	Eddy AC94c, Pt. I . . . . .	213
94	Eddy AC94c, Pt. II . . . . .	214
95	Tracking AC94c (8 Sept.–10 Oct. 1994) . . . . .	215

96	Orbital characteristics of drifters in C94a . . . . .	216
97	Eddy AC94c, Pt. III . . . . .	217
98	Drifter snapshots (Sept.–Dec. 1994) . . . . .	218
99	Drifter snapshots (Dec. 1994–Feb. 1995) . . . . .	219
100	Orbital characteristics of drifters in AC94c . . . . .	220
101	Altimetry in frame of reference moving with AC94c . . . . .	221
102	October–December 1994 AVHRR images . . . . .	222
103	Orbital characteristics of drifters in C94b . . . . .	223
104	Cruise TC9503 . . . . .	224
105	Eddy C95a . . . . .	225
106	July – August 1995 AVHRR images . . . . .	226
107	August – September 1995 AVHRR images . . . . .	227
108	Eddy C95b . . . . .	228
109	Drifters snapshots (Aug.–Oct. 1995) . . . . .	229
110	Drifters snapshots (Oct. 1995–Jan. 1996) . . . . .	230
111	Drifters snapshots (Jan.–Mar. 1996) . . . . .	231
112	Orbital characteristics of drifters in C95b, Pt. I. . . . .	232
113	Orbital characteristics of drifters in C95b, Pt. II. . . . .	233
114	Orbital characteristics of drifters in AC95a . . . . .	234
115	Orbital characteristics of drifters in AC95b . . . . .	235
116	Drifters snapshots (Apr.–June 1996) . . . . .	236
117	Drifters snapshots (June–Aug. 1996) . . . . .	237
118	April – June 1996 AVHRR images . . . . .	238
119	Orbital characteristics of drifters in C96b . . . . .	239
120	Orbital characteristics of a drifter in C96a . . . . .	240
121	Orbital characteristics of a drifter in AC96c . . . . .	241
122	Side view of the vortices . . . . .	258
123	Top view of the merging model . . . . .	259
124	Characteristics of the merged vortex, Part I. . . . .	260
125	Characteristics of the merged vortex, Part II. . . . .	261
126	Velocity and sea surface displacement . . . . .	262
127	Merged vortex with finite shear, Part IA . . . . .	263
128	Merged vortex with finite shear, Part IB . . . . .	264
129	Merged vortex with finite shear, Part IA . . . . .	265
130	Merged vortex with finite shear, Part IB . . . . .	266

# CHAPTER 1

## INTRODUCTION

The Hawaiian archipelago stretches over 2900 km across the central North Pacific Ocean (Fig. 1), within the North Pacific Subtropic Gyre. The major Hawaiian Islands are on the southeast end of the archipelago, near the latitude at which the gyre-scale flow turns westward to become the North Equatorial Current (NEC) (Fig. 2). Numerical models suggest that the islands block this westward current at its northern extent, leading to the creation of a pseudo-western boundary current known as the North Hawaiian Ridge Current (NHRC) [Qiu *et al.*, 1997]. Roden [1991] presents an overview of several processes which may arise from flow/topography interaction in the Hawaiian region.

Energetic eddies, both cyclonic and anticyclonic, are ubiquitous in the circulation immediately leeward of the Hawaiian Islands. They may be responsible for the westward-propagating oscillations seen in satellite altimetry and *in-situ* sea level measurements [Mitchum, 1995]. Patzert [1968] conducted the first extensive survey of these eddies. He showed that their peak speeds of  $O(1 \text{ m/s})$  can dominate the instantaneous currents along the west coast of Hawai'i and through the 'Alenuihaha Channel separating Hawai'i and Maui. Using hydrographic surveys through several eddies, Patzert examined their vertical and horizontal structure, and showed that they range in diameter from 50 to 150 km and extend to depths of 200 to 300 m. By comparing the hydrography to direct current measurements of several cyclonic eddies, Patzert demonstrated that they were nearly geostrophic. He noted that centrifugal effects may play a significant role in the dynamics of the anticyclonic eddies, but he did not have direct current measurements of the anticyclones to verify this hypothesis. When describing the generation, evolution and propagation of eddies, Patzert faced a considerable challenge: the data available to

him were typically hydrographic transects or short-term deployments of radio-tracked drifters. Thus, Patzert was forced to extrapolate a dynamical picture from what were essentially snapshots. He concluded that the eddies have a formation time of approximately one week to one month, and that they drift westward at speeds of 2.5 to 10 cm/s.

Hydrographic casts in the Hawaiian region have allowed mapping the gyre-scale circulation (c.f. [Wyrтки, 1974] and Fig. 2). However, these data do not reveal the sub-gyre-scale impact of the Hawaiian Islands upon the circulation: how do the islands modify the ambient impinging flow? In addition to the local effects (most notably, the lee eddies mentioned above), are there significant effects further downstream? Due to intense variability from lee eddies, long-term averaging is required to reveal the underlying mean currents west of the Hawaiian Islands. Before the advent of relatively cheap satellite observations, this was typically done by repeated hydrographic transects such as those of the Hawai'i-to-Tahiti Shuttle Experiment. During the Shuttle Experiment of 1979–1980, 43 hydrographic sections (to 1000 dbar) were made on 15 cruises [Wyrтки and Kilonsky, 1984]. Through most of the Hawaiian region, the transect ran along  $\sim 158^\circ \text{W}$ , thus providing a time series of zonal hydrographic currents in the wake of the Hawaiian Islands. These currents, reported by Wyrтки and Kilonsky [1984] and shown in Fig. 2, suggest that the island wake has a complex structure consisting of a series of opposite-flowing bands. Wyrтки and Kilonsky briefly noted the eastward flow at  $19.5^\circ \text{N}$ , associating it with the ubiquitous lee eddies. But what is the full two-dimensional structure of the island wake?

In the past, direct measurements of currents in the Hawaiian region have been mostly limited to the immediate coastlines of the islands. Klaus Wyrтки led an intense data gathering effort in the late 1960s and early 1970s; the resulting observations are presented in Wyrтки *et al.* [1967] and Wyrтки *et al.* [1969]. The mean currents from their

study, and from more recent current meter deployments, are shown in Fig. 3. As noted by Patzert and Wyrтки [1974], the observations suggest a mean clockwise flow around each island, possibly due to the rectification of higher-frequency motion [Luther, 1985].

In recent years, the database of WOCE drifting buoys in the Hawaiian region has grown dramatically, largely due to the deployment of 70 drifters in or near the immediate lee of Hawai‘i. Combined with shipboard ADCP measurements, satellite altimetry and AVHRR imagery, the data present a unique opportunity to observe the full life cycle of lee eddies, from birth and growth to propagation, interaction and spin-down. In addition, the database of CTD/XBT casts to depths of 1000 dbar has grown steadily. Using ships of opportunity, the database of shallower XBT casts has been greatly increased. The few ALACE drifters passing through the region offer some hints regarding the currents at the “level of no motion” of most current maps derived from hydrography. In addition, satellite scatterometer observations have provided two-dimensional maps of the evolving wind stress field, which can be used to estimate the Ekman drift of the WOCE surface drifters. *In-situ* measurements of the wind field around Hawai‘i, such as the Hawaiian Rainbands Project, allow the interaction of the trade winds with the islands to be characterized.

The goal of this study was to examine, characterize and understand the eddies and currents of the Hawaiian region in light of these data. The dissertation is organized in six chapters, as outlined below.

In Chapter 2, the data are presented. The design and operation of a standard WOCE drifter are described, including a discussion of positioning errors when tracking the drifter via satellite. The kriging method, used to interpolate the drifter fixes to 0.25-day intervals, is described in an appendix. Maps of the mean drifter speeds are presented, revealing the structure of the island wake: two elongated, counter-rotating gyres

extending 1000 km to the west of Hawai'i. Variance maps demonstrate the intensity of the eddy field in the island lee. The historical hydrography database is described, including a discussion of how density was estimated for the bathythermograph casts. The mean dynamic height field and its variance are calculated, and a map of the geostrophic currents is presented. The wind stress, satellite altimetry, *in-situ* sea level, sea surface temperature imagery, shipboard ADCP, and climatological data are also discussed.

Chapter 3 is devoted to the structure and life cycle of Hawaiian lee eddies. Accompanying this chapter, an appendix presents several commonly-used models of the radial structure of eddies, along with a generalized model developed for this study. The chapter begins with a discussion of their lowest-order dynamical balance, including the centrifugal effect noted by Patzert [1968]. As a result of this effect, anticyclones may have considerably stronger currents than given by thermal wind calculations from hydrography. A discussion of centrifugal instability demonstrates the significance of the “half-inertial” [Chew and Bushnell, 1990] anticyclone, several of which are noted in this study. A discussion of eddy generation follows, including a summary of Patzert’s [1968] conclusions regarding the significant mechanism leading to lee eddy generation. The data collected since 1969 continue to support his conclusion that the cyclones are wind-forced, but oceanic shear instability off Hawai'i’s South Point may be the dominant mechanism generating the anticyclones. The drifter, altimetry, and SST imagery data allow determination of the eddy generation frequency: strong eddies of both signs are generated at a 50–70 day period, while smaller cyclones occasionally form as rapidly as every 20 days. By tracking eddies in the altimetry and drifter tracks, their propagation characteristics are determined and compared to the theoretical calculations of Cushman-Roisin *et al.* [1990] and Chassignet and Cushman-Roisin [1991]. To lowest order, the eddies propagate westward at the speed of long baroclinic Rossby waves. De-

viations from this speed can be attributed to nonlinear effects, advection by the NEC, and eddy-eddy interaction. Several ADCP, drifter, altimetric, and SST imagery data of eddies are presented, giving a dynamical view of the Hawaiian lee eddy field. The data show that eddy decay can be modeled by entrainment, at a rate of  $\sim 2.7 \times 10^8$  kg/s. This result provides an estimate of an eddy's lifespan: the energy of the large anticyclones described in this study has an  $e$ -folding time scale of  $\sim 700$  days. The data shows that anticyclones propagate west-southwest from the South Point of Hawai'i in the form of a repeating vortex train, which crosses Johnston Atoll and contributes to the 90-day oscillations in sea level there. In addition, evidence is presented that the anticyclones may merge as they drift westward, in a repeating sequence governing the growth of the oceanic shear line defining the southern edge of the Hawaiian Island wake. The characteristics of a merged vortex are derived, and the relevant conservation laws for vortex merging are discussed, in an appendix.

In Chapter 4, the mean currents are examined in the drifter and hydrographic data. These data do not provide an identical picture of the currents in the Hawaiian region, and some sources of these discrepancies are discussed. A regression analysis is used to identify the directly wind-driven subinertial motion of the drifters. The drifter observations are used to calculate energy fluxes between the mean and eddy fields, and individual currents are examined in the two data sets. The banded structure of the island wake is demonstrated in both data sets. The counter-rotating, elongated wake gyres are separated by a narrow countercurrent the Hawaiian Lee Countercurrent (HLCC), which reaches a peak eastward speed of nearly 10 cm/s. Along the latitude of the HLCC, kinetic energy is converted from the eddy to the mean field at a rate of  $10\mu\text{W}/\text{m}^3$ , sufficient to spin up the HLCC from rest in  $\sim 10$  days. North of the HLCC, a newly-discovered current is identified which runs west-northwest along the leeward

coasts of the major Hawaiian Islands. This current is named the Hawaiian Lee Current (HLC). It has a mean speed of  $\sim 25$  cm/s, and is strongest when the HLCC is strongest, suggesting a similar dynamical origin. The HLCC joins with the North Hawaiian Ridge Current (NHRC) west of Kaua'i to form a strong, westward HLC/NHRC extension running along  $22^\circ\text{N}$  in the drifter data. The hydrography shows that dynamic height peaks in two nearly zonal ridges, one south of the HLCC (this feature is known as the North Equatorial Ridge) and one at  $22^\circ\text{N}$ , related to the HLC/NHRC extension seen in the drifter data.

Chapter 5 presents Lagrangian statistics calculated from the drifter trajectories. The chapter begins with a summary of the classical Taylor's Theorem for dispersion in a field of homogeneous, random turbulent motion, then describes how the diffusive properties of the lee eddies and the dominant space and time scales of variability are characterized using the drifter data. These calculations are performed in rectangular subregions of the Hawaiian area, showing that the lee eddies increase the effective eddy diffusivity by 1.3–1.6 times. The long-time meridional, and short-time zonal and meridional dispersion of drifters are consistent with classical theory for homogeneous turbulence. The long-time zonal dispersion is inconsistent with this theory, but (as shown in an appendix) can be attributed to the meridional shear in the predominantly zonal mean currents. The Lagrangian spectra, calculated from the drifter speeds, show that the peak eddy energy is from 5 to 40 days period. In the island lee, the anticyclonic component of the rotary spectra has several discrete peaks which may be a result of vortex merging. Outside of the eddy bands, the spectral slopes are close to  $-2$ , suggesting direct, off-resonant wind forcing [Hasselmann, 1976]. The relationship between the length and time scales of Hawaiian eddies is compared to previous studies; the eddies can be described by the kinematic law of Price (in [McWilliams *et al.*, 1983]), which assumes a constant length

scale.

In Chapter 6, the major conclusions of the study are summarized. Several questions remain to be answered conclusively, such as: What is the relative significance of the eddy generating mechanisms? Do anticyclones really merge as they drift westward from Hawai‘i? The dissertation concludes by outlining possible approaches to address these issues, for future researchers studying the physical oceanographic environment of the Hawaiian Islands.

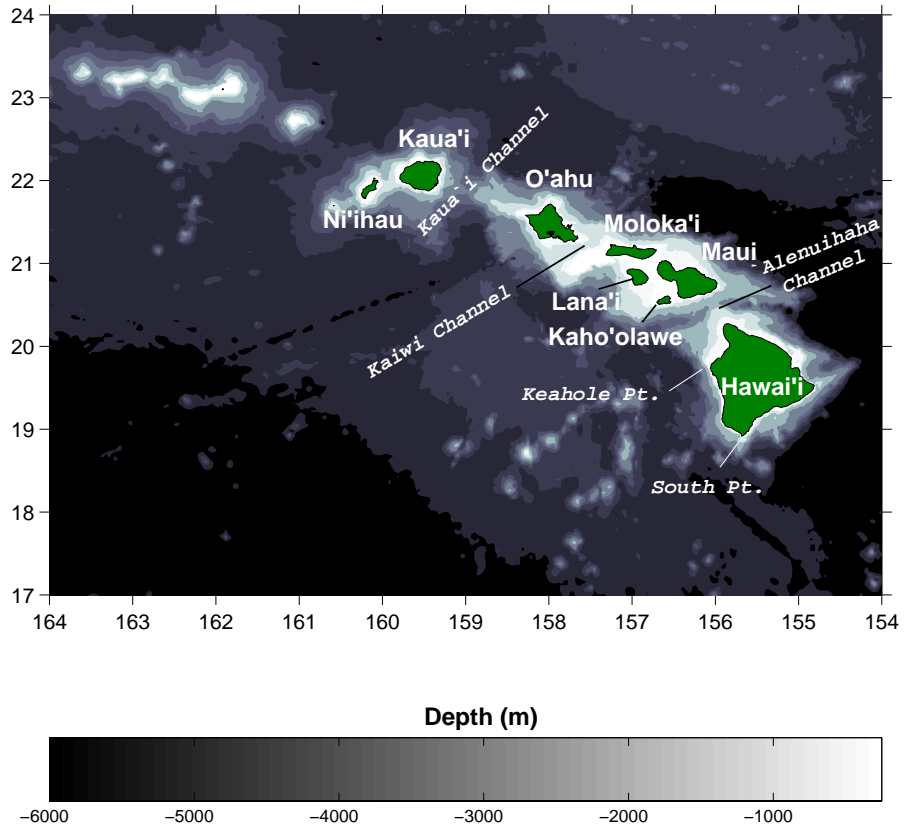


Figure 1: Map showing the major Hawaiian Islands and channels separating them. Bathymetry is from Smith and Sandwell [1995].

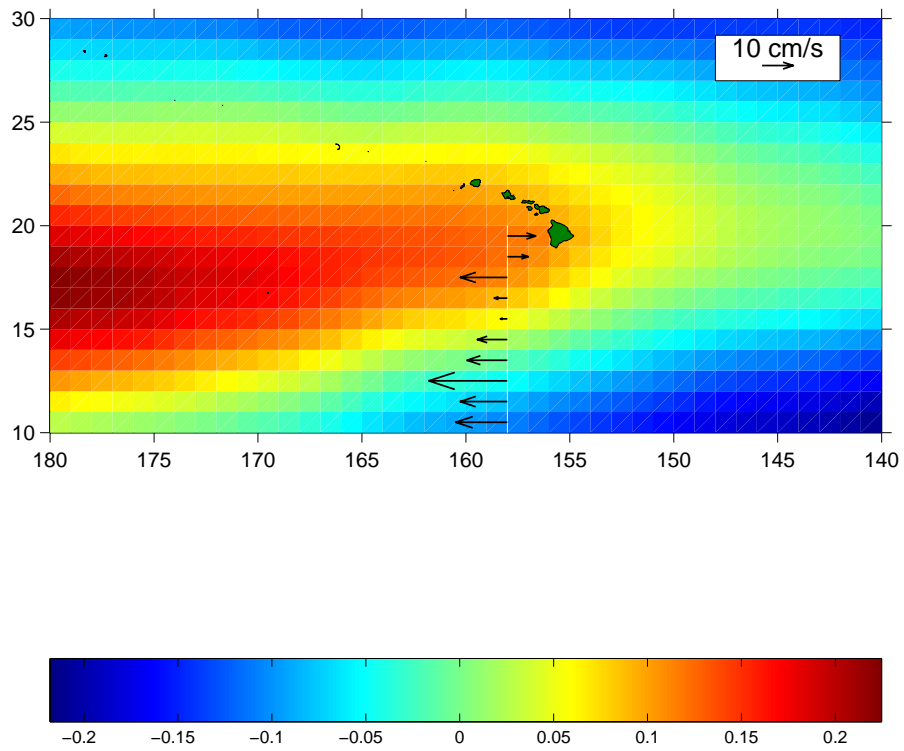


Figure 2: Shading: dynamic height from the Levitus94 climatology, with the mean removed. Arrows: zonal geostrophic currents from the mean Hawai'i-to-Tahiti Shuttle Experiment hydrography [Wyrтки and Kilonsky, 1984].

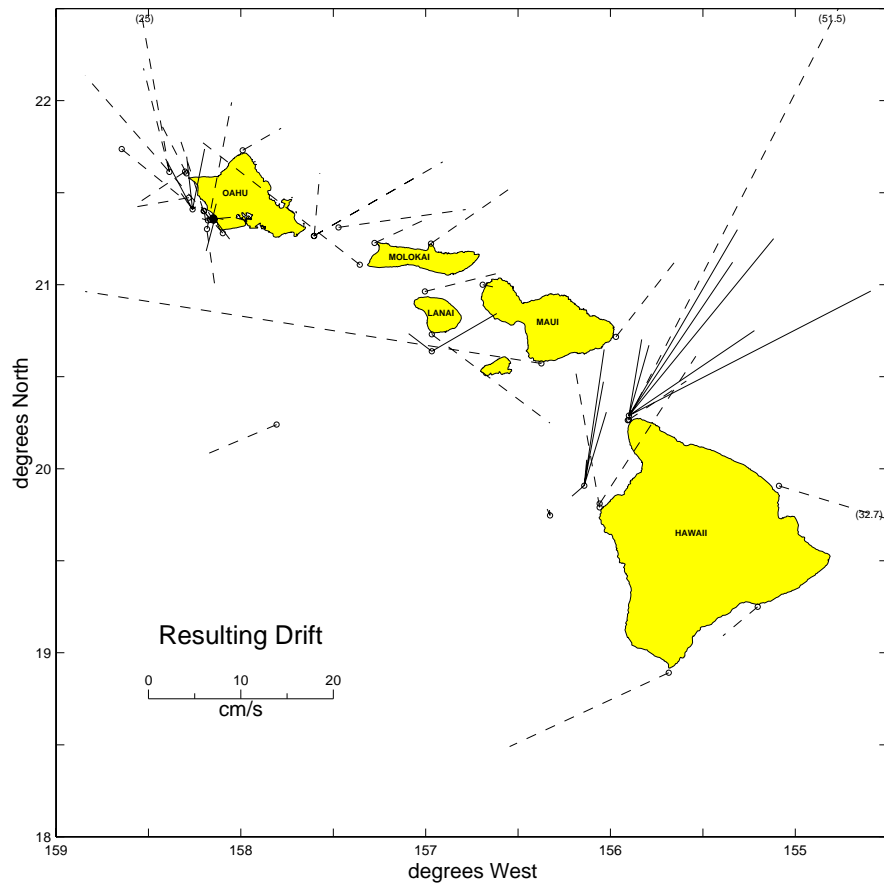


Figure 3: Mean currents measured by moorings in the Hawaiian Island region. Dashed lines are from Wyrтки *et al.* [1969]; solid lines are more recent measurements, including some deep deployments of Aanderaa current meters [Lumpkin, 1995].

## CHAPTER 2

### DATA

*The sources of data are presented, and the data are gridded to create maps of mean currents, temperature, dynamic height, sea level anomaly and their variance.*

#### 2.1 Satellite-tracked drifting buoys

As part of the WOCE Surface Velocity Program (SVP) and the Pelagic Fisheries Research Program, 356 satellite-tracked drifting buoys were deployed in or passed through the Hawaiian region ( $10^{\circ}$ – $30^{\circ}$ N,  $140^{\circ}$ – $180^{\circ}$ W). The resulting data set spans 286.3 drifter years.

A WOCE drifter is a fiberglass surface float containing a satellite (Argos) transmitter attached to a holey-sock drogue of diameter 1 m and length 6.5 m, centered at 15 m depth [Sybrandy and Niiler, 1991]. Drifters are not perfect water-followers: in addition to their inability to track vertical motion, they suffer from “slip,” or horizontal motion different than the current averaged over the drogue’s extent. Slip is caused by direct wind forcing, drag on the surface float induced by wind-driven shear, and surface gravity wave rectification [Niiler *et al.*, 1987; Geyer, 1989]. Other factors, such as shear-induced tilt and rectification of near-inertial waves [White, 1986], may play a lesser role (although these influences could become significant with very long tethers [Geyer, 1989]). In order to minimize surface wave rectification, the surface float is spherical and decoupled from the drogue by a neutrally-buoyant subsurface float [Niiler *et al.*, 1987; Niiler *et al.*, 1995]. The surface float has a submergence sensor, which can be used to identify drifters which have lost their drogues. The evenly-spaced holes in the drogue reduce vortex shedding, so that the drogue’s drag coefficient does not abruptly change across a critical Reynolds number [Nath, 1977]. To reduce wind-induced slip, the drogue’s drag area (drag coefficient times cross-sectional area) is roughly 50 times that of all other

drifter components; the resulting downwind slip has been measured at approximately  $7 \times 10^{-4}$  m/s per m/s of wind speed for winds up to 20 m/s [Niiler and Paduan, 1995].

Once deployed, a drifter's position is inferred from the Doppler shift of its 400 MHz transmission observed by NOAA Polar Orbiting Environmental Satellites [Niiler *et al.*, 1987]. The position-deducing algorithm is described in the Argos User Manual [1996], and can be summarized as follows. As the satellite approaches, passes, and recedes from the latitude of a drifter, its 7.4 km/s speed Doppler-shifts the signal. The timing of the swing from blue shift to red shift (but not exactly the latitude of zero Doppler shift; see below) gives the drifter's latitude, and the rapidness of the swing gives the off-track distance (the closer the satellite pass is to the drifter, the more step-like the swing is). The absolute motion of the drifter introduces an additional Doppler shift: at 20°N, a fixed point on the Earth's surface travels westward at 437 m/s. Thus, if the drifter is east of the satellite pass, an additional blue shift is added which reaches its maximum as the satellite passes the latitude of the drifter. This Doppler shift diminishes as the satellite moves off the drifter's latitude, with a rate of decay depending on the minimum satellite/drifter distance (greater minimum distance equals slower decay). The sign of this shift is estimated using least-squares fitting and the previous history of the drifter, and gives the off-track direction. As mentioned above, the drifter's latitude is not given by the satellite's latitude when there is no Doppler shift: the shift from the drifter's motion must be included as an offset. The largest positioning errors occur when a track is close to a drifter, but not directly over it. In this case, the Doppler shift from the absolute drifter motion is a relatively brief spike which can be difficult to resolve, possibly leading to a 180° error in the offtrack direction (and a slight latitudinal error due to the incorrect Doppler offset).

Positioning errors in the Hawaiian region were estimated by analyzing fixes of a sta-

tionary drifter. The drifter was allowed to transmit at Snug Harbor, O‘ahu for 70 days, yielding 325 fixes (Fig. 4). The latitudinal (approximately alongtrack) component of the positional fixes had a standard deviation of  $2.4 \times 10^{-3}$  degrees. This error was dominated by two outliers, the largest of which was  $1.4 \times 10^{-2}$  degrees north of the median. For the longitudinal component, the standard deviation was  $6.1 \times 10^{-3}$  degrees, dominated by a single outlier  $6.1 \times 10^{-2}$  degrees east of the median. These rms errors (approximately 630 m zonally, 270 m meridionally) are larger than the 300 m, 200 m errors estimated by Poulain and Niiler [1989], perhaps because their shorter time series did not include the dramatic but rare outliers seen in Fig. 4. The mean position with standard error bars is  $21.3166^\circ\text{N} \pm 1.3 \times 10^{-4}$ ,  $157.8870^\circ\text{W} \pm 3.4 \times 10^{-4}$ . To test for systematic error, the drifter’s position was measured with a hand-held GPS receiver. After 30 minutes, the GPS position stabilized at  $21.3161^\circ\text{N}$ ,  $157.8875^\circ\text{W}$ . The discrepancy in latitude is 11 m, while the longitude discrepancy is 156 m. This error is significant, and is due to the single large outlier. This erroneous fix was probably an incorrect “guess” of the offtrack direction for a pass along  $\sim 157.85^\circ\text{W}$ . Because the Doppler offset was assumed blue (when it should have been red) this fix is also the northernmost outlier. Of course, the median filter could be used on this data (the median position was  $21.3160^\circ\text{N} \pm 2.6 \times 10^{-4}$ ,  $157.8870^\circ\text{W} \pm 2.7 \times 10^{-4}$ ), but the mean statistics are more representative of errors inherent in any single fix of a deployed drifter.

To eliminate the more egregious errors in the raw fixes, a two-step quality evaluation scheme was used [Hansen and Poulain, 1996]. In this method, the velocity is calculated via finite differencing of the raw fixes, both forwards and backwards in time. A fix is flagged as “bad” if it generates a velocity greater than four standard deviations from the mean velocity in both the forward and backward pass. Two-way differencing is used because one-way approaches may fail if a bad value comes immediately after a

gap in data acquisition [Hansen and Poulain, 1996]. Fixes from drifters which had lost their drogues (indicated by the submergence sensor), grounded, or been picked up by fishermen were also discarded.

Upon deployment, most drifters continuously transmitted for 30 days, then switched to a 1/3 duty cycle (transmitting for 24 hours every 72 hours) to conserve power. While continuously transmitting, an average of  $6.220 \pm .104$  fixes per day were provided by service Argos. From day 31 to day 200 after deployment, an average of  $2.155 \pm 0.34$  fixes per day were obtained (excluding the four drifters which did not switch to a 1/3 duty cycle at day 30). Starting at about day 280, most drifters began losing their positive buoyancy (Fig. 5). At day 450, half the drifters had sunk beneath the ocean surface. Presumably, this loss of buoyancy was due to biofouling. Some drifters continued transmitting much longer than the half-life of 450 days, although the number of fixes per day for any particular drifter approached zero as time increased.

In order to create a homogeneously-spaced record of drifter positions, the raw positions (ranging from over 6 fixes per day to 30 days between fixes) were interpolated to 0.25-day intervals. Gaps greater than 30 days were not interpolated.<sup>1</sup>

Interpolation was done via the kriging method (Appendix A). Kriging assumes the observations consist of a true signal with known autocorrelation, plus noise of known variance. The variance from the grounded drifter characterized the noise, and the fractional Brownian structure functions of Hansen and Poulain [1996] gave the velocity autocorrelation function. Velocity was estimated by finite differencing these interpolated positions.

To examine the effect of position fix errors on eddy kinetic energy estimates, the quality evaluation and kriging algorithms were applied to the grounded drifter's fixes.

---

<sup>1</sup>The three largest interpolated gaps were 15.4, 12.2 and 10.0 days long.

The resulting time series had a variance of  $5.65 \times 10^{-4} \text{ m}^2/\text{s}^2$  zonally,  $5.36 \times 10^{-6} \text{ m}^2/\text{s}^2$  meridionally. The zonal variance is very close to Poulain and Niiler’s [1989] estimate of  $4 \times 10^{-4} \text{ m}^2/\text{s}^2$  for interpolated fixes of grounded drifters. Because this variance is approximately two orders of magnitude lower than the variance of deployed drifters, it can be concluded that position fix errors do not significantly contaminate observations of EKE.

Fig. 6 shows the full set of interpolated positions in the Hawaiian Island region. Coverage is densest immediately to the west of the island of Hawai’i, where 58 drifters were deployed between 1994 and 1996. The interpolated tracks in this area are predominantly cycloidal due to energetic lee eddies (Chapter 3). South of  $16^\circ\text{N}$ , coverage is sparser and the trajectories are considerably more zonal. In this region, variations in the trajectories are not organized cycloids, but rather large-scale migrations from purely zonal motion. East and north of the islands, the tracks are a mix of cycloids, meanders, and relatively straight trajectories without any visually-obvious pattern.

Drifter coverage is far from homogeneous in time. The drifters were deployed in batches; for example, 13 were deployed south of Moloka’i and Maui during a four-day cruise in September 1994. Another eight were deployed during a 10-day cruise in July–August 1995 in the immediate lee of Hawai’i. Fig. 7) shows the density of data coverage in subregions of the study region as a function of time. Data density increased sharply in 1990–1992 due to SVP deployments to the east; many of these drifters propagated westward into the study region. In the subregion  $16\text{--}23^\circ\text{N}$ ,  $155.5\text{--}180^\circ\text{W}$ , data density increased sharply in 1994 due to the local deployments.

Interpolation at 0.25-day intervals creates many more velocity measurements than there are independent degrees of freedom. To estimate the number of independent observations for means and their error bars, the following procedure was used. First,

interpolated data were divided into 20-day segments. The zonal and meridional components of the current were decomposed into mean components and fluctuations ( $u'$ ,  $v'$ ) about the means. The autocorrelation functions of  $u'$  and  $v'$  were calculated, giving the decorrelation time scales (lag of the first zero crossing) of  $u'$  and  $v'$ . The 20-day segments were then resampled at the larger of the two decorrelation time scales. This subsampled data will subsequently be referred to as the “independent” drifter data.

Mean currents were mapped by dividing the region into  $2^\circ$  (zonally) by  $1^\circ$  (meridionally) cells. All independent data within each cell were then averaged (Fig. 8). The mean currents (Fig. 9) show the westward North Equatorial Current (NEC) impinging on the island of Hawai'i (Fig. 10), where it bifurcates into the North Hawaiian Ridge Current (running along the northeast side of the ridge) and the main body of the North Equatorial Current south of the islands. In the lee of the islands, an extensive wake extends westward for hundreds of kilometers. The wake is composed of counter-rotating, elongated gyres separated by a narrow counter-current at  $19.5^\circ\text{N}$ . These currents will be discussed individually in Chapter 4.

The variance of the currents is dramatically magnified in the island lee (Fig. 11); the highest value,  $0.35\text{ m}^2/\text{s}^2$ , is 7.6 times the mean variance in the region  $140\text{--}154^\circ\text{W}$ ,  $18\text{--}20^\circ\text{N}$ . This increase in EKE is associated with the energetic lee eddies, which are discussed in Chapter 3. The variance ellipses (Fig. 12) reveal a nearly isotropic EKE field away from topography, with alongshore polarization close to the islands. Averaged over the entire region, zonal variance is  $2.70 \times 10^{-2} \pm 4 \times 10^{-4}\text{ m}^2/\text{s}^2$ , slightly but significantly greater than the mean meridional variance of  $2.12 \times 10^{-2} \pm 4 \times 10^{-4}\text{ m}^2/\text{s}^2$ .

Because the data density is very high in the immediate lee of the islands, it is possible to construct a relatively high-resolution current map in that region. Fig. 13 shows the mean drift speeds with standard error ellipses, revealing the eastward ends of

the counter-rotating lee gyres. From these currents, the mean divergence and curl can be calculated on a standard C-grid. These fields are shown at the bottom of Fig. 13. The standard errors were calculated via bootstrapping, and cells with divergence or curl significantly different from zero (to one standard error) are indicated by white dots. The mean curl map shows the predominantly cyclonic/anticyclonic vorticity of the northern/southern lee gyre.

Most of the WOCE drifters had temperature sensors at the base of the surface float, allowing them to transmit the *in-situ* SST at each satellite pass. These data were linearly interpolated to the 0.25-day grid of the velocity data. A total of 273.7 drifter-years of temperature data were collected. Because this study is primarily concerned with mesoscale fluctuations in SST, the seasonal signal was identified by performing a least-squares fit of a sinusoid (with annual period) onto the interpolated temperature, then removing it from the data (Fig. 14). The best fit had an amplitude of  $1.65^{\circ}\text{C}$  and peaked on day 241 (August 29). To test the assumption of spatial homogeneity in the amplitude and phase of the seasonal SST signal, this analysis was repeated over six rectangular subregions (constructed by evenly dividing the study region into 3 zonal by 2 meridional cells). The phase of the subregions was extremely consistent, with maximum temperature falling at most 16 days from the calculation performed over the whole region. In the northern four subregions (north of  $16.5^{\circ}\text{N}$ ), the amplitude was consistent, varying from the overall mean by a maximum of  $+0.32^{\circ}\text{C}$ . The southern two subregions had a considerably smaller seasonal signal, with amplitudes of  $0.47^{\circ}\text{C}$  and  $0.46^{\circ}\text{C}$ . Thus, the assumption of spatial homogeneity is reasonable for most of the region, but the resulting “corrected” SST data are not ideal for a study of baroclinic fluxes in the core of the NEC (which is outside the scope of this study). The spatially-averaged temperature (Fig. 15) shows that the isotherms near the Hawaiian Ridge run

approximately parallel to it, and that the mean temperature increases from  $\sim 20^{\circ}\text{C}$  to  $\sim 28^{\circ}\text{C}$  between the northern and southern extent of the study region. The SST variance is very large ( $> 2$  degrees squared) along the northwest edge of the study region, in the vicinity of the Subtropical Front (c.f. [Cushman-Roisin, 1984]).

## 2.2 Hydrography

Conductivity-temperature-depth (CTD), expendable bathythermograph (XBT), and mechanical bathythermograph (MBT) casts were used to provide independent current estimates in the Hawaiian region. Data were compiled from the January 1991 NODC archives [CD-ROM NODC-03], the Global Temperature-Salinity Pilot Project archives, and the World Ocean Atlas 1994. The area has been densely sampled by bathythermographs (hereafter referred to as XBTs, but including the older MBT data), with more coarse CTD sampling (Fig. 16).

### 2.2.1 Calculating density for bathythermograph casts

Because an XBT does not measure salinity, an appropriate salinity profile must be simulated for each cast. To do this, the study region was divided into non-overlapping  $10^{\circ}$ (zonal) by  $5^{\circ}$ (meridional) cells. In each cell, the mean temperature-salinity (T-S) curve was computed from CTD casts (Fig. 17). A salinity profile was then estimated for each XBT cast from its temperature profile and the mean T-S curve in the appropriate cell [Emery, 1975].

The mean T-S curves (Fig. 17) show the spatial distribution of water masses in the Hawaiian region. North Pacific Bottom Water (NPBW) is the coldest water in all T-S curves [Tung *et al.*, 1986; Johnson and Toole, 1991]; this water mass is a mixture of North Atlantic Deep Water, Antarctic Bottom Water, and Antarctic Circumpolar Water created in the southern oceans [Mantyla and Reid, 1983]. Overlying the NPBW

is the fresher (34.5 PSU) North Pacific Deep Water (NPDW), which marks a bend in many of the T-S diagrams at 4-6° C [Johnson and Toole, 1991]. In all cells south of 20°N, and in the cell centered at 20°N, 150°W, modified NPIW appears as a salinity maximum ( $\approx 34.7$  PSU) at 10° C. This extremely old water is believed to be produced by mixing in the North Equatorial Current/Countercurrent region [Wyrтки, 1977]. Above this, North Pacific Intermediate Water (NPIW) creates a salinity minimum at 8-12° C, reaching salinities as low as 34 PSU. NPIW is generated in high-precipitation regions of the northwest Pacific [Reid, 1965], and is most pronounced in the northern half of the region. Along the northern edge of the study region, the saline Tropical Water lies at the surface. Tropical Water is created in the subtropical front, where evaporation considerably exceeds precipitation [Tsuchiya, 1968]; following the subtropical gyre clockwise through the cells, Tropical Water is subducted under warmer, fresher surface water south of the subtropical front.

### *2.2.2 The dynamic height field*

For all casts, the specific volume anomaly was calculated using the UNESCO [1981] equation of state. This was then integrated to obtain dynamic height relative to 400 dbar and 1000 dbar. Dynamic height was not calculated from casts with less than 4 measurements between the surface and the reference depth, no data in the upper 25 m, or density not monotonically increasing with depth. Many XBT casts had maximum depth between 400 and 500 m; thus, data coverage drops precipitously as the reference level is deepened (Table 2.1).

The mean dynamic height anomaly relative to 400 dbar is shown in Fig. 9. The map was calculated by averaging the dynamic height data in 5°(zonal) by 2°(meridional) cells, spaced every 2.5°(zonally) and 1°(meridionally), and removing the overall mean. The corresponding number of data points per cell is shown in Fig. 8. Geostrophic cur-

Table 2.1: Number of dynamic height estimates as a function of reference level.

Reference level (dbar)	Number of estimates
400	60,169
500	13,015
600	8,777
1000	2,282

rents from the dynamic height gradients (superimposed in Fig. 9) show the subtropical gyre sweeping southeast along the island chain, turning southward at  $20 - 22^\circ\text{N}$ , and westward south of  $20^\circ\text{N}$  [Wyrтки, 1974]. An eastward countercurrent flows towards the islands from the western edge of the map, tracing the northern edge of the 0.2 m high North Equatorial Ridge which rises above the surrounding topography [Wyrтки, 1974]. With the high resolution of the XBT data set in this study, the North Equatorial Ridge appears narrower than in smoothed, large-scale maps such as those of Wyrтки [1975] and the Levitus94 climatology. It extends WSW from the immediate lee of the island of Hawai‘i.

There are a number of discrepancies between the currents seen by the drifters and those inferred from the hydrography, ranging from the gyre-scale pattern to the strengths of individual currents. Some sources of these differences are discussed in Chapter 4.

Variance in dynamic height is largest west of the Hawaiian Islands (Fig. 11). A swath of maximum variance coincides with the North Equatorial Ridge, extending from the island of Hawai‘i to  $15-18^\circ\text{N}$  at  $180^\circ$ . A secondary swath of high variance extends west of the islands to  $20-24^\circ\text{N}$  at  $180^\circ$ , separated by the former high variance region by a ribbon of relatively low variance extending along  $19^\circ\text{N}$  from  $180^\circ$  to  $165^\circ\text{W}$  (approximately the western edge of the counter-current seen in the drifter data). High variance is also found at  $10-12^\circ\text{N}$ ,  $140-150^\circ\text{W}$  (a relatively well-sampled region) and northwest of the islands (where the sampling is very sparse).

### 2.3 Winds

The easterly trade winds dominate the large-scale atmospheric circulation in the Hawaiian region. A time series of this wind stress has been provided by the European Research Satellite (ERS) since August 1991. The AMI scatterometer aboard the ERS-1 satellite measured radar backscatter at 5.3 GHz (C-band) over a 500 km swath [CD-ROM ERS-1]. The wind speed vector at 10 m height is estimated from the backscatter using an empirical model. Wind stress is calculated from wind speed using Smith's [1988] drag coefficient model and an air density of  $1.225 \text{ kg/m}^3$ . The estimates are averaged on a  $1^\circ \times 1^\circ$  grid; in our study region, each grid has an average of 2.6 independent estimates per week. These averages are then interpolated to one week intervals via Kriging, with structure functions evaluated from the European Center for Medium-Range Weather Forecasts (ECMWF) surface wind product. Compared to in-situ Tropical Atmosphere/Ocean buoy measurements, ERS-1 winds are slightly underestimated at speeds greater than 18 m/s, and have an rms error of 1.2 m/s; the means are not significantly different at the 95% confidence level [Graber *et al.*, 1996].

A time series of the spatially-averaged wind stress is shown in Fig. 18. Averaged over time, the mean stress is  $(\tau_x, \tau_y) = (-6.30 \times 10^{-2} \text{ Pa}, -2.35 \times 10^{-2} \text{ Pa})$ . The trade winds are steady from March to September, and tend to increase from mid-October to early December. Marked weakening of the westward wind stress (a condition known as "Kona winds") occur most frequently in January and February. Many of the prominent wind stress fluctuations are reflected in the zonal speed of drifters east of the islands (Fig. 18), presumably due to the gyre-scale wind stress curl varying with the speed of the trades.

The  $1^\circ$  resolution of the ERS-1 wind stress product is a significant weakness when examining mesoscale wind-driven motion. Because the major islands stand above the

trade wind inversion layer, the winds are forced to flow around them. This creates extensive wind shadows containing trapped atmospheric vortices in the island lees, and concentrated wind jets between the islands [Patzert, 1968]. High-resolution snapshots of wind at the island of Hawai'i were obtained by the NCAR aircraft *Electra* as part of the Hawaiian Rainbands Project (HaRP) in July and August 1990 [Smith and Grubisić, 1993]; a composite of these snapshots clearly reveals that interaction between the island and the large-scale trades produces extremely fine-scale features such as the shear lines along the edges of the island's wind shadow (Fig. 19). Unfortunately, while these features may be critical in understanding the generation of lee eddies, they are almost completely unresolved in the ERS-1 data.

## 2.4 Altimetry

ERS-1 and TOPEX satellite altimetry covering October 1992 to October 1995 were compiled for a subset of the study region ( $14\text{--}20^\circ\text{N}$ ,  $155\text{--}180^\circ\text{W}$ ) in order to examine the propagation of lee anticyclones. The European Space Agency ERS-1 satellite had a cross-track spacing of 80 km and a repeat cycle of 35 days, while the NASA/CNES TOPEX/Poseidon satellite has a cross-track spacing of 270 km and a repeat cycle of 35 days. The noisier ERS-1 data were corrected with the TOPEX data at their joint crossover points, using the minimization technique of Traon *et al.* [1995].

The mean altimetry (Fig. 20) is in general too contaminated by errors in the geoid to be useful for oceanographic purposes. However, the sea level anomaly (fluctuations around the mean) can dramatically reveal mesoscale features such as the lee eddies of this study. A map of the spatially-averaged SSH variance is shown in Fig. 20; it reveals a fan of high variance following the path of the North Equatorial Ridge WSW from Hawai'i. Another region of high variance lies along the northern edge of the map ( $20^\circ\text{N}$ ), from

170–180°W. These features have been studied by Munch [1996], who demonstrated that they originate at Hawai‘i and speculated that they are associated with lee eddies.

## 2.5 In-situ sea level

Johnston Atoll (16.75°N, 169.52°W) and Wake Island (19.28°N, 166.62°E) lie to the west of the Hawaiian Islands. As shown in chapter 3, lee eddies generated at Hawai‘i may frequently propagate across Johnston, and perhaps also influence sea level at Wake. While an anticyclonic eddy passes, sea level should be raised; the passage of a cyclonic eddy should lower sea level.

Hourly in-situ sea level from Johnston and Wake were obtained for the period 1 January 1985 to 15 March 1997.<sup>2</sup> There were no gaps in the Wake record. The Johnston record had three gaps, the largest of which was 11.3 days long in October 1991.

The tidal signal was estimated by fitting sinusoids of the 49 major tidal constituents to the sea level records. The frequencies of these constituents were calculated using the Doodson numbers presented in Godin [1972]. This tidal signal was then removed from the records.

After removing the tides, gaps in the Johnston record were filled by linear interpolation.

## 2.6 Sea surface temperature

Advanced Very-High Resolution Radiometer (AVHRR) images were used to examine sea surface temperature. These images were a valuable tool for examining cyclonic eddies, which were often clearly visible due to the cold water upwelled in their cores. Anticyclones, which press the thermocline down in their cores, were generally not visible in the AVHRR data.

---

<sup>2</sup>Available from the University of Hawai‘i Sea Level Center [<http://www.soest.hawaii.edu/UHSLC/>].

The resolution of the AVHRR images is  $1.25 \times 1.25$  km. The radiometers which collect these data are deployed aboard NOAA Polar-Orbiting Environmental Satellites. They collect data in the visible, near infrared, and infrared spectrum [<http://edcwww.cr.usgs.gov/glis/hyper/guide/avhrr>]. In 1993 and 1994, radiometers were deployed aboard satellites NOAA-11 and NOAA-12. NOAA-14 was launched in December 1994, and collected additional AVHRR images. Approximately 7–8 images per day were collected over the Hawaiian region.

Due to errors in the satellite clock and horizon tracker, the satellite position can be up to 10 km off [SeaSpace, 1992]. These errors are corrected by image navigation, a process in which the image coastline is shifted to fit the known positions of the islands. On average, approximately half the images could not be navigated (usually due to heavy cloud cover) and were rejected for this study.

Sea surface temperature was calculated from radiometer observations in two infrared bands using a NOAA/NESDIS algorithm, which uses the view angle of the satellite and differences between the IR channels to correct for atmospheric water vapor attenuation [Dousset and Flament, 1995].

## **2.7 Shipboard ADCP**

Shipboard Acoustic Doppler Current Profiler (ADCP) data were obtained from the NODC/UH SAC Shipboard ADCP Global Database. Within this database, 22 cruises passed through the Hawaiian region. On several occasions, the ADCP transects provided valuable cross-sections through lee eddies, revealing their currents to depths of  $\sim 400$  m.

## **2.8 Mixed-layer depth**

Monthly mixed layer depth on a  $1^\circ \times 1^\circ$  grid was obtained from the Levitus94 climatology [<http://ingrid.ldgo.columbia.edu/SOURCES/LEVITUS94>].

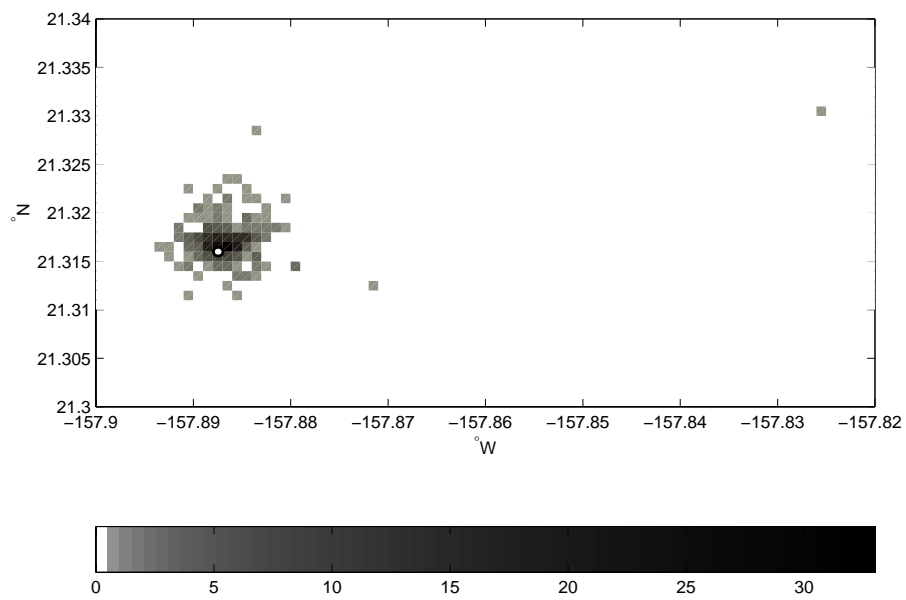


Figure 4: Raw fixes of a drifter grounded at Snug Harbor, O'ahu (shading, units: number of fixes). The drifter was stationary for 70 days; 325 fixes were obtained. The GPS position of the drifter is indicated by the dot.

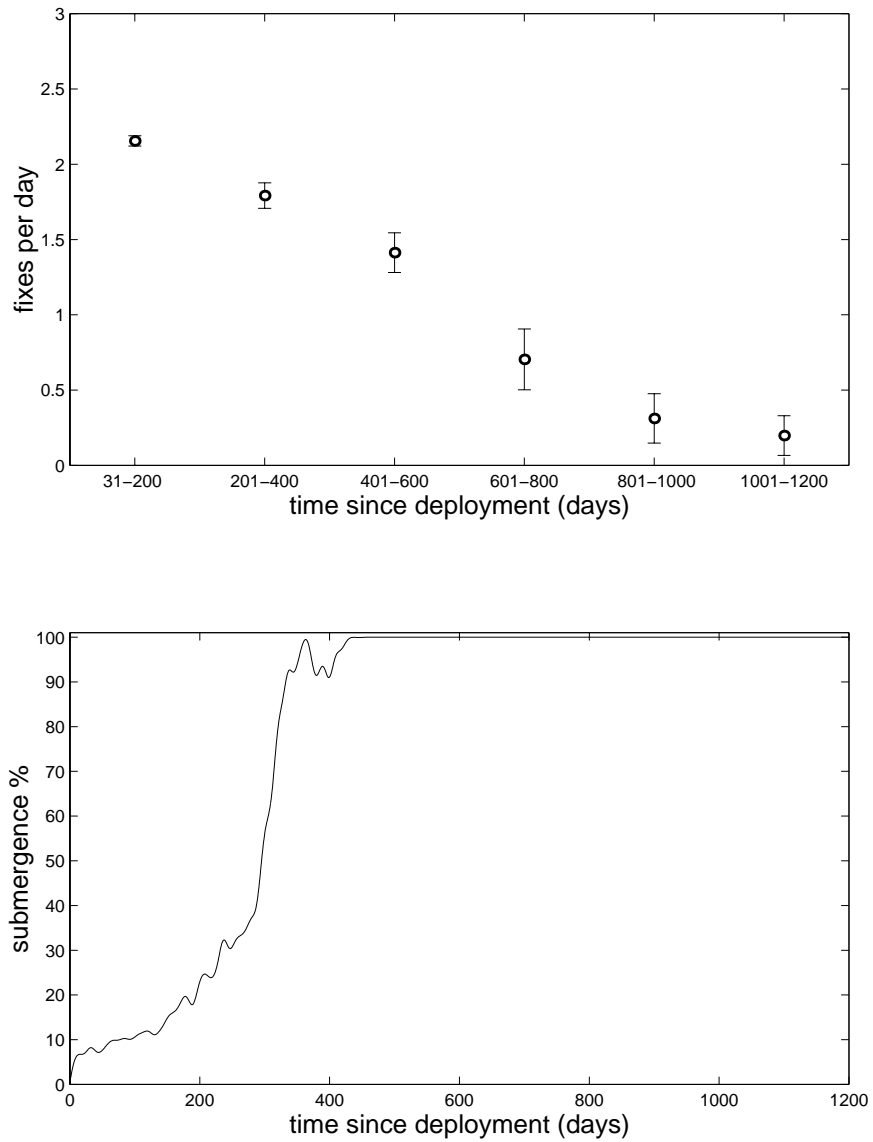


Figure 5: *Top*: Mean number of fixes per day as a function of days since deployment for 42 drifters deployed in the Hawaiian Island region. Drifters have not been included which lost their drogues, ran aground, or were taken by fishermen. *Bottom*: Median submergence of the 42 drifters as a function of time since deployment. The half-life of the drifters is approximately 450 days.

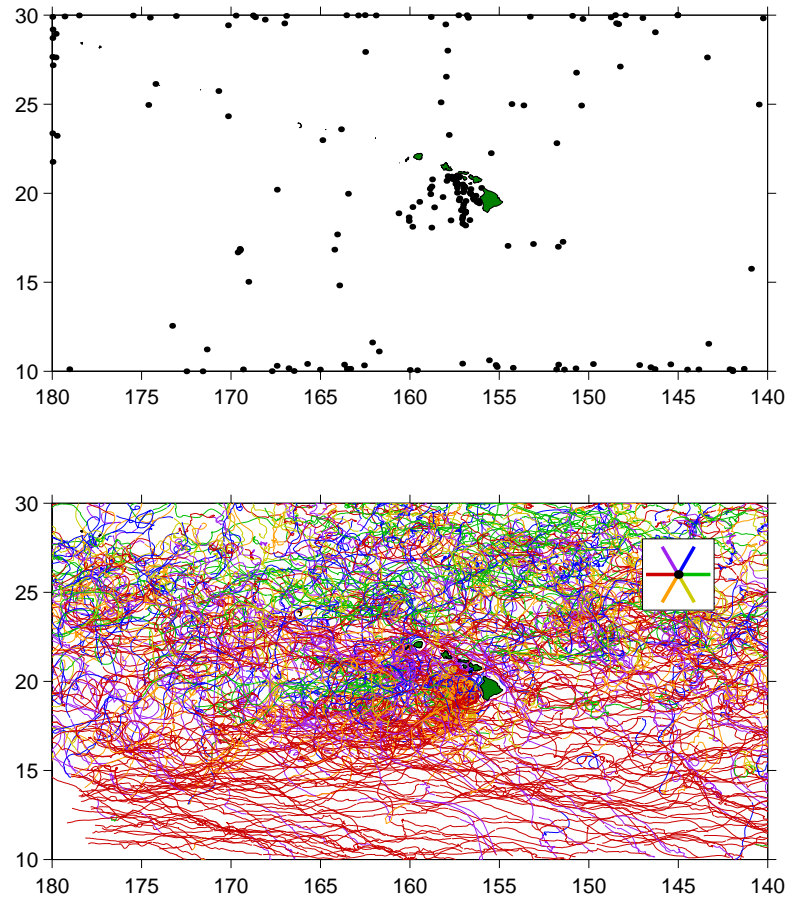


Figure 6: *Top:* initial locations of drifters. Away from the edges, a point indicates where a drifter was first fixed by satellite. Along or near the edge, a point shows where a drifter entered the study region.

*Bottom:* spaghetti plot of the drifter tracks in the study region, interpolated to 0.25 days. The tracks have been broken into 20-day segments and colored according to the direction of mean drift (see legend at upper-right).

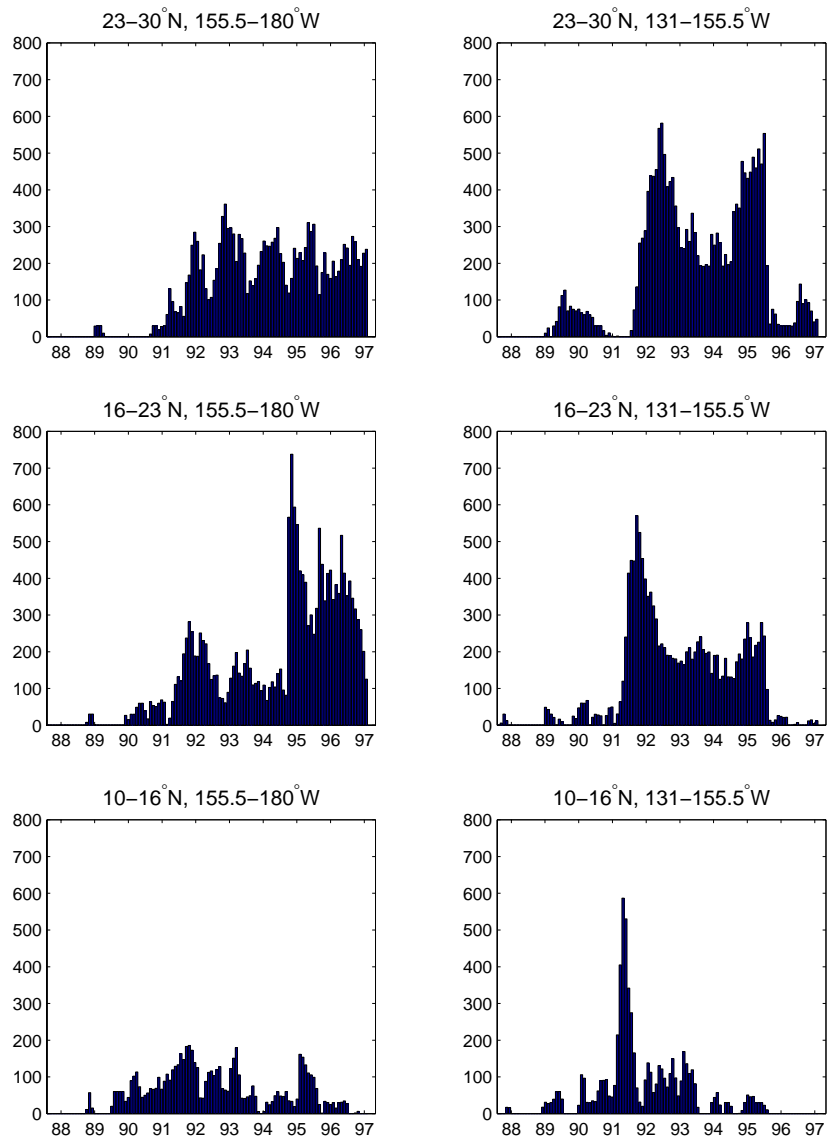


Figure 7: Density of drifter coverage in subregions of the Hawaiian region, showing number of drifter days (vertical axes) in each 30-day period from July 1987 to March 1998 (horizontal axes). The title of each subpanel gives the coordinates of the rectangular subregion.

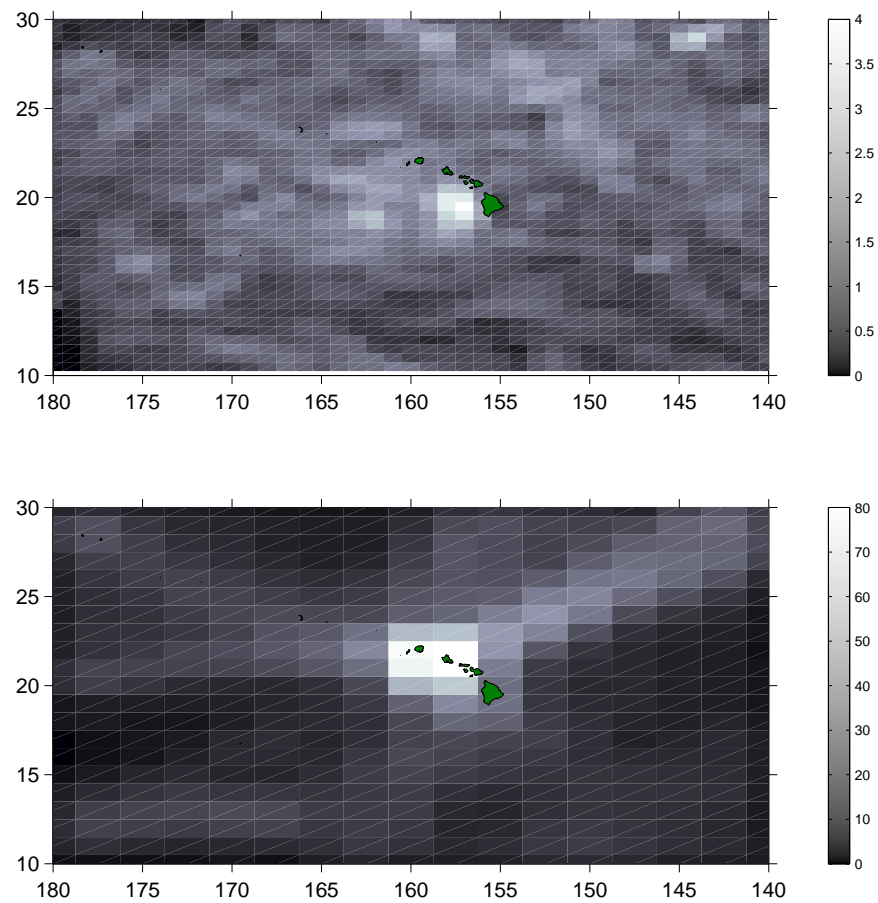


Figure 8: *Top*: Number of independent observations (1=100 observations) in each cell for the drifter-derived mean currents.  
*Bottom*: Number of XBT/CTD casts (1=100 casts) exceeding 400 dbar.

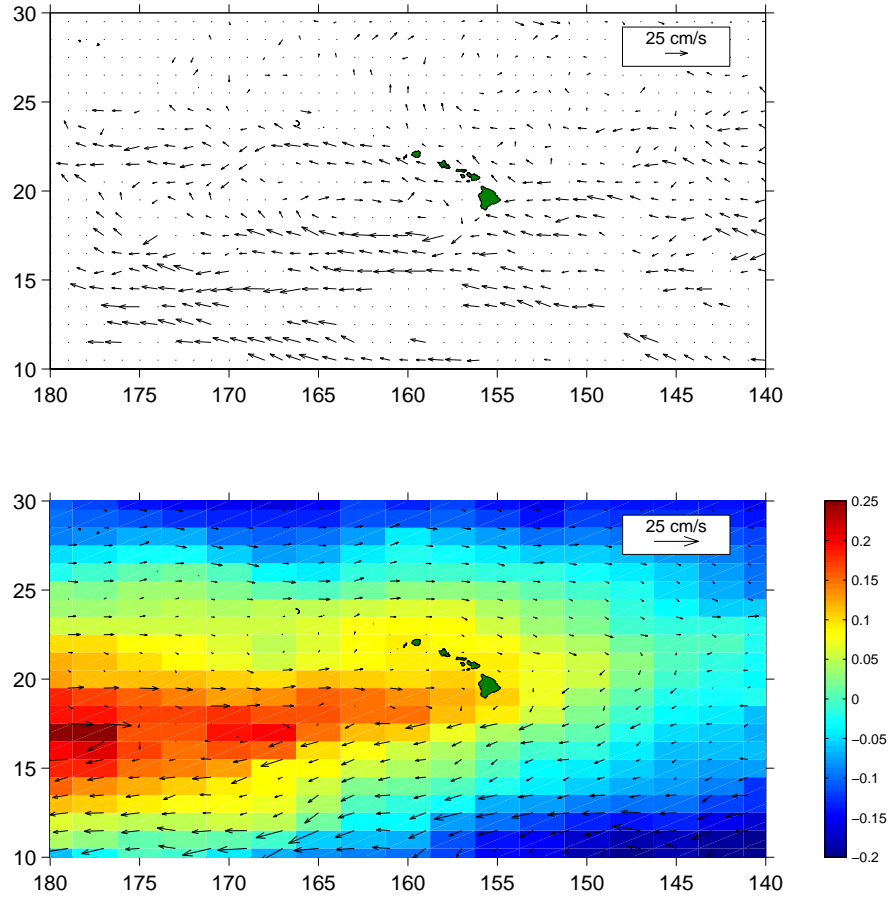


Figure 9: *Top:* Mean speed of drifters in the Hawaiian region. Arrows are not shown where the current is not significantly different than zero or where less than 25 observations fall in that cell. Meridionally, every arrow is independent. Zonally, every other arrow is independent.

*Bottom:* Mean dynamic height anomaly (shaded, in m) relative to 400 dbar. Every other cell is independent. Arrows show the geostrophic currents, estimated from four-point finite differencing.

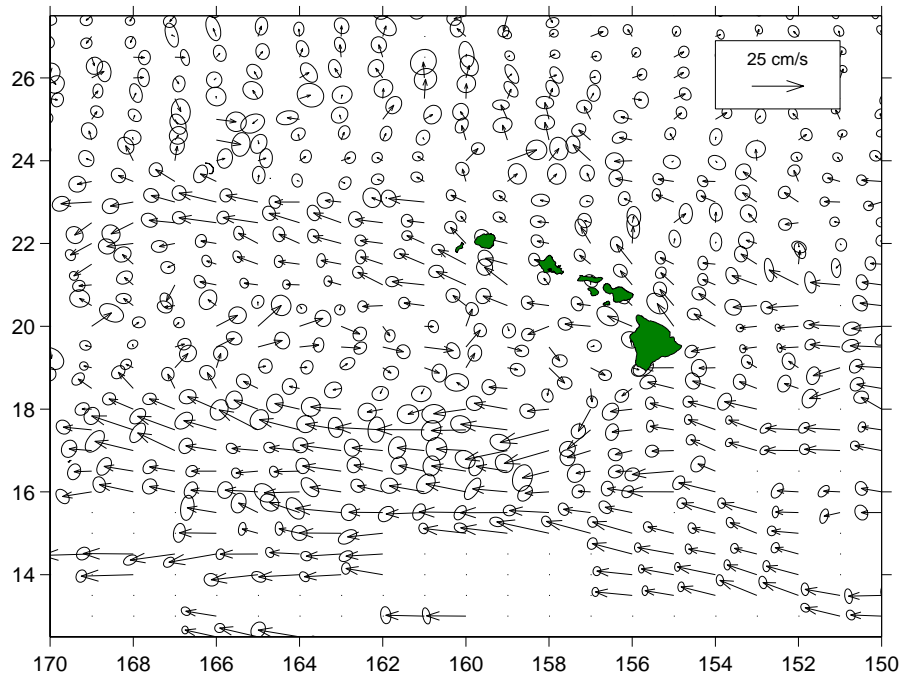


Figure 10: Closeup of the drifter-derived mean currents. Standard error ellipses are shown around each arrow head. Every other arrow is independent.

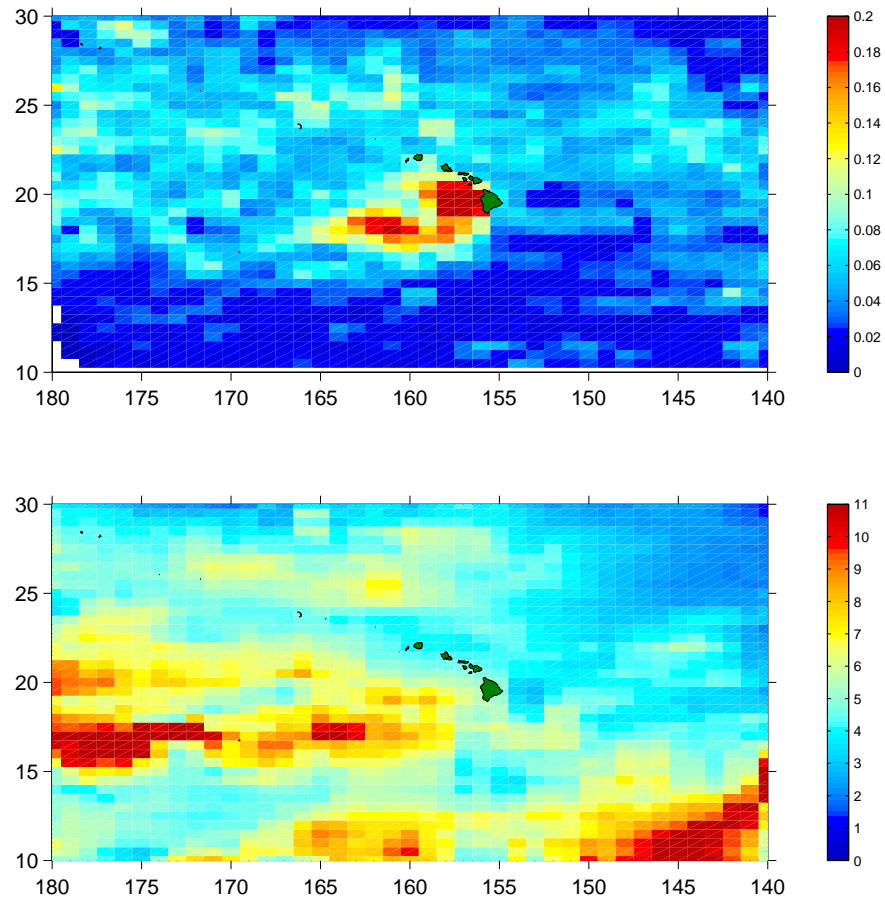


Figure 11: *Top*: variance  $u'^2 + v'^2$  (m<sup>2</sup>/s<sup>2</sup>) of the drifter-derived currents. *Bottom*: variance of dynamic height relative to 400 dbar (10<sup>-3</sup> m<sup>2</sup>).

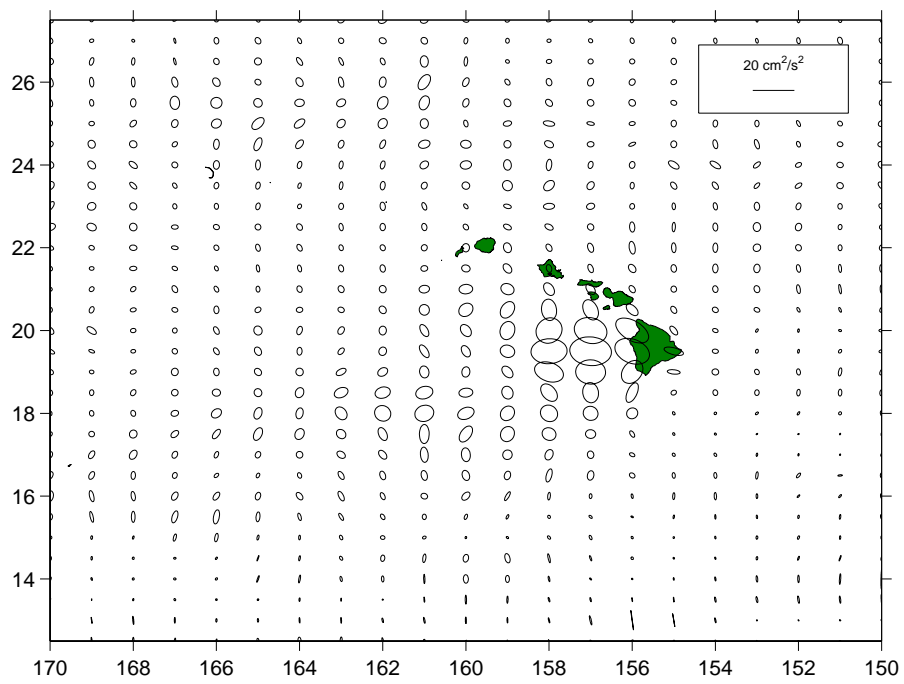


Figure 12: Variance ellipses of drifter-derived currents.

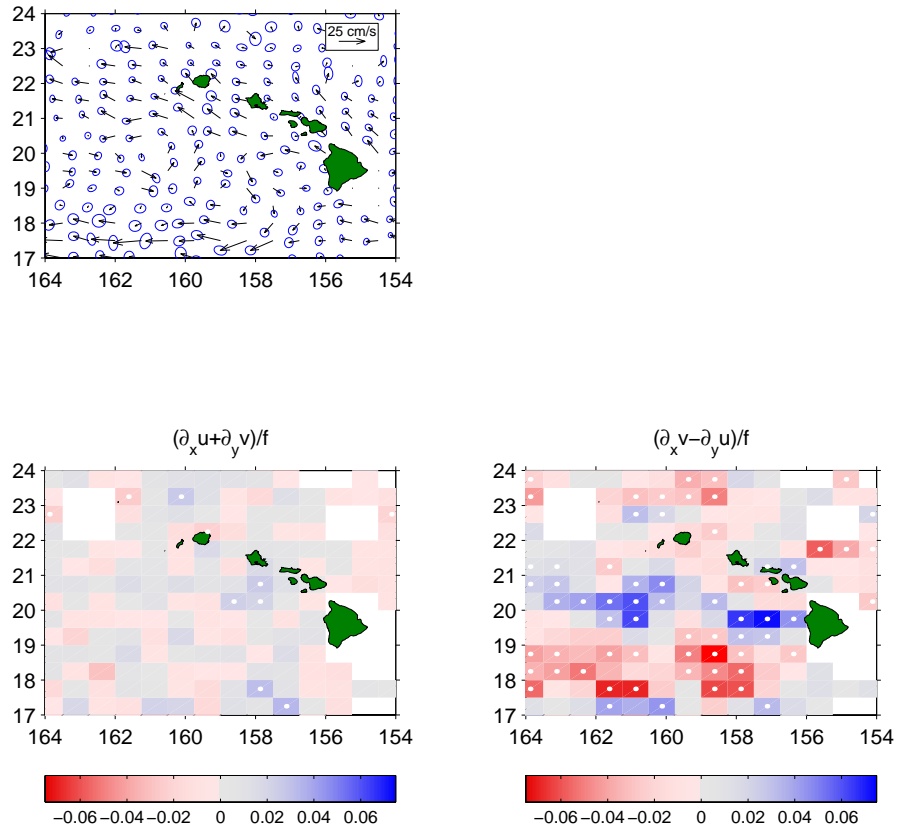


Figure 13: *Top*: mean drifter speeds with standard error ellipses. The speeds are calculated on a 1.5 (zonally) by 1° (meridionally) grid, overlapping such that every other point is independent.

*Bottom*: mean divergence (left) and curl (right) divided by the Coriolis parameter  $f$ , calculated from the mean currents.

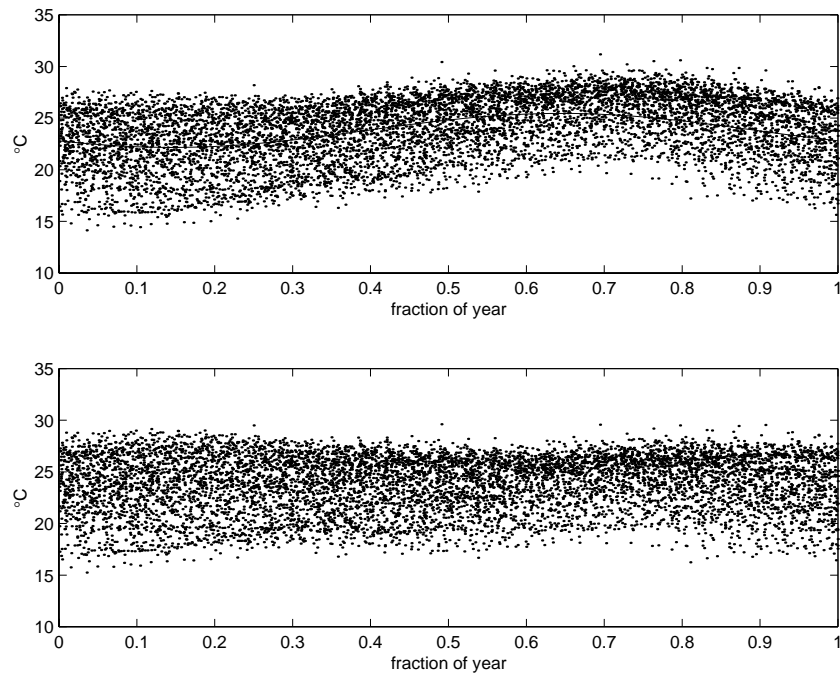


Figure 14: *Top*: interpolated *in-situ* SST measured by the drifters, as a function of the fraction of the year. The solid line is a least-squares fit of a sinusoid of annual period. *Bottom*: SST with the annual variation removed.

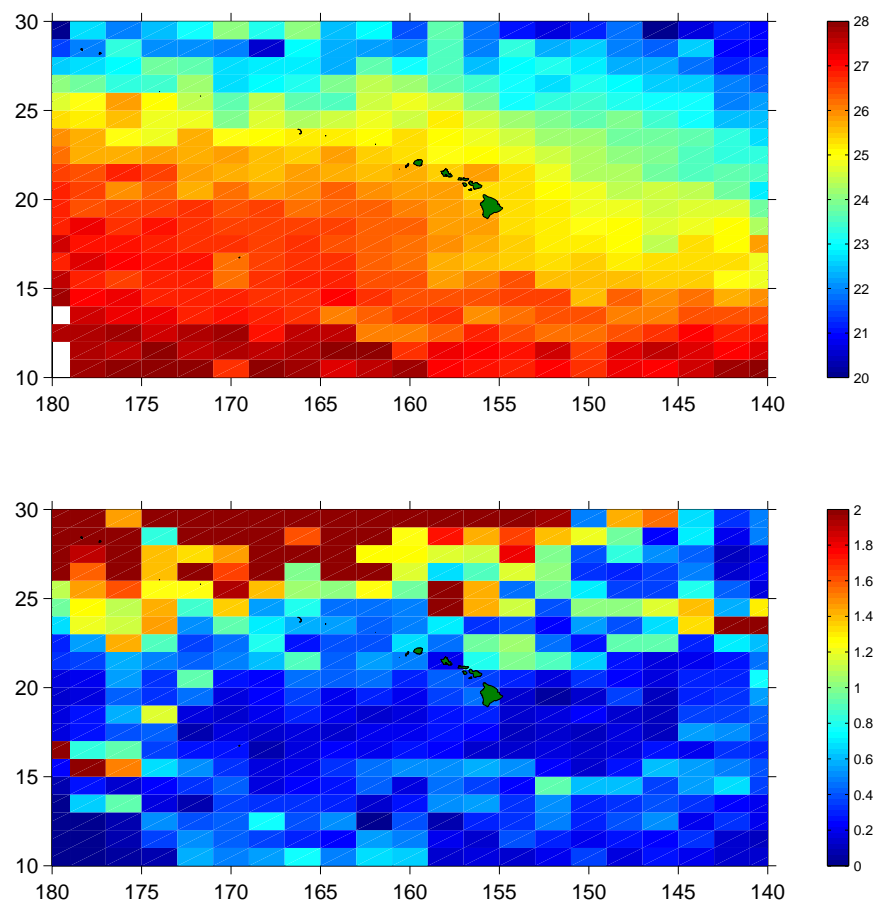


Figure 15: *Top*: mean SST ( $^{\circ}\text{C}$ , annual signal removed). Every other point is calculated from independent data.  
*Bottom*: variance of SST ( $^{\circ}\text{C}^2$ ).

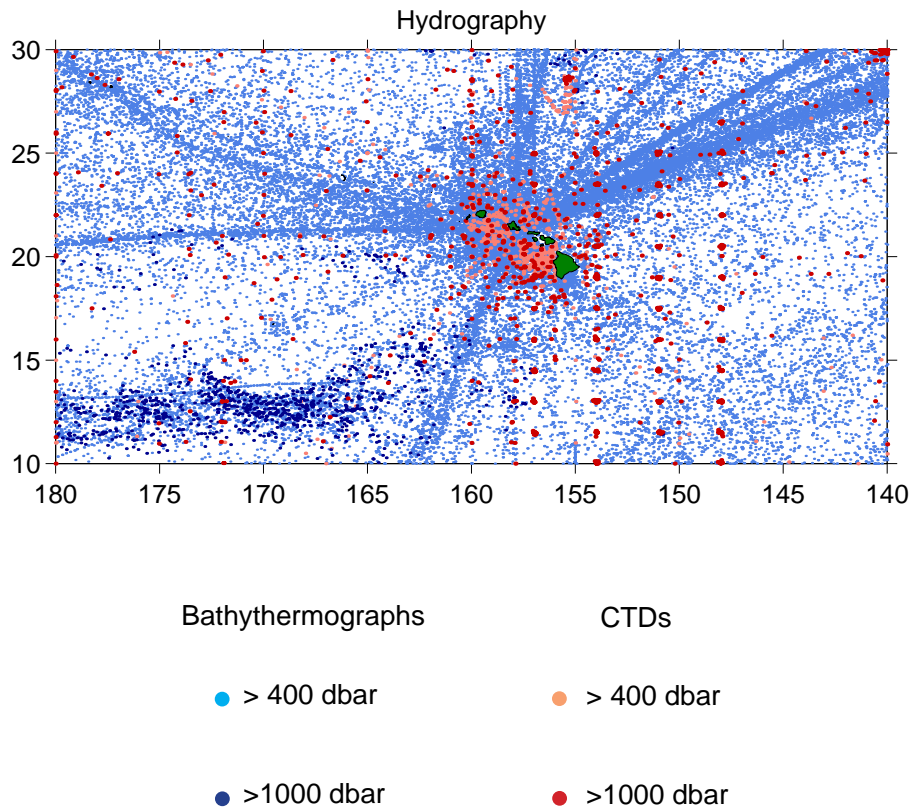


Figure 16: Locations of CTD (red, to at least 1000 dbar; orange, to at least 400 dbar) and bathythermograph (dark blue, to at least 1000 dbar; light blue, to at least 400 dbar) casts in the Hawaiian region.

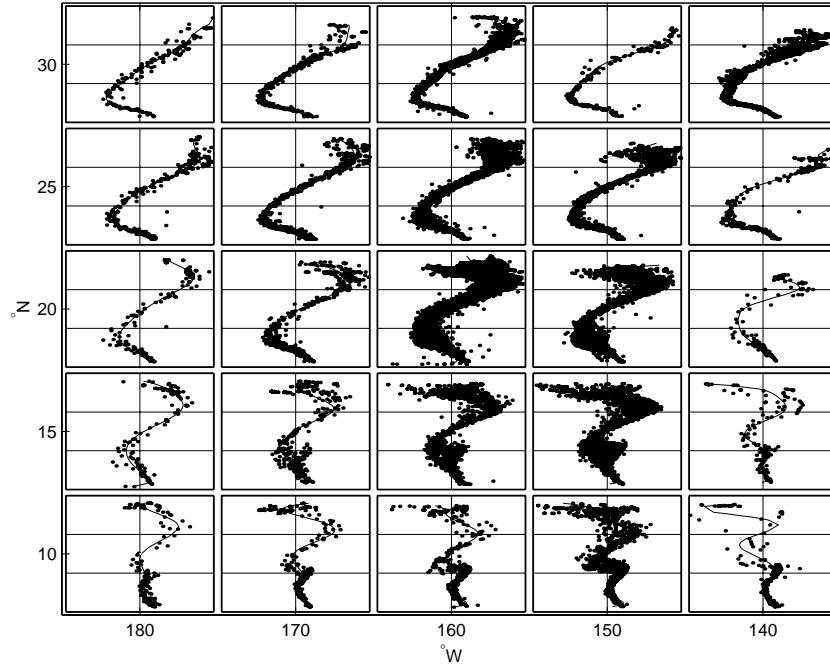


Figure 17: T-S profiles in  $10^\circ$  (zonal) by  $5^\circ$  (meridional) cells. Each profile shows salinity (horizontal axis) vs. temperature (vertical axis) for individual CTD casts (dots). The corresponding mean T-S profile (solid line) was derived by a least-squares fit of an eighth-order polynomial. The salinity axes run from 33.5 to 35.5 PSU; thin vertical lines mark 34.5 PSU. The temperature axes run from 0 to  $30^\circ\text{C}$ ; thin horizontal lines mark 10 and  $20^\circ\text{C}$ .

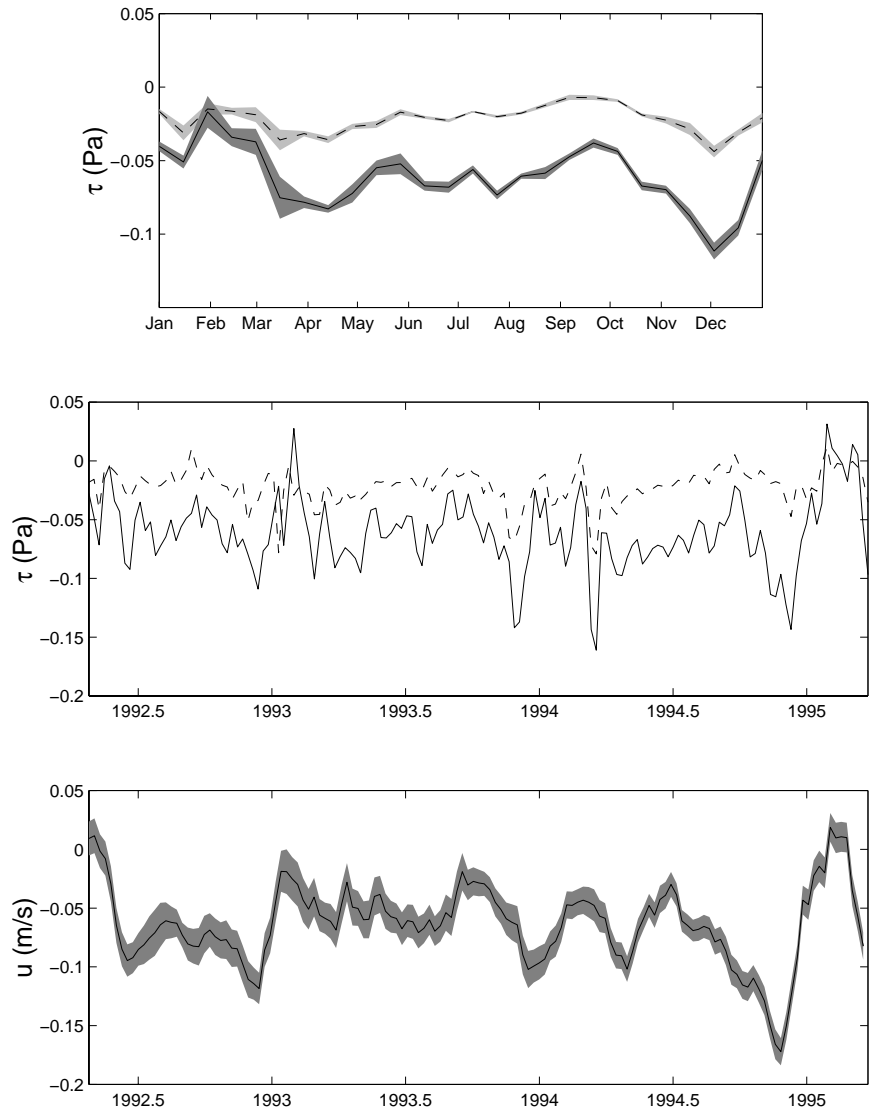


Figure 18: *Top*: ERS-1 wind stress averaged over the Hawaiian region, as a function of time of year (solid: zonal stress, dashed: meridional stress). Shading indicates the standard error bars.

*Middle*: Time series of weekly wind stress averaged over the region (solid: zonal stress, Dashed: meridional stress).

*Bottom*: Running 30-day mean of the independent zonal speeds of drifters east of  $154^\circ\text{W}$  and between  $14^\circ$  and  $26^\circ\text{N}$ , with standard error bars.

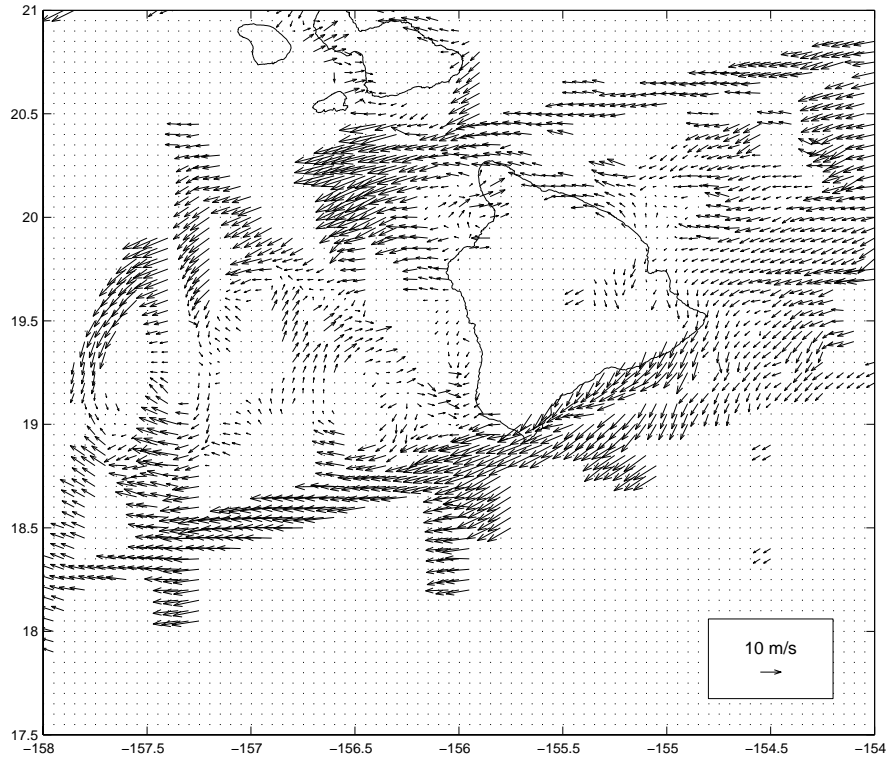


Figure 19: Wind at 0-500 m altitude observed by the NCAR aircraft *Electra* in the Hawaiian Rain Band Project (HaRP). Hawai'i's wind shadow is approximately 150-200 km long. This image is a composite of 17 flights over the period 24 July to 11 August, 1990; the five flights which entered the island's wake were on 24 July, 28 July, 6 August, 9 August and 11 August [Smith and Grubisić, 1993].

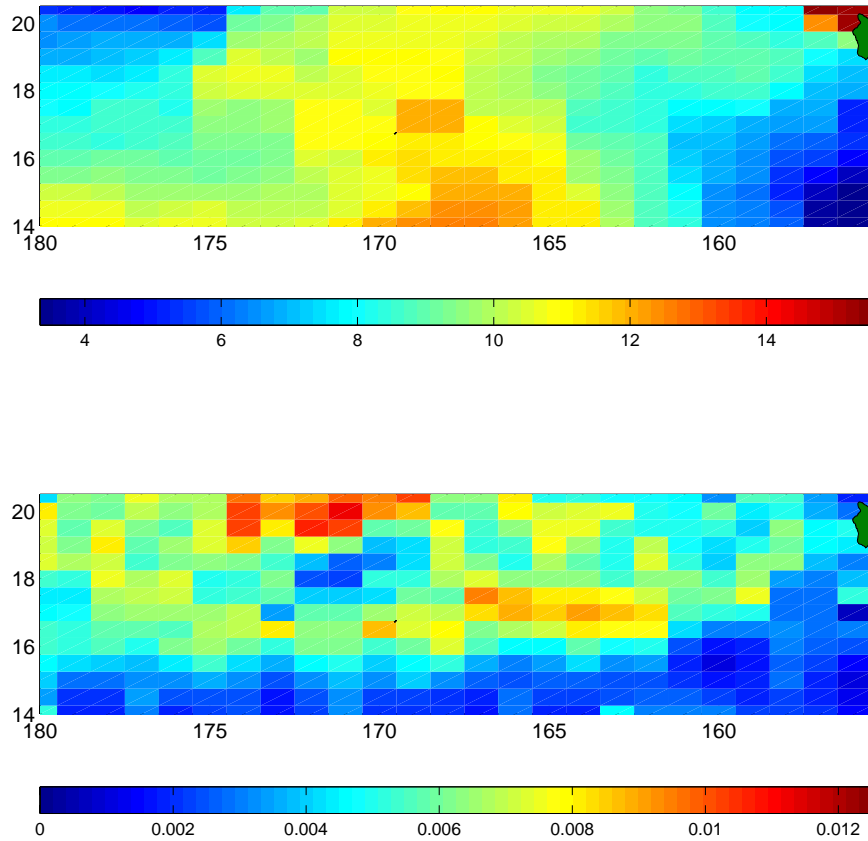


Figure 20: *Top*: median sea surface height (m) from ERS-1 and TOPEX altimetry. Every other grid point is composed of independent data. *Bottom*: variance of sea surface height ( $\text{m}^2$ ). In each grid, the data were lowpassed at 10 days and the annual signal was removed before calculating SSH variance.

## CHAPTER 3

### EDDIES

*The dynamics and life cycle of lee eddies are discussed, including generation, propagation, interaction, decay and merging. The propagation characteristics of the eddies are examined, and related to the observed structure of the overall eddy field as seen in the current and sea level observations.*

From their birthplace in the lee of Hawai'i, intense cyclonic and anticyclonic eddies dominate the circulation west of the islands [Patzert, 1968]. Individual eddies can be over 100 km in radius, with maximum currents greater than 1 m/s. Their biological impact can be significant; in the core of young cyclonic eddies, nutrient-rich water from beneath the mixed layer is upwelled into the euphotic zone. The plankton bloom responding to this input can stand far above the background oligotrophic levels of primary production. The rate of photosynthesis in a Hawaiian lee cyclone has been measured at 66% higher than outside the eddy, with chlorophyll *a* concentrations 32% higher [Allen *et al.*, 1995]. In addition, the eddies can entrain and transport fish larvae and other planktonic life over considerable distances [Lobel and Robinson, 1986].

Most of a lee eddy's dynamic height gradient is contained in the upper 200 m [Patzert, 1968]. They are born in the immediate lee of the islands, with the most energetic ones originating west of Hawai'i. After  $\sim 1$  month of spin-up, the eddies typically begin to drift westward. Individual eddies are tracked for nearly a year in this study, and given the observed spin-down rate it seems quite likely that they live even longer.

This chapter is organized in six sections. In the first two, the relevant dynamics of lee eddies are discussed, including the balance of forces which determine their radial structure (the cyclogeostrophic balance) and the role of instability in limiting their maximum core rotation rate. Following these theoretical sections, the generation of

Hawaiian lee eddies is reviewed in light of some recent observations. Next, a section is devoted to the mean propagation characteristics of the lee eddies, from both empirical and dynamical viewpoints. A descriptive section presents individual events in the data, typically involving ADCP transects through eddies, deployments of drifters in the lee eddy field, eddies tracked in altimetry, and/or AVHRR images of lee eddies. The final two sections speculate on the dynamics underlying the more surprising observations and summarize the major findings of this study.

### 3.1 The cyclogeostrophic balance

Several models have been proposed for the radial structure of reduced gravity eddies. Three commonly-used structures are presented in Appendix B, along with a generalized structure (the “core/shell” model) developed for this study. The  $1\frac{1}{2}$ -layer reduced gravity framework is used, in which the fluid is assumed to be an active upper layer (of density  $\rho$ ) of undisturbed thickness  $H_1$ , and an infinitely deep lower layer (density  $\rho + \delta\rho$ ).

An eddy in the upper layer extends vertically from the sea surface  $z = \eta(r)$  to a depth of  $z = -H_1 - h(r)$ . If it is assumed to be steady and azimuthally-symmetric, the radial component of the momentum equation relates  $\eta$  to the azimuthal speed  $v$ :

$$\frac{v^2}{r} + fv = g\partial_r\eta, \quad (3.1)$$

where  $r$  is the radial distance from the vortex center and  $g$  is gravity. Since there are no horizontal pressure gradients in the lower layer,

$$h = \frac{g}{g'}\eta, \quad (3.2)$$

where the reduced gravity  $g'$  is  $g'/g = \delta\rho/\rho$ . Because oceanic values of  $g'$  are typically  $O(3 \times 10^{-3}g)$  [Gill, 1982], the surface deflection in the eddy is small compared to the

displacement of the layer interface. Substituting (3.2) into (3.1) yields

$$\frac{v^2}{r} + fv = g' \partial_r h. \quad (3.3)$$

This balance (Eq. 3.3) includes both the centrifugal term  $v^2/r$  and the Coriolis term  $fv$ .

By definition, the centrifugal force in a small Rossby number vortex is much smaller than the Coriolis force. Dropping  $v^2/r$  from the momentum equation yields the geostrophic balance. In a cyclone, the inwards-acting pressure gradient is balanced by an outwards-acting Coriolis force, requiring counter-clockwise particle motion (northern hemisphere). In an anticyclone, the direction of the forces are reversed, requiring the motion to be clockwise. For very large Rossby number vortices, the Coriolis term is negligible and the balance is cyclostrophic. This balance describes small, rapid vortices such as the flow down a sink (far enough from the drain that vertical motion can be neglected). The outward centrifugal force is balanced by an inward pressure gradient force. The flow can rotate in either direction, but the core pressure must be lower than its surroundings.

Because Hawaiian eddies have Rossby numbers of magnitude 0.3 to 1, both terms on the left-hand side of (3.3) can be significant: the eddies are “cyclogeostrophic.” Why is this important? In Patzert’s [1968] examination of the lee eddy field, most of the eddies were seen by their dynamic height gradients; there were few direct current measurements available to him, and none of anticyclonic eddies. However, the centrifugal term in (3.3) biased the strengths of the eddies in the hydrography, making the anticyclonic eddies appear weaker and the cyclonic eddies stronger. To demonstrate this, consider a solid-body eddy (see Appendix B). Equation (B.2) gives the total change in upper layer thickness divided by the eddy radius, which scales as the dynamic height gradient of the eddy. This is plotted as a function of the Rossby number  $\zeta/f$  in Fig. 21. For comparison,  $h(r=0)/r_o$  neglecting the centrifugal term is also shown. The two curves are nearly identical in the geostrophic regime  $|\zeta|/f \ll 1$ . For increasingly fast cyclonic

( $\zeta > 0$ ) eddies, the magnitude of the pressure gradient is larger than if the eddy were truly geostrophic. As an anticyclone increases in strength from  $\zeta = 0$  to  $\zeta = -f$ , the pressure gradient increases, though not as rapidly as if the eddy were geostrophic. A maximum pressure gradient is reached at  $\zeta = -f$ . This is the half-inertial flow described by Chew and Bushnell [1990]: particles in the eddy orbit with a period of one pendulum day. For anticyclones in the range  $-2f < \zeta < -f$ , the pressure gradient diminishes as the eddy's rotational speed is increased. At  $\zeta = -2f$ , the pressure gradient is exactly zero; the “eddy” has become a field of inertial oscillations. Past  $\zeta = -2f$ , the eddy becomes increasingly cyclostrophic, with a low-pressure core and clockwise rotation.

Suppose that one observes the pressure gradient  $h(r = 0)/r_o$  of a solid-body eddy, then estimates a vorticity  $\zeta_g$  using the purely geostrophic relation. The ratio of the calculated vorticity  $\zeta_g$  to the true vorticity  $\zeta$  is

$$\frac{\zeta_g}{\zeta} = 1 + \frac{\zeta}{2f}. \quad (3.4)$$

The vorticity of a cyclone is smaller than estimated, because the pressure gradient force must balance both the Coriolis and the centrifugal force. For a Rossby number 1 cyclone, the true vorticity is 2/3 the calculated value (this same relationship applies to the edge speed). Conversely, the magnitude of vorticity in an anticyclone is larger than calculated, because the Coriolis force is held in check by both the pressure gradient and the centrifugal force. Rossby number -1 anticyclones have twice the vorticity as estimated from geostrophy. While these specific values do not extend to the more complex eddy models presented in Appendix B, the effect of the centrifugal force is identical.

### 3.2 Centrifugal instability

If a fluid parcel orbiting a cyclogeostrophic vortex is infinitesimally perturbed, it will experience a restoring force proportional to

$$F = \partial_r \left( vr + \frac{1}{2} f r^2 \right)^2 \quad (3.5)$$

[Kloosterziel and van Heijst, 1991]. If  $F < 0$  anywhere within the vortex, perturbations will grow exponentially, and the vortex is “centrifugally unstable.” Kloosterziel and van Heijst examined the behavior of (3.5) with two models of the azimuthal speed, and showed that at a relatively small critical Rossby number, anticyclonic eddies become unstable close to their centers. At progressively larger Rossby numbers, the unstable region rapidly moves outward and broadens. In contrast, cyclonic eddies are stable for much larger Rossby numbers; at their critical Rossby number, the unstable region appears in the region of anticyclonic vorticity surrounding the cyclonic core.

Kloosterziel and van Heijst’s results show that anticyclones are generally less stable than cyclones. To understand the physical reason for this, consider a fluid parcel orbiting a cyclone: the outward centrifugal and Coriolis forces balance the inward pressure gradient force. If the parcel is nudged slightly outward, it will conserve angular momentum and thus lose some azimuthal speed. Both of the outward-acting forces consequently diminish; unless the pressure gradient force drops quite rapidly over the distance of the nudge, it will pull the parcel back towards the equilibrium position. On the other hand, a parcel orbiting an anticyclone has an inward Coriolis force balanced by the outward centrifugal and pressure gradient forces. As with the cyclone, an outward nudge results in weaker centrifugal and Coriolis forces. However, because these forces oppose each other in the anticyclone, the net effect of this change is more nearly cancelled. Unless the pressure gradient force drops off relatively rapidly over the distance of the nudge, it

will not be held in check and the parcel will begin accelerating outward.

Kloosterziel and van Heijst defined the Rossby number as the maximum azimuthal speed of the vortex divided by  $f$  and the radius at which the maximum speed occurs. This definition was unfortunate, because as a consequence the critical Rossby number for anticyclones varied with the azimuthal velocity model.<sup>1</sup> If the Rossby number is instead defined as the core vorticity  $\zeta$  divided by  $f$ , the critical Rossby number for anticyclones is fixed at  $-1$ . This can be demonstrated as follows: suppose that the eddy's azimuthal speed can be described by a smooth function of the form

$$v = \frac{\zeta}{2}(r - \epsilon r^n), \quad (3.6)$$

where  $\epsilon > 0$  and  $n > 1$ . In the range  $\epsilon r^{n-1} \ll 1$ , this profile is an order  $n$  Taylor series expansion of any smooth velocity profile with a solid-body core at small  $r$ . Substituting (3.6) into (3.5) gives

$$F = (\zeta + f)^2 r^3 - \frac{1}{2}(n + 3)\epsilon \zeta (\zeta + f) r^{n+2}. \quad (3.7)$$

If the core vorticity is rewritten as  $\zeta = -(1 + \alpha)f$ , this becomes

$$F = \alpha^2 f^2 r^3 - \frac{1}{2}(n + 3)\epsilon (1 + \alpha)\alpha f^2 r^{n+2}. \quad (3.8)$$

Consider an anticyclone spun up from rest. The parameter  $\alpha$  starts at  $-1$ , and steadily approaches 0 as the Rossby number  $\zeta/f$  approaches  $-1$ . Throughout the range  $-1 < \alpha < 0$ , both terms in (3.8) are positive: the eddy is stable. When the eddy reaches  $\alpha = 0$ , Rossby number  $-1$ , the restoring force on perturbed parcels disappears and the eddy becomes neutrally stable. Once  $\alpha$  is infinitesimally larger than zero (specifically,  $\alpha/(n + 3) \ll \epsilon r^{n-1} \ll 1$ ),  $F$  is less than zero and the eddy is unstable. For increasing values of  $\alpha$ , the unstable region moves outward from the core, requiring explicit treatment of the higher-order Taylor series terms.

---

<sup>1</sup>Kloosterziel and van Heijst found critical Rossby numbers of  $-0.57$  and  $-0.65$  for the two models they considered.

### 3.2.1 Stability of a solid-body eddy

For the solid-body vortex described by  $v = \zeta r/2$ , the stability criterion (3.5) becomes

$$F = (f + \zeta)^2 r^3. \quad (3.9)$$

Cyclones are always stable. As an anticyclone is spun up from rest, it becomes progressively less stable until  $\zeta = -f$ , at which point it is neutrally stable. A more rapidly-spinning solid-body anticyclone is again stable.

### 3.2.2 Stability of the core/shell model

For eddies described by (B.9), the stability of the core is described above. At Rossby number  $-1$  the core is neutrally stable, and gains stability if it spins faster. However, as suggested by Kloosterziel and van Heijst [1991] and by the stability of a smooth velocity profile derived earlier, a region of instability will be born on the inner edge of the shell as the Rossby number  $-1$  threshold is crossed.

In the shell,

$$\frac{f^2}{r} F = \left[ \left( 1 - a \frac{\zeta}{f} \right) r^2 + a \frac{\zeta}{f} r_o^2 \right] \left( 1 - a \frac{\zeta}{f} \right), \quad (3.10)$$

where  $a = r_i^2 / (r_o^2 - r_i^2)$ . Evaluated at  $r = r_i + \epsilon$  in the limit  $\epsilon \rightarrow 0$  (i.e. on the inner edge of the shell), this is

$$\frac{f^2}{r_i^4} F = \left( 1 + \frac{\zeta}{f} \right) \left( 1 - a \frac{\zeta}{f} \right). \quad (3.11)$$

(3.11) is a downward-opening parabola intersecting with zero at  $\zeta = -f$  and  $\zeta = f/a$ . Thus, for  $\zeta < -f$ , the shell will always be unstable. Half-inertial eddies, such as the ones found in this study and those described by Chew and Bushnell [1990], have reached their maximum sustainable rotation rate.

The  $\zeta = f/a$  intersection indicates that cyclonic eddies become unstable if

$$\frac{\zeta}{f} > \frac{\zeta}{|\zeta_o|}, \quad (3.12)$$

where  $\zeta_o$  is the anticyclonic vorticity of the outer shell. The more irrotational the outer shell of a cyclone is, the stronger it can be without becoming unstable. This result is consistent with the laboratory experiments of Kloosterziel and van Heijst [1991], in which narrow-shelled cyclones were less stable than those with wide shells. In the Rankine limit  $\zeta_o \rightarrow 0$ , centrifugal instability never limits the strength of a cyclone.

### 3.3 Eddy birth

The most energetic lee eddies are born in the immediate lee of the island of Hawai‘i. Sea level altimetry in this area shows alternating highs and lows with a mean period of  $\sim 60$  days (Fig. 22). Combined with the drifter and/or AVHRR data, several of the well-defined extrema have been identified as eddies; their names appear in Fig. 22, and will be individually discussed in the descriptive section of this chapter.

The alternating production of cyclones and anticyclones combine with their westward propagation (to be discussed in the next section) to create a formation similar to the Kármán vortex street [von Kármán, 1954]. Kármán streets are typically generated when a background current flows around a 2D cylindrical obstacle. At low Reynolds numbers ( $R_e < 4$ ), the flow smoothly wraps around the obstacle (Reynolds numbers quoted from Kundu [1990]). If the Reynolds number is increased to 4–40, the flow separates from the obstacle, forming trapped counter-rotating vortices in its wake; the atmospheric flow around Hawai‘i is typically in this regime [Patzert, 1968]. In the Reynolds number range 40–80, transition to vortex shedding begins, and for  $80 < R_e < 200$ , alternating-signed vortices are generated and advected away by the background flow. At higher Reynolds numbers, the Kármán street is visually “washed out” by smaller-scale turbulence, although the characteristic frequency of vortex generation still dominates the wake’s spectrum. The similarity between the lee eddy field and the

Kármán vortex street led McGary [1955] to propose that the westward North Equatorial Current flows around the island of Hawai‘i, with a Reynolds number in the vortex shedding regime. It is important, however, to note that the Kármán street formation is significant because it is stable to small perturbations, unlike other patterns such as an infinite train of dipoles [von Kármán, 1954]. Thus, if the generation mechanism(s) produces cyclones to the north and anticyclones to the south, and any physical process (not necessarily advection) causes the eddies to drift westward, they will tend to organize themselves into a Kármán street-like pattern regardless of whether this analogy applies to their generation.

### *3.3.1 Cyclones*

Cyclonic lee eddies typically first appear 30–50 km west of Keahole Point, the westernmost point of the island of Hawai‘i. Fig. 23 show a representative sequence of AVHRR images during the birth of a cyclone. On 6 May 1994, Hawai‘i’s warm pool lay undisturbed in the island’s lee. This pool is driven by diurnal surface heating in the absence of wind-forced mixing (compare this figure with Fig. 19) [Wenzel, 1992]. The cold core of an eddy appeared off Keahole Point on 8 May, at the northern edge of the island’s wind shadow. The eddy began advecting the warm pool around it as it spun up; a day later, the warm water was wrapped tightly around the eddy. On 12 May, the eddy had drifted westward and the warm pool had reformed. This sequence suggests a spin-up time of  $\sim 6$  days, consistent with Patzert’s [1968] estimate of a week for all but the most intense cyclones.

As mentioned earlier, altimetry in the island lee suggests a mean generation frequency of  $\sim 60$  days. However, smaller cyclones are less likely to be seen in the altimetry, and their signatures could be reduced by the concurrent presence of an anticyclone. At least twice in the AVHRR data set, relatively small cyclones form within 20 days of each

other. There is a 20 day peak in the spectrum of sea level anomaly (Fig. 22), which may reflect periods of rapid cyclone generation.

If lee cyclones are generated by a mean flow around Hawai'i, the flow must pass westward through the 'Alenuihaha Channel (see Fig. 1). However, there is little evidence that this can account for the observed cyclones. For example, on 26 April–5 May 1966, a cyclonic eddy was discovered 50 km WNW of Keahole Point [Patzert, 1968]. The hydrography suggested that the eddy was in the process of spinning up. Drifters were deployed in the channel, but they did not significantly drift westward. Patzert noted that if the mean surface current through the channel is  $u_o = 30$  cm/s, and that if *all* the energy of this flow (with a depth structure similar to the eddy) goes into even the smallest observed cyclones, the required spin-up time is over six months; larger cyclones would require over 2.8 years to spin up. Because the energy flux through the channel is proportional to  $u_o^3$ , this estimate is quite sensitive to the choice of through-channel flow. Repeating Patzert's calculations for a hypothetical 1 m/s current through the channel (with all other parameters identical) gives a spin-up time estimate of  $\sim 5$  and 30 days for small and large cyclones, respectively. Thus, if the cyclones are current-driven, mesoscale variability east of the Hawaiian Ridge must drive  $\sim 1$  m/s currents westward through the channel for spans of up to a month at a time, at intervals of  $\sim 60$  days. As discussed in Chapter 4, there is no evidence of this in the data.

As an alternative to the vortex shedding hypothesis, Patzert [1968] proposed that the cyclones are directly wind-driven. The trade winds are funneled between Maui and Hawai'i, creating a wind jet through the 'Alenuihaha Channel. At the southern edge of this jet, cyclonic shear could drive Ekman pumping which spins up the eddies. The observed wind stress curl in Hawai'i's lee could spin-up eddies in 10–20 days [Patzert, 1968]. A similar process is believed to generate eddies off Mexico's west coast, where the

wind funnels through gaps in the coastal Sierra Madre del Sur mountains and blows over the ocean in narrow, intense jets [Stumpf and Legeckis, 1977]. In numerical models, this forcing spins up opposite-signed eddies on either side of the jet [McCreary *et al.*, 1989]. However, strong anticyclones are not observed to be generated west of Kaho’olawe, in the anticyclonic edge of the wind jet through the ‘Alenuihaha Channel.<sup>2</sup> McCreary *et al.* [1989] considered a jet with a half-Cosine cross-section, i.e. the jet smoothly tapered to zero at its edges with a decay scale of  $\sim 70$  km. However, the jet through the ‘Alenuihaha Channel has a total width of 40 km, with edges of extremely strong vorticity created as the jet separates from the islands. On its northern edge, shear instability (c.f. [Holton, 1979]) smears out the region of Ekman convergence; however, the more stable southern edge retains its intense cyclonic vorticity for a considerable distance.<sup>3</sup>

### 3.4 Anticyclones

Anticyclonic lee eddies typically form west of Hawai‘i’s southernmost point. The drifter and altimetric observations collected in this study suggest that they are generated every 50–60 days (c.f. Fig. 22), although it is possible (as with the cyclones) that smaller ones are generated more frequently. Because the thermocline is pushed downward in anticyclones, they are not intrinsically visible in AVHRR images. They may be indirectly revealed, however, by their advection of ambient temperature gradients. While examining Hawai‘i’s warm pool in SST images, Wenzel [1992] noted that on two occasions the southern edge of the pool became cusp-shaped. She hypothesized that this was due to anticyclonic eddies. In this study, several more examples were found; as shown in Fig. 22, they are concurrent with sea level anomaly peaks marking the ap-

---

<sup>2</sup>A small anticyclone may have been born here in August 1995, as will be discussed in the descriptive section of this chapter.

<sup>3</sup>This shear line can be seen by eye from a good vantage point on Hawai‘i, and clearly appears in visual-band satellite images of the island lee [Wenzel, 1992].

pearance of anticyclones in Hawai'i's lee. A particularly dramatic example is shown in Fig. 24, where an anticyclonic swirl (which superficially resembles a Kelvin-Helmholtz roll) appears in the southern edge of the island's lee. Eleven days later, the eddy is a much larger feature in the SST image, discernible by the advection of warm water to its north. This sequence (and also Fig. 102) suggests an anticyclonic generation time of  $O(10 - 20 \text{ days})$ .

Fig. 25 shows an ADCP transect past Hawai'i's south point, made on 16 August 1994 (two days before the earliest image of Fig. 24). In addition to circulation from the eddy, the transect shows a core of westward-flowing water just south of the island flank. This persistent (Fig. 26) feature shall be called the NEC jet: after the westward-flowing NEC impinges on the island of Hawai'i, water south of the bifurcation point is accelerated as it flows toward the south point of the island. Upon separation, the intense anticyclonic shear is highly susceptible to shear instability (c.f. [Holton, 1979]). In laboratory experiments of a velocity discontinuity introduced in a fluid, the unstable shear line quickly organizes itself into a train of coherent vortices (c.f. [Brown and Roshko, 1974]). If an analogous process is creating the anticyclones, Patzert's [1968] energy calculations can be applied to estimate the spin-up time of anticyclones. Using a width of  $\sim 50 \text{ km}$  and assuming the jet is a homogeneous  $30 \text{ cm/s}$  to a depth of  $100 \text{ m}$ , the required spin-up times are 80 to 430 days for weak to strong eddies. These values are considerably larger than the observed generation time; however, it must be noted that at least two times,<sup>4</sup> drifters passing south of Hawai'i accelerated to  $\sim 1 \text{ m/s}$ . With a speed of  $1 \text{ m/s}$  and the same length scales, the NEC jet can spin up anticyclones in  $\sim 2\text{--}12 \text{ days}$ .

As with the cyclonic eddies, the anticyclones may also be directly wind-forced, as

---

<sup>4</sup>see the sections on AC94a and AC94b in the descriptive section

the wind shear along the southern edge of Hawai‘i’s shadow could drive Ekman convergence and downwelling. It is even possible that wind forcing and shear instability work in concert to produce the anticyclones. But what is their relative significance? This question cannot be easily answered from a purely empirical approach; because the large-scale wind and currents are highly correlated (see Fig. 18), their effects cannot be differentiated with techniques such as multiple regression analysis. A dynamical approach is required, which hinges on the relative energy input from the two sources. If 30 cm/s is a representative strength of the NEC jet, Patzert’s energy arguments suggest that the wind is more important. If the NEC jet has pulses of  $O(1 \text{ m/s})$  every  $\sim 60$  days or so (the generation frequency of anticyclones) which last at least  $\sim 10$  days (the spin-up time), it may be the dominant mechanism forcing the anticyclones.

### 3.5 Propagation

Fig. 27 shows the paths taken by individual cyclonic (blue) and anticyclonic (red) eddies tracked by drifters. As they propagate westward, cyclones tend to drift northward [Patzert, 1968], while anticyclones drift southward. This process tends to sort the like-signed eddies onto either side of their mean generation latitude,  $\sim 19.5^\circ\text{N}$ . Averaged over the passage of many eddies, a mean vorticity gradient is generated in the island lee. To calculate this, the drifter trajectories were divided into independent 60-day segments. For each segment, the rotary spectra were calculated. These were integrated over the subinertial frequencies to give the total counter-clockwise and clockwise subinertial variance (Fig. 28). The ratio of clockwise to total variance was then calculated, and scaled from  $-1$  (purely clockwise, anticyclonic) to  $+1$  (purely counter-clockwise, cyclonic), and averaged on a  $3^\circ$  (zonally) by  $1^\circ$  (meridional) grid, overlapping by  $6^\circ$  by  $1^\circ$  (i.e. every other grid point composed of independent data). The resulting image (Fig. 27) is a map

of mean vorticity in the Hawaiian region.<sup>5</sup> East of the islands, is no obvious pattern to the distribution of vorticity. In the island lee, a clear pattern emerges: west of the islands and north of 19.5°N, the vorticity is predominantly cyclonic. South of this, a predominantly anticyclonic swath aligns with the North Equatorial Ridge. This distribution of vorticity coincides with the elongated, counter-rotating lee gyres seen in the mean currents (Fig. 27).

When the ERS-1/TOPEX altimetry is averaged in latitude bands, many of the eddies observed in this study can be identified with westward-moving high (anticyclones) or low (cyclones) anomalies (Figs. 29–31). These westward-propagating anomalies were noted by Mitchum [1995], who suggested they accounted for the 90-day oscillations in Wake Island sea level (Figs. 32, 33).

### 3.5.1 Observations of eddy propagation

How fast are lee eddies? If the eddy positions shown in Fig. 27 are interpolated on a 30-day grid, finite differencing gives the zonal and meridional speeds plotted in Fig. 34. The observed zonal speeds can be crudely described by a quadratic function in latitude; the best fit in a least-squares sense is

$$u = -8.82 \times 10^{-3} \text{lat}^2 + 3.54 \times 10^{-1} \text{lat} - 3.60. \quad (3.13)$$

The observed meridional speed is roughly proportional to the zonal speed:

$$v \sim \pm 0.155u \quad (3.14)$$

(+ for an anticyclone, – for a cyclone). Given the starting latitude of an eddy, integration of (3.13, 3.14) predicts the mean eddy trajectory. These paths are shown in Fig. 27.

---

<sup>5</sup>Strictly speaking, this is a map of mean drifter trajectory curvature rather than mean vorticity. This distinction may not always be subtle. For example, in a steady zonal current with meridional shear, a zonally-propagating drifter will have zero curvature. A meridional component to the drifter's velocity must be introduced for it to bend with the background vorticity.

### 3.5.2 Linear theory: $\beta$ -induced drift

In an elegant derivation by Cushman-Roisin *et al.* [1990], it is shown that small Rossby number eddies in an inviscid, reduced-gravity, rigid lid, 1.5 layer fluid will propagate at speed

$$\frac{d}{dt}X = -\frac{\beta g'}{f_o^2} \left\langle H_1 h + \frac{h^2}{2} \right\rangle, \quad \frac{d}{dt}Y = 0, \quad (3.15)$$

where the center of mass of the eddy  $(X, Y)$  is defined by

$$X = \langle xh \rangle, \quad Y = \langle yh \rangle, \quad (3.16)$$

the averaging operator  $\langle \cdot \rangle$  is

$$\langle \cdot \rangle = \frac{\int \int dx dy \cdot}{\int \int dx dy h}, \quad (3.17)$$

where  $\beta$  is the gradient of the Coriolis parameter  $f(y)$ ,  $f_o$  is the mean value of  $f$ ,  $g'$  is the reduced gravity,  $H_1$  is the undisturbed thickness of the upper layer, and  $h(x, y, t)$  is the perturbation of the layer interface due to the eddy. Equation (3.15) gives the zonal speed of an eddy as a function of its structure. The following two examples illustrate the range of speeds for relevant values of the physical parameters.

#### *Lens-shaped eddies*

In the geostrophic limit, the solid-body lens-shaped anticyclone described in Appendix B has total thickness

$$h = -\frac{\zeta}{2} f \frac{r_o^2 - r^2}{2g'}, \quad (r \leq r_o), \quad (3.18)$$

where  $\zeta$  is the core vorticity (twice the rotation rate) and  $r_o$  is the eddy radius. Substitution into (3.15) gives

$$\frac{d}{dt}X = -\frac{1}{3} \beta \frac{g'h(0)}{f_o^2} \quad (3.19)$$

[Nof, 1981], where  $h(0) = \zeta f_o r_o^2 / 4g'$  is the central depth of the eddy. For  $g' = 0.03 \text{ m/s}^2$ ,  $\beta = 2.1 \times 10^{-11} \text{ m}^{-1} \text{ s}^{-1}$ ,  $f = 5 \times 10^{-5} \text{ s}^{-1}$ ,  $h_o = 200 \text{ m}$ , the zonal propagation speed is a sluggish 1.7 cm/s.

### *Cylindrical, solid-body eddies*

For cylindrical, solid-body eddies imbedded in an active upper layer of thickness  $H_1$  (see Appendix B), (3.15) gives

$$\frac{d}{dt}X = -\beta R_d^2 \left( 1 + \frac{h(0)}{3H_1} \right) \quad (3.20)$$

[Cushman-Roisin *et al.*, 1990], where  $R_d = \sqrt{g'H_1}/f_o$  is the Rossby deformation radius and  $h(0)$  is the deflection of the layer interface at the eddy center (defined positive for downward deflection). In the limit  $h(0) \rightarrow 0$ , the eddy will propagate at the long Rossby wave speed  $c_R = -\beta R_d^2$ . Because of the term containing  $h(0)$ , anticyclones drift slightly faster than the Rossby wave speed and cyclones drift slightly slower. In the Hawaiian region, a typical first baroclinic mode deformation radius is 60 km [Emery *et al.*, 1984]. Using this value, the long Rossby wave speed is shown in Fig. 34 as a function of latitude. North of  $\sim 18^\circ\text{N}$ , (3.20) is a reasonable lowest-order dynamical description of the observed zonal drift of eddies.<sup>6</sup> The final term in (3.20) can be rewritten as  $g\eta/3f_o^2R_d^2$ , where  $\eta$  is the sea level displacement at the eddy's center. Using  $\eta=0.2-0.3 \text{ m}$ ,  $f_o = 5 \times 10^{-5} \text{ s}^{-1}$  and  $R_d = 60 \text{ km}$ , an anticyclone will propagate 3.7–12.4% faster than the long Rossby wave speed.

---

<sup>6</sup>For similar examples in the literature, see Stumpf and Legeckis [1977] and Bernstein and White [1974]. In Stumpf and Legeckis, an anticyclone is tracked for 13 days in SST images, during which time it drifts westward at  $\sim 1.08$  times the long Rossby wave speed. In Bernstein and White, mesoscale features in bathythermograph data from the central North Pacific are shown to propagate at  $\sim 1.07$  times the long Rossby wave speed, or almost exactly the combined Rossby wave and mean current speed.

### *The core/shell eddy*

In Appendix B, a model of an eddy's azimuthal velocity structure is presented which has a solid-body core to  $r = r_i$ , surrounded by a shell of constant, opposite-signed vorticity extending to  $r = r_o$ . This velocity structure can be integrated to give the interface displacement  $h$ , and substitution into (3.15) then gives the  $\beta$ -induced drift of the eddy (Fig. 35). For fixed  $r_i$  and  $h(0)/H_1$ , the westward drift of the core/shell eddy approaches  $c_R$  as  $r_o$  is increased. For  $r_o = 3r_i$ ,  $\eta=0.2-0.3$  m,  $f_o = 5 \times 10^{-5} \text{ s}^{-1}$  and  $R_d = 60$  km, an anticyclonic shell/core eddy will propagate 0.3–1.26% faster than the long Rossby wave speed.

Using a primitive equation 2-layer isopycnal model, Chassignet and Cushman-Roisin [1991] examined the effects of nonlinearities on the propagation of lens-shaped and cylindrical eddies. They showed that the zonal propagation predicted by (3.15) is quite accurate for small eddies (not significantly greater in size than the Rossby radius) when the lower layer depth  $H_2$  is much greater than the upper layer depth  $H_1$ , even when the eddy had a Rossby number of  $O(1/2)$ . However, the (zero) meridional drift predicted by the linear theory was no longer accurate. In the model, cylindrical eddies bled energy into a Rossby wave wake in the upper layer, and interaction with this wake caused cyclonic eddies to drift northward and anticyclonic ones to drift southward. Chassignet and Cushman-Roisin modeled their cylindrical eddies with a Gaussian sea level profile, and set the initial interface displacement  $h(0) = 0.5H_1$ . In the limit  $H_2 \gg H_1$ , their eddies drifted zonally at  $\sim 0.9 c_R$  (cyclones) and  $\sim 1.1 c_R$  (anticyclones).<sup>7</sup> The eddies' meridional drift was initially  $\pm 0.18 - 0.19c_R$  (– for northward-drifting cyclones, + for southward-drifting anticyclones). As an eddy propagated westward, it became

---

<sup>7</sup>For comparison, core/shell eddies with  $h(0) = 0.5H_1$  will drift at these speeds if  $r_o \approx 2r_i$ .

progressively more linear as energy was lost into the Rossby wave wake; consequently, the zonal drift of the eddy approached the long Rossby wave speed and the meridional speed decayed to zero. The propagation paths of these eddies, shown in their Fig. 3, outline a parabola which is strikingly similar to the observed paths of Hawaiian lee eddies. Chassignet and Cushman-Roisin showed that the lower layer did not affect eddy propagation until the aspect ratio  $\delta = H_1/H_2$  was greater than  $\sim 1/50$ ; as  $\delta$  was increased past this value, drag at the base of the eddy slowed its zonal propagation and generated a Rossby wave wake in the lower layer [Flierl, 1984]. The steady balance of  $\beta$ , Coriolis and drag force resulted in faster meridional propagation [Chassignet and Cushman-Roisin, 1991]. For  $\delta \sim 1/20$  (a reasonable choice for Hawai'i), this drag effect had altered the speeds by  $\sim 10\%$  (resulting in a westward drift at  $c_R$  for the anticyclones in their model).

### *3.5.3 Other processes affecting eddy speed*

South of  $17.5^\circ\text{N}$ , the observed zonal speeds of anticyclones are up to 10 cm/s (100%) faster than the long Rossby wave speed. As shown earlier, this is well outside the theoretical drift for reasonable values of Hawaiian lee anticyclones; nonlinear effects reduce the westward speed, and thus cannot account for this discrepancy. This suggests that  $\beta$ -drift alone cannot account for the observed speed of these eddies. The additional westward speed is most likely due to advection by the North Equatorial Current, which the anticyclones propagate into as they drift southward. At  $16^\circ\text{N}$ , the discrepancy between the empirical speed given by (3.13) and the long Rossby wave speed is  $\sim 8.5$  cm/s. As shown in Chapter 4, the NEC is approximately 10 cm/s at this latitude; given the scatter in the observed eddy speeds, the observations are not inconsistent with an advection +  $\beta$ -drift model for their propagation.

In the immediate lee of the islands ( $18.5\text{--}19^\circ\text{N}$ ), the observed zonal speeds of several

anticyclones are as low as half the long Rossby wave speed. Nonlinear effects could be invoked to explain this, but a more likely hypothesis (supported by observations presented later in this chapter) is that the eddies in this region cannot be treated in isolation. As mentioned earlier, the alternating production of cyclones and anticyclones creates a Kármán street-like formation in the immediate lee of Hawai‘i. In a Kármán street, the mean impinging current advects the vortices downstream; interaction between each vortex and its opposite-signed neighbors slow it to  $\sim 0.8$  times the speed of the background current. Although lee eddies may initially propagate westward due to  $\beta$  drift rather than advection, the interaction of eddy pairs/triplets could have a similar slowing effect. Later, as their meridional propagation carries opposite-signed eddies apart, this effect would become less pronounced.

Patzert [1968] noted that between three cruises spaced  $\sim 1$  month apart, a cyclonic eddy traveled south for one month before returning to the more typical WNW propagation. In this study, several more cyclones are shown to exhibit this behavior. It is hypothesized that these anomalous trajectories are due to advection by nearby anticyclonic eddies. In the most dramatic example, a strong anticyclone passes south of a weaker cyclone, which then turns from a WNW to a SE heading. Such examples suggest that the instantaneous eddy field can vary significantly from the Kármán street formation; perturbations from the Kármán street arise from natural variations in the sizes of the eddies, and because the anticyclones propagate faster due to a more rapid  $\beta$ -drift and advection by the NEC.

### **3.6 Eddy observations: a descriptive view of the lee eddy field**

In Chapters 4 and 5, Eulerian and Lagrangian statistics give a time-averaged view of currents in the region. However, a statistical picture alone fails to reveal the richly-

complex details of the lee eddy field. When Patzert [1968] synthesized shipboard hydrography, wind measurements, geomagnetic-electrokinetograph (GEK) current meter fixes [Wyrтки *et al.*, 1969], and radio-tracked drifters, he demonstrated both the intensity and ubiquity of lee eddies. One of the great challenges of his work was to “connect the dots,” i.e. describe an energetic, evolving field from a series of what were essentially snapshots.

In recent years, many additional snapshots of lee eddies have been provided by shipboard ADCP and by in-situ sea level records at islands west of Hawai‘i. In addition, the plethora of satellite-collected data presents a unique opportunity to observe the evolution, interaction, and decay of eddies. This section is a compilation of such snapshots, and (when possible), short stories of the lives and times of Hawaiian lee eddies, as seen by WOCE drifters, shipboard ADCP, in-situ sea level, satellite altimetry and AVHRR imagery. As in Patzert [1968], the azimuthal structure of the eddies will be reconstructed from the drifter observations whenever possible. While Patzert presented a picture of intense lee cyclones and relatively weak anticyclones, a distinctly different picture emerges from this work: a train of strong and interacting anticyclones radiates WSW from the south point of Hawai‘i, dominating the leeward circulation south of  $\sim 19.5^\circ\text{N}$  and at times actively steering the lee cyclones. As in the pair of papers by Davis [1985a; 1985b], it is hoped that this descriptive section complements the statistics presented elsewhere.

### 3.6.1 1989 ADCP transect

On 22 March 1989, the R/V *Moana Wave* was traveling south along  $\sim 159^\circ\text{W}$ , on its way from Honolulu to the equator. From  $19^\circ\text{N}$  to  $15^\circ\text{N}$ , its shipboard ADCP measured the velocity structure of a strong anticyclonic lee eddy at  $17.2^\circ\text{N}$ ,  $159.7^\circ\text{W}$  (Fig. 36).

The center of the eddy was estimated by dividing the region into a  $1 \times 10^{-3^\circ}$  square

grid. For each grid point, the ADCP currents at 50 m were decomposed into azimuthal and radial components. The point which gave the minimum fraction of total variance in the radial components was defined as the center.

The azimuthal current vs. distance from eddy center is shown in the middle panel of Fig. 36. Within 100 km, the magnitude of the azimuthal speed increases approximately linearly with distance; this suggests that the eddy had a solid-body core extending to  $\sim 100$  km, with a vorticity of  $\sim -1.2 \times 10^{-5} \text{ s}^{-1}$  ( $-0.28f$ , rotational period 12.0 days). Maximum speeds at the edge of the core were  $\sim 60$  cm/s. Outside of this core, the approaching and receding profiles of azimuthal speed were not symmetric. To the south, speed dropped off nearly as  $1/r$  (irrotationally). The North Equatorial Current may have contaminated the observed speeds on this side of the eddy, however. To the north, azimuthal speed dropped off more rapidly, and could be described by a shell of constant cyclonic vorticity  $0.24f$  (nearly the same magnitude as the inferred core vorticity) extending to  $\sim 150$  km.

At the bottom of Fig. 36, the azimuthal current is shown as a function of depth and distance from the eddy center. The eddy had core speeds of 60 cm/s which extended to 150 m. The transport through this ADCP section is 10.0 Sv. This surpasses the 8.0 Sverdrups of the most energetic lee cyclones described by Patzert [1968].

### 3.6.2 Eddy AC94a

Anticyclone AC94a may have been born in December 1993, when a  $\sim 20$  cm peak in sea level anomaly occurred off the south point of Hawai'i (Fig. 22). By 1 February 1994, the eddy had drifted west to  $\sim 19^\circ\text{N}$ ,  $157^\circ\text{W}$ .

On 1 February 1994, a drifter approached the south point of Hawai'i from the east (Fig. 37). As it passed the south point, it accelerated to over 1 m/s, completed a large anticyclonic half-loop, and ran aground on the leeward coast of Hawai'i.

While the first drifter was heading to shore, a second one passed the south point, accelerating from 3.3 cm/s (mean speed between 130°–140° W) to over 80 cm/s. It completed four anticyclonic orbits before leaving the eddy at 20.2°N, 161°W.

To estimate the radii and periods of the drifter orbits, the following procedure was used. First, the eddy center was estimated on a 1 day grid from the position and curvature of the drifter’s trajectory. The estimate of the eddy center trajectory was then lowpassed at 2.5 days to reduce noise. The raw satellite fixes of the drifter were then shifted to the frame of reference moving with the eddy center. For each complete orbit, a least-squares fit of a circle was performed on the raw satellite fixes of the drifter. This gave a correction to the eddy center location and the mean radius  $R$  of the drifter’s orbit. In the moving frame of reference, the raw fixes were used to calculate the meridional and zonal speed of the drifter around the eddy center. A least-squares fit of the form

$$x + iy = Re^{i(\omega t + \phi)} \quad (3.21)$$

gave the period  $T = 2\pi/\omega$  of the orbit, and the mean azimuthal speed  $U$  was given by  $U = 2\pi R/T$ .

The first orbit of the drifter around AC94a had a radius of 64 km and a period of 6.2 days. The second and third orbits had periods of 4.0, 4.9 days with radii of 25, 44 km. These orbits may have been in a solid-body core of radius  $\sim 50$  km, vorticity  $-3.2 \times 10^{-5} \text{ s}^{-1}$  ( $-0.7f$ , rotational period 4.5 days), although the sparse amount of data precludes any definite conclusions (Fig. 37).

### 3.6.3 Eddy AC94b

In November 1992, a WOCE drifter was deployed off the coast of northern California. It traveled south for over 400 days, then in January 1994 turned west and was carried by the North Equatorial Current toward Hawai‘i. From January to March, the drifter

moved at a mean speed of 0.21 m/s. It reached the south point of Hawai'i on 23 March, and accelerated to 1.2 m/s as it passed within 23 km of the island. It then became entrained in anticyclone AC94b at 18.4°N, 157.7°W (Fig. 38), and continued to orbit the eddy for nearly eleven months. It crossed the dateline in December 1994 and left the eddy near the end of February 1995.

AC94b formed  $\sim 100$  days after AC94a; the altimetry suggests that a third anticyclone may have formed between them (Fig. 22). As the drifter entered AC94b, it spiraled inward from  $\sim 37$  km orbits to an extremely tight  $\sim 6$  km orbit at the end of May. The orbits had periods ranging from 2.5 to 3.6 days, with a mean of  $3.00 \pm 0.07$  days; the local pendulum day (twice the inertial period) was 3.07 days.

On 10-14 June, as the eddy crossed 159.2°W, the drifter's orbit increased to  $\sim 36$  km in radius, with a period of 4.4 days. Over the next 70 days, the orbits increased to  $\sim 55$  km radius, then decreased to a minimum of 37 km on 3 August, then increased again to 50 km. Concurrently, the orbital period steadily increased from 4.5 days to 7.8 days.

On 24 August, the drifter began an elliptical orbit of mean radius 53 km, with a nearly north-south semimajor axis of  $\sim 62$  km and a semiminor axis of  $\sim 45$  km. It completed this orbit in  $\sim 10$  days, then made two more nearly circular orbits of radii 78, 85 km, period 14.2, 12.8 days.

Throughout this time, the winds had been relatively steady trades (Fig. 39). Then, in the last week of September, a marked trade wind reversal lasted into early October. Approximately concurrent with this, the drifter jumped to a very large ( $\sim 110$  km) orbit of period 23.7 days. On 20 October, as it was close to completing this large orbit, the drifter suddenly began meandering in a generally SW direction for 20 days. It then slowed, meandered northward for another 7 days, then (on 17 November) returned to

smooth anticyclonic orbits.<sup>8</sup> The drifter completed two more orbits and began a third before leaving the eddy near 16°N, 176°E around 27 February 1995. The final orbits had radii of 110–120 km, with period of 26–28 days.

Fig. 40 shows the ERS-1/TOPEX altimetry in the frame of reference moving with AC94b. The altimetry has been divided into four time spans, corresponding to the  $\sim$ 3, 6, 14 and 27-day orbits of the drifter. For each span, the sea surface displacement of the core/shell model (B.9) was fit to the altimetry. To do this, the central height  $h(r = 0)$  was fixed, and the core vorticity  $\zeta$  and radius  $r_i$  were varied until the model sea level curve matched the observed profile in a least-squares sense. The outer radius  $r_o$  was given by  $h(r = 0)$ ,  $\zeta$  and  $r_i$ . The best-fit values of the core/shell model parameters are presented in Table 3.1; because of the sparsity of data near the eddy center during 1–21 September, the estimates for this span are the least certain.

Table 3.1: Structure of AC94b from altimetry.

Dates	$r_i$ (km)	$r_o$ (km)	$\zeta$ ( $10^{-5} \text{ s}^{-1}$ )	$\zeta/f$	$4 \pi/\zeta$ (days)
15 Apr.-6 June 1994	37	269	-4.20	-0.97	3.5
11 June-22 Aug. 1994	58	431	-2.12	-0.49	6.9
1-21 Sep. 1994	100?	380?	-1.12?	-0.26?	13.0?
26 Sep. 1994-28 Feb. 1995	95	393	-1.01	-0.23	14.4

#### 3.6.4 October 1994 to September 1996 deployments

From October 1994 to September 1996, a large number of drifters were deployed in several clusters within the Hawaiian lee region. For brevity, these data (and concurrent observations from the other data) are summarized here, and presented in detail (with accompanying figures) in Appendix C.

On 15 August and 8 September 1994, 13 drifters were deployed from the R/V

---

<sup>8</sup>The orbital characteristics could not be determined during this meandering phase.

*Townsend Cromwell*, which passed near a newly-born anticyclone (AC94c) close to Hawai‘i’s South Point. The eddy had a core rotational period of  $\sim 3$  days. AC94c could be followed in the altimetry as it propagated WSW from 8 September to 4 October 1994. On 4 October, the *Cromwell* again passed through the eddy, and deployed 9 drifters. The shipboard ADCP and drifter orbits showed that the core rotational period of the eddy had approximately doubled since 8 September. The drifters also circled a large ( $\sim 200$  km diameter) cyclonic eddy (C94a) for a few orbits, then several became entrained in AC94c and tracked it until late January 1995. Drifter and altimetric observations of AC94c show that the eddy followed a very similar trajectory to that of AC94b. In mid-October 1994, a cyclonic eddy (C94b) formed in Hawai‘i’s lee; two drifters orbited the eddy from mid-December 1994 to late February 1995. In early February, the eddy abruptly turned from WNW propagation to SE propagation. Altimetry and AVHRR imagery show that a very large anticyclone (AC94g) passed south of C94b at about this time, suggesting that the anomalous propagation of C94b may have been due to advection by the larger anticyclone.

On 27 July–5 August 1995, the *Cromwell* sampled two cyclonic lee eddies with its shipboard ADCP and deployed eight drifters in the island lee. One of the cyclones (C95b) was a large ( $\sim 100$  km diameter) eddy which had formed around 7 July and subsequently propagated into the west coast of Hawai‘i, perhaps due to advection by a large anticyclone to its south. The eddy was pressed tightly against Hawai‘i during the cruise, creating currents of  $\sim 1$  m/s along Hawai‘i’s coast. AVHRR imagery suggests that the cyclone may have become unstable and shed anticyclonic vorticity from its shell into satellite vortices, creating a tripole vortex such as those described by van Heijst *et al.* [1991]. The eddy entrained several drifters as it drifted westward, one of which remained in the eddy for nearly 240 days. Other drifters encountered two anticyclones,

which may have been interacting (rotating anticyclonically about their joint center of mass and drawing together).

On 5–8 April 1996, nine drifters were deployed in the island lee region. The drifters revealed the presence of two lee cyclones and two anticyclones. An eddy dipole (composed of a paired anticyclonic and cyclonic eddy) may have formed in May 1996, which subsequently propagated southward at 8 cm/s. An additional drifter was deployed off the west coast of Hawai‘i in September 1996, within the core of a newly-born anticyclone with a rotational period of  $\sim 3$  days.

### 3.7 Discussion

When Wyrcki [1974] assembled a  $2^\circ$  resolution map of dynamic height in the Pacific Ocean, he discovered the presence of a pronounced North Equatorial Ridge running along  $\sim 20^\circ\text{N}$ .<sup>9</sup> A comparison between Fig. 9 and Fig. 27 shows that the mean propagation path of lee anticyclones coincides almost perfectly with the ridge. Because the ridge is highly variable (Fig. 11), its sharpness is confined within the upper 500 dbar [Wyrcki, 1974] (as are the eddies themselves [Patzert, 1968]), and lee anticyclones can lift sea level 20–30 cm, it is hereby proposed that the North Equatorial Ridge is the superposition of the smooth, gyre-scale dynamic height field and the mean signature of lee anticyclones. This hypothesis is consistent with all Wyrcki’s [1974] dynamic height maps except his Fig. 5 (May–June), which shows a well-defined ridge extending to  $\sim 145^\circ\text{W}$ . However, the May–June XBT/CTD observations compiled for this study show only the broad crest of the gyre-scale dynamic height field east of the islands.<sup>10</sup>

---

<sup>9</sup>While this feature is also the crest of the gyre-scale dynamic topography, Wyrcki used the term “ridge” to indicate that this crest was very sharply-defined. For example, he noted that “[n]o similar feature seems to exist in the South Pacific Ocean.” While later investigators (c.f. Kessler [1990]) have used the phrase “North Equatorial Ridge” interchangeably with the crest of the North Equatorial Subtropical Gyre spanning the entire Pacific, its earlier usage is intended here.

<sup>10</sup>Dynamic height climbs from 1.1 m to 1.17 m between  $14^\circ\text{N}$  and  $20^\circ\text{N}$ , then drops to 1.1 m at  $25.4^\circ\text{N}$ ; the overall average east of the islands, shown in Fig. 55, is quite similar. In contrast, dynamic

### 3.7.1 *Half-inertial lee eddies*

Several young lee anticyclones (AC94a, AC94c, AC96c) had core vorticities close to the local value of  $-f$ , i.e. core rotational periods close to one pendulum day. As shown in the section on inertial instability, these “half-inertial” [Chew and Bushnell, 1990] eddies have reached the limit on their vorticity set by centrifugal instability. If further energy was being added to them while they were observed, it presumably cascades rapidly to submesoscales by overturning at the eddies’ edge. Thus, these eddies may be associated with significant mixing immediately southwest of Hawai‘i.

In two examples (AC94a and AC96b), the data suggested that recently-formed lee anticyclones had periods longer than the local pendulum day. Apparently, the upper limit on the eddies’ strength is not always reached, or merging events (see below) can occasionally happen quite rapidly after vortex formation.

### 3.7.2 *Spin-down*

From mid-June to mid-August, the drifter caught in anticyclone AC94b recorded what appears to be spin-down of the eddy core (Fig. 38). The drifter’s orbits increased in radius from 40 km to 55 km, then decreased to 37 km, then increased again to 50 km; throughout this span, the orbital period steadily increased from 4.4 days to 7.85 days. This behavior is consistent with the drifter being in the solid-body core of the eddy (hence, the orbital period was independent of the radius) while the eddy’s core was spinning down.

A similar spin-down may have been seen for anticyclone AC94c. If the orbital period of drifters within 55 km of the eddy center are plotted as a function of time (Fig. 41), their period increases from  $\sim 4.7$  days to  $\sim 7.3$  days from 1 October to 1 December.

---

height west of the islands climbs from 1.21 m to 1.29 m between  $15.7^\circ\text{N}$  and  $18.5^\circ\text{N}$ , then drops to 1.21 m at  $20.9^\circ\text{N}$  (Fig. 65).

In Appendix D, a simple model is described which can be tuned to match these observations. The model uses the core/shell eddy structure (B.9). It assumes that mass is entrained into the core of the eddy at a rate proportional to  $\sqrt{A}$ , where  $A$  is a viscosity constant. As the mass is entrained, angular momentum is conserved; this causes the eddy’s spin rate to decrease as a function of time. This model was applied to AC94b by setting an initial inner radius  $r_i = 53$  km, outer radius  $r_o = 200$  km<sup>11</sup> and period of 4.4 days. The upper layer width was  $H_1 = 230$  m, the reduced gravity  $g' = 0.0353$  m/s<sup>2</sup>, and the Coriolis parameter  $f = 4.26 \times 10^{-4}$  s<sup>-1</sup>; these values give a Rossby radius of 66.8 km, and are reasonable choices for the Hawaiian region [Qiu *et al.*, 1997]. For  $A = 0.25$  m<sup>2</sup>/s, the model closely matches the observations (Fig. 41). At the end of 77 model days, the core rotational period increases to 8 days, the core radius to 70.1 km, and the shell radius to 205.3 km. The final mass of the eddy’s shell is 0.994 times its initial value, while the core mass increases by 1.70 times. The model eddy’s energy is shown as a function of time in Fig. 42; the final energy of the eddy is 0.82 times its initial value. Energy is initially lost at a rate of  $4\mu\text{W}/\text{m}^3$ , which drops to  $2.3\mu\text{W}/\text{m}^3$  by the end of the run. Because the eddy grows in size while it decays, an ever-increasing fraction of its total energy is partitioned in potential energy as it ages (c.f. Gill [1982], p. 206). As a result, while the eddy’s total energy monotonically decreases with time, its potential energy increases through the first 27 days of the model run. The angular momentum of the eddy remains unchanged, due to the spin-down model’s assumptions. The entrainment rate into the eddy’s core is  $2.65 - 2.8 \times 10^8$  kg/s.

The same value of the diffusivity constant does a reasonable job of simulating AC94c’s observed spin-down (using an initial core radius of 60 km and all other values identical). However, throughout May 1994, the drifter orbiting AC94b had a nearly

---

<sup>11</sup> the core spin-down is not sensitive to this choice in the limit  $r_i/r_o \ll 1$ . The curve in Fig. 41 is only slightly higher for  $r_o = 150$  km, and virtually unchanged for  $r_o > 200$  km.

constant period of  $\sim 3$  days. With  $A = 0.25 \text{ m}^2/\text{s}$ , the entrainment model cannot simulate this. If the model eddy has an initial core period of 3 days, with inner and outer radii of 40 and 150 km, the spin-down model predicts that the period will increase to 4.7 days after 30 days. It is possible that early in its life, AC94b was maintaining its core vorticity by extracting energy from the shear between the NEC jet and Hawai'i's lee. The model eddy loses energy at a rate of  $0.3 \text{ J}/\text{m}^3$  per day ( $3.5 \mu\text{W}/\text{m}^3$ ). This could be balanced by a source term of the form

$$-\rho \langle u'v' \rangle \partial_y \langle v \rangle \quad (3.22)$$

(c.f. [Hansen and Paul, 1984]). The drifter observations from  $156.5$  to  $160^\circ\text{W}$  (Figs. 58, 59) show that the Reynolds shear stress  $\langle u'v' \rangle$  in this region is  $(-1.0 \pm 0.5) \times 10^{-2} \text{ m}^2/\text{s}^2$  and the mean shear (from  $18$  to  $19^\circ\text{N}$ ) is  $\sim 2 \times 10^{-6} \text{ s}^{-1}$ . These values give a mean to eddy kinetic energy conversion rate of  $(19.6 \pm 11.2) \mu\text{W}/\text{m}^3$ , suggesting that there is a sufficient pool of energy to maintain the anticyclones' half-inertial rotation until they have drifted several degrees downstream or leave the shear layer.

### 3.7.3 Eddy merging

At the beginning of June 1994, the drifter orbiting AC94b abruptly switched from 3.0 day, 6 km orbits to 4.5 day, 40 km orbits. The simplest explanation for this behavior is that the drifter moved into the outer shell of the eddy, where azimuthal speed diminishes with increasing distance. However, as noted in the previous section, the orbital characteristics of the drifter from June to mid-August suggest that it was still within the eddy's solid-body core. Twice more, in late August and late September, the drifter's orbits abruptly increased in both their period and radius.

The altimetric observations of the eddy (Fig. 40) strongly suggest that the eddy's structure was not stagnant. As the eddy aged, its core grew larger and rotated more

slowly. Qualitatively, this behavior is consistent with the entrainment model described in the previous section. But how well does it quantitatively agree with the observed orbital characteristics of the drifter?

To answer this question, a simulated eddy, described by the core/shell structure (B.9), was assumed to spin-down according to the entrainment model. The diffusivity constant was chosen to be  $A = 0.25 \text{ m}^2/\text{s}$ . The model simulated 260 days of spin-down, with an initial core radius of 40 km and shell radius of 200 km. This was approximately the size of AC94b in mid-May 1994, so model day 1 was defined as “14 May.” The initial rotational period of the core (3.5 days) was chosen so that the model output matched the observations for June to mid-August (see Fig. 43).

Suppose a drifter was placed in the simulated eddy, and it moved toward and away from the eddy center as in Fig. 38. The period of its orbits would then be set by the model eddy’s evolving structure. To create this simulated drifter trajectory, the time series of the (real) drifter’s orbital radius around AC94b was interpolated to a 0.25-day grid. This fixed the radial position  $R(t)$  of the model drifter in the eddy. The rate of change of the drifter’s azimuthal position  $\theta(R(t), t)$  was then given by the eddy’s speed at radius  $R$ . The simulated trajectory was integrated in 0.25-day steps, then subsampled at the times when ARGOS fixes were made on the real drifter. For each complete orbit of the model drifter, a time series of the orbital period was given by the least-squares technique described earlier.

Fig. 43 shows the evolution of the model drifter’s orbits, compared to those of the real drifter around AC94b. The model cannot capture the sudden jump from half-inertial orbits to  $\sim 4.5$ -day orbits in early June. However, it does simulate the early September transition to 13-day orbits, because the drifter exits the solid-body core at the beginning of this month. As the drifter moves to  $\sim 110$  km orbits in early October,

its period jumps to 45 days, approximately twice the observed period. This discrepancy diminishes as the core expands outward due to entrainment; by early December, the orbital period of the model drifter has dropped to  $\sim 37$  days.

Thus, while it may be fortuitous, the spin-down model can account for one of the observed period jumps of the real drifter. However, no amount of tweaking will allow the model to simulate an abrupt 3 to  $\sim 4.5$ -day jump in the core period, followed by a much slower spin-down. This behavior is consistent, however, with eddy merging.

In the laboratory, an unstable shear layer grows by developing into a train of vortices which, as they advect downstream, pair and merge into larger vortices (c.f. [Brown and Roshko, 1974; Winant and Browand, 1974]). These in turn pair and merge, and the process continuously expands the width of the shear layer until the side walls of the laboratory tank stabilize the vortices. In this paper, it has been hypothesized that the NEC jet separates from Hawai‘i’s south point, leading to the formation of a train of half-inertial anticyclones. Unlike in the nonrotating tank experiments, the eddies are stable as long as their core vorticity is lower in magnitude than  $f$ . However, they may still spontaneously merge, as demonstrated in rotating tanks [Nof and Simon, 1987; Griffiths and Hopfinger, 1987], oceanic observations [Cresswell, 1982; Tokos *et al.*, 1994], and numerical experiments [Melander *et al.*, 1988; Verron and Valcke, 1994; Carton and Bertrand, 1994; Valcke and Verron, 1997]. If two eddies merge, what are the characteristics of the resulting eddy? This question is addressed in Appendix E, which uses simple conservation laws and the core/shell eddy structure. It is shown that eddies can conserve mass and angular momentum when they merge, but in so doing they will lose some fraction of their total energy. Physically, this is analogous to the Rossby adjustment problem, in which the lost energy is due to radiation away from the equilibrium solution (c.f. Gill [1982], pp. 191–203). Alternatively, eddies can

conserve energy and angular momentum when they merge, but they will then lose mass; the lost mass may be ejected in thin filaments which bear negligible energy or angular momentum [Cushman-Roisin, 1989]. Both cases predict that if identical vortices merge, the core period of the resulting eddy will be longer than that of the parent eddies.

In Fig. 40, the sea level anomaly of the eddy is shown in four spans, each separated by one of the period jumps of the drifter. During the span when the drifter had 3-day orbits, altimetry suggests that this was the eddy's core period. When the drifter had 4.5 to 8 day orbits, the altimetry suggests a mean core period of 6 days. During the remaining two spans, the altimetry suggests a  $\sim 12$ -day rotational period of the core. Thus, the first two period jumps of the drifter may have been associated with an increase in the core vorticity of the eddy itself. As an alternative to a pure spin-down model, it is proposed that the eddy merged twice with neighbors in the anticyclone train.

This hypothesis was tested in a similar manner to the spin-down simulation. The model eddy was started with identical characteristics, but instead of spinning down, it was assumed to merge with an identical eddy on 6 May and 24 August. The merging was assumed to occur instantaneously. As before, a simulated drifter was placed in the eddy, giving a time series of orbital period which can be compared to the observations Fig. 44 shows the model output. If energy is conserved during a merging, the eddy's period increases by 1.41 times on 6 May; this is close to the observed jump. The resulting eddy has 74% of the mass of its parents. The 24 August merging causes the period to increase by 1.47 times, and 77% of the mass is conserved. After early June, the simulated orbital period of the drifter falls below the observed curve, and is half its value at the end of the model run. In contrast, if mass is conserved in a merging, the period almost exactly doubles on 6 May and 24 August. The simulated periods are longer than the observations throughout June, and fall below them in July through August. With

the 24 August period doubling, the simulated period jumps to the observed value, and climbs with them to  $\sim 24$  days as the drifter leaves the eddy’s core in October.

Of course, without entrainment the merging model cannot simulate the decrease in core vorticity observed from June to mid-August. The models can be easily combined, by assuming mergings on 6 May and 24 August, and allowing the eddy to spin-down via entrainment between mergings. Because the observations show that the period remained steady until after the first period jump, the model entrainment was not “switched on” until after 6 May.

The simulated curves for this combined model are shown in Fig. 45. When energy is conserved in the merging model, the model prediction closely follows the observations until October, when it fails to climb above 16 days. The mass-conserved merging model predicts periods higher than the observations until late in the run. These model runs show that the observed 6 May and 24 August period jumps are consistent with eddy merging, particularly under the assumption that energy is conserved in the merging. In all cases, the mass-conserving mergings predict too large a period jump. However, this is largely a consequence of the assumption that the model eddy merges with an *identical* eddy. Variations in the sizes of lee eddies could arise from fluctuations in the trade winds and/or the strength of the NEC impinging on Hawai’i. If two eddies having the same core vorticity but different sizes are merged, the resulting period jump will always be less than for identical eddies.<sup>12</sup> In the model, variations in eddy size can easily be included: for example, the model eddy can merge with an eddy  $\alpha$  times its size, with the same core vorticity, on 6 May and 24 August. Of course, without direct observations of the eddies adjacent to AC94b,  $\alpha$  simply becomes a free parameter which can be arbitrarily tuned to fit the model output to the observations. For example, Fig. 46 shows the evolution

---

<sup>12</sup>This is most easily illustrated by considering the limit in which one eddy is vanishingly small compared to the other: after the merging, the characteristics of the larger eddy remain unchanged.

of the core radius and simulated orbital periods if the model eddy merges with an eddy 0.6 times its size on 6 May and 24 August, mass is conserved in the mergings, and entrainment proceeds exactly as in the previous models. The parameter  $\alpha$  has added a degree of freedom which allows the model to match the observations extremely closely. Of course, this model run cannot demonstrate that mergings are occurring, but it does suggest that the merging-plus-entrainment hypothesis is at least consistent with the observations.

### 3.8 Conclusions

Patzert [1968] showed that Hawaiian lee eddies have lifetimes in excess of 3 months. In this study, this estimate can be extended to 8 months for cyclonic eddies, and over a year for anticyclones. Perhaps the most surprising result from this study is the organized train of extremely energetic anticyclonic eddies, generated at a mean period of  $\sim 50$  days in Hawai'i's lee and possibly merging as they drift WSW to the edge of the study region. Indeed, one cannot help but wonder how far these eddies continue across the Pacific Ocean!<sup>13</sup> The altimetric and drifter observations demonstrate that the eddies grow larger and rotate more slowly as they propagate westward, presumably due to entrainment and possibly vortex merging. This growth can help explain the location of maximum dynamic height variance, west of the maximum drifter speed variance (see Fig. 11). The ratio of potential to kinetic energy for a quasigeostrophic eddy is proportional to the eddy's size divided by the deformation radius (c.f. Gill [1982], p. 206). Thus, the mean eddy potential energy (and associated dynamic height variations) may initially increase as the eddy ages, as seen in the spin-down simulation (see Fig. 42). In addition, if there is downstream vortex merging, the potential energy can abruptly

---

<sup>13</sup>For the spin-down model run of AC94b, the energy of the model eddy has an  $e$ -folding time scale of 680 days. At a mean westward speed of 10 cm/s, and starting at 155°W, this suggests the eddies reach 150°E.

increase along the eddies' trajectory due to the increase in mean eddy size.

If the anticyclones are often produced with half-inertial cores, then tend to pair and merge downstream, a quantization of their period could be expected. For example, the mass-conserving model predicts that the period will roughly double with each (identical) merging. This may explain the ADCP and drifter observations of AC94c, which suggest that the core period of the eddy doubled between 8 September and 4 October. Evidence for this quantization in the Lagrangian spectra of all drifters is presented in Chapter 5 (see Fig. 88). The quantization is eroded by the gradual spin-down of the eddies and by natural variations in their sizes. Also, some eddies (such as AC94a) appear to be produced at lower initial core periods.

Mitchum [1995] showed that energetic altimetric signals originate at Hawai'i, propagate westward, and may account for the 90-day oscillations in Wake Island sea level; a peak in the same frequency band can be seen at Johnston Atoll as well (Fig. 33). Mitchum proposed that these oscillations were long Rossby waves radiated in the decay of anticyclonic lee eddies [Flierl, 1984], because they propagated near the long Rossby wave speed and because Rossby waves with a  $20^\circ$  turning latitude have a period of  $\sim 120$  days (which could be Doppler-shifted to 90 days by background currents). In this study, several westward-propagating altimetric anomalies have been identified as lee eddies; drifters entrained within them clearly demonstrate cycloidal trajectories, as opposed to the transverse motion of drifters in a Rossby wave packet [Price and Rossby, 1982]. These coherent vortices are observed to propagate at speeds close to the long Rossby wave speed. As shown in Fig. 32, many of the peaks at Johnston Atoll can be identified as lee anticyclones. Thus, these observations suggest that the 90-day peak in the Johnston Atoll spectrum is directly due to the passage of lee eddies, rather than an indirect process such as Rossby wave radiation. The 90-day signals at Wake cannot

be as clearly related to the passage of lee eddies: Wake Island is well-off the mean WNW/WSW trajectories of the lee eddies (which should lower the Eulerian period of their passage) and eddy decay should significantly weaken their sea surface fluctuations by that longitude. Because the variance of the 90-day signal at Wake is actually *larger* than the signal at Johnston (see Fig. 33), an additional, and perhaps more significant, mechanism may be occurring there, such as local generation of mesoscale fluctuations from baroclinic instability in the Subtropical Countercurrent [Qiu, 1998].

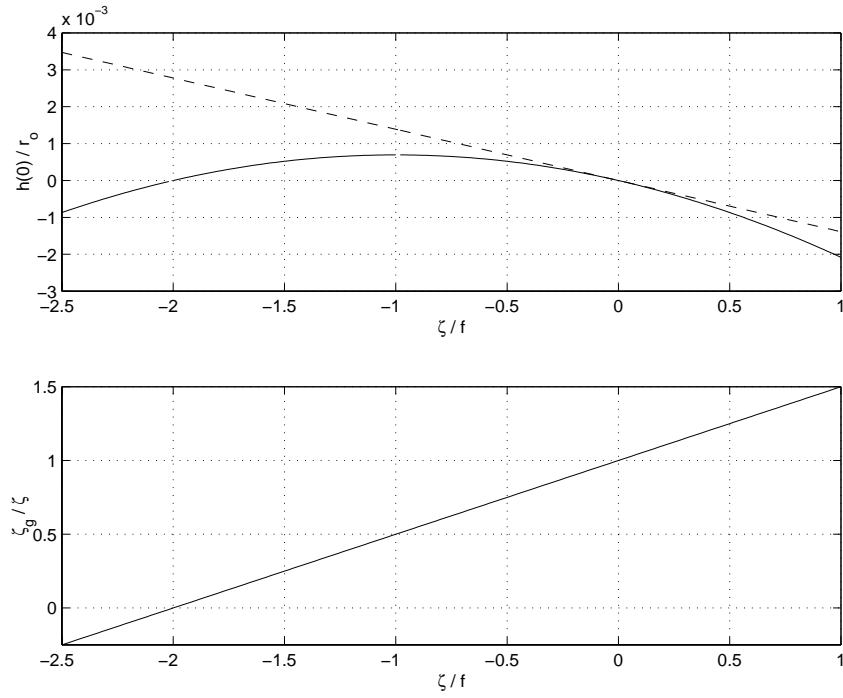


Figure 21: *Top*: total change in thickness of a solid-body cyclogeostrophic eddy divided by its radius, as a function of the Rossby number  $\zeta/f$  (solid). For comparison, the same relationship is shown for an eddy assumed to be purely geostrophic (dashed). *Bottom*: ratio of vorticity estimated from geostrophy to true vorticity of a solid-body cyclogeostrophic eddy, as a function of Rossby number.

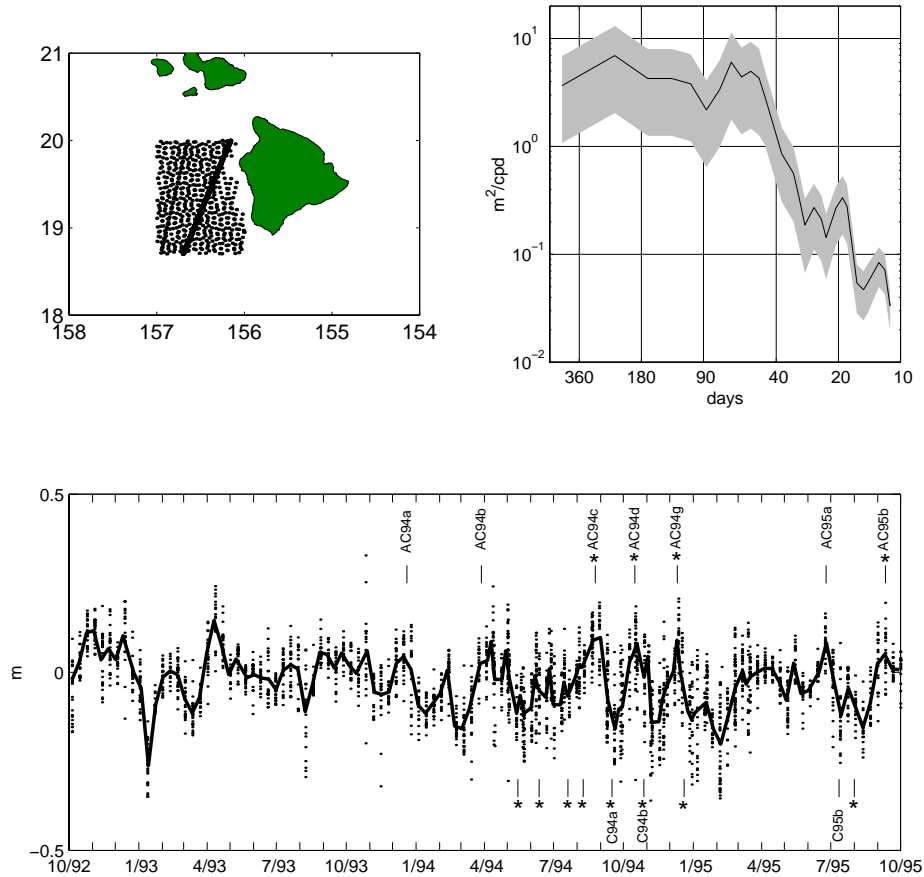


Figure 22: Sea level anomaly (SLA) in the immediate lee of Hawai'i.

*Top, left:* SLA observations in the lee of Hawai'i.

*Top, right:* spectrum of the 5-day running mean of SLA.

*Bottom:* SLA vs. time. The solid line is a 5-day running mean. Names of anticyclones (top) and cyclones (bottom) are given when they were in Hawai'i's lee. Stars indicate where AVHRR showed a cyclone first appearing off Keahole Point (bottom) or an anticyclonic cusps immediately west of Hawai'i's south point (top).

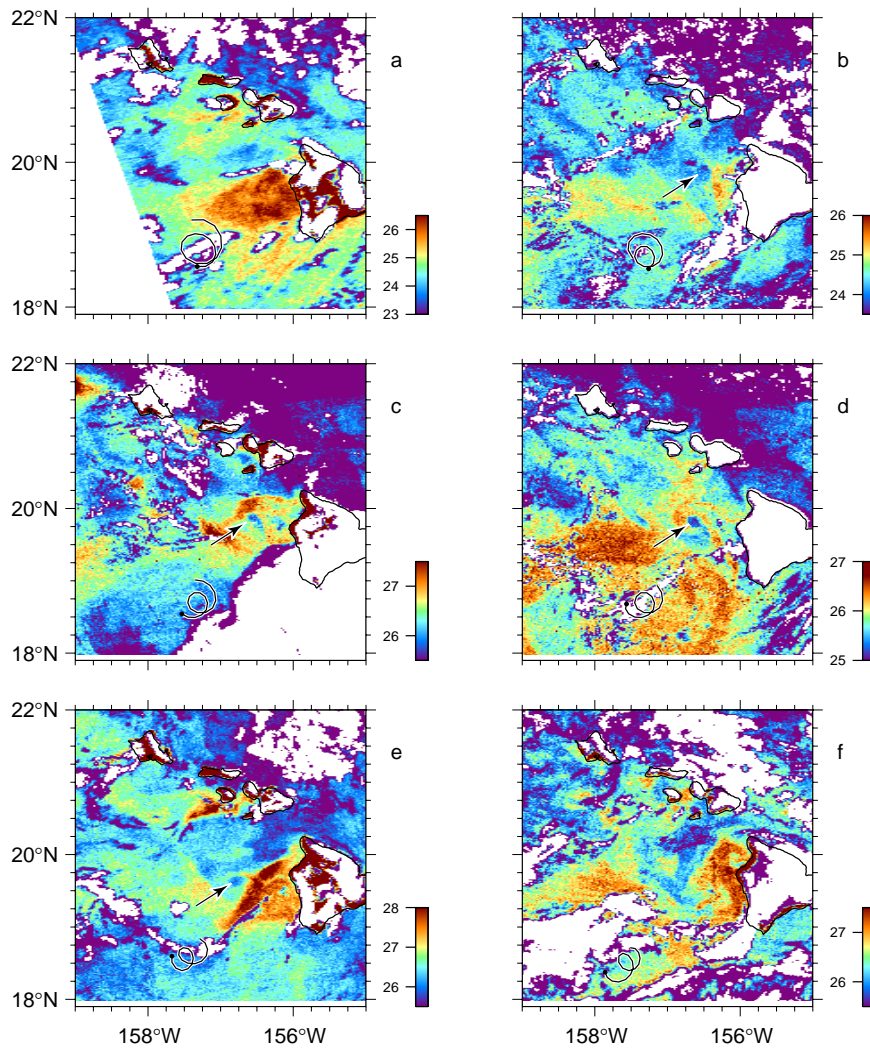


Figure 23: AVHRR SST images ( $^{\circ}\text{C}$ ), with concurrent drifter positions (points, with lines showing previous five days) overlaid. Arrow shows the location of a cyclonic eddy. Temperatures colder than  $22^{\circ}\text{C}$  have been flagged as clouds (white). The images were taken on 6 May 1994 at 0159 UTC (a), 8 May at 0548 UTC (b), 9 May at 0303 UTC (c), 9 May at 1536 UTC (d), 12 May at 0226 UTC (e) and 14 May at 1746 UTC (f).

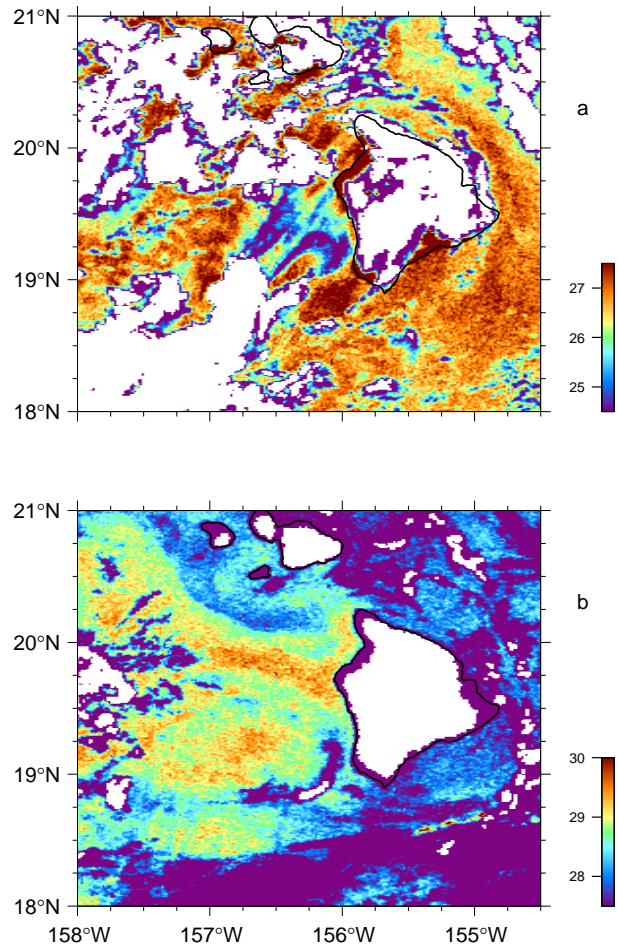


Figure 24: AVHRR SST images ( $^{\circ}\text{C}$ ). Temperatures colder than  $22^{\circ}\text{C}$  have been flagged as clouds (white). The images were taken on 18 August 1994 at 1811 UTC (a) and 29 August at 1608 UTC (b).

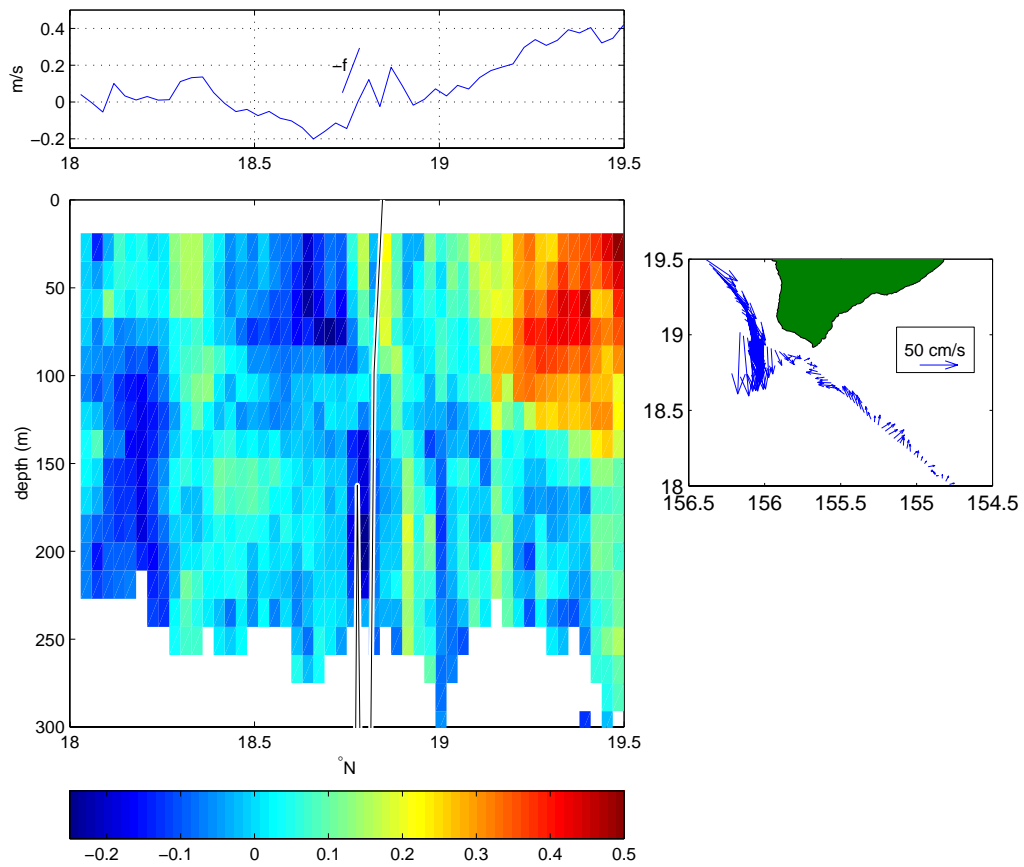


Figure 25: An ADCP profile of the NEC passing the south point of Hawai'i. ADCP data from cruise TC9407, 16 August 1994.

*Right:* current vectors averaged over the upper 70 m, showing the ship track.

*Left, top:* zonal current averaged over the upper 70 m vs. latitude.

*Left, bottom:* zonal currents vs. depth. Negative values are westward, into the figure. The black line is the bathymetry of Hawai'i projected SW onto the ship track.

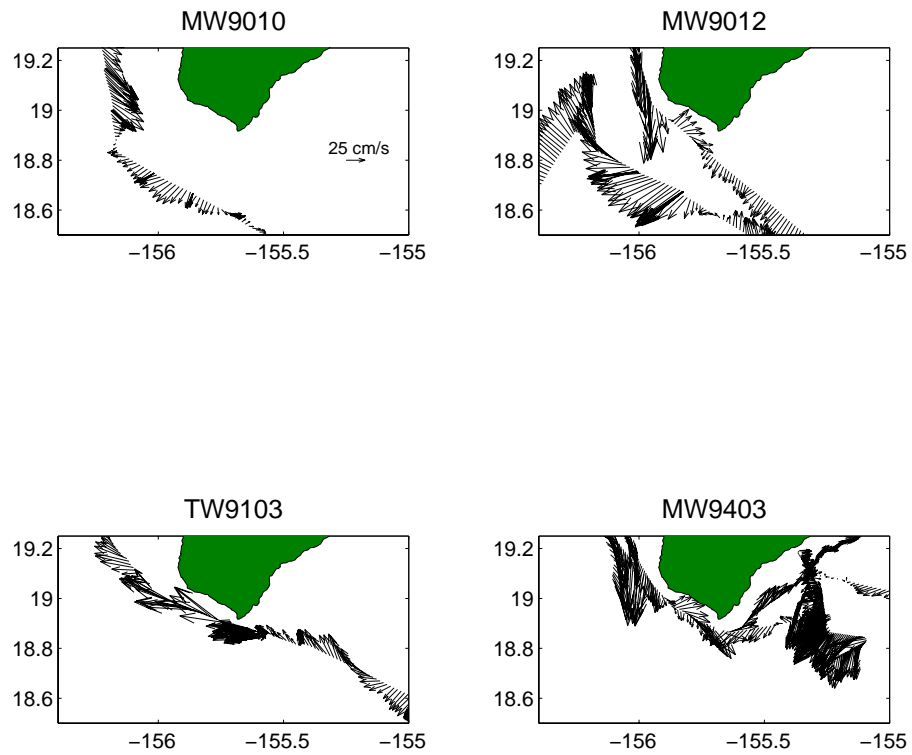


Figure 26: ADCP profiles of the NEC jet after passing the south point of Hawai'i. Cruise names (ship and year) are given in the titles. “MW” is the R/V *Moana Wave*, “TW” is the R/V *Thomas Washington*.

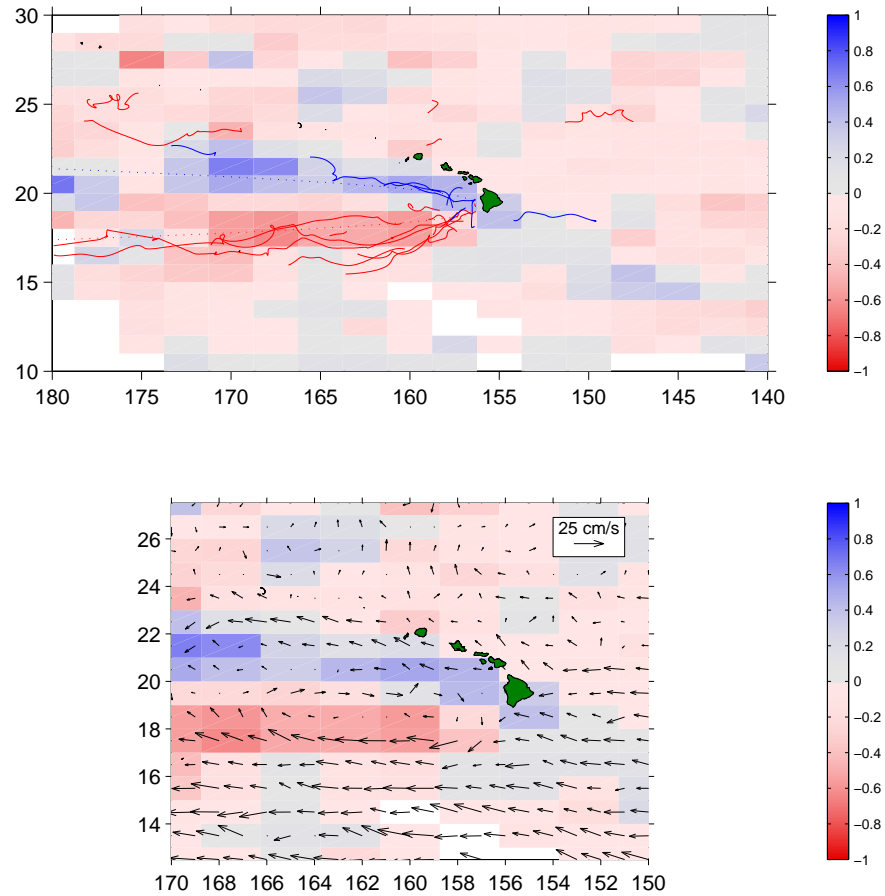


Figure 27: Mean parsing of subinertial variance into counter-clockwise (blue) and clockwise (red) motion. The fraction of CCW variance from Fig. 28 (top) was divided by the total variance, then scaled from +1 (purely CCW) to  $-1$  (purely CW). Superimposed (top panel) are the trajectories of individual cyclonic (blue) and anticyclonic (red) eddies tracked by drifters. Dashed lines show the trajectories of cyclonic (blue) and anticyclonic (red) eddies given by (3.13), (3.14).

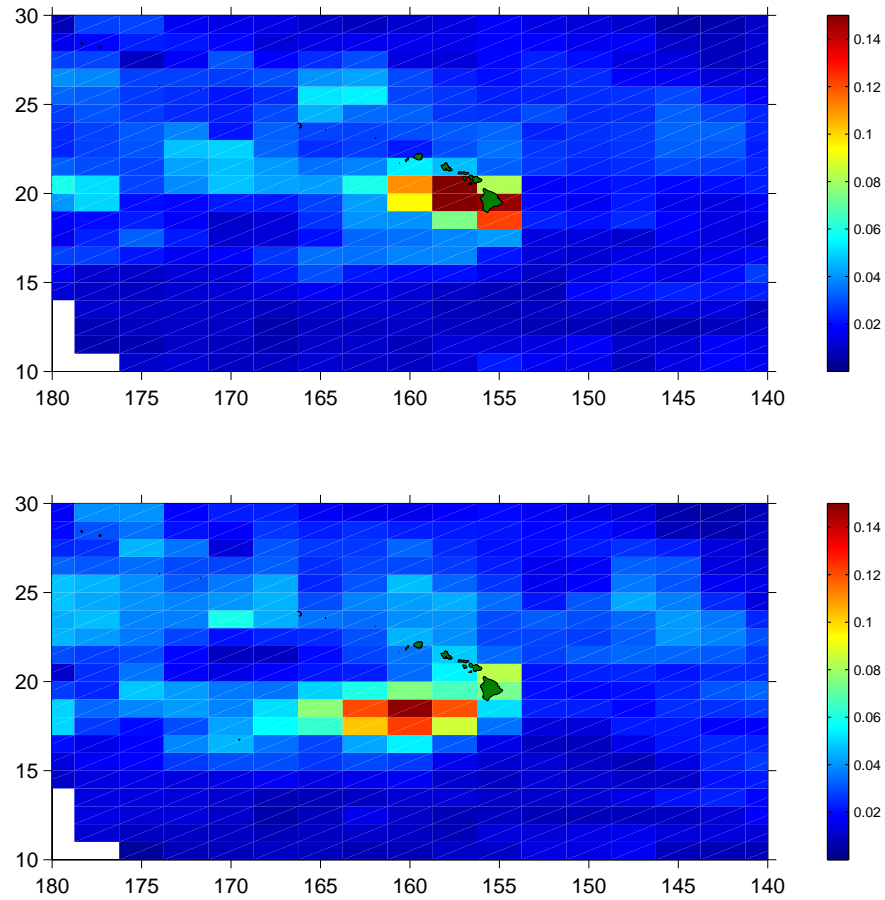


Figure 28: Mean CCW (top) and CW (bottom) variance  $\langle u'^2 + v'^2 \rangle$  ( $\text{m}^2/\text{s}^2$ ), calculated by integrating the rotary spectra of 60-day drifter trajectories and plotting the median value in each cell. Every other cell is calculated from independent data.

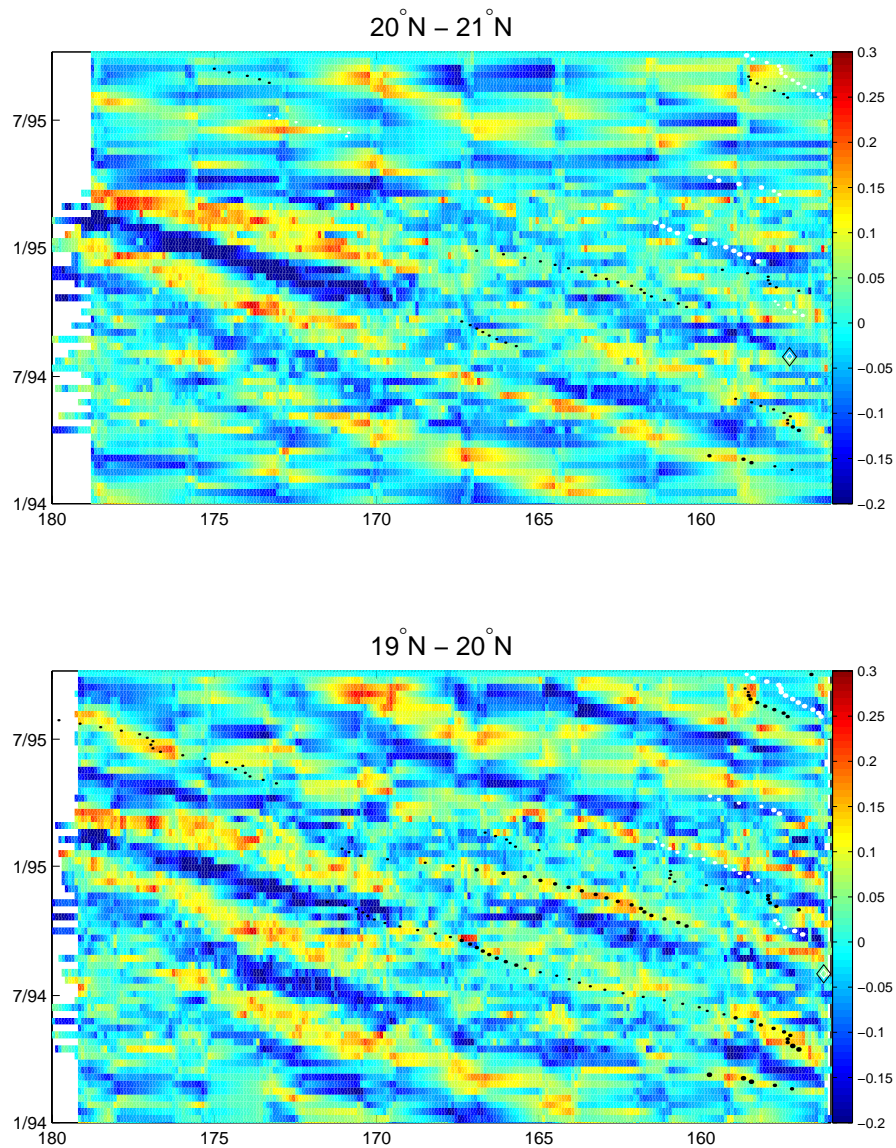


Figure 29: Longitude vs. time plots of sea level anomaly in fixed latitude bands. Dots indicate the paths of cyclonic (white) and anticyclonic (black) eddies followed by drifters. Heavy dots show when the eddy was in the latitude band of that panel; medium-sized dots show when the eddy was in an adjacent  $1^\circ$  band, and light dots show when the eddy was two bands away.

In the top figure, a diamond shows the ADCP-observed center of eddy C95a (see Fig. 105). In the bottom figure, a diamond shows the ADCP-observed center of eddy C95b (see Fig. 108).

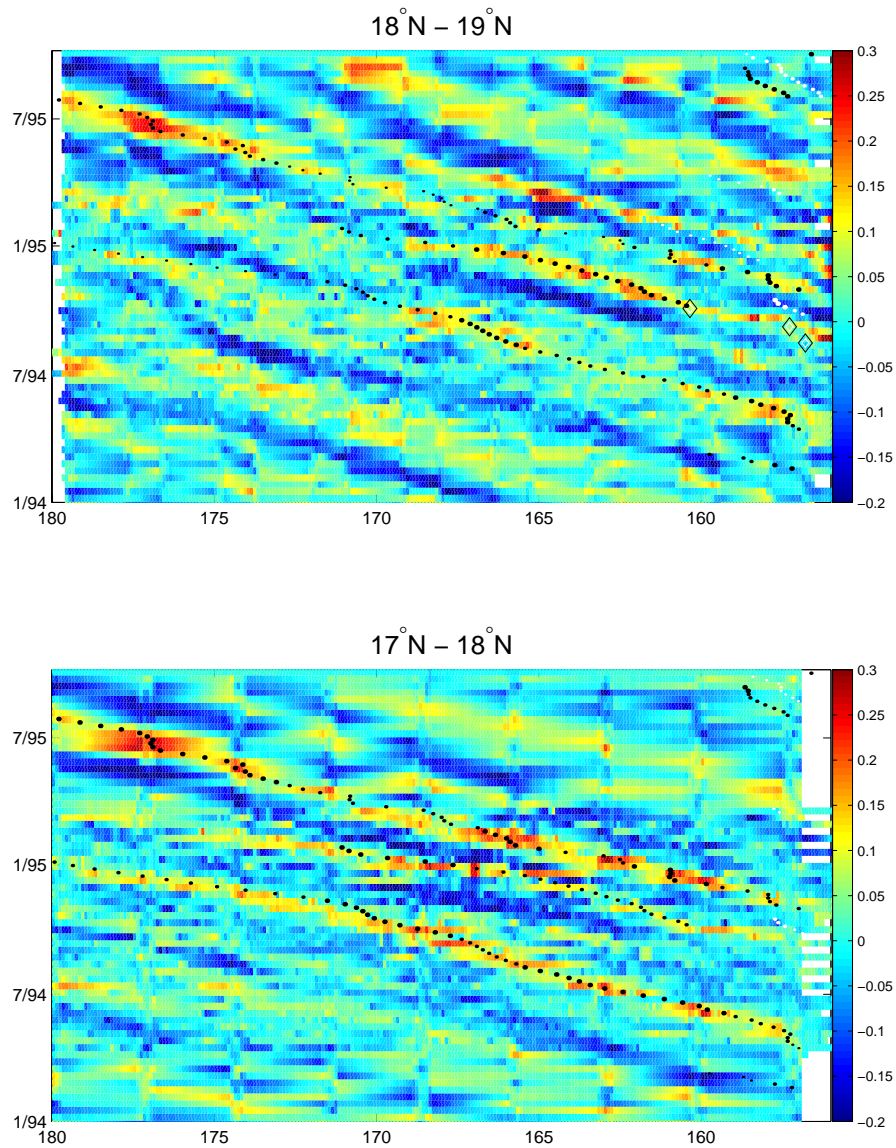


Figure 30: Longitude vs. time plots of sea level anomaly in fixed latitude bands. Dots indicate the paths of cyclonic (white) and anticyclonic (black) eddies followed by drifters. Heavy dots show when the eddy was in the latitude band of that panel; medium-sized dots show when the eddy was in an adjacent  $1^{\circ}$  band, and light dots show when the eddy was two bands away. In the top figure, diamonds show the ADCP-observed centers of eddy AC94c (see Figs. 93, 94, 97).

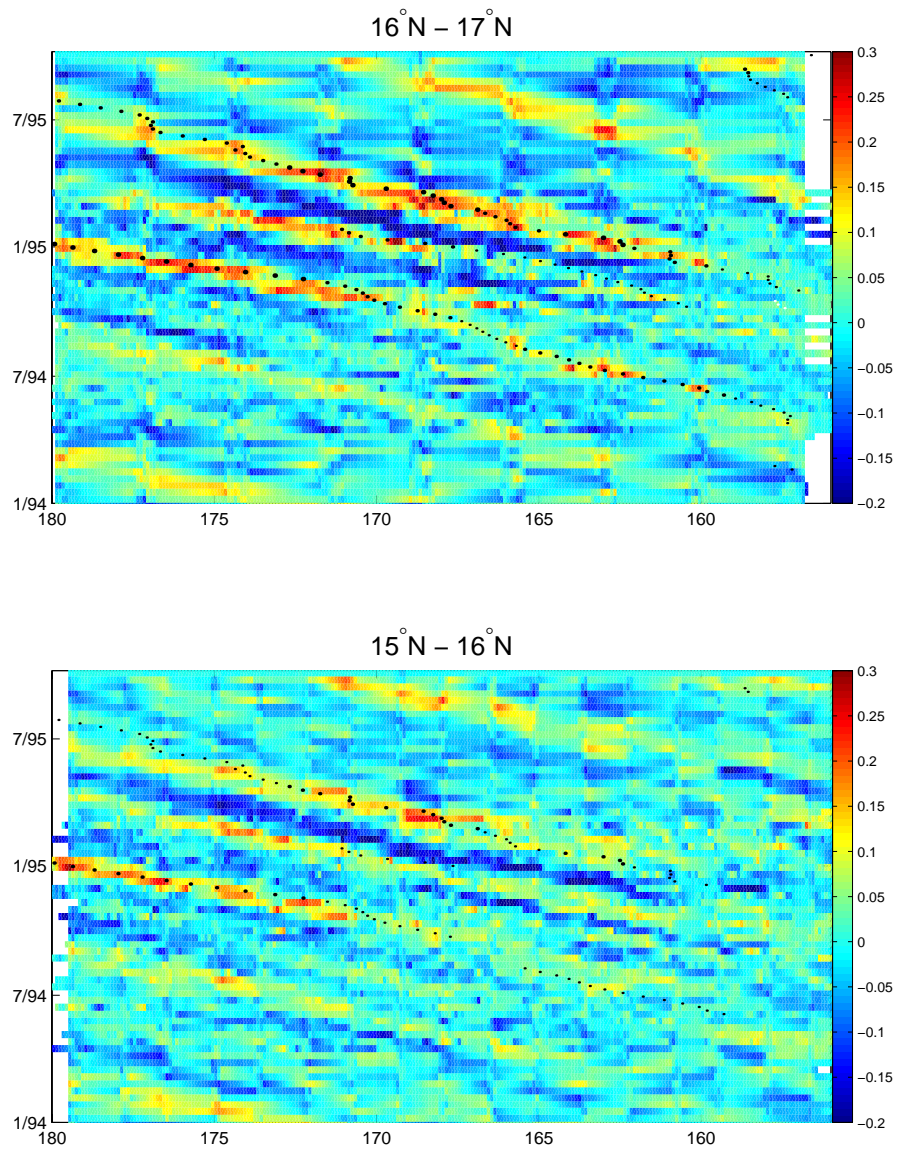


Figure 31: Longitude vs. time plots of sea level anomaly in fixed latitude bands. Dots indicate the paths of cyclonic (white) and anticyclonic (black) eddies followed by drifters. Heavy dots show when the eddy was in the latitude band of that panel; medium-sized dots show when the eddy was in an adjacent  $1^{\circ}$  band, and light dots show when the eddy was two bands away.

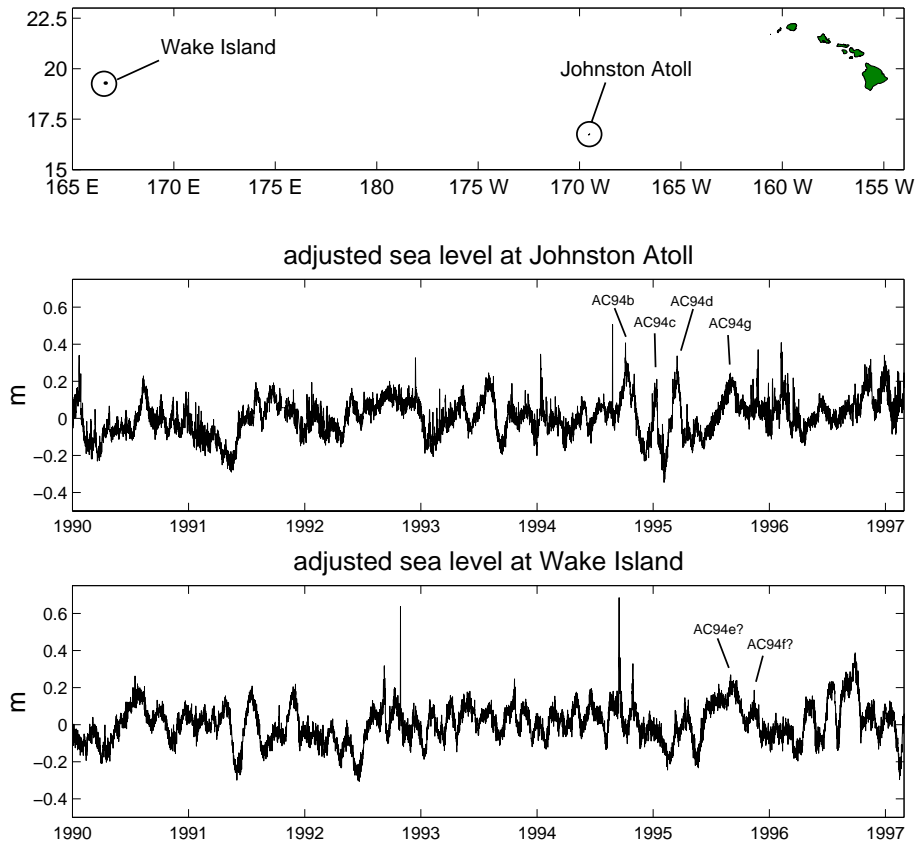


Figure 32: *Top*: location of Johnston Atoll and Wake Island.  
*Middle*: hourly sea level at Johnston Atoll, with tides removed.  
*Bottom*: hourly sea level at Wake Island, with tides removed.

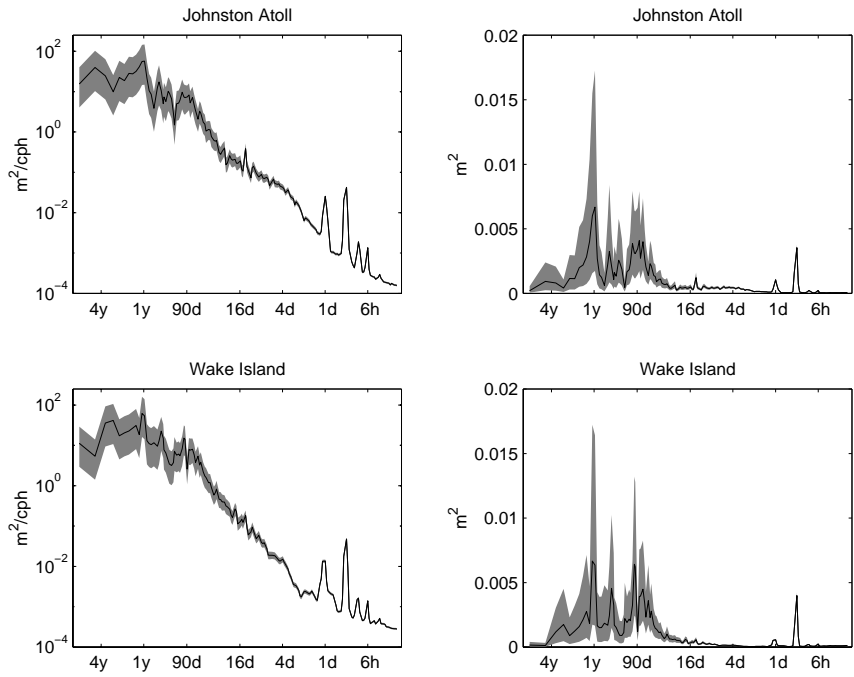


Figure 33: *Top*: spectrum of 12.16 years of hourly sea level at Johnston Atoll in log-log (left) and energy-preserving (right) form. Low-frequency peaks are at the annual period, 227 days, 163 days, and  $\sim 90$  days.

*Bottom*: spectrum of 12.16 years of hourly sea level at Wake Island in log-log (left) and energy-preserving (right) form. Low-frequency peaks are at the annual period, 200 days, 95 days and  $\sim 78$  days.

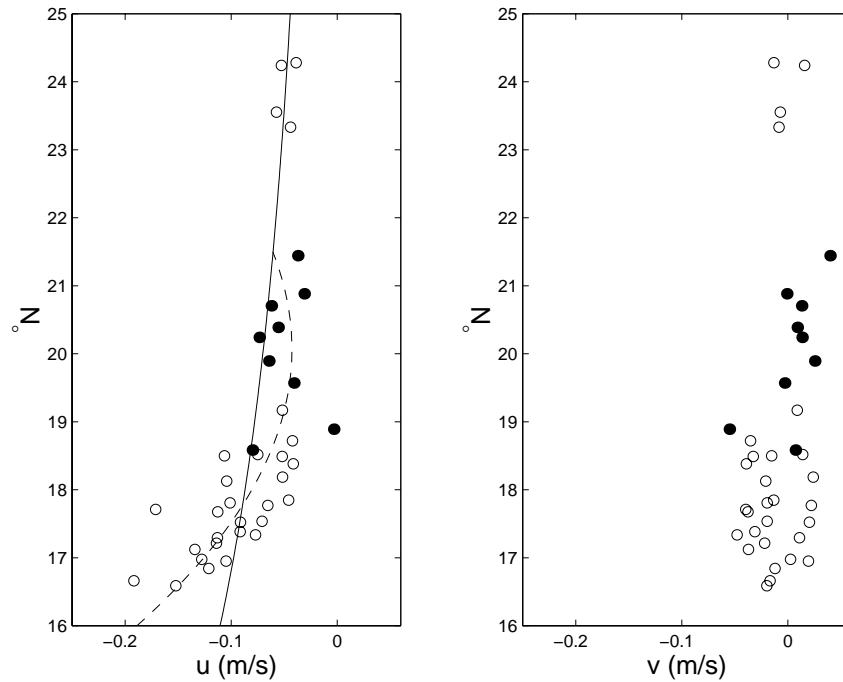


Figure 34: *Left*: zonal speeds of cyclonic (black dots) and anticyclonic (white dots) eddies as a function of latitude. Speeds are calculated from ten-day differences of the eddy location. The solid line is the long Rossby wave speed for  $g' = .0353 \text{ m/s}^2$ ,  $H = 230 \text{ m}$  [Qiu *et al.*, 1997]. The dashed line is a least-squares fit of a polynomial  $alat^2 + blat + c$  onto the speeds south of  $22^\circ\text{N}$ . *Right*: meridional speeds of cyclones (black dots) and anticyclones (white dots) as a function of latitude.

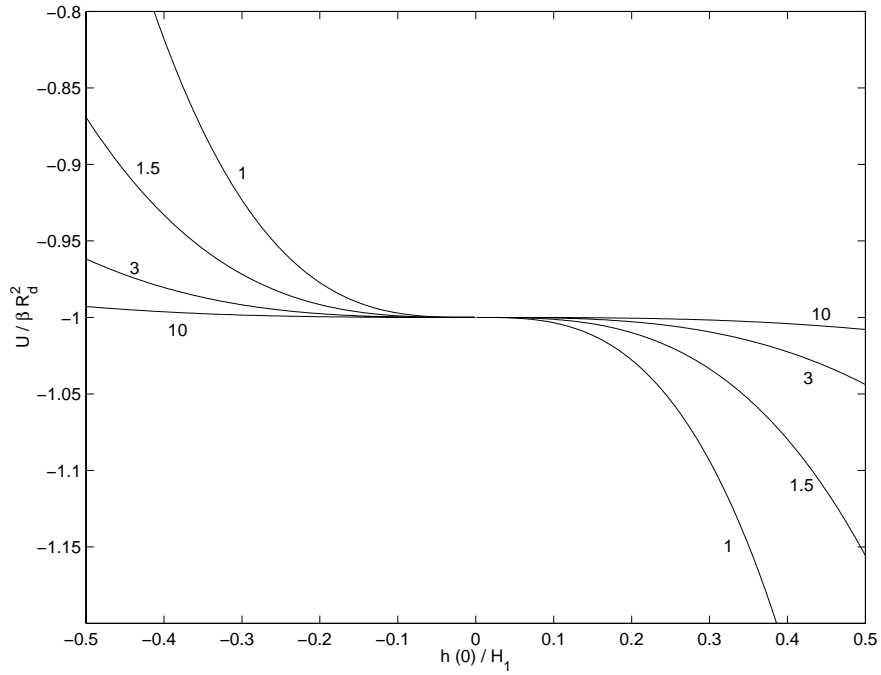


Figure 35: The  $\beta$ -induced zonal speed of eddies described by the core/shell model (B.9), plotted as a function of the interface displacement at their center  $h(0)$  divided by the undisturbed upper-layer thickness  $H_1$ . Negative  $h(0)$  corresponds to cyclones, positive to anticyclones. The number by each curve gives the ratio of  $r_o$  (the radius of the outer shell) to  $r_i$  (the radius of the solid-body core) for that curve.

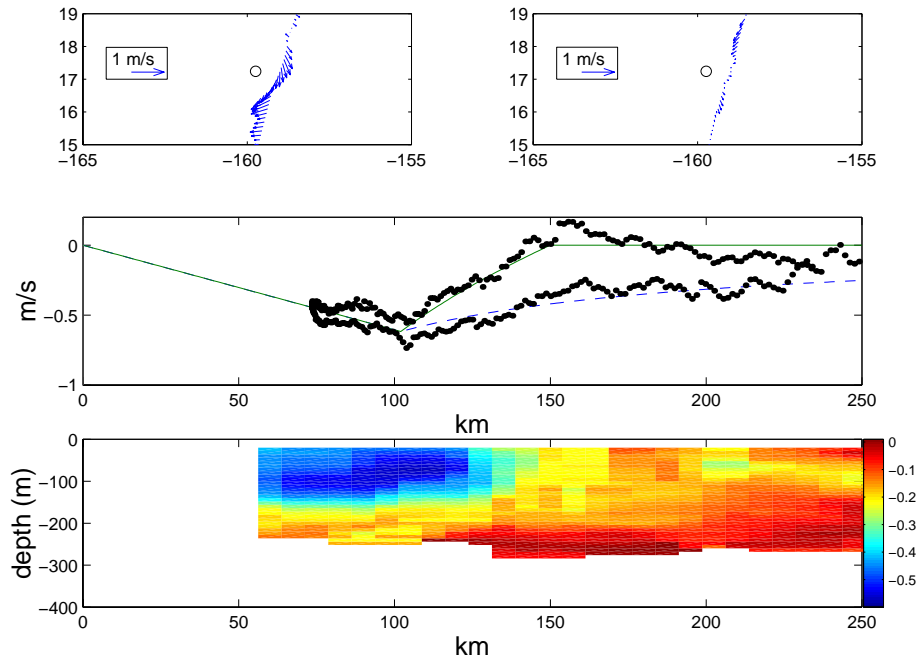


Figure 36: *Top*: A circle marks the center of anticyclonic eddy AC89. The azimuthal (left) and radial (right) components of velocity are shown.

*Middle*: azimuthal speed vs. distance from eddy center. Negative values indicate clockwise rotation. The dashed line is an estimated fit of a Rankine vortex structure, and the solid line is a fit of the core/shell model.

*Bottom*: azimuthal speed (m/s) as a function of depth. Negative values are clockwise.

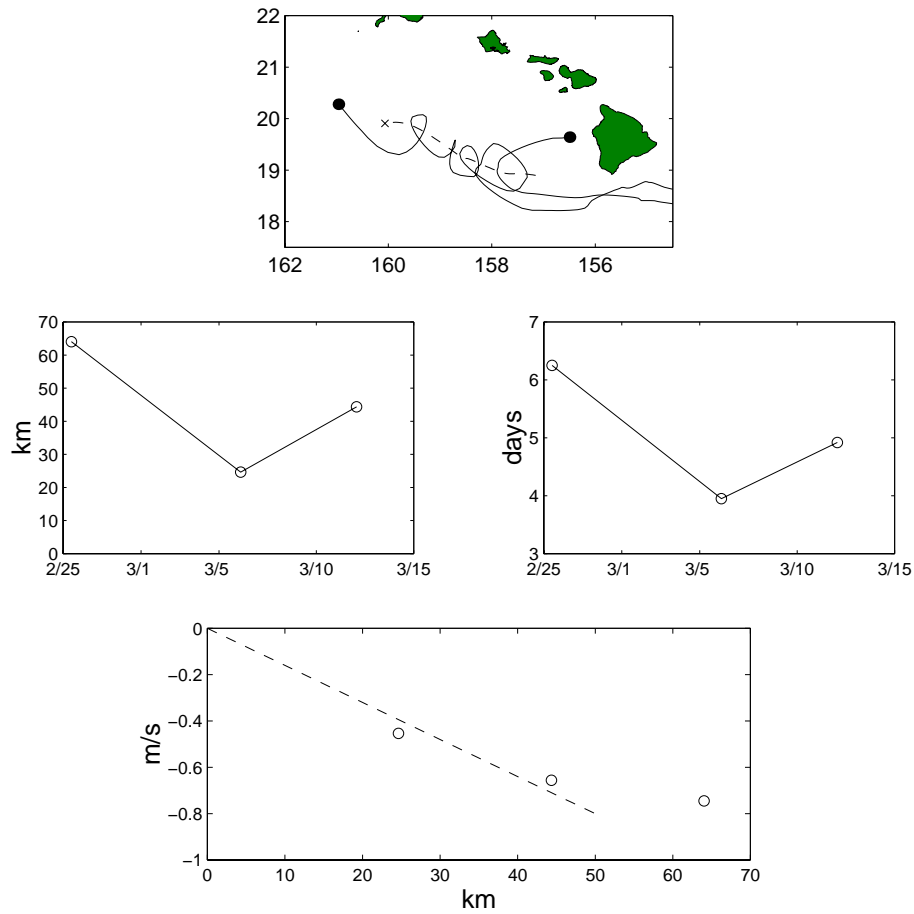


Figure 37: Orbital characteristics of a drifter in AC94a.

*Top:* trajectories of drifters around eddy (solid lines), with dots marking the location of the drifter when it left the eddy or was about to run aground. The dashed line is the path of the eddy center, with an **x** marking its last known location.

*Middle, left:* orbital radius vs. time.

*Middle, right:* orbital period vs. time.

*Bottom:* orbital speed vs. radius. The dashed line is for solid-body rotation at a period of 4.5 days.

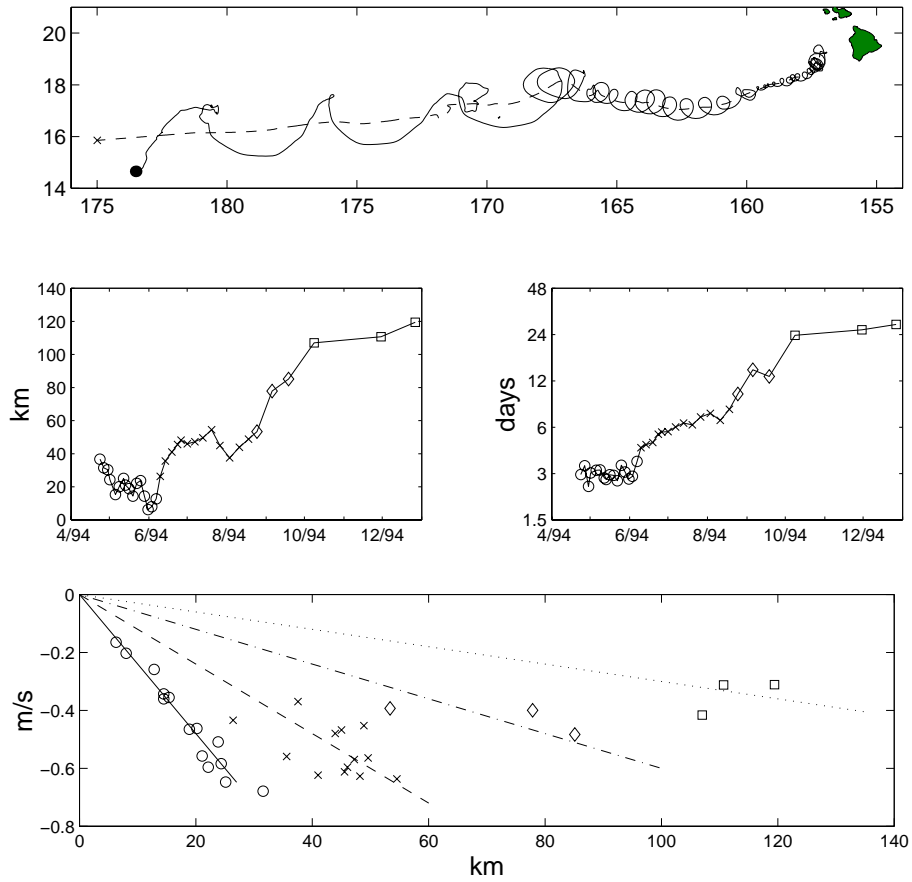


Figure 38: Orbital characteristics of a drifter in AC94b.

*Top:* trajectory of drifter around eddy (solid lines), with dots marking the location of the drifter when it left the eddy. The dashed line is the path of the eddy center, with an **x** marking its last known location.

*Middle, left:* orbital radius vs. time. Different symbols are used for orbits with period of 3 days (**o**),  $\sim 6$  days (**x**),  $\sim 12$  days (diamonds) and 24–36 days (squares).

*Middle, right:* orbital period vs. time.

*Bottom:* orbital speed vs. radius. The lines are for solid-body rotation at 3.0 days (solid), 6.1 days (dashed), 12.1 days (dot-dash) and 24.2 days (dotted).

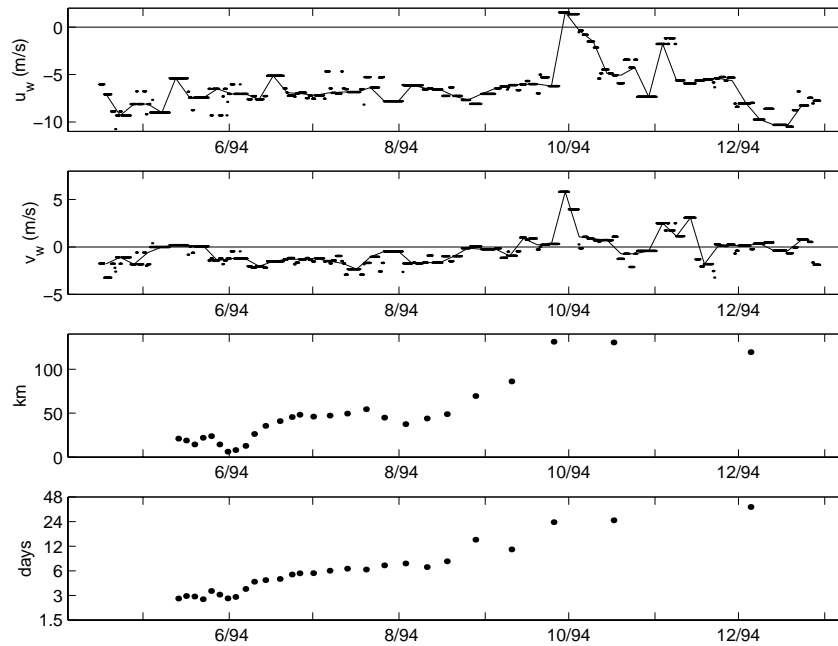


Figure 39: *Top:* ERS-1 scatterometer zonal wind at the grid point closest to the drifter orbiting AC94b.

*Middle, upper:* ERS-1 scatterometer meridional wind at the grid point closest to the drifter orbiting AC94b.

*Middle, lower:* orbital radius of the drifter.

*Bottom:* orbital period of the drifter.

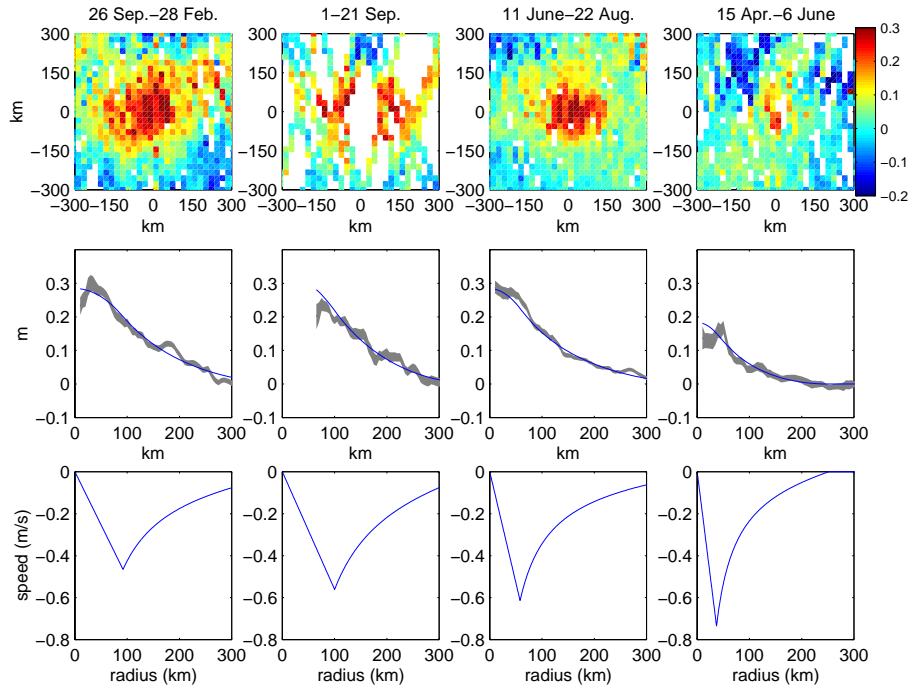


Figure 40: *Top*: ERS-1 and TOPEX altimetry in the frame of reference moving with eddy AC94b. Four time spans are shown; the earliest (far right) is concurrent with the 3-day orbits of the drifter, the second (middle, right) with the  $\sim 6$ -day orbits, the third (middle, left) with the  $\sim 12$ -day orbits, and the last (left) with the 24–36-day orbits. *Middle*: azimuthally-averaged sea level anomaly for each time span ( $\pm 1$  standard error, shaded). Smooth lines are least-squares fits of the core/shell model sea surface displacement. *Bottom*: corresponding velocity structure from the least-squares fits.

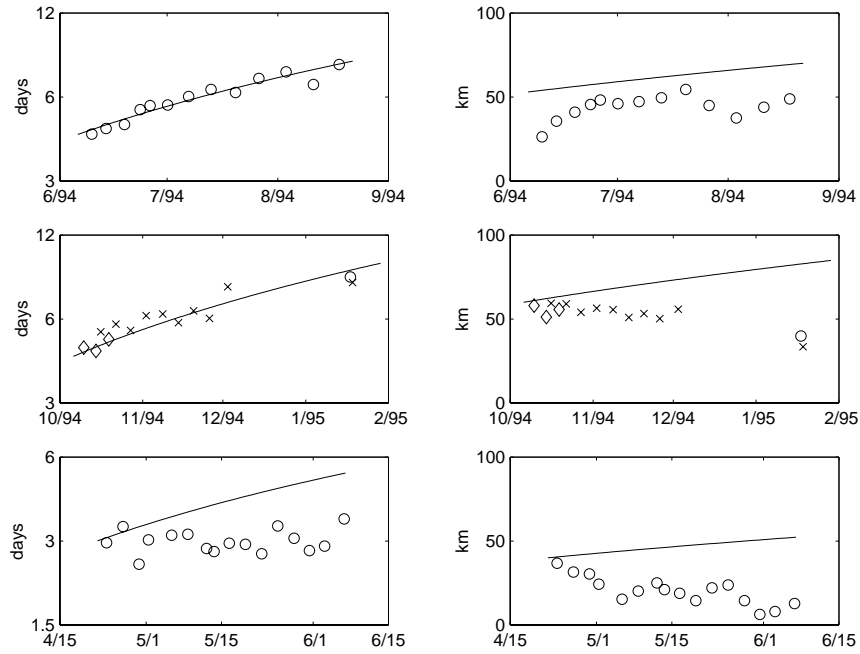


Figure 41: *Top:* Left: Observed orbital period vs. time of drifter in AC94b (circles). The solid line is the model fit (see text). Right: Radius of drifter orbits (circles) and core radius of model (solid line).

*Middle:* Left: Observed orbital period vs. time of drifters in AC94c within 55 km of the eddy center (different symbols used for different drifters). The solid line is the model with diffusivity derived from the fit to AC94b. Right: Radius of drifter orbits (symbols) and core radius of model (solid line).

*Bottom:* Left: Observed orbital period vs. time (month/day in 1994) of drifters in AC94b. The solid line is the model with diffusivity derived from the May-September AC94b fit. Right: Radius of drifter orbits (symbols) and core radius of model (solid line).

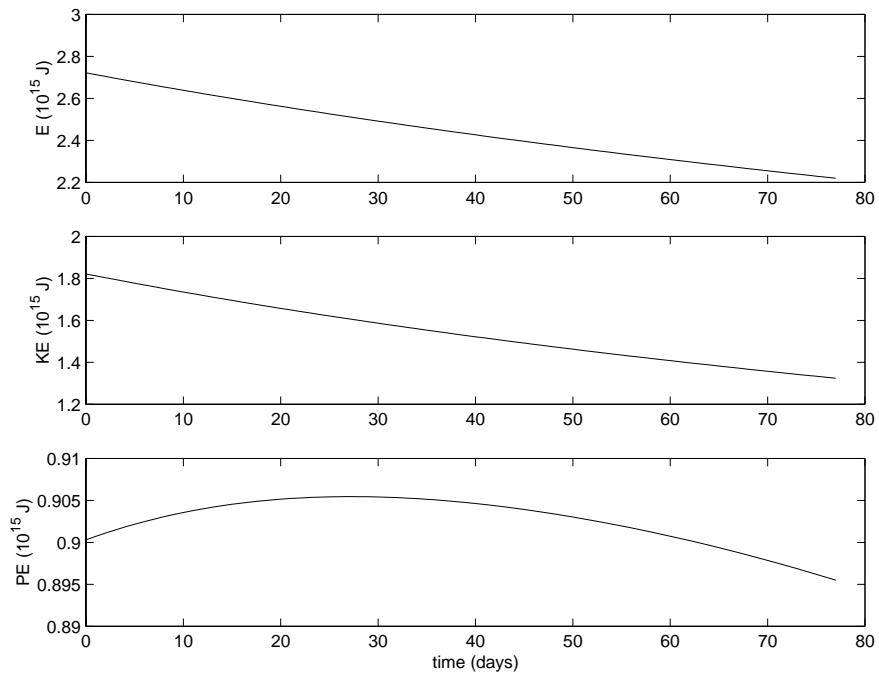


Figure 42: Energy ( $10^{15}$  J) as a function of time (days) for the model eddy in the spin-down simulation (Fig. 41, top). Top: total energy. Middle: kinetic energy. Bottom: potential energy.

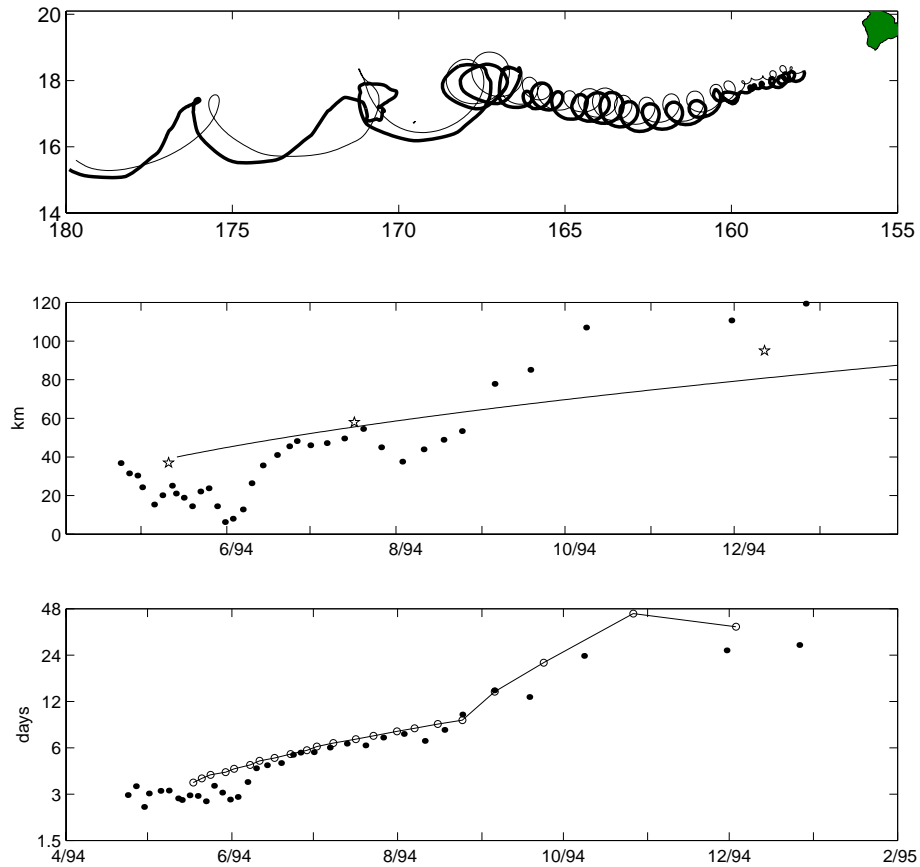


Figure 43: Modeling AC94b, Pt. I: entrainment only

*Top:* A simulated drifter trajectory in an eddy which starts at the approximate size of AC94b and spins down according to the entrainment model (thin line). The heavy line is the trajectory of the real drifter.

*Middle:* Growth of the model eddy's core radius (solid line) vs. estimates from altimetry (stars). Also shown are the radii of the drifter's orbits (dots).

*Bottom:* Periods of the model drifter's orbits (solid line with circles). For comparison, the real drifter's orbital periods are shown (dots).

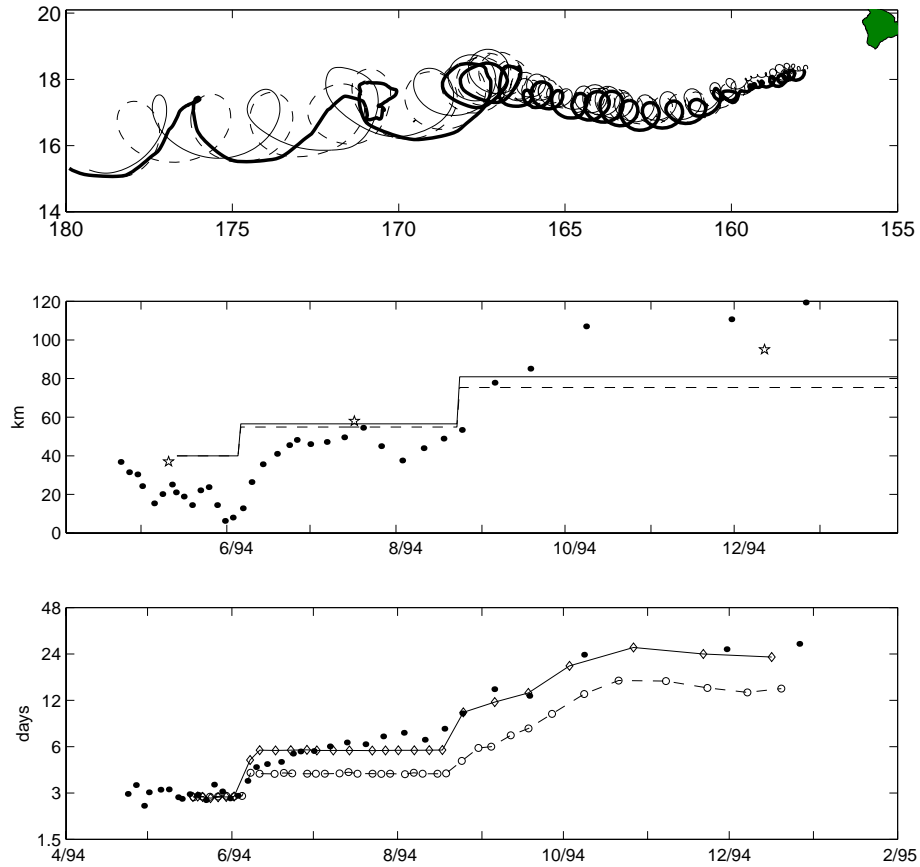


Figure 44: Modeling AC94b, Pt. II: merging only

*Top:* A simulated drifter trajectory in an eddy which starts at the approximate size of AC94b and merges twice with identical eddies. Both merging cases are shown (thin solid line, mass conserved; dashed line, energy conserved). The heavy line is the trajectory of the real drifter.

*Middle:* Growth of the model eddy's core radius (solid line, mass conserved; dashed line, energy conserved) vs. estimates from altimetry (stars). Dots show the radii of the drifter's orbits.

*Bottom:* Periods of the model drifter's orbits (solid line with diamonds, mass conserved; dashed line with circles, energy conserved). For comparison, the real drifter's orbital periods are shown (dots).

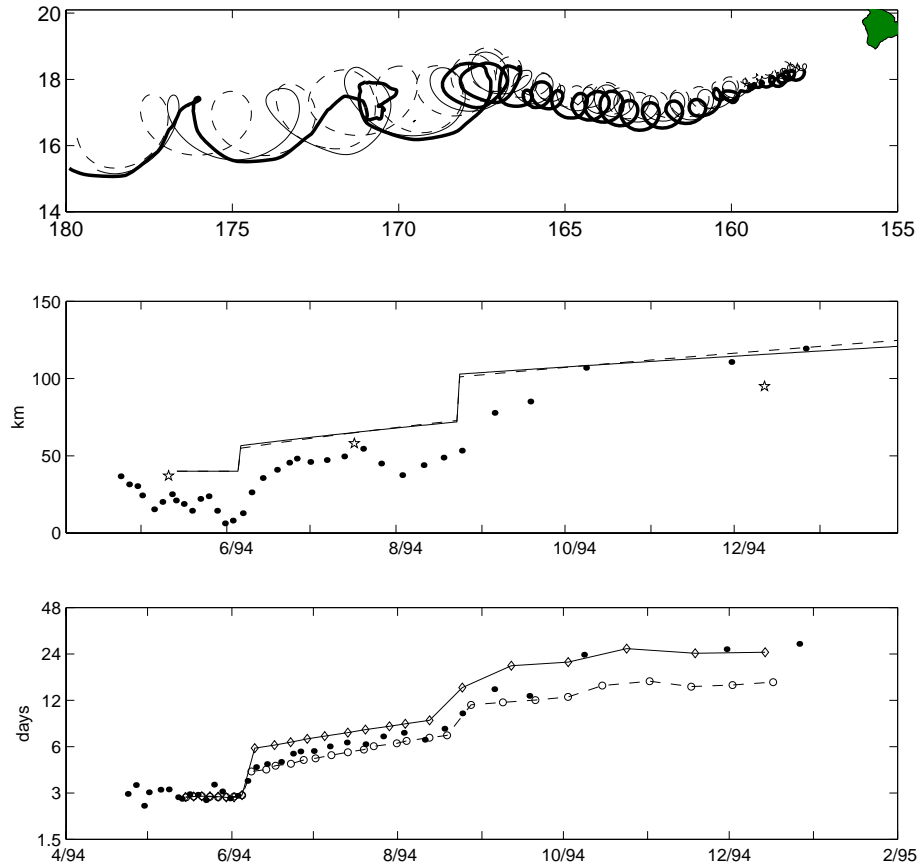


Figure 45: Modeling AC94b, Pt. III: merging + entrainment

*Top:* Simulated drifter trajectory in an eddy which starts at the approximate size of AC94b, merges twice with identical eddies, and spins down according to the entrainment model. Both merging cases are shown (thin solid line, mass conserved; dashed line, energy conserved). The heavy line is the trajectory of the real drifter.

*Middle:* Growth of the model eddy's core radius (solid line, mass conserved mergings; dashed line, energy conserved) vs. estimates from altimetry (stars). Dots show the radii of the drifter's orbits.

*Bottom:* Periods of the model drifter's orbits (solid line with diamonds, mass conserved mergings; dashed line with circles, energy conserved). Dots show the real drifter's orbital periods.

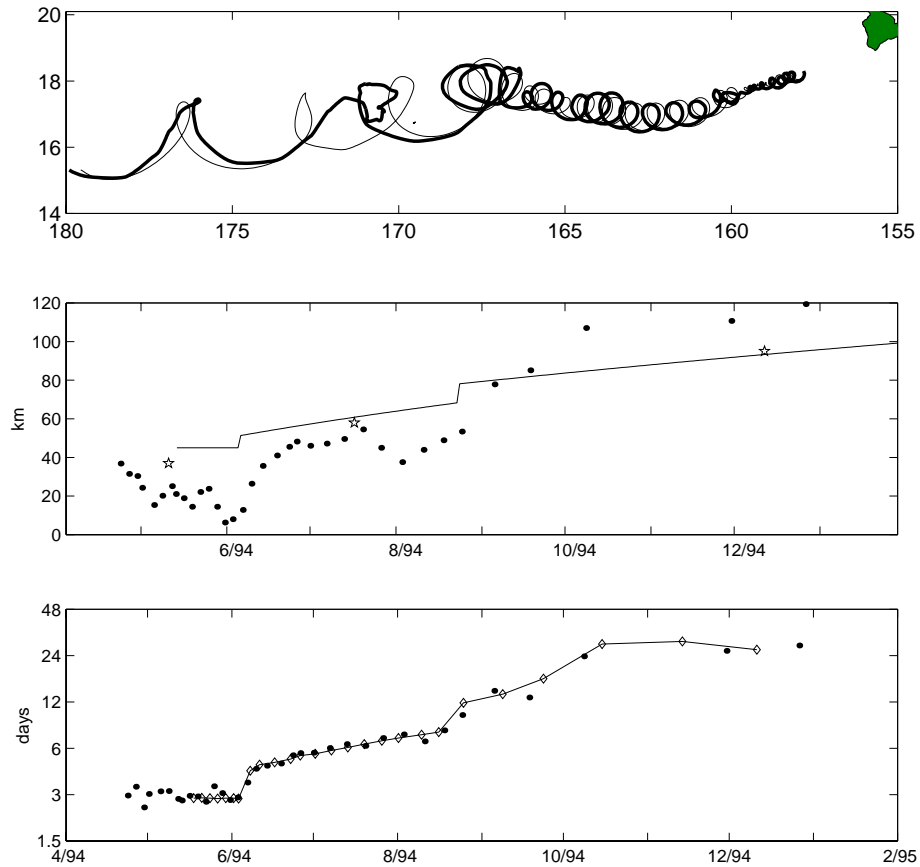


Figure 46: Modeling AC94b, Pt. IV: tuning the model.

*Top:* Simulated drifter trajectory in an eddy which starts at the approximate size of AC94b, merges twice with smaller eddies, and spins down according to the entrainment model (thin solid line). The heavy line is the trajectory of the real drifter.

*Middle:* Growth of the model eddy's core radius (solid line) vs. estimates from altimetry (stars). Dots show the radii of the drifter's orbits.

*Bottom:* Periods of the model drifter's orbits (solid line with diamonds). Dots show the real drifter's orbital periods.

## CHAPTER 4

### MEAN CURRENTS

*The directly wind-forced motion of drifters is identified, and the drifter motion is compared to the mean dynamic height gradient in several regions. The complex structure of the Hawaiian Island wake is seen in both data. Energy fluxes suggest that this mean structure is at least partly driven by the lee eddies.*

In a comparison between the trajectories of 16 NORPAX-type drifters (most drogued at 30 m depth) and dynamic topography relative to 500 dbar, McNally *et al.* [1983] found drifter motion orthogonal to the geostrophic flow east of the Hawaiian Islands, and 180° opposed to it north of the islands. They demonstrated that the drifter trajectories were generally aligned with isobars of sea level pressure. In the Hawaiian region, they reasoned that an additional northward flow (opposing the southward component of the geostrophic flow) was provided by Ekman drift. As noted by Niiler and Paduan [1995], NORPAX drifters have an effective drag area ratio less than a fifth that of WOCE drifters if the parachute drogue does not remain fully flooded. Studies of similar drifters have found that the trajectories of drogued and undrogued drifters are not significantly different [A. D. Kirwan *et al.*, 1978; McNally and White, 1985], suggesting that downwind slip may dominate their motion.

In this chapter, this comparison is re-performed between the WOCE drifter speeds and geostrophic currents derived from hydrography. Individual currents are compared in these independent data, demonstrating the existence of the elongated gyres forming the Hawaiian wake. The dynamics of these currents, including energy fluxes between the mean and eddy field, will be examined. Preliminary sections address two of the major differences between the drifter and hydrographic currents (geostrophic currents below the reference level, and wind-forced ageostrophic drift), define how the eddy and mean fields are separated in the data, and present the relevant energy equations.

#### 4.1 Deep geostrophic currents

In Fig. 9, the dynamic height has been referenced to 400 dbar. This choice of reference depth was motivated by the need for high-resolution data coverage (see Table 2.1). However, gyre-scale dynamic height gradients are significant to 1000 dbar in this region; referenced to 1000 dbar, the center of the subtropical gyre shifts northwestward, and geostrophic flow at the islands is more nearly zonal [Wyrski, 1974]. Between 400 dbar and 1000 dbar, the dynamic height reaches a minimum at  $14^\circ\text{N}$  (Fig. 47). The associated mean zonal current is  $O(1.5 \text{ cm/s})$  from  $20^\circ$  to  $26^\circ\text{N}$ . Sub-gyre-scale features such as the North Equatorial Ridge do not appear in dynamic height at 400 dbar referenced to 1000 dbar [Wyrski, 1974], suggesting they are contained within the upper 400 dbar. Dynamic height at 1000 dbar relative to 3000 dbar is nearly flat in this region (the mean slope is an order of magnitude less than in the 1000–400 dbar map [Wyrski, 1974]), and thus does not significantly contribute to the overall baroclinic geostrophic flow.

The abyssal baroclinic shear and depth-independent geostrophic currents are the final “ingredients” needed to estimate absolute geostrophic flow. Unfortunately, direct current measurements at the 1000 dbar reference level are relatively sparse in this region. From 1991 to 1996, nine Autonomous Lagrangian Circulation Explorer (ALACE) drifting buoys passed through the Hawaiian region (Fig. 48). The buoys are designed to be neutrally-buoyant at 1000 m depth, and pop to the surface at one-month intervals to transmit their position. Data coverage is too poor to construct a spatial map of the currents at this depth, although the overall pattern of the trajectories suggests a nearly zonal flow south of the islands. The mean speed of all ALACE buoys in the region is  $(u, v) = (1.8 \pm 0.3 \text{ cm/s}, 0.1 \pm 0.2 \text{ cm/s})$ .

These observations suggest that the absolute geostrophic flow (dynamic height referenced to 1000 dbar plus the absolute motion at that depth) is more zonal than the

geostrophic flow referenced to 400 dbar, with westward speeds larger by approximately 2 cm/s (at 14°N) to 3-4 cm/s (from 22° to 26°N). Of course, without better maps of the deep flow's spatial variations, this is at best a crude estimate of the additional geostrophic flow not seen in Fig. 9.

## 4.2 Ekman drift

Drifters measure the instantaneous current at 15 m depth. Thus, ageostrophic motion which does not disappear in a spatio-temporal average will affect the drifter-derived mean current map. The most significant flow of this nature is the directly wind-driven Ekman drift.

At periods much longer than inertial, homogeneous winds drive the mixed layer according to

$$ifU_E = \frac{1}{\rho}\partial_z\tau, \quad (4.1)$$

where  $U_E = u_E + iv_E$  is the Ekman drift, and  $\tau = \tau_x + i\tau_y$  is the stress. For simplicity, the stress  $\tau$  is often assumed to be a linear function of depth, decreasing from  $\tau_s$  at the surface (the wind stress) to 0 at the base of the mixed layer:

$$\tau = \tau_s \left( \frac{z}{h_{mix}} + 1 \right). \quad (4.2)$$

Substitution into (4.1) yields

$$U = -i\tau_s/\rho f h_{mix}. \quad (4.3)$$

The mixed layer moves as a depth-independent slab to the right ( $f > 0$ ) of the wind. Using the Levitus94 monthly mixed layer depth (Fig. 49) and the ERS-1 monthly surface wind stress, the time-averaged Ekman flow given by (4.3) is shown in Fig. 50. Averaged over space and time, the mixed layer depth is 69 m. Using the mean wind stress of  $(\tau_x, \tau_y) = (-6.30 \times 10^{-2} \text{ Pa}, -2.35 \times 10^{-2} \text{ Pa})$ ,  $\rho = 1030 \text{ kg/m}^3$  and  $f = 5 \times 10^{-5} \text{ s}^{-1}$ , this

gives a mean Ekman drift of

$$(u_E, v_E) \approx (-0.7 \text{ cm/s}, 1.8 \text{ cm/s}).$$

The slab model provides a lower estimate on the Ekman drift. A more precise estimate was derived by Niiler and Paduan [1995], in a study of 16 holey-sock drifters deployed in the northeast Pacific as part of the OCEAN STORMS experiment. They removed a downwind slip of  $7 \times 10^{-4}$  m/s per m/s of wind from the drifter speeds, then band-passed the speeds and ECMWF wind stress between 5 and 20 days period to minimize contamination by near-inertial and nonlocally-forced currents. They then applied a regression model of the form

$$U = b\tau_s. \tag{4.4}$$

By band-passing and relaxing the slab model assumptions, Niiler and Paduan hoped to avoid the poor results of previous regression attempts [Brink *et al.*, 1991]. They found  $|b|=0.28$  m/s Pa,  $\arg(b)=-77^\circ$  explained 35% of the variance in  $U$ . Comparing (4.3) to (4.4), this regression coefficient is equivalent to a complex mixing depth of magnitude 33.7 m. Niiler and Paduan called this the “apparent mixing depth,” noting that it is 0.56 times the observed depth of the mixed layer in the region. This result suggests that stress drops off more rapidly than does the linear profile assumed in the slab model [Niiler and Paduan, 1995].

In the Hawaiian region, this technique produces similar results: the regression model (4.4) was applied to 76 nonoverlapping drifter tracks of 120 days lying entirely within the Hawaiian region. The ERS-1 wind stress was linearly interpolated to the drifter positions, and the downwind slip (assumed identical to that of Niiler and Paduan [1995]) was removed. Due to the one-week ERS-1 sampling, the data were lowpassed at 14 days period. Because eddy energy in this region peaks at Lagrangian periods smaller than 20

days (see Chapter 5), the data were not highpassed at 20 days as in the Niiler and Paduan study. The regression gives  $|b|=0.30$  m/s Pa,  $\arg(b)=-60^\circ$ , corresponding to an apparent mixing depth of magnitude 64.7 m (0.93 times the mean Levitus mixed layer depth in the Hawaiian region). The magnitude of the regression coefficients for individual drifter segments does not show any obvious latitudinal dependence, suggesting that the apparent mixing depth decreases from north to south. However, the scatter of regression coefficients is large: the real part of  $b$  is  $0.149 \pm 0.086$  m/s Pa, and the imaginary part is  $-0.260 \pm 0.077$  m/s Pa. Within these standard error bars,  $|b|$  lies between 0.22 and 0.38 m/s Pa and  $\arg(b)$  is between  $-44^\circ$  and  $-77^\circ$ . Consistent with these large error bars, the model explains only 8% of the variance of all 76 segments. Presumably the combination of relatively weak winds and enhanced eddy energy in the Hawaiian region reduces the skill of the regression far more seriously here than in the northeast Pacific (although Niiler and Paduan do not explicitly state error bars, they note that they “can be expected to be large” due to the geostrophic noise).

Using the ensemble-averaged  $b$  and the mean ERS-1 wind stress, the mean Ekman drift is shown in Fig. 50. Spatially averaged, the drift is  $(u_E, v_E) = (-1.6$  cm/s,  $1.3$  cm/s). Combined with the downwind slip, this gives a directly wind-forced current of  $(-2.0$  cm/s,  $1.1$  cm/s). Due to the large error bars on  $b$ , this can only be considered a rough estimate of the drift; however, the consistency of these results with those of Niiler and Paduan [1995] suggest that this is a better estimate than is provided by the slab model.

### 4.3 Calculating means and variances

To describe a “mean” property in the drifter and hydrographic data, many observations must be averaged over space and time. These calculations were performed in an area of zonal width  $X$  and meridional width  $Y$ , chosen such that a particular feature of

interest (such as the Hawaiian Lee Countercurrent) did not appreciably change across  $X$ . All observations of property  $\psi$  within the area were sorted by latitude. For the southernmost  $N$  observations of  $\psi$ , the mean  $\langle\psi\rangle$  and fluctuations  $\psi'$  were calculated in the standard way, i.e.

$$\langle\psi\rangle = \frac{1}{N} \sum_{i=1}^N \psi_i, \quad \psi' = \psi - \langle\psi\rangle. \quad (4.5)$$

The calculation was repeated on observations  $1+N-n$  to  $2N-n$ ,  $1+2(N-n)$  to  $3N-2n$ , etc., until the averaging window included the northernmost point in the area, thus giving the meridional profile of  $\langle\psi\rangle$ . Each time the zonal average was performed, the averaging window contained the northernmost  $n$  points from the previous calculation, to produce smooth profiles of  $\langle\psi\rangle$ . In the plots of the averaged quantities, points calculated from fully-independent data will be marked.<sup>1</sup>

For averages along the Hawaiian Ridge, an identical calculation was performed, except the coordinate system was rotated so that the  $x$ -axis lay along the ridge (defined positive to the ESE), and the orthogonal  $y$ -axis pointed off-ridge (positive to the NNE).

Standard error bars were calculated with the bootstrap method, i.e. the original population of  $N$  points were resampled, with the possibility of repeating points, to create hundreds of ensembles of  $N$  points. The means were calculated, and the standard error defined as  $\pm 1$  standard deviation of the bootstrapped means. These bootstrap error bars tended to be visually indistinguishable from the typical definition of the standard error (standard deviation divided by  $\sqrt{N}$ ).

---

<sup>1</sup>A more standard method of calculating zonally- and temporally-averaged quantities is to take the mean in bands of fixed meridional width. However, the data were inhomogeneously-distributed; the method chosen for this study allowed the meridional resolution of the averaging operator to scale with the data density. This was particularly useful for dynamic height near O'ahu, where sampling density drops off extremely rapidly with increasing distance.

#### 4.4 Energy fluxes

In the spirit of Hansen and Paul [1984], the drifter data can be used to estimate some of the energy flux terms between the mean and eddy components of the flow. The turbulent kinetic energy equation is derived from the governing equations under the Boussinesq, hydrostatic, incompressible and Traditional approximations, and can be expressed as

$$\begin{aligned} \partial_t \langle EKE \rangle = & -(\langle \mathbf{u} \rangle \cdot \nabla) \langle EKE \rangle - \langle (\mathbf{u}' \cdot \nabla) EKE \rangle \\ & - \rho_o \langle \mathbf{u}' \cdot (\mathbf{u}' \cdot \nabla) \rangle \langle \mathbf{u} \rangle - \langle \mathbf{u}' \cdot \nabla p' \rangle - g \langle \rho' u'_3 \rangle, \end{aligned} \quad (4.6)$$

(c.f. [Kundu, 1990]), where

$$EKE = \frac{1}{2} \rho_o \mathbf{u}' \cdot \mathbf{u}' \quad (4.7)$$

and  $\rho_o(z)$  is the background hydrostatic density. The turbulent potential energy equation can be expressed as

$$\begin{aligned} \partial_t \langle EPE \rangle = & -C(\langle \mathbf{u} \rangle \cdot \nabla) \frac{1}{2} \langle \rho'^2 \rangle - C \left\langle (\mathbf{u}' \cdot \nabla) \frac{1}{2} \rho'^2 \right\rangle \\ & - C \langle \rho' u'_\alpha \rangle \partial_\alpha \langle \rho \rangle + g \langle \rho' u'_3 \rangle, \end{aligned} \quad (4.8)$$

where

$$EPE = \frac{1}{2} C \rho'^2 \quad (4.9)$$

and

$$C = -\frac{g}{\partial_3(\rho_o + \langle \rho \rangle)} \approx -\frac{g}{\partial_3 \rho_o} \left( 1 - \frac{\partial_3 \langle \rho \rangle}{\partial_3 \rho_o} \right). \quad (4.10)$$

The index  $\alpha$  is summed over only the horizontal components 1, 2 due to the inclusion of  $\partial_3 \langle \rho \rangle$  in  $C$  [Luther and Johnson, 1990]. The terms associated with pressure forces and vertical motion in (4.6) and (4.8) cannot be observed by the drifters. Dropping these terms and the zonal gradients  $\partial_x$  yields

$$\begin{aligned} \partial_t \langle EKE + EPE \rangle = & -\langle v \partial_y EKE \rangle - C \left\langle v \partial_y \frac{1}{2} \rho'^2 \right\rangle \\ & - \rho_o \langle v'^2 \rangle \partial_y \langle v \rangle - \rho_o \langle u' v' \rangle \partial_y \langle u \rangle - C \langle \rho' v' \rangle \partial_y \langle \rho \rangle. \end{aligned} \quad (4.11)$$

Hansen and Paul [1984] were able to estimate the final three terms in WOCE drifter data collected in the equatorial Pacific. Of these terms, the first two represent the barotropic flux of kinetic energy between the mean and eddy fields caused by the mean eddy transport of momentum across a mean shear. The final term represents baroclinic conversion of mean potential energy to the eddy field caused by the mean eddy transport of density fluctuations across a mean density gradient.

Estimating the baroclinic flux term with the drifter data requires making assumptions about the T-S relationship and the mean stratification of the upper ocean [Hansen and Paul, 1984]. The WOCE drifters of this study measured *in-situ* temperature, but not salinity. Thus, only the sign of the energy flux can be directly calculated (assuming reasonable values of salinity). Because it was desirable to at least estimate the magnitude of this physically-important term, a mean T-S diagram was calculated by plotting salinity vs. temperature of all CTD observations in the upper 20 m, and fitting a fifth-order polynomial to the T-S observations. This curve was used to estimate the salinity of each drifter observation. Density was then calculated using the UNESCO [1981] equation of state. This procedure can be expected to introduce some error by neglecting variations of salinity for a given temperature, but a greater source of error is the unknown value of  $C$ . Because the drifters provide no measure of the stratification, this term must be estimated from regional averages of the buoyancy frequency. Emery *et al.* [1984] provide seasonal maps of  $N(z)$  for the Hawaiian Region; the curves typically climb from a minimum of  $2 \times 10^{-3} \text{ s}^{-1}$  at 2000 m depth to maxima of  $1.1\text{--}1.4 \times 10^{-2} \text{ s}^{-1}$  at 50–200 m. For the purposes of this study,  $N = 10^{-2} \text{ s}^{-1}$  was chosen as a representative value of the upper-ocean stratification, giving  $C \sim 940 \text{ m}^5/\text{kg s}^2$ . While these approximations introduce an unknown error in the magnitude of the baroclinic energy flux, it is hoped that at least crude estimates are provided.

Under the assumptions described above, the mean eddy kinetic and potential energy and energy fluxes between the mean and eddy field were calculated in zonally-averaged bands within the Hawaiian region. Error bars for terms such as  $\langle u'v' \rangle \partial_y \langle u \rangle$  were calculated by the following procedure: first, the observed variations in  $u'v'$  and  $u$  were used to calculate the standard error for  $\langle u'v' \rangle$  and  $\langle u \rangle$ . The term  $\partial_y \langle u \rangle$  was calculated by finite differencing; the calculation was performed  $10^5$  times, with the values of  $\langle u \rangle$  perturbed by a normally-distributed random value with standard deviation equal to the standard error in  $\langle u \rangle$ . The standard deviation in the  $10^5$  estimates of  $\partial_y \langle u \rangle$  then gave the standard error of that term. Finally, the standard error in  $\langle u'v' \rangle \partial_y \langle u \rangle$  was estimated using the same Monte Carlo technique (i.e. carrying out the multiplication  $10^5$  times, with scatter set by the standard errors of the two terms).

#### 4.5 Observations of the mean currents and eddy field

In Fig. 51 (top), the drifter-derived currents are shown after the downwind slip and Ekman drift (from the regression analysis; see Section 4.2) have been removed. They are superimposed on the high-resolution dynamic height anomaly referenced to 400 dbar (Fig. 9), added to the map of dynamic height anomaly between 1000 and 400 dbar (Fig. 47) linearly interpolated to the same grid size. Immediately south of the islands, and southwest to the edge of the study region, the mean drifter-observed currents lie along isolines of dynamic height. The narrow Hawaiian Lee Countercurrent runs along the northern edge of the North Equatorial Ridge from  $168^\circ$  to  $160^\circ$ W. West of the HLCC in the latitude band of the islands, the drifter-derived currents are orthogonal or completely opposed to the geostrophic currents relative to 1000 dbar.

At the bottom of Fig. 51, the difference between the adjusted (for Ekman drift and slip) drifter speeds and the geostrophic currents (derived from finite differencing the

dynamic height field) are shown where they are significantly different from zero by at least one standard error. East of  $155^{\circ}\text{W}$ , the adjusted drifter speeds are more strongly zonal by  $4.7 \pm 0.5$  cm/s. The ALACE data suggests that  $\sim 2$  cm/s of this discrepancy is due to motion at the 1000 dbar level, leaving a residual of  $\sim 3$  cm/s. West of Hawai'i, and particularly in the latitude band  $22\text{--}23^{\circ}\text{N}$ , the drifter speeds are significantly stronger than the geostrophic currents relative to 1000 dbar; the mean adjusted drifter speed west of  $155^{\circ}\text{W}$  is more zonal by  $6.8 \pm 0.4$  cm/s. If it is assumed that the currents at 1000 dbar are homogeneous, and this motion is accounted for, the remaining discrepancy is  $\sim 5$  cm/s. What is the source of this discrepancy? The 1000 dbar circulation may possibly be more strongly westward north of  $18^{\circ}\text{N}$  and west of  $155^{\circ}\text{W}$ , a hypothesis which denser ALACE sampling will address. Additionally, the data are non-concurrent; the hydrography was collected relatively homogeneously over many decades, while much of the drifter data were collected after bursts of deployments in late 1994–1996. Thus, interannual fluctuations of currents may cause them to appear differently in the two data sets. However, even in the relatively steady NEC south of  $14^{\circ}\text{N}$ , the adjusted drifter speeds are more strongly westward by  $5.4 \pm 0.7$  cm/s. Accounting for the mean drift at 1000 dbar, an underlying  $\sim 3 - -4$  cm/s residual remains. Perhaps this residual is due to drifter motion being more strongly influenced by wind slip and/or wave rectification than anticipated from previous laboratory experiments and limited field tests (c.f. [Niiler *et al.*, 1987; Geyer, 1989]). Evaluating this possibility will require extended field tests under heavy wind and swell conditions; while this task may be necessary to fully explain the discrepancies between drifter and hydrographic observations, it extends beyond the scope of this study. Having noted this caveat, individual currents in the Hawaiian region will now be examined in the data.

#### 4.5.1 North Equatorial Current

The NEC is the westward-flowing branch of the North Pacific Subtropical Gyre (north of  $\sim 15^\circ\text{N}$ ) and the North Pacific Tropical Gyre (from  $10\text{--}15^\circ\text{N}$ ).

##### *East of the Hawaiian Islands*

Upstream of the islands ( $130\text{--}154^\circ\text{W}$ ), the mean zonal speed of the drifters is a nearly linear function of latitude (Fig. 52). From  $12$  to  $27^\circ\text{N}$ ,  $\langle u \rangle$  drops from  $16$  cm/s to rest. This gives a shear of  $10^{-7}$  s $^{-1}$ ,  $1.5\text{--}3 \times 10^{-3}$  times the local value of the Coriolis parameter  $f$ . Eddy kinetic energy peaks between  $20$  and  $25^\circ\text{N}$  (Figs. 54), while the Reynolds shear stress remains relatively low throughout the area, fluctuating between  $\pm 10$  cm $^2$ /s $^2$ . In the presence of the meridional shear of  $\langle u \rangle$ , these observations indicate a mean barotropic energy flux of  $O(\pm 0.1 \mu\text{W}/\text{m}^3)$  (Fig. 54). From  $11.6^\circ\text{N}$  to  $28.0^\circ\text{N}$ , the mean density  $\langle \rho \rangle$  increases from  $1022.5$  to  $1024.3$  kg/m $^3$ , for a mean density gradient of  $1.03 \times 10^{-6}$  kg/m $^4$ . The eddy density advection  $\langle v' \rho' \rangle$  works against this gradient, reaching a minimum of  $(-7.5 \pm 2.0) \times 10^{-3}$  kg/m $^2$ s at  $24^\circ\text{N}$ . This suggests a conversion of mean to eddy potential energy at the rate of  $\sim 7 \mu\text{W}/\text{m}^3$  at  $23\text{--}25^\circ\text{N}$ .

Referenced to  $400$  dbar, dynamic height upstream of the islands reaches a maximum at  $\sim 22^\circ\text{N}$  (Fig. 55). North of  $23^\circ\text{N}$ , the slope is approximately constant, yielding eastward geostrophic flow of  $3\text{--}4$  cm/s. South of  $21^\circ\text{N}$ , dynamic height slopes parabolically; the westward geostrophic current thus increases approximately linearly with decreasing latitude. At  $12^\circ\text{N}$ , the current is  $\sim 11$  cm/s. Referenced to  $1000$  dbar (Fig. 56), the NEC is stronger south of  $22^\circ\text{N}$ , with a speed of  $13$  cm/s at  $12^\circ\text{N}$ .

From  $12^\circ$  to  $24^\circ\text{N}$ , there is a  $6\text{--}7$  cm/s offset between the zonal drifter speed and the hydrographic zonal current referenced to  $400$  dbar (Fig. 57). Approximately  $1\text{--}2$  cm/s of this is due to geostrophic shear from  $400$  to  $1000$  dbar, and the regression analysis of

Section 4.2 suggests that an additional  $\sim 2$  cm/s is due to Ekman drift and downwind slip. The remaining discrepancy, shown in Fig. 57, ranges from 0.5 to 4.5 cm/s. Under the assumption that the gyre-scale flow is predominantly geostrophic, this discrepancy must be due to the absolute motion at 1000 dbar (earlier estimated at  $\sim 2$  cm/s) and the other potential sources of error noted earlier.

### *West of the Hawaiian Islands*

After impinging on the island of Hawai'i, the NEC bifurcates. The southern branch may occasionally accelerate to  $\sim 1$  m/s as it passes the South Point of Hawai'i (see Chapter 3). The mean drifter speed between  $156.5$  and  $160^\circ$ W has a westward maximum of 20 cm/s at  $17.5^\circ$ N (Fig. 58), which can still be seen (reduced to 18 cm/s) from  $160$ – $168^\circ$ W (Fig. 62).

Wyrтки and Kilonsky [1984] presented the mean hydrography along the Hawai'i-to-Tahiti Shuttle Experiment transect,  $158^\circ$ W through most of the Hawaiian region. They showed that the NEC extends from  $9^\circ$  to  $18^\circ$ N, and is split into two cores of strengthened westward flow. The northern core is centered at  $17^\circ$ N, with speeds greater than 10 cm/s extending to depths of 150–200 m; this core is the downstream signature of the NEC jet seen in the drifter data and hydrography (c.f. Figs. 58, 61, 62, 65). It weakens to the west, and cannot be seen past  $170^\circ$ W (Figs. 66, 69). The southern core described by Wyrтки and Kilonsky (and also by White and Hasunuma [1982]) is centered at  $12^\circ$ N, and has a maximum strength of 20 cm/s extending to 100 m depth. There is no evidence of this southern core in the drifter data, although a broad maximum at  $13$ – $14^\circ$ N reaches this strength (Fig. 62). It is clearly seen in the hydrography (Figs. 65, 69), which suggests that the  $12^\circ$ N core extends across the study region.

In their examination of hydrography at  $155^\circ$ E, White and Hasunuma [1982] found an accelerated core of the NEC at  $16^\circ$ N (in addition to the  $12^\circ$ N core). This feature

does not appear to be connected to the  $17.5^{\circ}\text{N}$  NEC jet discussed earlier, as the latter feature does not extend past  $170^{\circ}\text{W}$ .

#### 4.5.2 North Hawaiian Ridge Current

After bifurcating at Hawai‘i, the northern branch of the NEC follows the island ridge to Kaua‘i before turning westward (Fig. 9). This branch is known as the North Hawaiian Ridge Current (NHRC) [White, 1983; Firing, 1996].

The NHRC is a relatively weak current buried in a highly variable and energetic eddy field. Hence, years of averaging are often required to detect it; relatively short-term snapshots such as the hydrographic surveys in Sun *et al.* [1998] and Bingham [1998] are overwhelmed by mesoscale variability [Price *et al.*, 1994]. The NHRC has been observed in historical XBT data [White, 1983], in long-term ADCP averages [Firing, 1996] and in WOCE drifter data [Qiu *et al.*, 1997; Bingham, 1998]. In the drifter data, it has a maximum mean speed of  $\sim 14$  cm/s (Fig. 70). Averaged over the full set of hydrographic observations, the NHRC can be seen out to 100–150 km off the island ridge (Fig. 73).

The NHRC does not have a strong seasonal signal, but strongly fluctuates at intraseasonal to interannual periods [Firing, 1996; Firing *et al.*, 1998]. Bingham [1998] noted strong intermittency of the NHRC in WOCE drifter data. He stated that “[t]he average NHRC [in the drifter data] . . . is based on only a few months of data,” referring to the coherent alongridge motion of several drifters in late 1991. From this, he concluded that “[t]he drifter data showed that the current is not there most of the time.” However, in the overlapping data of this study, the current is significant in 1991–1993, 1995 and 1996 (Fig. 74), although the late-1991 mean speed of  $\sim 30$  cm/s is the strongest appearance of the NHRC in the data. Although the drifters sample the NHRC rather coarsely, the resulting time series reflects some of the variability seen in ADCP sections between O‘ahu and station ALOHA [Firing, 1996; Firing *et al.*, 1998] (Fig. 74).

Mysak and Magaard [1983] offered the first dynamical explanation of the NHRC in their development of Rossby wave reflection off a nonzonal boundary. They showed that the interaction of incident long Rossby waves and reflected short Rossby waves could rectify into an along-boundary current  $u$  governed by

$$\beta u \sin \alpha + R \partial_y u = \partial_y^2 \langle u'v' \rangle, \quad (4.12)$$

where  $\beta$  is the gradient of the Coriolis parameter  $f$ ,  $\alpha$  is the counter-clockwise angle from the along-ridge coordinate  $x$  to a line of constant latitude, and  $R$  is a damping term. The observed Reynolds shear stress  $\langle u'v' \rangle$  is shown in Fig. 71; unfortunately, the driving term on the right-hand side of (4.12) depends on the curvature of this stress, which cannot be resolved within the error bars of the drifter measurement [Bingham, 1998].

White and Walker [1985] proposed that the NHRC is a pseudo-western boundary current, which could be described by integrating the Sverdrup model between the North American continent and the Hawaiian Ridge. This suggestion was developed by Qiu *et al.*, who showed that Godfrey's [1989] island rule<sup>2</sup> predicts a transport similar to that observed by Firing [1996]. This theory was extended in Firing *et al.* [1998] to the nonsteady case, demonstrating that many aspects of the intraseasonal to interannual variability are consistent with large-scale extra-equatorial wind forcing. If the NHRC is a pseudo-WBC, its lowest-order dynamics are geostrophic. The similarity between the drifter-observed current and the dynamic height slope suggests this may indeed be the case, although the current appears to be stronger and narrower in the hydrography.

Firing [1996] showed that there was a rapid flux of mean to eddy kinetic energy in the NHRC, suggesting a dissipation timescale of  $\sim 5$  days. In the drifter data, the mean

---

<sup>2</sup>The NHRC is assumed to balance the Sverdrup transport in the ocean interior between Hawai'i and North America with the net Ekman transport into this area.

alongridge current  $\langle u \rangle$  goes from  $-0.13$  m/s at 68 km off the ridge to rest at 140 km offridge, yielding a gradient of  $\partial_y \langle u \rangle = 1.7 \times 10^{-6} \text{ s}^{-1}$ . In the presence of the observed Reynolds shear stress minimum of  $(-1.1 \pm 0.5) \times 10^{-2} \text{ m}^2/\text{s}^2$  at 90 km off the ridge, the mean to eddy energy flux is  $\sim 10 \mu\text{W}/\text{m}^3$  (but not significantly different than zero to one standard error; Fig. 72). Using the peak speed of  $\langle u \rangle = 0.14$  m/s, this gives a dissipation timescale of  $\sim 11$  days.

#### 4.5.3 Currents in the Island Lee

West of the islands, the drifter-derived currents show elongated, counter-rotating gyres extending from the immediate lee of Hawai'i ( $156^\circ\text{W}$ ) to  $\sim 170^\circ\text{W}$ , a distance of approximately 1500 km. The southern, anticyclonic gyre follows the North Equatorial Ridge and the mean path of anticyclonic eddies (see Fig. 27); the accelerated NEC jet at  $17^\circ\text{N}$  defines its southern edge, while the Hawaiian Lee Countercurrent at  $19.5^\circ\text{N}$  defines its northern edge. North of this, the cyclonic gyre is centered on the mean path of cyclonic eddies. Its northern edge is defined by a westward current which has not previously been identified, and shall herein be called the Hawaiian Lee current (HLC).

#### *Hawaiian Lee Current*

Latham [1967] noted that several hydrographic surveys revealed westward flow south of Kaua'i and the Kaua'i Channel. He found that, between 0 and 500 dbar, the mean westward transport in this area was  $\sim 3$  Sv. Rather than a current extending along the island chain, Latham interpreted this flow as the northern edge of a cyclonic swirl south of Kaua'i. However, the drifter data show that this current is continuous (in a time-averaged sense) along the island chain, flowing along the leeward coasts of the major islands from Maui to Kaua'i (Fig. 75). A time series of drifters within the HLC is shown in Fig. 76, and suggests that there may be significant interannual fluctuations

in the strength of the current (although the patchiness of drifter sampling makes this impossible to demonstrate conclusively).

In the drifter data averaged along the island ridge (Fig. 70), the HLC reaches a maximum speed of 20 cm/s at a distance of 125 km offridge. As the current flows along the ridge, it appears to broaden and weaken, but retains a well-defined southwest edge  $\sim 150$  km from the ridge. The HLC can be seen in the hydrography (albeit barely significantly; Fig. 73) with the dynamic height gradient yielding a current of maximum strength  $\sim 13.5$  cm/s at a distance of  $\sim 125$  km from the ridge. Within the HLC, the Reynolds shear stress is not significantly different from zero; it climbs to  $(1.36 \pm 0.4) \times 10^{-2} \text{ m}^2/\text{s}^2$  at 140 km offridge. The mean alongridge current goes from rest at 184 km offridge to  $-0.19$  m/s at 125 km offshore, giving  $\partial_y \langle u \rangle \sim -3 \times 10^{-6} \text{ s}^{-1}$ . In the presence of the shear stress, this suggests a mean to kinetic energy conversion at a rate of  $\sim 8\mu\text{W}/\text{m}^3$  (Fig. 72). Past 180 km offridge, the Reynolds shear stress changes sign; the energy flux in this region will be discussed in the section on the Hawaiian Lee Countercurrent.

After the HLC flows around Kaua'i and Ni'ihau, it joins with the NHRC to form a single, relatively narrow westward current running along  $22^\circ\text{N}$ . This HLC/NHRC extension persists to the edge of the study region (Fig. 66). The dynamic height map (Fig. 51) suggests that the HLC/NHRC extension is  $180^\circ$  opposed to the gyre-scale flow, and there is no evidence of the extension in the smoothed map. However, the zonally-averaged dynamic height field reveals a persistent ridge along  $22^\circ\text{N}$  (Figs. 65, 69). The ridge is only  $\sim 1$  degree in width, suggesting an extremely narrow ( $\sim 50$  km) westward jet along  $21.5\text{--}22^\circ\text{N}$ . This jet may be the signature of the HLC/NHRC extension in the hydrography; it is not clear, however, why the extension appears considerably wider and stronger in the drifter speeds. As mentioned earlier, the sporadic and relatively short-

term drifter observations may not represent this current when averaged over interannual time scales. Along the latitude of the HLC/NHRC extension, the drifter data do not suggest significant fluxes between the eddy and mean fields.

### *Hawaiian Lee Countercurrent*

The eastward-flowing Hawaiian Lee Countercurrent extends along  $19.5^{\circ}\text{N}$  from  $168^{\circ}$  to  $160^{\circ}\text{W}$  (a distance of over 800 km), with a peak eastward speed of 10 cm/s (Fig. 62). It is relatively narrow: the total width of eastward flow is  $\sim 190$  km, with the core (speeds greater than 5 cm/s) less than 100 km across. In hydrography, it appears as a wider ( $19^{\circ}$ – $21^{\circ}\text{N}$ ), slightly weaker ( $\sim 7.5$  cm/s max) eastward flow (Fig. 65). This study is the first to show the HLCC in drifter data. Presumably, previous examinations of drifters in the island lee did not contain enough trajectories to identify the countercurrent.<sup>3</sup>

A time series of drifter speeds in the HLCC is shown in Fig. 76. The strengths of the HLC and HLCC appear to be correlated: in years when the westward-flowing HLC is strong, the eastward-flowing HLCC is also strong. This suggests a similar mechanism is responsible for both currents. When Wyrteki and Kilonsky [1984] noted the HLCC in the mean Hawai'i-to-Tahiti Shuttle Experiment hydrography, they proposed it was “related to the appearance of eddies behind the island of Hawaii and south of Oahu.” The drifter data are consistent with this hypothesis: the HLCC in Fig. 62 is primarily due to the rotary motion of drifters within lee eddies. To demonstrate this, the drifter trajectories were divided into 60-day segments, and the rotary spectra of each was calculated. A segment was flagged as “eddy-trapped” if the subinertial variance of one rotary component was 1.5 times (or more) greater than the other. The value 1.5 was chosen because larger values did not flag segments which were clearly orbiting

---

<sup>3</sup>For example, Roden [1991] showed 3–4 tracks of drifters which traveled westward along the latitude of the HLCC. He concluded that the discrepancy between this motion and the eastward flow suggested by hydrography was due to Ekman drift and the non-stationarity of the flow.

eddies for a few loops. The flagged and unflagged segments are shown on the left-hand side of Fig. 77. Visually, the unflagged tracks appear relatively straight or randomly-meandering. They spanned 20% of the drifter-years of flagged tracks in the area 160–168°W, 17–21°N. When the zonally-averaged zonal speed is calculated, the eastward countercurrent is only present in the “eddy-trapped” subset of data; the mean westward speed of unflagged drifters reaches a minimum at  $\sim 20^\circ\text{N}$  which is not significantly different from zero. This suggests that there may be an additional process weakening the westward flow at this latitude, similar to the mass-balancing countercurrent in White and Walker’s [1985] Sverdrup model.

If the lee eddy field consisted of randomly-placed cyclones and anticyclones, their superposition would not create a countercurrent like the HLCC. However, as shown in Chapter 3, the configuration of the lee eddy field in the longitude band of the HLCC is far from random. Because of their divergent meridional drift, opposite-signed lee eddies tend to be sorted on either side of  $19.5^\circ\text{N}$  (see Fig. 27). Drifters around an eddy trace cycloids, with the retrograde portion of each orbit falling near the latitude band of the HLCC. This process can also be described in terms of the mean dynamic height field: anticyclones tend to lift mean dynamic height south of  $19.5^\circ\text{N}$ , while cyclones depress it to the north. This process creates a mean dynamic height gradient along  $19.5^\circ\text{N}$ , which in geostrophic balance leads to the HLCC.

Averaged from 160 to 168°W, the mean density  $\langle \rho \rangle$  increases from 1022.6 at  $14.5^\circ\text{N}$  to 1023.0  $\text{kg}/\text{m}^3$  at  $21.5^\circ\text{N}$ . The mean eddy advection of density  $\langle v' \rho' \rangle$  works against this gradient, reaching a minimum of  $(-6.5 \pm 2.0) \times 10^{-3} \text{ kg}/\text{m}^2\text{s}$  at  $20.3^\circ\text{N}$ . This suggests a conversion of mean to eddy potential energy at the rate of  $\sim 4\mu\text{W}/\text{m}^3$  between 20 and  $22^\circ\text{N}$ , dropping to half that value at the latitude of the HLCC (see Fig. 64). At 16– $18^\circ\text{N}$  (the band of mean anticyclone passage),  $\langle v' \rho' \rangle$  is not significantly different

from zero. In contrast to the PE flux, the data suggests that there is an eddy-to-mean kinetic energy flux along the paths of the anticyclonic and cyclonic eddies. In the anticyclone band,  $\langle u \rangle$  goes from  $-14.0$  cm/s at  $18.0^\circ\text{N}$  to  $9.0$  cm/s at  $19.3^\circ\text{N}$ , giving a mean gradient of  $\partial_y \langle u \rangle \sim 1.5 \times 10^{-6} \text{ s}^{-1}$ . The mean eddy meridional advection of zonal momentum (i.e. Reynolds shear stress) works to *reinforce* this gradient, reaching a maximum of  $(5.0 \pm 2.8) \times 10^{-3} \text{ m}^2/\text{s}^2$  at  $18.5^\circ\text{N}$ . The associated energy flux is nearly  $10 \mu\text{W}/\text{m}^3$  from the eddy to the mean field.<sup>4</sup> In the band of the cyclonic eddies, the mean zonal speed drops from  $4.9$  cm/s at  $20.0^\circ\text{N}$  to  $-12.1$  cm/s at  $21.1^\circ\text{N}$ , yielding a mean gradient of  $\partial_y \langle u \rangle \sim -1.3 \times 10^{-6} \text{ s}^{-1}$ . The Reynolds shear stress reaches a minimum of  $(-2.7 \pm 2.0) \times 10^{-3} \text{ m}^2/\text{s}^2$  at  $20.0^\circ\text{N}$ , implying eddy-to-mean kinetic energy conversion at a rate of  $\sim 3.5 \pm 2.7 \mu\text{W}/\text{m}^3$  (but not significantly different from zero; see Fig. 64). Further downstream ( $170\text{--}180^\circ\text{W}$ ), the kinetic energy flux is considerably smaller due to the reduced gradient of the mean zonal current (Fig. 66). From  $17.4$  to  $18.8^\circ\text{N}$ , the mean current increases from  $-11.0$  to  $-5.0$  cm/s, yielding a gradient of  $\partial_y \langle u \rangle \sim 3.8 \times 10^{-7} \text{ s}^{-1}$ . The Reynolds shear stress reaches a maximum of  $(5.0 \pm 1.5) \times 10^{-3} \text{ m}^2/\text{s}^2$  at  $19.1^\circ\text{N}$  (nearly the same as its value in the  $160\text{--}168^\circ\text{W}$  band), giving an eddy to mean kinetic energy flux of  $\sim 2 \mu\text{W}/\text{m}^3$  (Fig. 68).

In addition to being driven by the eddy field, there may be an underlying Sverdrup component to the HLCC. White and Walker [1985] calculated a “blocked” Sverdrup flow by integrating wind stress curl across the Pacific, and adding a boundary current along the Hawaiian Ridge which forced no normal flow through the ridge. From continuity, they found two eastward-flowing bands west of the islands, which owed their existence to the ridge’s blocking effect; however, the connection between these bands and the

---

<sup>4</sup>The total (kinetic plus potential) energy loss of AC94b and AC94c in the spin-down model of Chapter 3 was  $\sim 3 \mu\text{W}/\text{m}^3$ . Thus, this kinetic energy flux seems excessive if these spin-down rates are representative. The discrepancy may be due to baroclinic conversion of mean to eddy potential energy, although this remains speculative as the observed flux is not significantly different from zero.

HLCC is tenuous, as they were at  $24^{\circ}\text{N}$  and  $26^{\circ}\text{N}$ . In the  $2\frac{1}{2}$ -layer model of Qiu *et al.* [1997] (which included Sverdrup dynamics, but did not capture the intensity of the lee eddy field), there was no lee countercurrent. The linearized Navy Layered Ocean Model (NLOM) has a Sverdrup-driven countercurrent at the latitude of the HLCC [Leonardi, 1998]. The strength of this current is highly sensitive to the flow through the model's 'Alenuihaha Channel, and disappears completely when the through-channel transport exceeds  $\sim 3$  Sv [H. Hurlburt, pers. comm.]. The nonlinear NLOM includes a highly energetic lee eddy field, which substantially alters the countercurrent and strengthens it along  $156\text{--}165^{\circ}\text{W}$  [Leonardi, 1998].

Averaged between  $170^{\circ}\text{W}$  and  $180^{\circ}$ , the drifters have a mean westward speed of  $\sim 5$  cm/s at  $19\text{--}20^{\circ}\text{N}$  (Fig. 66), while the dynamic height gradient suggests an eastward current of  $\sim 5$  cm/s in the same latitude band (which peak at over 10 cm/s at  $21^{\circ}\text{N}$ ; Fig. 69). The  $\sim 10$  cm/s discrepancy is roughly 4 cm/s larger than that of the upstream flow at this latitude (Fig. 57), and  $\sim 5$  cm/s larger than the discrepancy of the HLCC's strength in the  $160\text{--}168^{\circ}\text{W}$  band (Figs. 62, 65). The difference may be at least partially due to increased westward shear beneath 400 dbar, but unfortunately the database of deep XBT/CTD casts is extremely sparse in the area (there are only 21 casts reaching 1000 dbar in the rectangle  $170\text{--}180^{\circ}\text{W}$ ,  $19\text{--}21^{\circ}\text{N}$ ).

Is the HLCC associated with (or identical to) the Subtropical Countercurrent? It is difficult to give a definitive answer to this question, as the latter term has been inconsistently used in the literature. Wyrтки [1974] described the North Equatorial Ridge as separating the westward NEC from the eastward Subtropical Countercurrent, suggesting that the HLCC is a segment of the Subtropical Countercurrent. White and Walker [1985] defined the Subtropical Countercurrent as *any* eastward-flowing current between  $18^{\circ}$  and  $28^{\circ}\text{N}$  in the central North Pacific. Their dynamic height map showed

three narrow countercurrents at  $20^{\circ}\text{N}$ ,  $24^{\circ}\text{N}$  and  $26^{\circ}\text{N}$ . The HLCC coincides with their  $20^{\circ}\text{N}$  band, but the relationship between the two is not clear: they showed the band extending from the Philippines to the coast of Mexico, while this study finds no evidence of mean eastward flow to the east of Hawai'i at  $20^{\circ}\text{N}$ . White and Hasunuma [1982] showed that, in hydrographic data between  $137^{\circ}$  and  $155^{\circ}\text{E}$ , the Subtropical Countercurrent consisted of two eastward-flowing bands at  $22\text{--}24^{\circ}\text{N}$  and  $28^{\circ}\text{N}$ , which shifted northward as they ran eastward. This banded system of currents appears to be too far north to be related to the HLCC. Cushman-Roisin [1984] described the Subtropical Countercurrent as the thermal wind manifestation of the Subtropical Front, which runs across the Pacific Ocean well north of the HLCC's latitude (Cushman-Roisin's Fig. 1 shows the front running from  $26^{\circ}\text{N}$  at  $140^{\circ}\text{E}$  to  $33^{\circ}\text{N}$  at  $150^{\circ}\text{W}$ ). By this definition, the HLCC and the Subtropical Countercurrent are separate features.

#### *4.5.4 Flow through the channels separating the major islands*

The major Hawaiian Islands are separated by deep channels of width 40–60 km (Fig. 1). As with most of the study region, the mean flow through these channels is weak; instantaneous snapshots are often overwhelmed by tidal and mesoscale fluctuations.

##### *'Alenuihaha Channel*

The 'Alenuihaha Channel separates the islands of Hawai'i and Maui. It is a deep ( $\sim 1$  km) channel of width 40 km. Numerical models of the flow through this channel are highly sensitive to the fine-scale bathymetry; increasing the resolution from  $1/4^{\circ}$  to  $1/16^{\circ}$  greatly weakens the through-channel flow [Leonardi *et al.*, 1998]. The transport through the channel has a strong effect on the strength of the NHRC and of the HLCC, with the HLCC disappearing completely if the through-channel flow is intense [H. Hurlburt, pers. comm.]. Quantifying the direction and magnitude of through-channel flow is

also important in assessing its importance as an eddy-generating mechanism [Patzert, 1968].

Price *et al.* [1994] presented several examples of cold intrusions extending WSW from the ‘Alenuihaha Channel in AVHRR imagery; many similar images were found in this study (c.f. Fig. 23). However, in many cases it is unclear whether this feature is actually thermocline-deep motion through the channel, or wind-driven mixing delineated by unmixed, diurnally-heated water in the islands’ wind shadows (see Fig. 19). A notable exception can be seen in the composite AVHRR/drifter images for 21 August–4 September 1995 (Fig. 107), which show a drifter passing into a cold plume of water south of Maui, then traveling west at  $\sim 25$  cm/s. The drifter traced a narrow orbit around Kaho‘olawe over the next 4.5 days, suggesting that at least part of the plume wrapped clockwise around this island.

Patzert [1968] noted that dynamic height measurements on either side of the channel suggest a 20 cm/s current WSW through it, corresponding to a transport of  $\sim 2$  Sv. Dynamic height solely within the channel itself is quite consistent with this conclusion (Fig. 78). Patzert also showed that the presence of a strong lee cyclone can drive  $\sim 50$  cm/s currents through the channel for several weeks before the eddy propagates away from the mouth of the channel.

Not much drifter data have been collected in the ‘Alenuihaha Channel. In a short (41 hour) deployment of six parachute-drogued drifters in May 1966, the currents were found to be predominantly tidal; the low-frequency drift was virtually nil, despite concurrent dynamic topography indicating westward through-flow [Wyrтки *et al.*, 1967]. Figure 79 shows the passage of all WOCE drifters which neared or passed through the ‘Alenuihaha Channel (including the one mentioned earlier). The mean through-channel speed of the drifters is not significantly different than zero, but the large number of

drifters deployed east of the channel may be strongly biasing this result (i.e. more drifters had the opportunity to drift ENE through the channel). The overall pattern of trajectories suggests WSW flow in NW half of the channel and NE flow near the island of Hawai‘i.

From mid-1991 to mid-1993, an electromagnetic (Seadata) current meter was deployed off the northern tip of Hawai‘i, at a depth of 20 m (Fig. 80). The currents were predominantly semidiurnal, superimposed on a mean of  $17.5 \pm 0.1$  cm/s to the northeast. Very close to the same location, Wyrski *al.* [1969] found a mean current of 51.5 cm/s to the NE on 22 July–12 August 1967, and a mean current of 7.5 cm/s to the NE on 2 August–8 September 1968. These relatively short-term measurements are not inconsistent with the low-frequency variability of the current in Fig. 80.

Patzert and Wyrski [1974] speculated that rectification of tidal waves may produce a clockwise mean flow around Hawai‘i; Luther [1985] noted that this process may also occur with island-trapped waves. In the Seadata record, peaks in the demodulated semidiurnal amplitude are often concurrent with low-frequency peaks (Fig. 80). However, in early February 1993, the largest peak in the low-frequency flow is unaccompanied by significant energy in the semidiurnal, diurnal or island-trapped wave bands. This eastward pulse came less than one week after a reversal in the trade winds (Fig. 80). AVHRR images (Fig. 81) show that as the trades relaxed, warm water in Hawai‘i’s lee propagated around the northern point and down the NE coast in a narrow ( $\sim 10$  km) jet. It is not clear from this image what is driving the jet: it may have been due to relaxation of the wind-driven pressure gradients in the channel, or may possibly be a clockwise coastal squirt driven by an anticyclone/wall interaction [Nof, 1988a]. The latter explanation seems less likely, as the AVHRR imagery does not show anticyclonic circulation of the SST gradients in the island’s lee, and the satellite altimetry does not

suggest an anticyclone was formed near this time (although there was an extremely low sea level anomaly the previous month; Fig. 22).

In summary,  $\sim 50$  cm/s semidiurnal tidal fluctuations dominate the instantaneous currents of the ‘Alenuihaha Channel. Occasionally, excitation of island-trapped waves around Hawai‘i and the Maui group of islands (Maui, Moloka‘i, Lana‘i, Kaho‘olawe) create lower-frequency oscillations of magnitude 20–50 cm/s [Luther, 1985; Lumpkin, 1995]. During steady trade wind conditions, the Ekman flow is NW, towards the SE coast of Maui. This nearly linear coast spans 80 km from the eastern tip of Maui to the SW point of Kaho‘olawe, approximately paralleling the trades. It thus acts as a barrier to the Ekman flow, creating downward pumping and (during spin-up) a linearly growing WSW coastal jet. A steady-state condition is reached when Ekman convergence against the Maui coast is balanced by boundary-layer flow around either side of the island,<sup>5</sup> with a mean 20 cm/s flow WSW through the channel. On the Hawai‘i side, the less-linear bathymetry may cause the Ekman-driven divergence to be more rapidly balanced by northward flow around both sides of the island. Nevertheless, because the cross-channel scale (40 km) is smaller than the internal Rossby radius ( $\sim 60$  km [Emery *et al.*, 1984]), the coastal jet extends across the channel. Superimposed on these channel-scale fluctuations, rectification of the tidal oscillations may create  $O(40$  cm/s), low-frequency clockwise flow around Maui and Hawai‘i [Patzert and Wyrтки, 1974]. With the onset of Kona winds, relaxation of the cross-channel dynamic height gradient may be associated with a  $\sim 60$  cm/s, extremely narrow jet propagating clockwise around the northern tip and northeast coast of Hawai‘i.

---

<sup>5</sup>This may explain the divergent mean currents against the SE coast of Maui measured by Wyrтки *et al.* [1969]; see Fig. 3.

### *Kaiwi and Kaua'i Channels*

The Kaiwi Channel is the narrow (42 km), relatively shallow (750 m maximum depth) passage between Moloka'i and O'ahu. Using hydrographic surveys, parachute-drogued drifters, and current meter records, Burks [1967] showed that the subinertial flow through the channel was  $\sim 6$  cm/s to the NE during steady trade winds. In Kona wind conditions, the low-frequency flow reversed direction and weakened in magnitude.

The Kaua'i Channel is the wide (63 km) and deep ( $> 1$  km for most of its width) channel separating Kaua'i from O'ahu. After passing O'ahu, the NHRC and HLC meet, flow to Kaua'i, bifurcate and flow around Kaua'i and Ni'ihau, and finally rejoin to form a 14 cm/s westward current along  $22^\circ\text{N}$  (Fig. 66). Latham [1967] demonstrated this cross-channel mean flow in dynamic topography, current meter records, and the trajectories of parachute-drogued drifters. In contrast with Burks' [1967] findings for the Kaiwi Channel, Latham found that there was no correlation between local winds and the low-frequency flow in the Kaua'i Channel.

## **4.6 Conclusions**

The northern edge of the westward-flowing North Equatorial Current is effectively blocked by the Hawaiian Ridge. The NEC bifurcates at  $\sim 19.5^\circ\text{N}$ ; the southern branch is accelerated as it passes the South Point of Hawai'i, creating a core of relatively fast westward flow at  $18\text{--}18.5^\circ\text{N}$  which extends to  $\sim 170^\circ\text{W}$ . North of the bifurcation point, the flow follows the Hawaiian Ridge to Kaua'i before turning westward, creating the North Hawaiian Ridge Current. Very little flow appears to pass through the channels separating the islands, including the 'Alenuihaha Channel between Hawai'i and Maui. To the west of the island chain, the blocking effect of the ridge creates a wake which extends 1500 km across the central Pacific ocean. Within this region, instantaneous

snapshots of the currents are dominated by lee eddies. In relatively low-resolution numerical models such as the  $2\text{-}\frac{1}{2}$  layer model of Qiu *et al.* [1997] and early runs of the Navy Layered Ocean Model (NLOM), the island wake is a relatively structureless swath of near-zero currents. With higher resolution allowing for the presence of less-damped mesoscale fluctuations, the NLOM shows a similar structure to that observed in this study [Leonardi, 1998; Leonardi *et al.*, 1998]: the wake consists of counter-rotating, elongated gyres which owe their mean vorticity to the propagation paths of the cyclonic and anticyclonic eddies. Along the northern edge of the wake, a strong ( $\sim 20$  cm/s) and previously undocumented current, here called the Hawaiian Lee Current, runs along the leeward coasts of the major Hawaiian Islands from Maui to Kaua‘i. After passing Kaua‘i and Ni‘ihau, the HLC joins with the NHRC to form a westward-flowing current which extends to the edge of the study region.

The eddies, particularly the anticyclones, may initially draw energy from the mean shear in the lee of Hawai‘i. However, as they drift westward into the  $160\text{--}168^\circ\text{W}$  band, they converge eastward momentum between  $16\text{--}21^\circ\text{N}$  to  $19.5^\circ\text{N}$ , at a rate of  $\sim 10\mu\text{W}/\text{m}^3$ . This may be a primary factor driving the narrow Hawaiian Lee Countercurrent; this flux can accelerate the current from rest to its observed maximum of  $\sim 10$  cm/s in  $O(10)$  days. Farther to the north and south, baroclinic energy conversion returns potential energy to the eddy field, and a relatively large gradient in the mean meridional speed along  $18^\circ\text{N}$  suggests relatively strong conversion of mean to eddy kinetic energy at this latitude. As opposite-signed eddies continue to propagate westward, their divergent meridional drift carries them progressively further apart, until west of  $\sim 170^\circ\text{W}$  they no longer converge momentum along the band of the HLCC.

While the drifter and hydrographic data qualitatively agree on many features of the Hawaiian flow field, they disagree on the magnitude of currents by  $\sim 5\text{--}10$  cm/s even

when the Ekman drift has been taken into account. While some of this discrepancy is due to the absolute motion at 1000 dbar and geostrophic shear between 400 and 1000 dbar, spatial averaging in the NEC (where the ALACE data density is greatest) suggests an underlying 3–4 cm/s residual remains. To address this, future studies will need to draw upon more extensive field tests of the water following characteristics of WOCE drifters and denser sampling by ALACE floats and deep hydrographic casts.

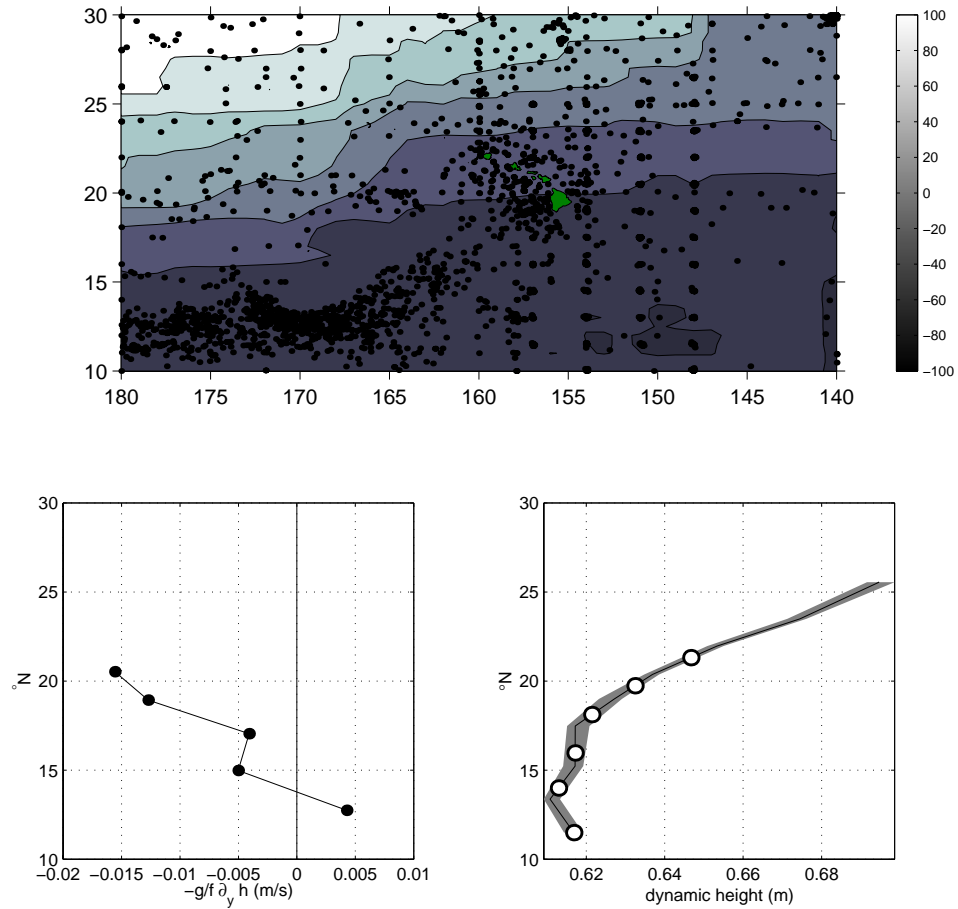


Figure 47: *Top*: dynamic height anomaly at 400 dbar relative to 1000 dbar (shading, mm). Dots indicate locations of CTD/XBT casts.

*Bottom, right*: dynamic height, zonally averaged between 165°W and 140°W. The width of the median averaging window is set by the density of observations; every white dot is calculated from independent data.

*Bottom, left*: zonal geostrophic current calculated from independent points of the previous panel.

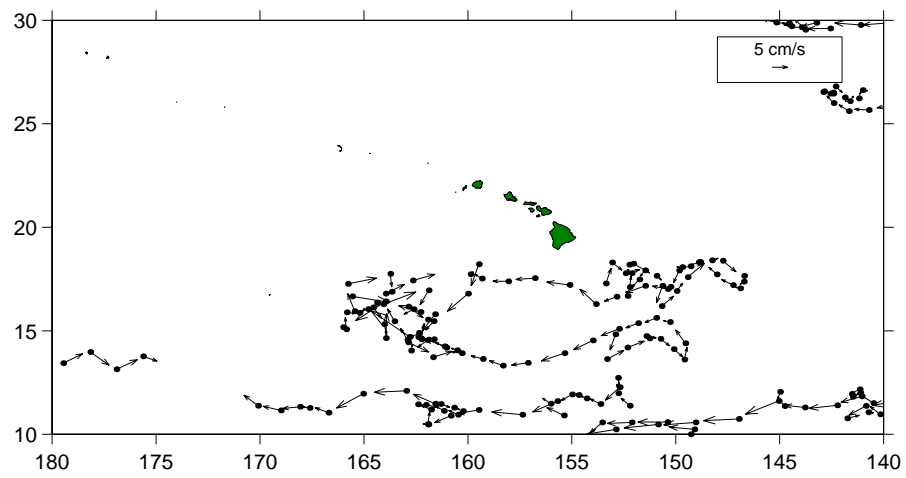


Figure 48: Speeds of ALACE drifting buoys at a nominal depth of 1000 m. Data courtesy Russ E. Davis.

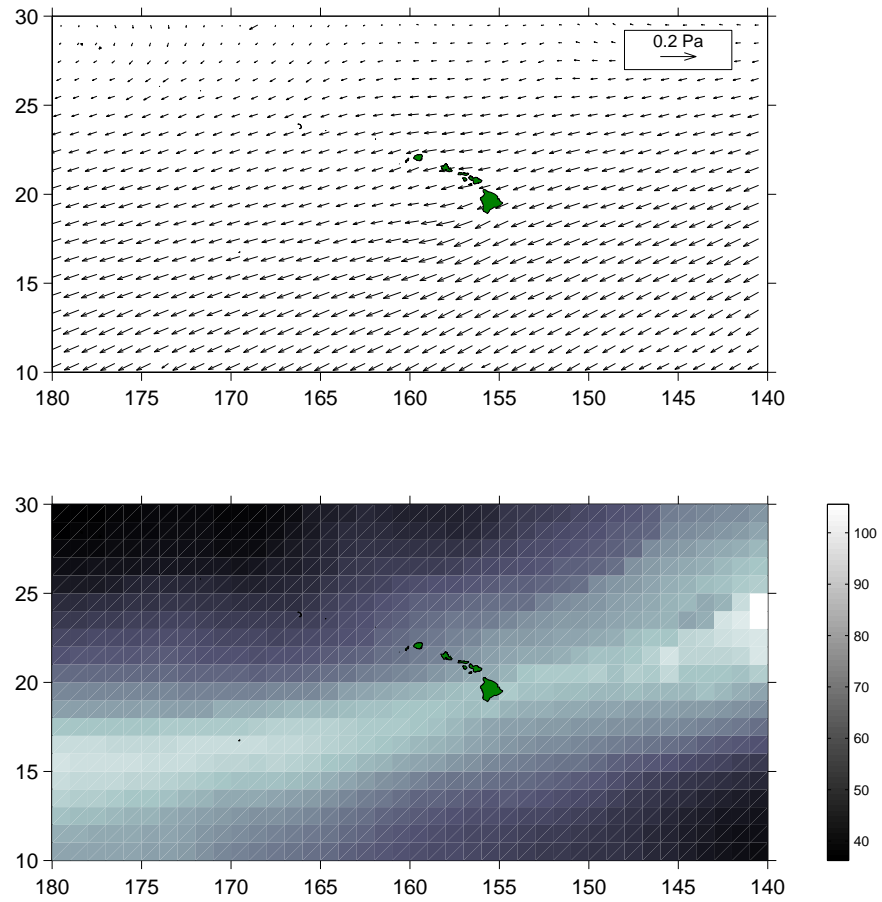


Figure 49: *Top*: mean wind stress from ERS-1 scatterometer.  
*Bottom*: mean mixed layer depth (m) from Levitus94 climatology.

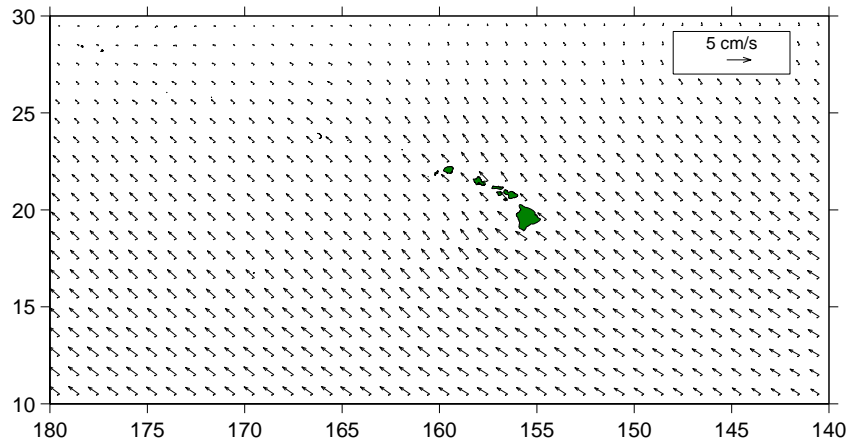
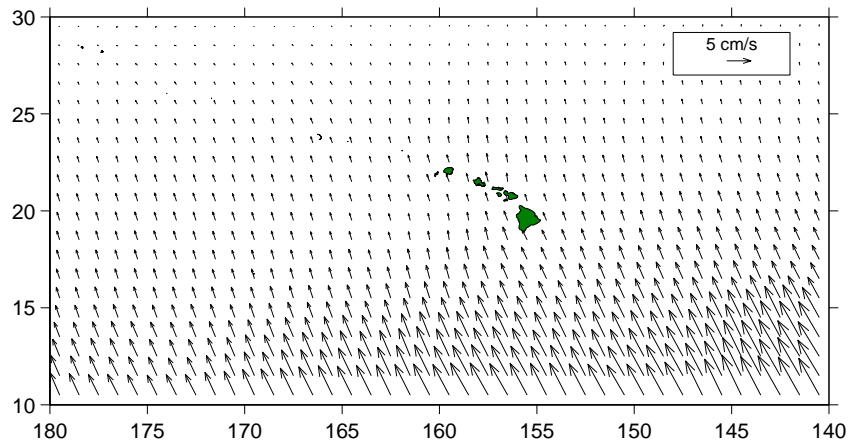


Figure 50: *Top*: Ekman drift from slab model (linearly decreasing stress and constant horizontal velocity in mixed layer). The strong drift at low latitudes is caused by the  $1/f$  dependence of  $U_E$ .

*Bottom*: Ekman drift from the regression model (arrows). Also shown is the downwind slip (short lines pointing SSW), caused by wind-induced drag on the surface and subsurface float [Niiler and Paduan, 1995].

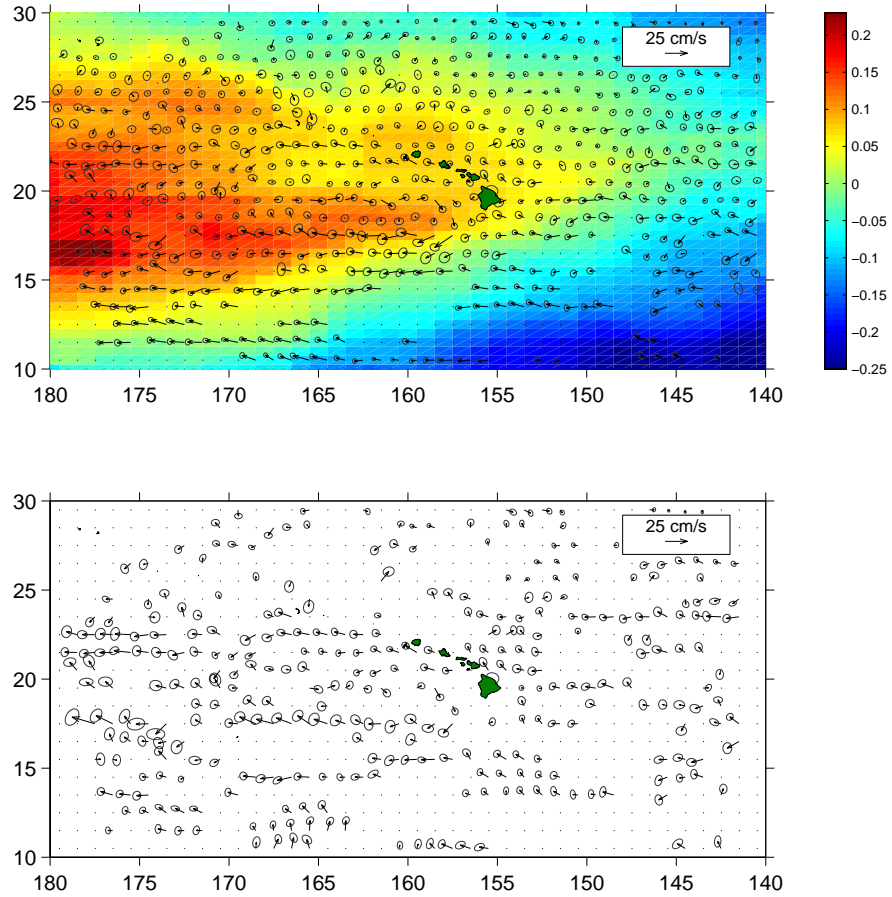


Figure 51: *Top*: dynamic height anomaly from 0 to 400 dbar added to the dynamic height anomaly from 400 to 1000 dbar, linearly-interpolated to the same grid spacing. The mean drifter-derived currents with the Ekman flow and downwind slip removed are superimposed, with standard error ellipses.

*Bottom*: difference between the adjusted drifter speeds (from top panel) and geostrophic currents from the dynamic height slope relative to 1000 dbar. Arrows are shown where the difference is significantly different from zero by at least one standard error.

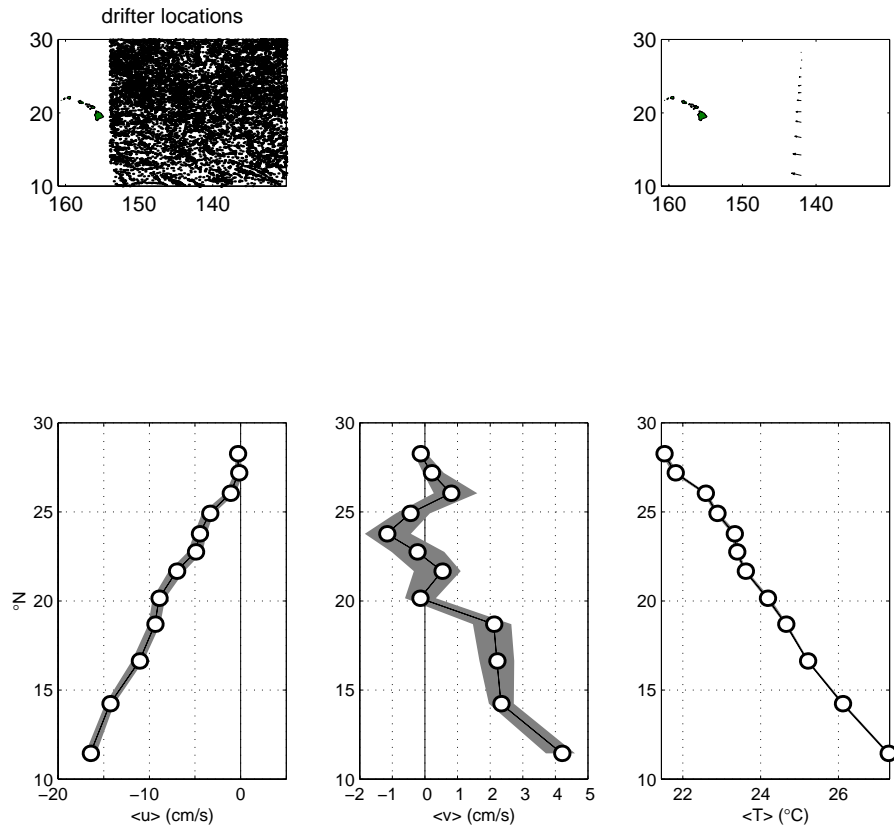


Figure 52: Zonally-averaged drifter observations east of the Hawaiian Islands.  
*Top:* Locations of the data (left) and mean currents (right).  
*Bottom:* Mean zonal speed (left), meridional speed (middle) and temperature (right).  
 Every white circle is calculated from independent data. Shading gives the standard error bars.

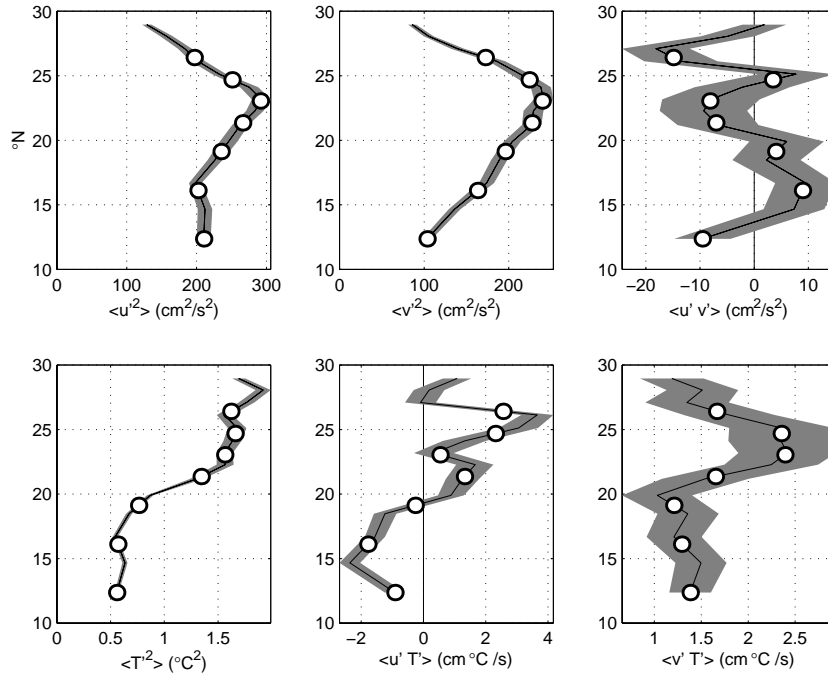


Figure 53: Zonally-averaged drifter observations east of the Hawaiian Islands (see Fig. 52). At top is the variance of the zonal current (left), meridional current (middle) and covariance between them (right). At bottom is the variance of the temperature (left), the covariance between temperature and zonal current (middle) and covariance between temperature and meridional current (right). Every white circle is calculated from independent data. Shading gives the standard error bars.

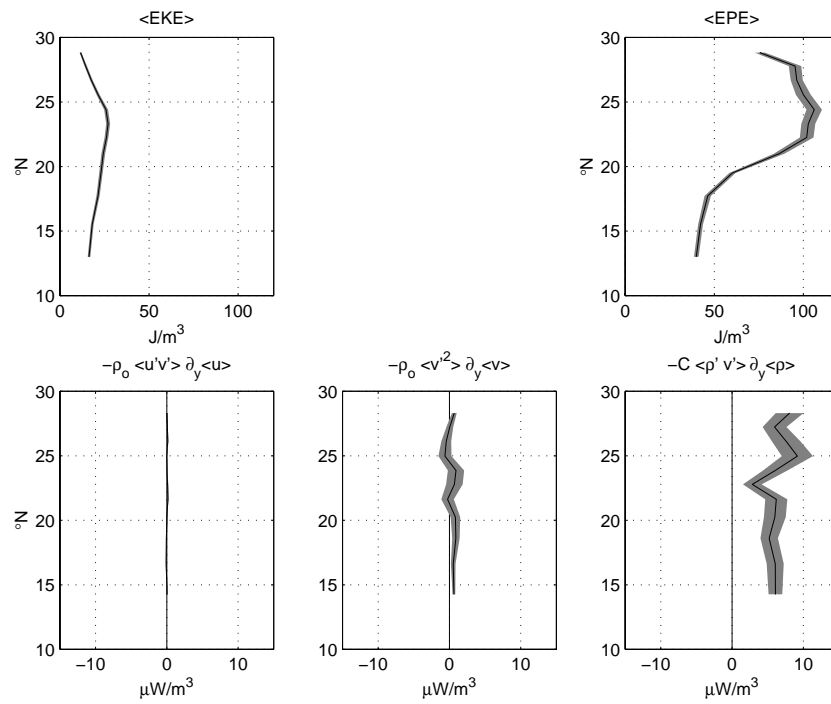


Figure 54: *Top*: mean eddy kinetic (left) and potential (right) energy east of the Hawaiian Islands.

*Bottom*: mean energy fluxes, calculated from the drifter observations.

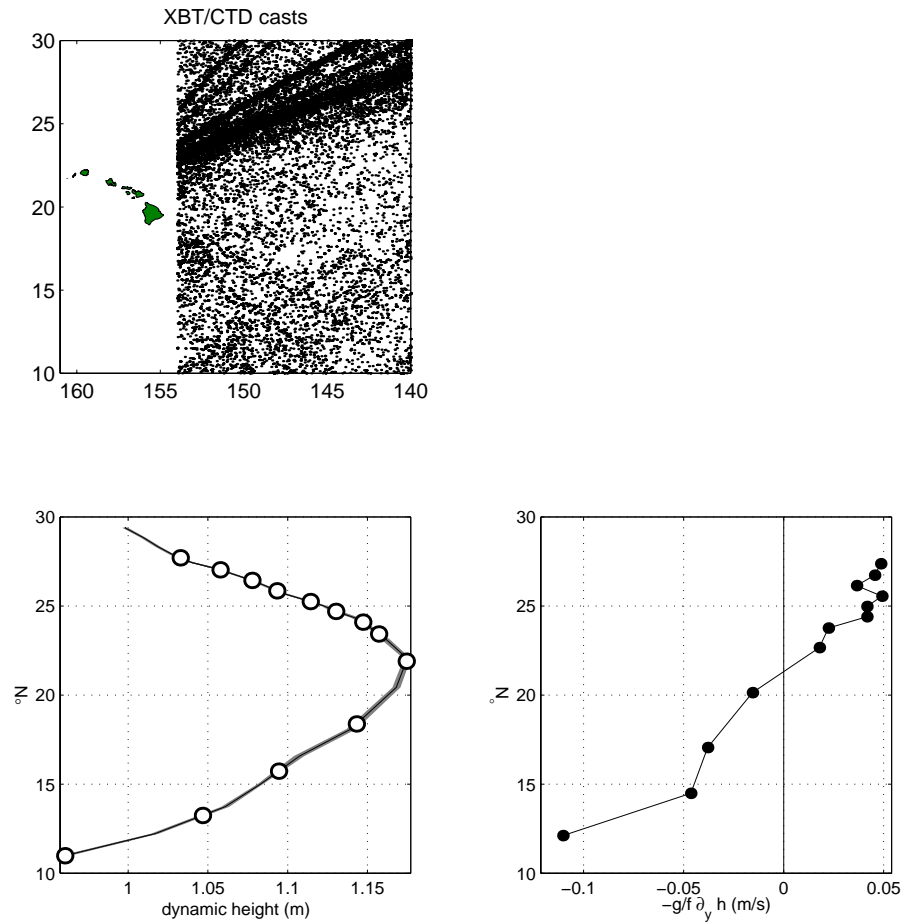


Figure 55: Zonally-averaged dynamic height east of the Hawaiian Islands, referenced to 400 dbar.

*Top:* Points used for zonally-averaged curve.

*Bottom, left:* Median dynamic height. Every white circle is calculated from independent data. Shading gives standard error bars.

*Bottom, right:* Geostrophic zonal current calculated from independent points of the dynamic height curve.

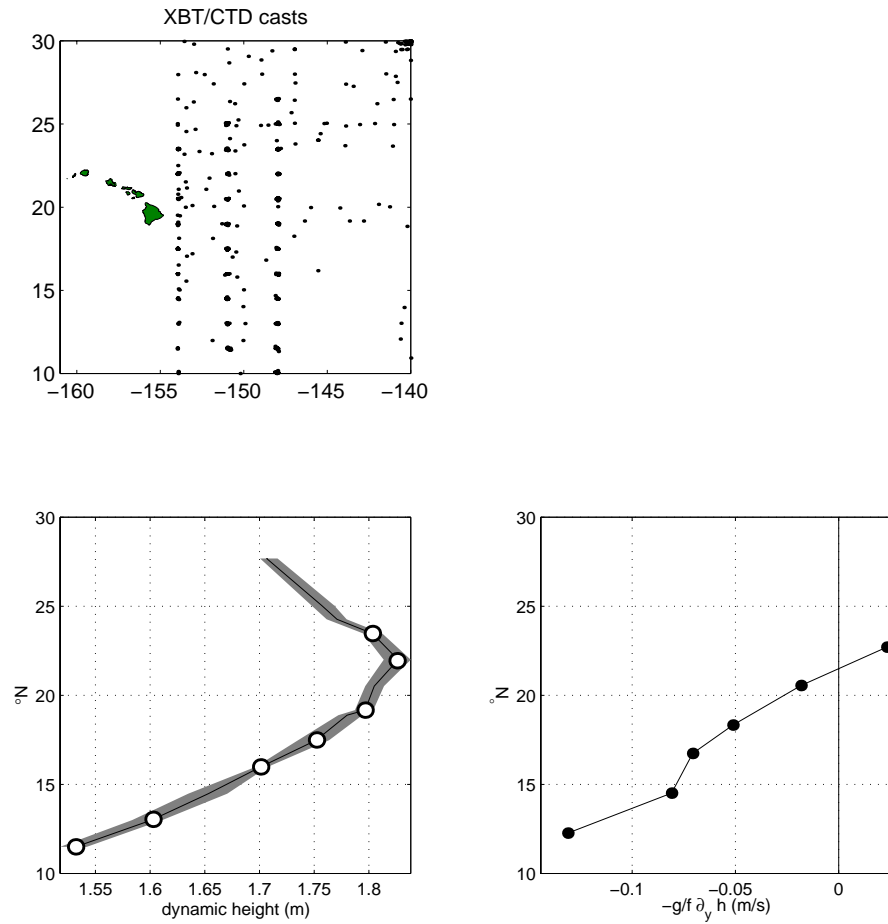


Figure 56: *Right:* Median dynamic height east of the Hawaiian Islands, referenced to 1000 dbar. Every white circle is calculated from independent data. Shading gives standard error bars.

*Left, top:* Points used for zonally-averaged curve.

*Left, bottom:* Geostrophic zonal current calculated from independent points of the dynamic height curve.

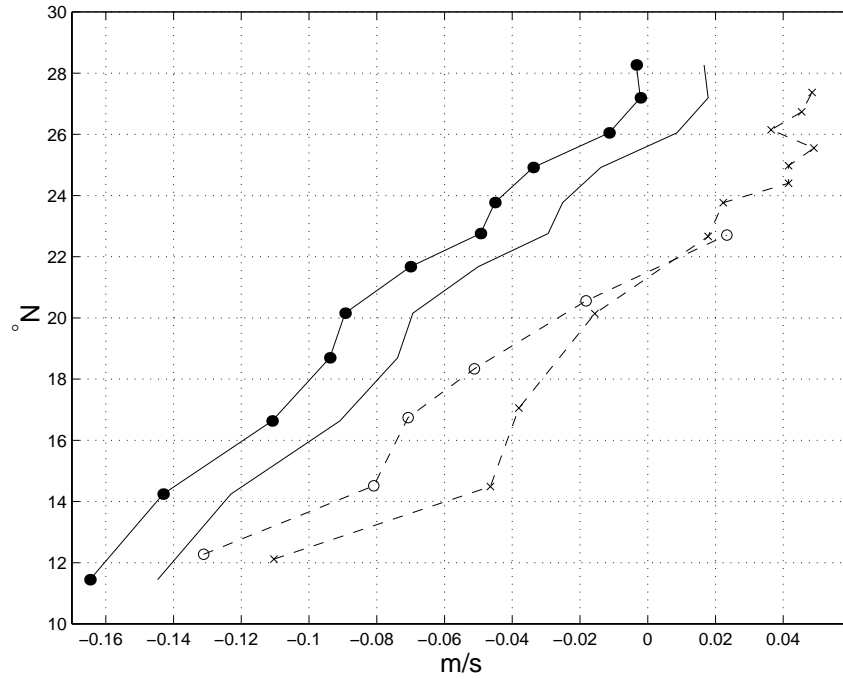


Figure 57: Zonal speed east of Hawaiian Islands, from Figs. 52, 55 and 56. Solid line with dots is drifter-observed speed. Solid line without dots is the same profile, shifted by 2 cm/s to account for Ekman drift and downwind slip. Dashed line with “x” is the surface geostrophic current relative to 400 dbar. Dashed line with “o” is the surface geostrophic current relative to 1000 dbar.

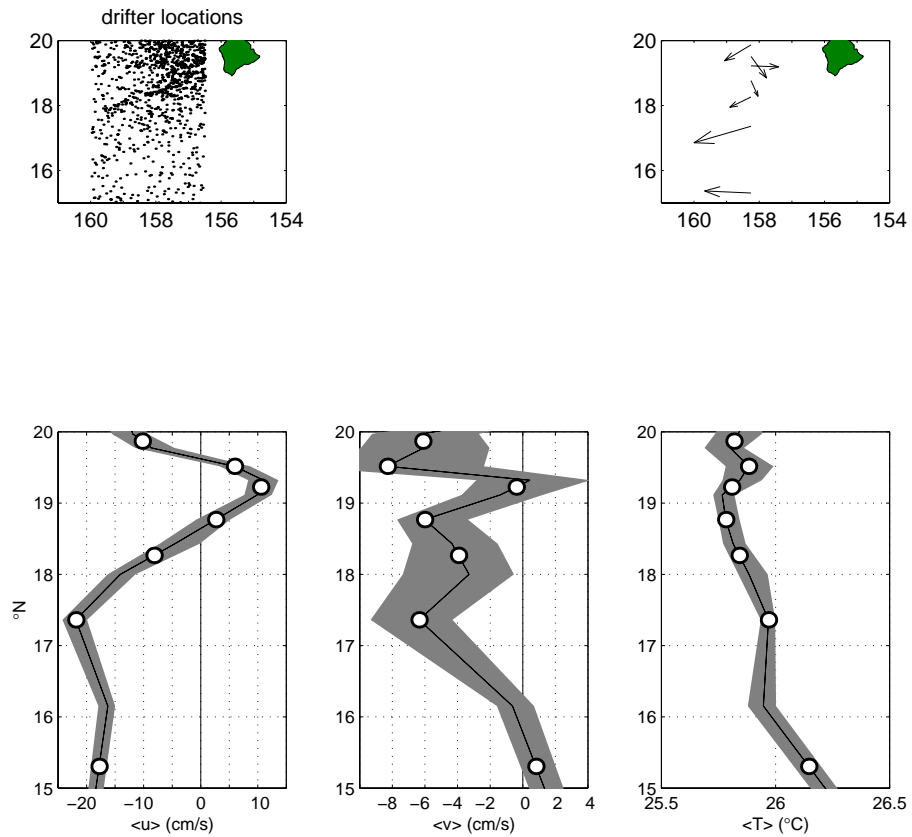


Figure 58: Zonally-averaged drifter observations between 156.5 and 160°W.  
*Top:* Locations of the data (left) and mean currents (right).  
*Bottom:* mean zonal speed (left), meridional speed (middle) and temperature (right).  
 Every white circle is calculated from independent data. Shading gives the standard error bars.

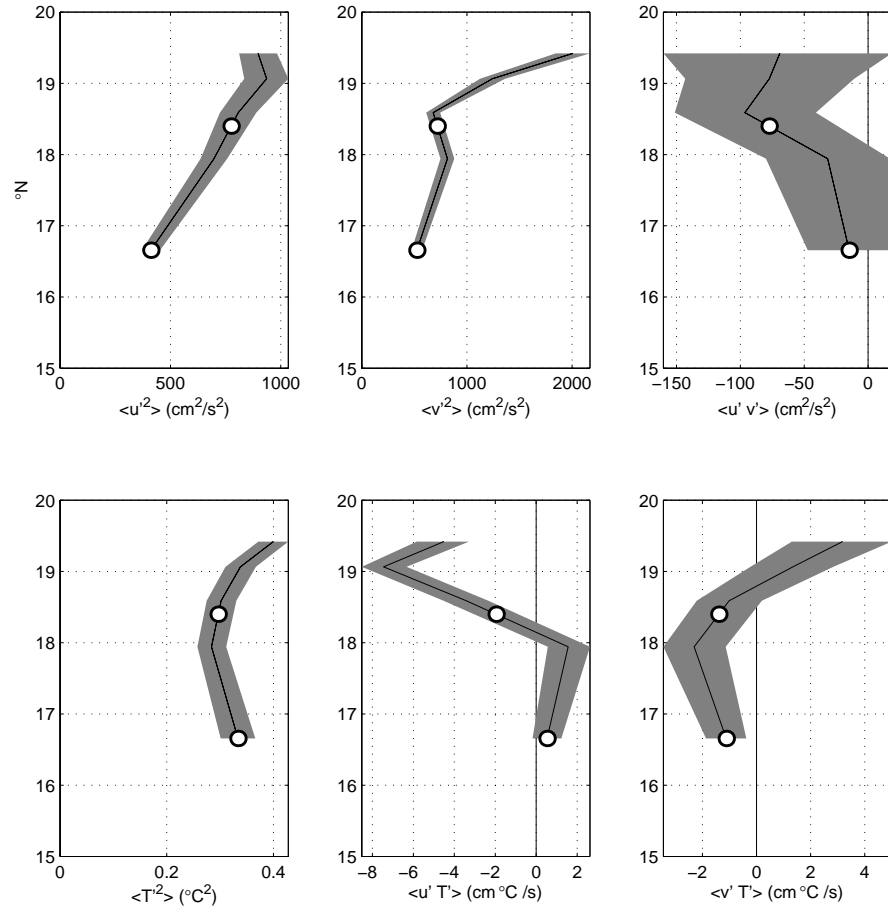


Figure 59: Zonally-averaged drifter observations between 156.5 and 160°W (see Fig. 62). At top is the variance of the zonal current (left), meridional current (middle) and covariance between them (right). At bottom is the variance of the temperature (left), the covariance between temperature and zonal current (middle) and covariance between temperature and meridional current (right). Every white circle is calculated from independent data. Shading gives the standard error bars.

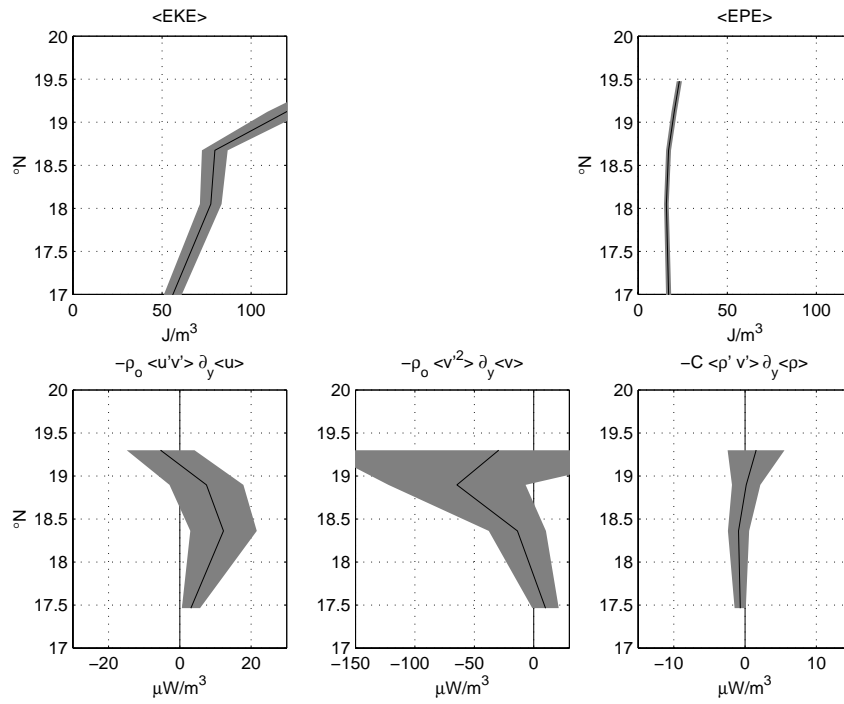


Figure 60: *Top*: mean eddy kinetic (left) and potential (right) energy, 156.5–160° W. *Bottom*: mean energy fluxes, calculated from the drifter observations.

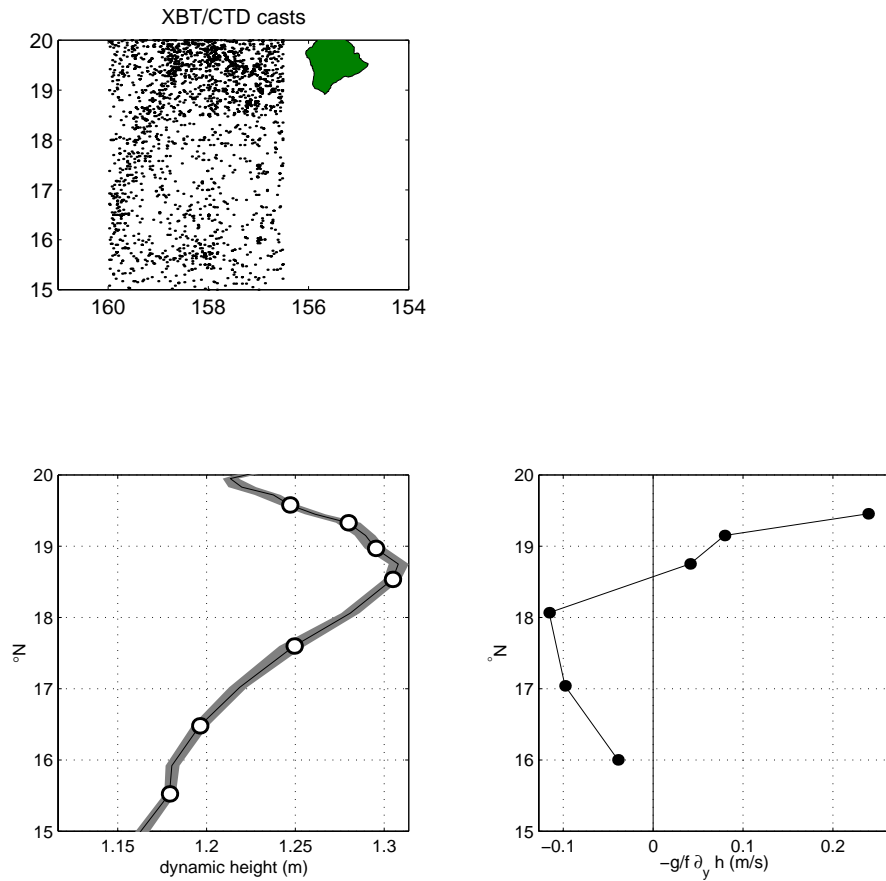


Figure 61: Zonally-averaged dynamic height at the surface relative to 400 dbar, between 156.5 and 160°W.

*Top:* Points used for zonally-averaged curve.

*Bottom, left:* Median dynamic height. Every white circle is calculated from independent data. Shading gives standard error bars.

*Bottom, right:* Geostrophic zonal current calculated from independent points of the dynamic height curve.

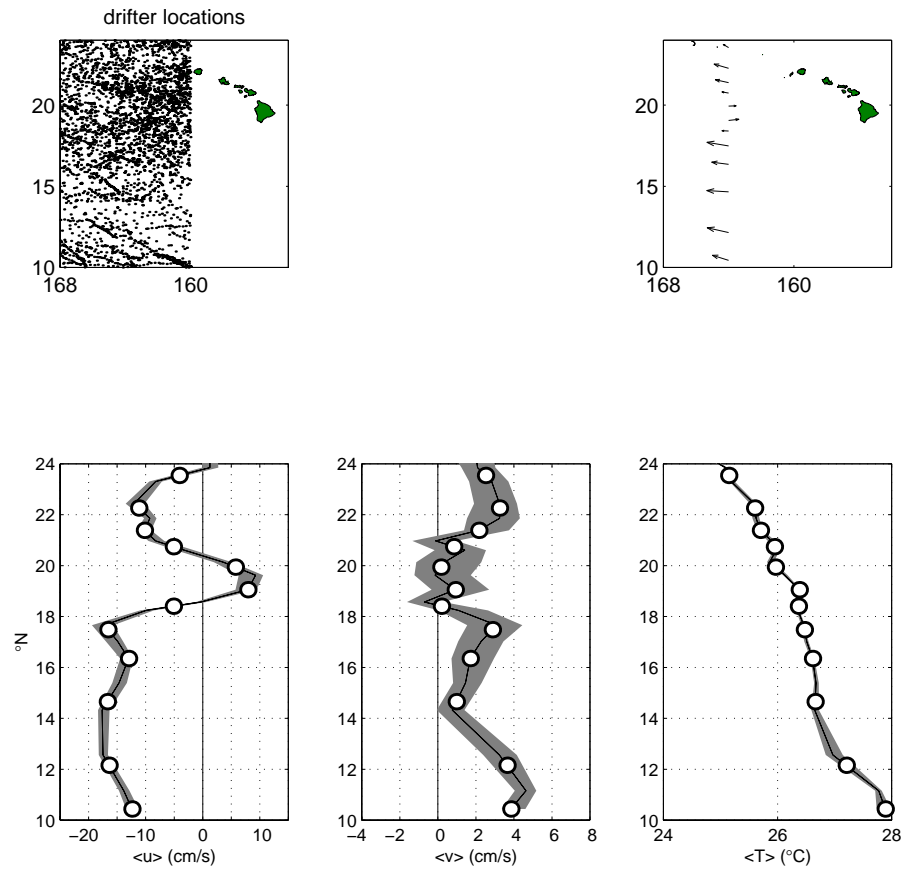


Figure 62: Zonally-averaged drifter observations between 160 and 168°W.

*Top:* Locations of the data (left) and mean currents (right).

*Bottom:* mean zonal speed (left), meridional speed (middle) and temperature (right). Every white circle is calculated from independent data. Shading gives the standard error bars.

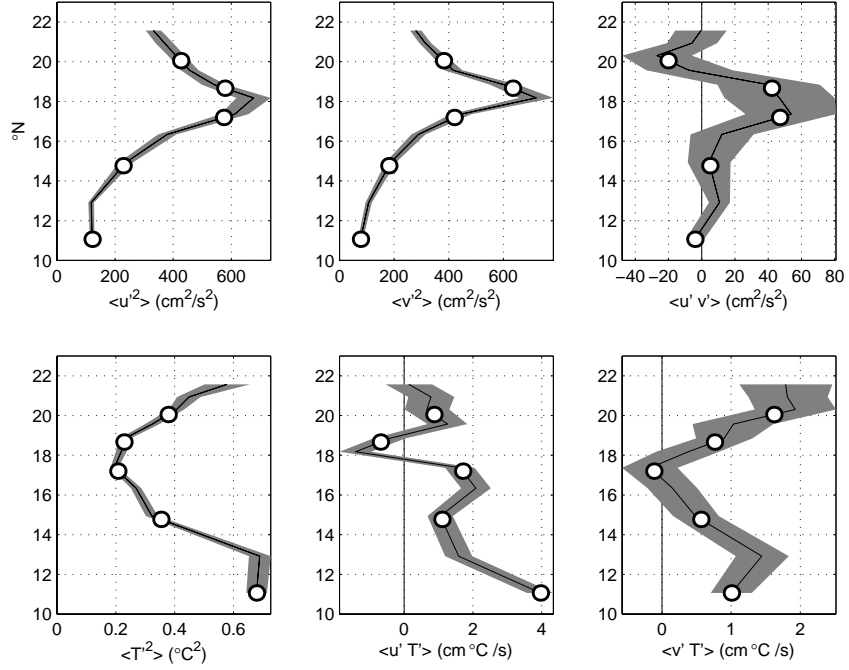


Figure 63: Zonally-averaged drifter observations between 160 and 168°W (see Fig. 62). At top is the variance of the zonal current (left), meridional current (middle) and covariance between them (right). At bottom is the variance of the temperature (left), the covariance between temperature and zonal current (middle) and covariance between temperature and meridional current (right). Every white circle is calculated from independent data. Shading gives the standard error bars.

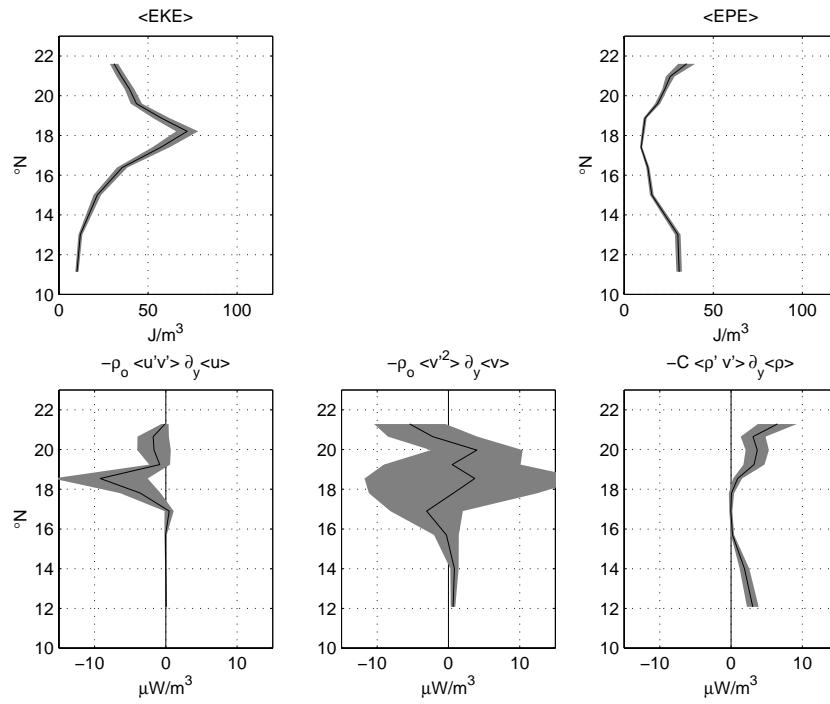


Figure 64: *Top*: mean eddy kinetic (left) and potential (right) energy, 160–168° W. *Bottom*: mean energy fluxes, calculated from the drifter observations.

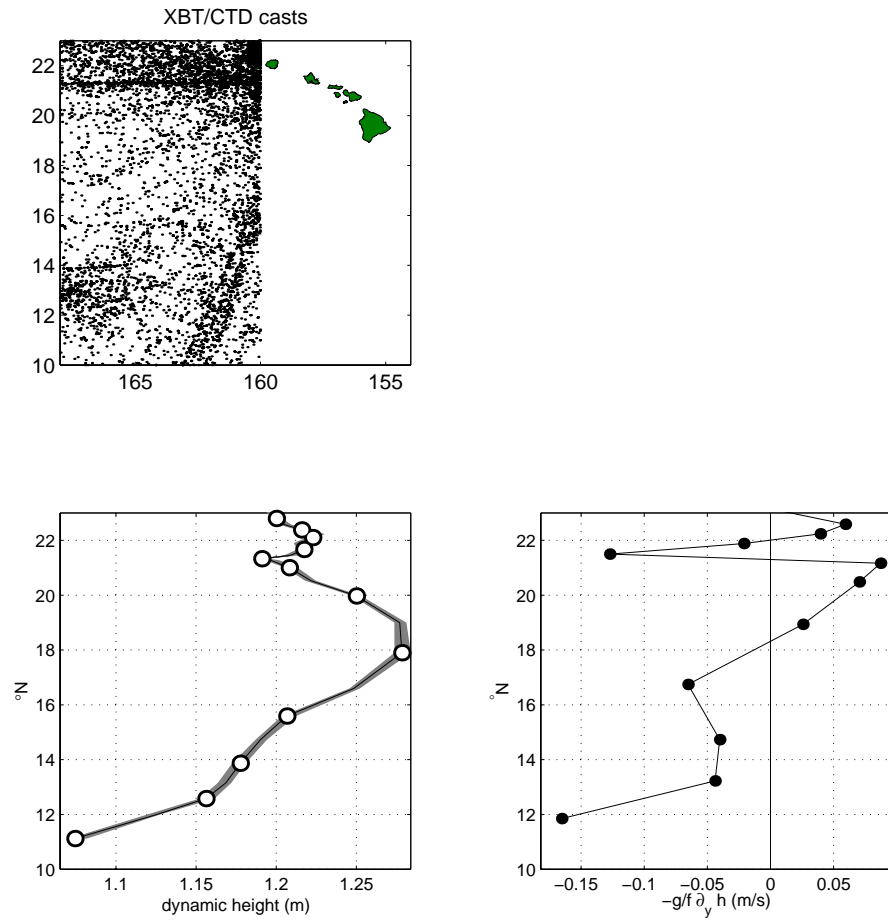


Figure 65: Zonally-averaged dynamic height at the surface relative to 400 dbar, between 160 and 168°W.

*Top:* Points used for zonally-averaged curve.

*Bottom, left:* Median dynamic height. Every white circle is calculated from independent data. Shading gives standard error bars.

*Bottom, right:* Geostrophic zonal current calculated from independent points of the dynamic height curve.

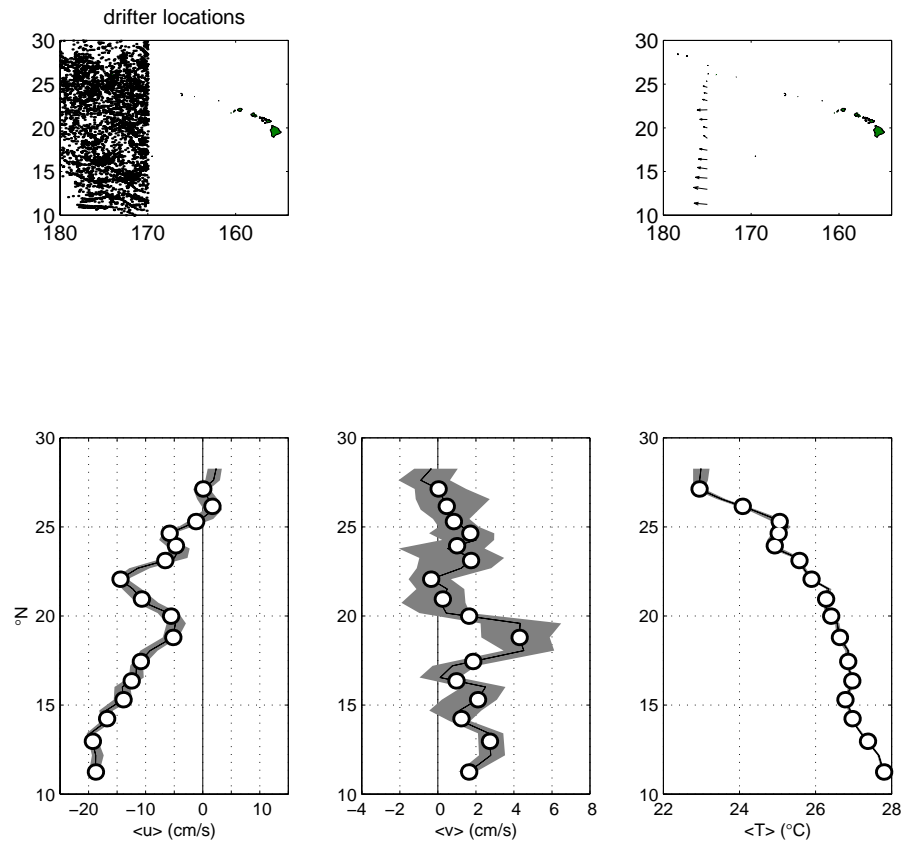


Figure 66: Zonally-averaged drifter observations between 170 and 180°W.

*Top:* Locations of the data (left) and mean currents (right).

*Bottom:* mean zonal speed (left), meridional speed (middle) and temperature (right). Every white circle is calculated from independent data. Shading gives the standard error bars.

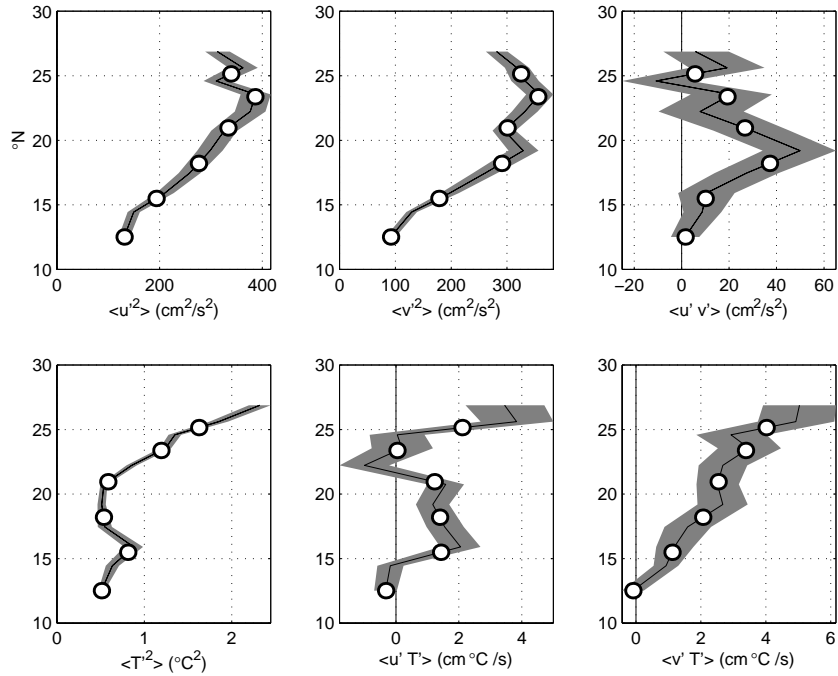


Figure 67: Zonally-averaged drifter observations between  $170$  and  $180^\circ\text{W}$  (see Fig. 66). At top is the variance of the zonal current (left), meridional current (middle) and covariance between them (right). At bottom is the variance of the temperature (left), the covariance between temperature and zonal current (middle) and covariance between temperature and meridional current (right). Every white circle is calculated from independent data. Shading gives the standard error bars.

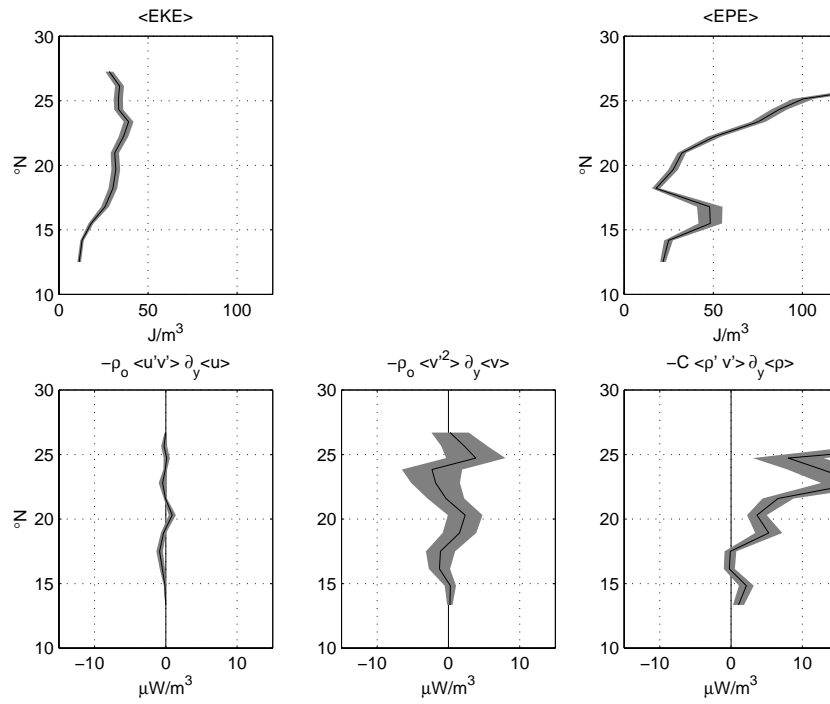


Figure 68: *Top*: mean eddy kinetic (left) and potential (right) energy, 170–180° W. *Bottom*: mean energy fluxes, calculated from the drifter observations.

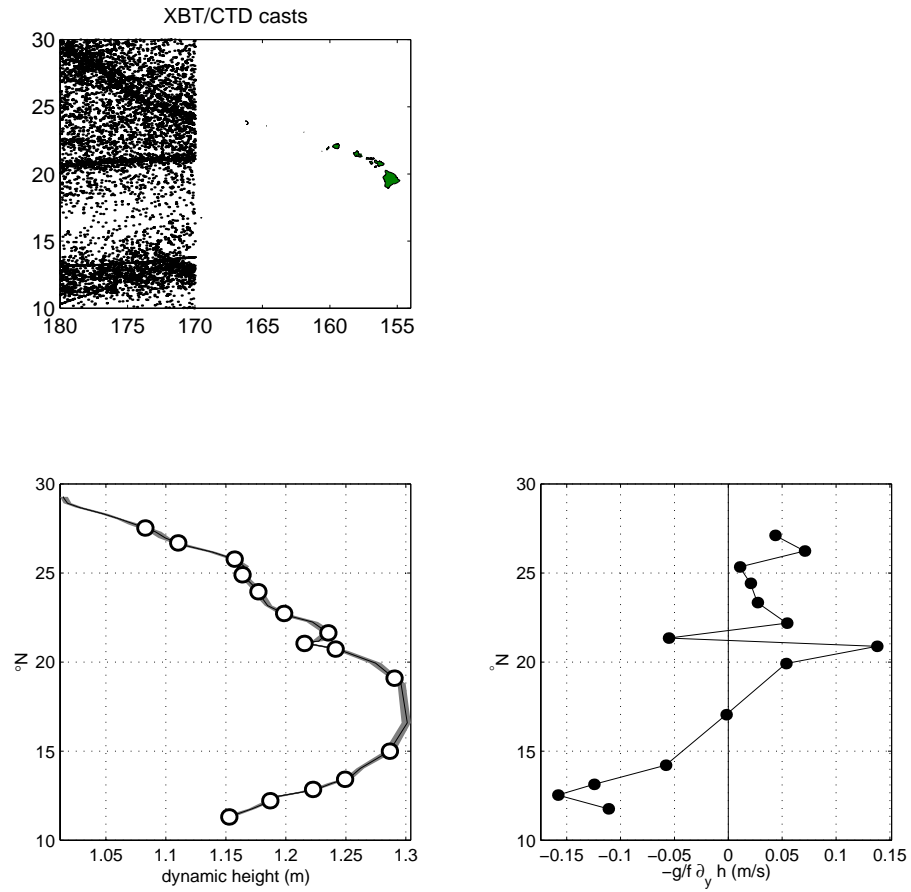


Figure 69: Zonally-averaged dynamic height at the surface relative to 400 dbar, between 170 and 180°W.

*Top:* Points used for zonally-averaged curve.

*Bottom, left:* Median dynamic height. Every white circle is calculated from independent data. Shading gives standard error bars.

*Bottom, right:* Geostrophic zonal current calculated from independent points of the dynamic height curve.

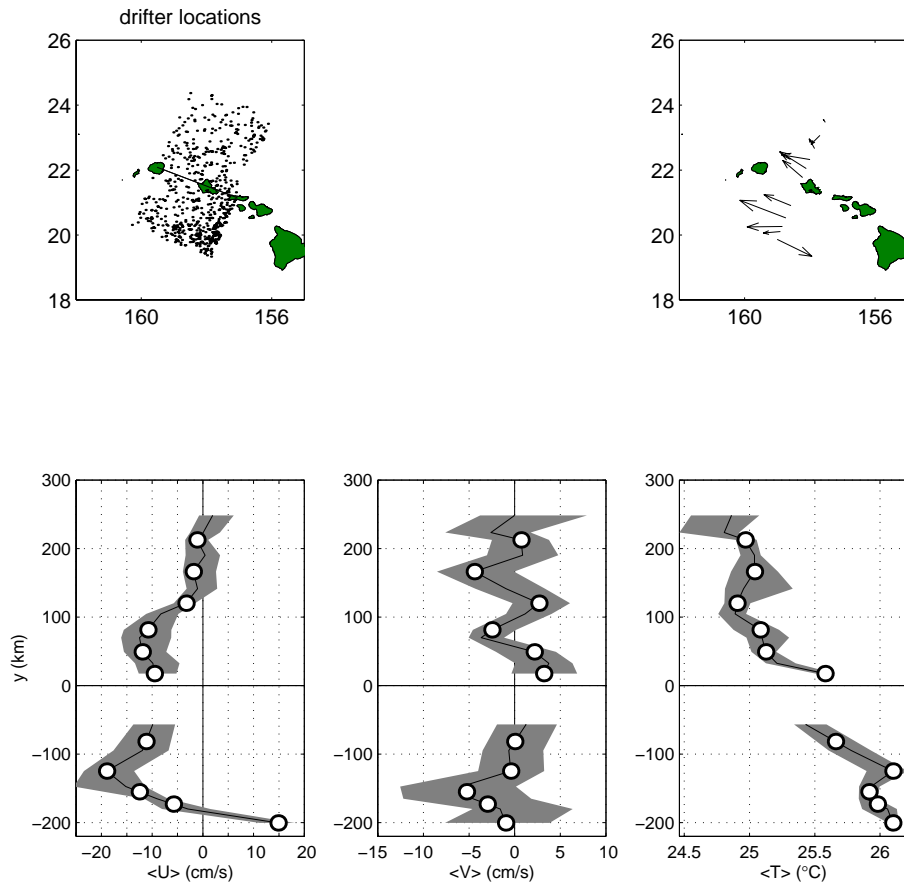


Figure 70: Drifter observations averaged along the Hawaiian Ridge.  
*Top:* Locations of the data (left) and mean currents (right). The solid line indicates the  $y = 0$  axis for the along-ridge/cross-ridge coordinate system.  
*Bottom:* mean along-ridge speed (left), cross-ridge speed (middle) and temperature (right). Every white circle is calculated from independent data. Shading gives the standard error bars.

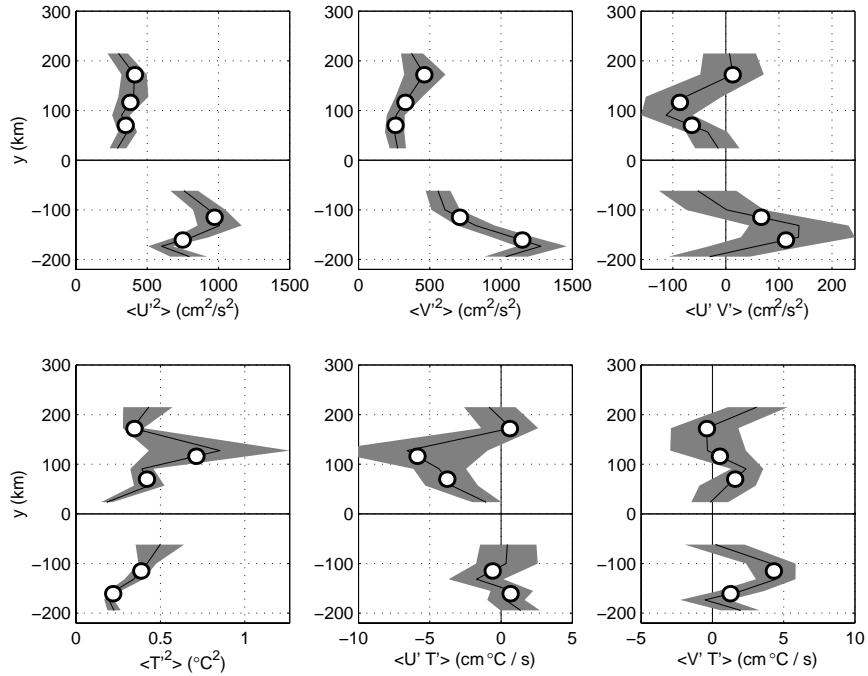


Figure 71: Zonally-averaged drifter observations along the Hawaiian Ridge (see Fig. 70). At top is the variance of the along-ridge current (left), cross-ridge current (middle) and covariance between them (right). At bottom is the variance of the temperature (left), the covariance between temperature and along-ridge current (middle) and covariance between temperature and cross-ridge current (right). Every white circle is calculated from independent data. Shading gives the standard error bars.

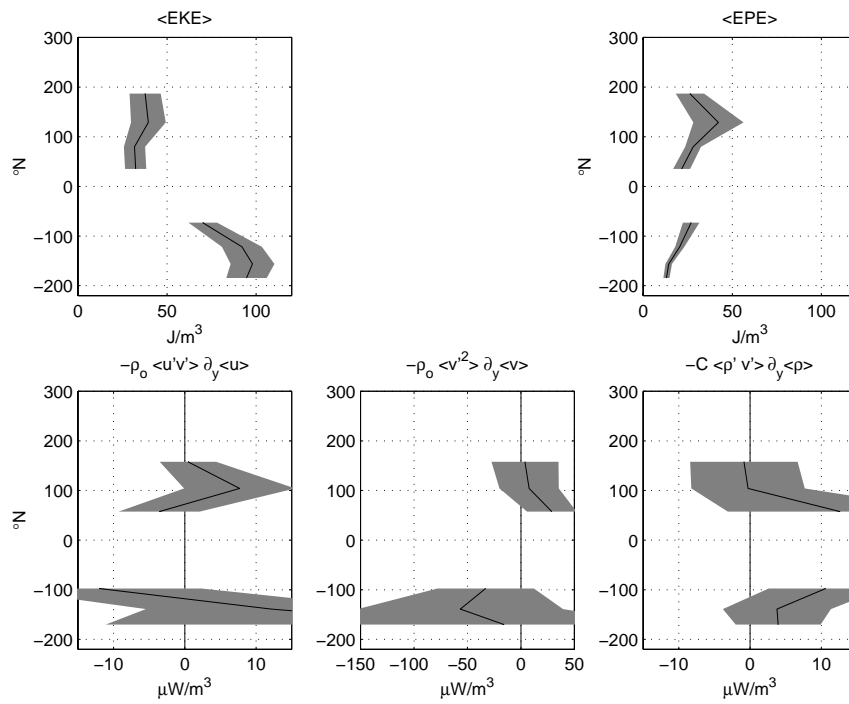


Figure 72: *Top*: mean eddy kinetic (left) and potential (right) energy along the Hawaiian Ridge (see Fig. 70).

*Bottom*: mean energy fluxes, calculated from the drifter observations.

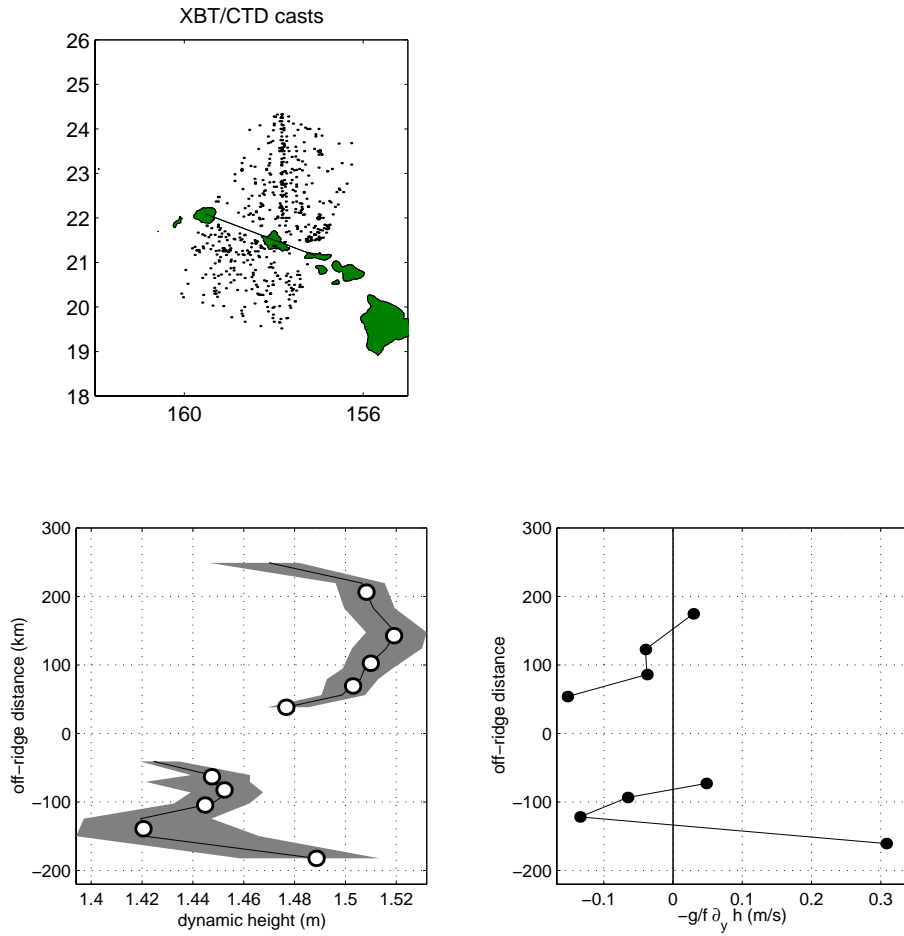


Figure 73: Dynamic height at the surface relative to 400 dbar, averaged along the Hawaiian ridge.

*Top:* Points used for zonally-averaged curve.

*Bottom, left:* Median dynamic height. Every white circle is calculated from independent data. Shading gives standard error bars.

*Bottom, right:* Geostrophic zonal current calculated from independent points of the dynamic height curve.

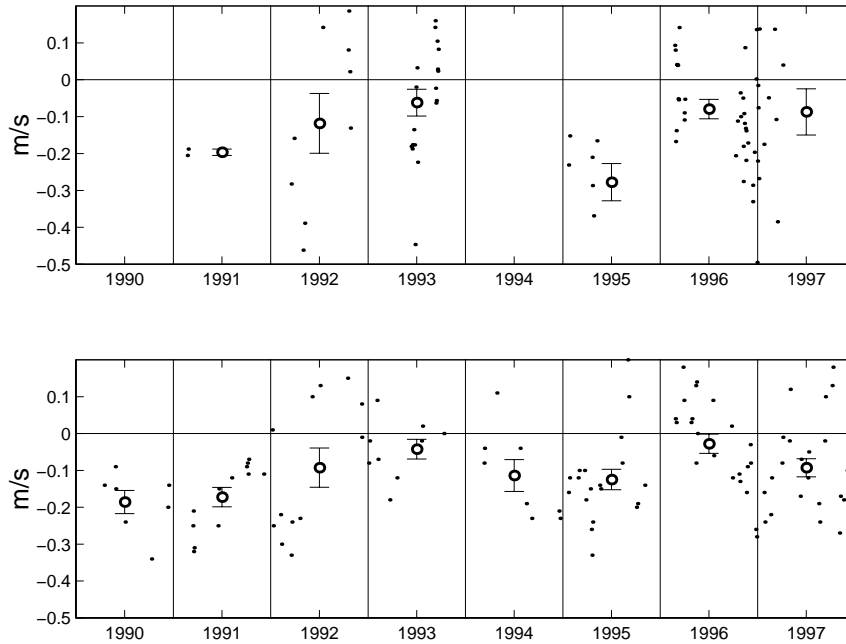


Figure 74: *Top*: Along-ridge speed of drifters within 100 km NE of the line in Fig. 70. Negative is to the WNW. Circles with standard error bars are the yearly averages. The overall mean is  $-10.1 \pm 2.0$  cm/s, with a standard deviation of 18.5 cm/s. *Bottom*: Depth-averaged alongridge current from 20 to 120 m depth measured by ship-board ADCP,  $21.7\text{--}22.6^\circ\text{N}$ ,  $\sim 158^\circ\text{W}$ . Negative is to the WNW. Circles with standard error bars are the yearly averages. The overall mean is  $-10.8 \pm 1.1$  cm/s, with a standard deviation of 13.0 cm/s. Figure adapted from Firing *et al.* [1998].

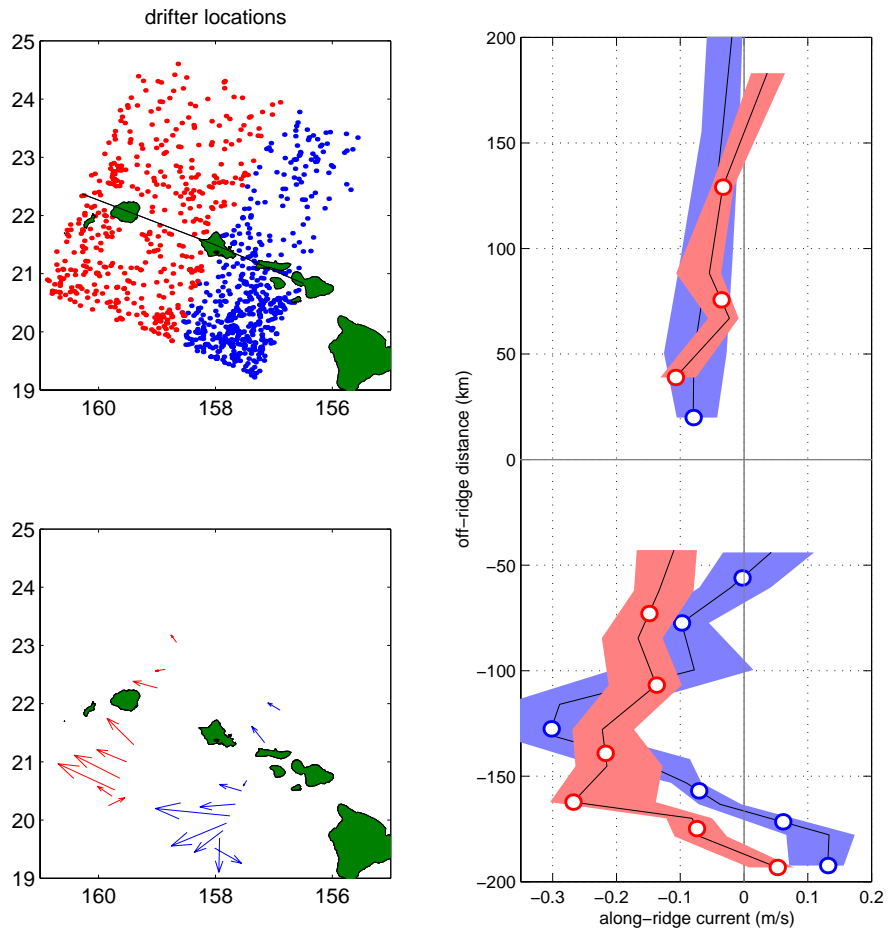


Figure 75: *Right*: Mean speed of drifters along the Hawaiian ridge. Blue dots are for the drifters ESE of O‘ahu; red dots for drifters WNW of O‘ahu. Shading gives standard error bars.

*Left, top*: Points averaged along-ridge for curve at right.

*Left, bottom*: Quiver plot of mean currents (both components).

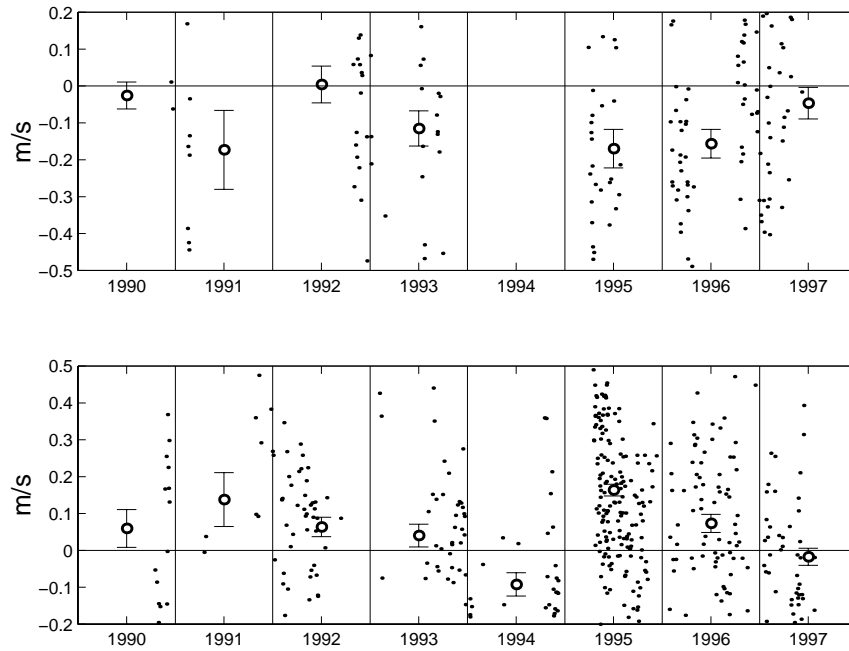


Figure 76: *Top*: Along-ridge drifter speeds in the Hawaiian Lee Current (from 0–150 km offshore of the line in Fig. 70). The vertical axis has been compressed to focus on the yearly averages (circles, with standard error bars).

*Bottom*: Zonal drifter speeds in the Hawaiian Lee Countercurrent (18.5–20.5°N, 160–168°W). The vertical axis has been shrunk to focus on the yearly averages (circles, with standard error bars).

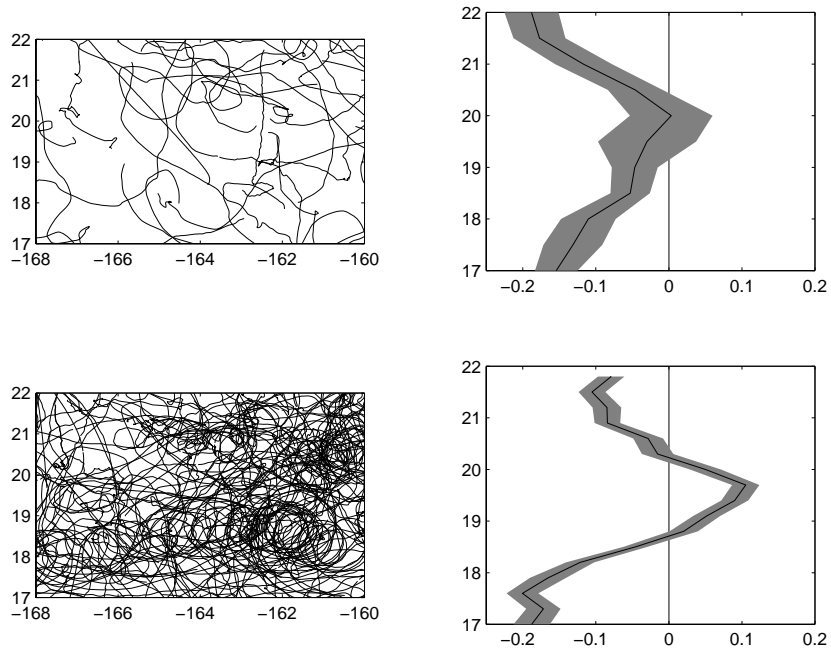


Figure 77: *Left:* Drifter trajectories flagged as eddy-trapped (bottom) and not eddy-trapped (top), in the region of the Hawaiian Lee Countercurrent. *Right:* Mean zonal speed of the drifters, with standard error bars.

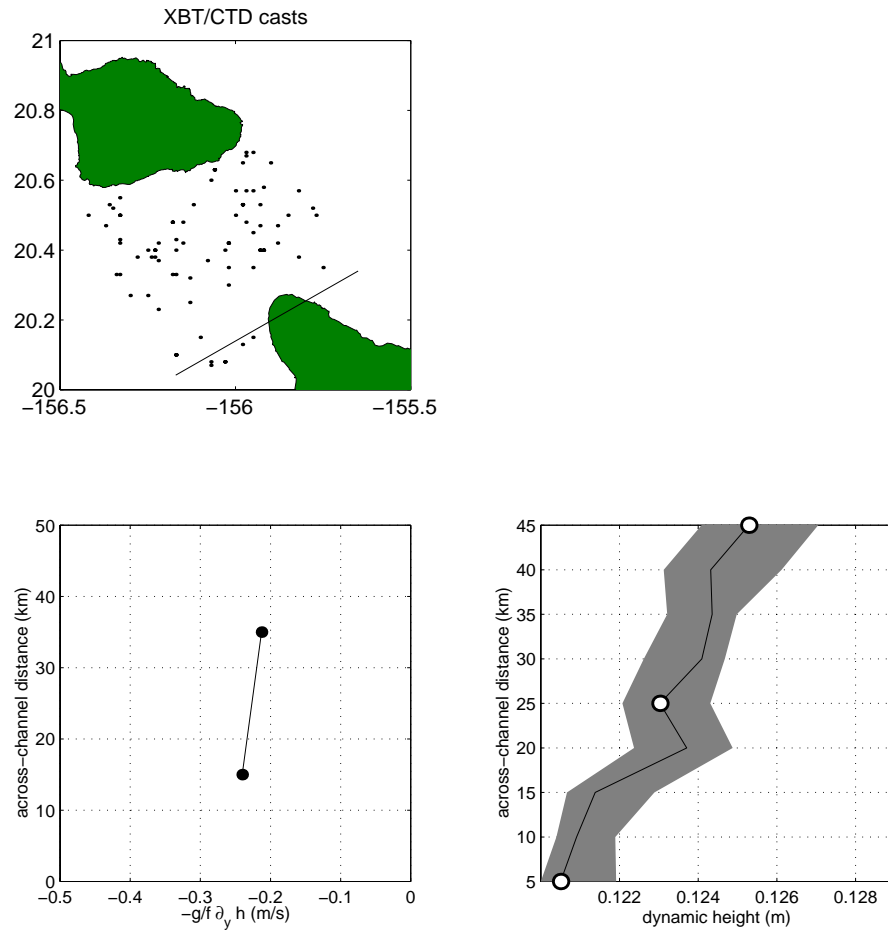


Figure 78: *Right:* Mean dynamic height at the surface referenced to 400 dbar, averaged across the ‘Alenuihaha Channel separating Hawai‘i from Maui. Every white circle is calculated from independent data. Shading gives standard error bars.

*Left, top:* Points used for curve at right.

*Left, bottom:* Geostrophic through-channel current calculated from independent points of the dynamic height curve.

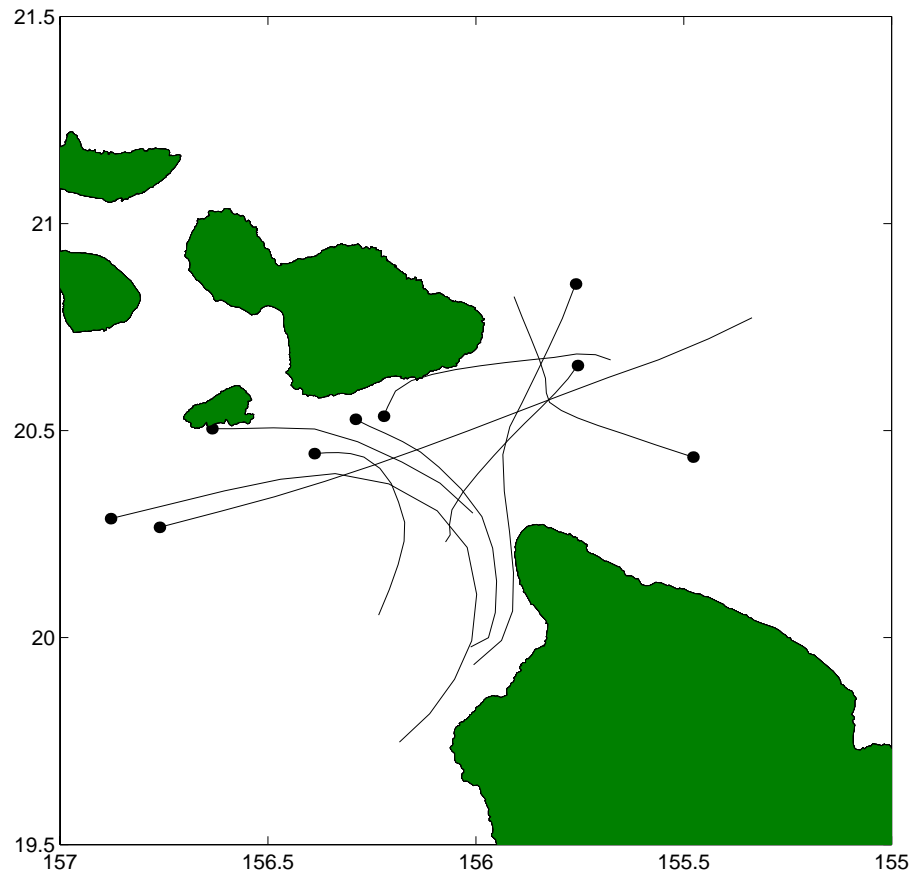


Figure 79: Three-day trajectories of drifters near the 'Alenuihaha Channel. Dots indicate the position at the end of three days. This is a composite of trajectories, and not a snapshot at any one time. Four drifters passed through the channel, at speeds of 11.4 cm/s, 26.1 cm/s, -19.2 cm/s and -58.3 cm/s (positive to the ENE). The overall through-channel flow is  $10.0 \pm 18.7$  cm/s.

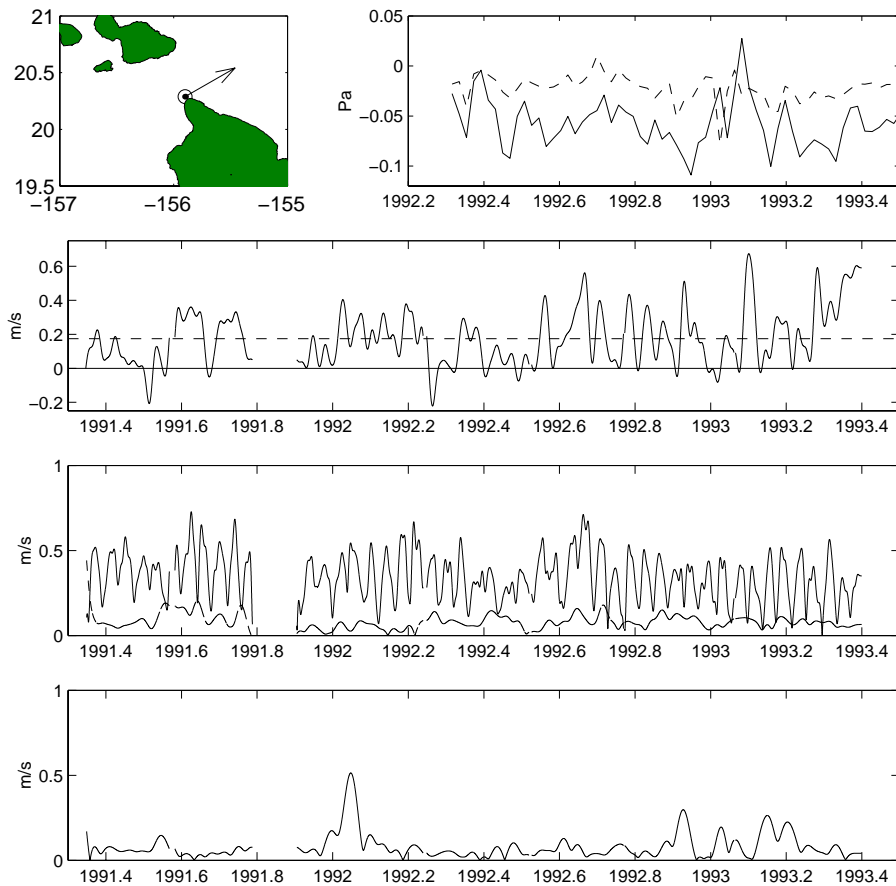


Figure 80: *Top, left*: Location of an electromagnetic (Seadata) current meter. An arrow indicates the direction of the mean current.

*Top, right*: ERS-1 scatterometer weekly wind stress averaged over study region. Solid: zonal stress, dashed: meridional stress.

*Middle, upper*: Time series of the current  $30^\circ$  north of east (through-channel), lowpassed at 10 days. Gaps are due to instrument servicing. The dashed line is the mean.

*Middle, lower*: Complex demodulation of the through-channel current. Upper curve: 11-13 h. Lower curve: 23-25 h.

*Bottom*: Complex demodulation of the through-channel current at 60 h (gravest island-trapped wave eigenfrequency [Luther, 1985]), lowpassed to admit 50-70 h.

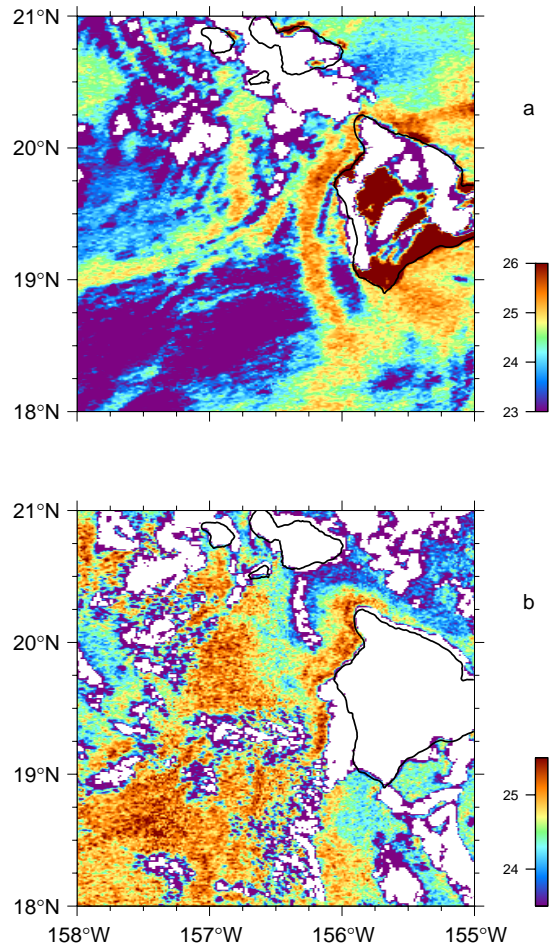


Figure 81: AVHRR SST images ( $^{\circ}\text{C}$ ). Temperatures colder than  $22^{\circ}\text{C}$  have been flagged as clouds (white). The images were taken on 3 February 1993 at 0101 UTC (a) and at 1745 UTC (b).

## CHAPTER 5

### DISPERSION AND EDDY DIFFUSIVITY

*Lagrangian statistics are calculated for individual drifter trajectories. The dominant length and time scales of variability and apparent eddy diffusivity are found for several subregions, and the long-time dispersion is compared to classical theory.*

As shown in Chapter 3, drifter clusters are rapidly spread out by eddies in the lee of the islands. Eddies are particularly adept at this, due to their intense currents, relatively small length scales, and their ability to transport tracers over thousands of kilometers. Quantifying this dispersive capacity is essential in order to anticipate the environmental impacts of discharged pollutants and oil spills and understand observed nutrient and plankton distributions [Bennett and Denman, 1985].

Lagrangian quantities describing drifter dispersion are derived using classical dispersion theory. However, this theory assumes stationary and homogeneous currents; a drifting buoy travels through spatially inhomogeneous mean currents, in an eddy field which changes in both space and time. Because of this, Freeland *et al.* [1975] concluded that even the short-time dispersion of SOFAR floats (neutrally buoyant at  $\sim 1500$  m) in the MODE region cannot be described by classical theory. Subsequent studies of near-surface drifters [Colin de Verdiere, 1983; Krauss and Böning, 1987; Paduan and Niiler, 1993] have not found this inconsistency for short-time dispersion.

In this chapter, drifter dispersion in the Hawaiian region is examined. The Lagrangian integral time and length scales and the apparent eddy diffusivity are calculated in six subregions. The short- and long-time dispersion is compared to predictions made by classical dispersion theory, thus testing its applicability to the Hawaiian region. Finally, the Lagrangian spectra are examined for significant zonal/meridional and rotary motion in the subregions.

### 5.1 Classical theory: Taylor's Theorem and eddy diffusivity

Consider a cloud of particles released into a fluid at a single point. In the absence of any macroscopic fluid motion, the cloud slowly diffuses outward due to the Brownian dance of the water molecules. Within a fluid in motion, advection strongly affects this process. The instantaneous current  $u(t)$  experienced by a particle can be divided into a mean component  $u_o$  (identical for all particles), and a fluctuating component  $u'(t)$  (which may vary from one particle to the next). The mean current advects the cloud's center of mass along the trajectory  $x_o = u_o t$ ; advection by the random fluctuations spreads the cloud orders of magnitude more rapidly than via molecular diffusion (c.f. Tennekes and Lumley [1972]).

The position of an individual particle in the cloud is  $x(t) = u_o t + x'(t)$ , where

$$x' = \int_0^t d\tau u'(\tau). \quad (5.1)$$

Dispersion is quantified as  $\langle x'^2 \rangle$ , where the brackets denote an ensemble average over all particles. Under the assumption that  $u'$  is ergodic, (5.1) can be used to derive Taylor's Theorem:

$$\langle x'^2 \rangle = 2 \langle u'^2 \rangle \int_0^t d\tau (t - \tau) R_u(\tau) \quad (5.2)$$

[Taylor, 1921], where the autocorrelation function  $R_u$  is

$$R_u(\tau) = \lim_{T_m \rightarrow \infty} \frac{1}{\langle u'^2 \rangle T_m} \int_0^{T_m} dt u'(t) u'(t + \tau), \quad (5.3)$$

Because the autocorrelation function is the Fourier transform of the spectral density  $E(\omega)$  [Bendat and Piersol, 1986], Taylor's Theorem can be expressed as

$$\langle x'^2 \rangle = 4 \int_{-\infty}^{\infty} d\omega \frac{E_u(\omega)}{\omega^2} \sin^2 \left( \frac{\omega t}{2} \right) \quad (5.4)$$

[Kampé de Férièr, 1939]. If  $u'$  has a white-noise spectrum  $E_u(\omega) = E_o$ , (5.4) shows that

the rms displacement is proportional to  $\sqrt{t}$ . Dispersion at this rate is called a “random walk.”

The dispersive motion can be described by a characteristic time and space scale. The time scale, defined as

$$T_u = \int_0^\infty d\tau R_u, \quad (5.5)$$

is known as the Lagrangian interal time scale. It can be combined with the rms speed to derive the Lagrangian length scale  $L_u = u_{rms}T_u$ . Because the integral time scale  $T_u$  is the scale over which  $R_u$  decays, it is a useful dividing line between the “short-time” and “long-time” dispersion. If  $t \ll T_u$ ,  $R_u \approx 1$  and the dispersion is

$$\langle x'^2 \rangle \approx \langle u'^2 \rangle t^2 \quad (t \ll T_u). \quad (5.6)$$

Initially, the rms particle displacement increases linearly with time with a slope equal to the rms velocity. However, once  $t \gg T_u$ ,  $R_u \approx 0$  and

$$\langle x'^2 \rangle \approx 2 \langle u'^2 \rangle T_u t \quad (t \gg T_u). \quad (5.7)$$

The rms particle displacement slows from the initial growth ( $\propto t$ ) to a random-walk ( $\propto \sqrt{t}$ ).

Batchelor [1949] demonstrated that dispersion could be parameterized as an apparent eddy diffusivity  $K_{xx}$ , defined by

$$K_{xx} = \frac{1}{2} \frac{d}{dt} \langle x'^2 \rangle. \quad (5.8)$$

Using (5.7), one finds that the diffusivity approaches the asymptotic value

$$K_{xx} = \langle u'^2 \rangle T_u \quad (5.9)$$

for  $t \gg T_u$  (again assuming that  $u'$  is stationary).

## 5.2 Direct calculation of Lagrangian properties

In the Hawaiian region, the mean currents and the eddy kinetic energy field are quite inhomogeneous (see Figs. 9, 11). This challenges the basic assumptions of the classical theory . . . how relevant are Lagrangian scales and eddy diffusivities calculated under the assumptions of stationarity and homogeneity? In an attempt to minimize these effects, I divided the study region into six rectangular cells (shown in Fig. 82). Within each cell, I proceed with the calculations as if the assumptions of classical theory were valid. In the next section, I explicitly test Taylor's Theorem by comparing the directly-observed short- and long-time dispersion with the asymptotic limits (5.6) and (5.7).

The integral time scales and diffusivities were calculated from 90-day nonoverlapping segments of the drifter tracks, grouped into the cells according to their center of mass. Invariably, a direct estimate of the autocorrelation function  $R$  is contaminated by noise and uncertainties in the mean current. This contamination is significant at large lags, where  $R$  should in theory approach zero. To minimize the effects of these errors on the Lagrangian time scale calculation, it has become standard practice (c.f. [Freeland *et al.*, 1975; Krauss and Böning, 1987; Poulain and Niiler, 1989]) to integrate only to the first zero crossing of  $R$ . Because some of the negative lobes in  $R$  may reflect true oscillatory motion (for example, the cycloidal trajectories of drifters trapped in eddies), this procedure produces an upper estimate of the Lagrangian time scale.

For each segment within a cell, the ensemble-averaged mean speed was removed and the autocorrelation functions for  $u'$  and  $v'$  were calculated. These functions were then integrated to get the integral time scale. The mean zonal and meridional time scales are shown in Fig. 82 and listed in Table 5.1. The meridional scale is quite homogeneous, especially in the northern four cells. In all cells, the meridional time scale is shorter than the zonal scale. The outstanding feature of Fig. 82 is the 7-8 days zonal time

scale in the southern two cells. The asymmetry between the zonal and meridional time scales suggests that meanders, rather than eddies, dominate the variability in this region [Krauss and Böning, 1987]. This interpretation is visually consistent with the raw drifter tracks south of  $\sim 16^\circ\text{N}$  (Fig. 6).

Table 5.1: Lagrangian properties in each cell, calculated from independent 90-day segments. The data are grouped by the cell's central longitude (horizontal axis) and latitude (vertical axis). Data are number of 90-day segments within the cell, zonal/meridional time scale, zonal/meridional rms velocity, and zonal/meridional eddy diffusivity

	167.75°W	143.25°W
	173 segments	145 segments
26.5°N	3.7±0.4 / 3.0±0.2 days	5.5±0.5 / 3.2±0.3 days
	16.7±0.4 / 15.9±0.3 cm/s	12.6±0.3 / 11.7±0.3 cm/s
	8800±1100 / 7500±600 m <sup>2</sup> /s	8100±900 / 4200±400 m <sup>2</sup> /s
	174 segments	140 segments
19.5°N	4.3±0.4 / 3.1±0.2 days	4.9±0.6 / 3.2±0.3 days
	19.0±0.5 / 18.2±0.5 cm/s	15.0±0.3 / 13.9±0.3 cm/s
	12400±1000 / 9100±500 m <sup>2</sup> /s	9700±1200 / 5600±400 m <sup>2</sup> /s
	55 segments	64 segments
12.5°N	7.6±1.0 / 4.4±0.5 days	7.2±1.0 / 4.0±0.7 days
	10.6±0.6 / 10.2±0.6 cm/s	11.9±0.5 / 10.5±0.4 cm/s
	8900±1200 / 3000±1300 m <sup>2</sup> /s	9100±1700 / 3800±700 m <sup>2</sup> /s

Apparent eddy diffusivities were calculated using (5.9) (Fig. 82 and Table 5.1). Diffusivity ranges in value from  $12.4 \times 10^3$  m<sup>2</sup>/s in the eddy-rich island lee to  $3\text{--}4 \times 10^3$  m<sup>2</sup>/s in the southern cells. In the northern four cells, the zonal diffusivity is on average 1.5 times greater than the meridional diffusivity. Because the mean rms velocity is nearly isotropic for these regions ( $u_{rms}/v_{rms} = 1.05$ ), this is primarily due to the anisotropy in time scales.

Fig. 83 shows the zonal and meridional scales and diffusivities as functions of the rms speed. For comparison, data are included from Colin de Verdier [1983] (eastern North Atlantic; Turbillon region), Krauss and Böning [1987] (central North Atlantic from  $30^\circ\text{N}$  to  $55^\circ\text{N}$ ), and Poulain and Niiler [1989] (southern California Current System).

With two exceptions (the 7–8 day zonal scales in the southern two cells), the Hawaiian time scales are similar to those of the previous studies. The zonal length scales suggest that, for a given rms speed, Hawaiian eddies are slightly larger than their North Atlantic counterparts but similar to those off Mexico. Because the drifters tend to travel greater distances in a given time, the Hawaiian diffusivities are generally larger than those of Krauss and Böning; they are close to (zonally), or slightly less than (meridionally), those of Poulain and Niiler.

### 5.3 Asymptotic behavior of the dispersion

Expression (5.7) gives an independent method of calculating the Lagrangian time scale based on the long-time dispersion. To exploit this, the drifter tracks were divided into 120-day segments, with each track resampled every 10 days (i.e. there was a 110 day overlap). Within each cell, all segments were treated as if they originated from a single point in space and time [Freeland *et al.*, 1975] and were statistically independent [Poulain and Niiler, 1989]. The rms displacements in each cell are shown in Figs. 84 and 85. Over the first day, (5.6) accurately describes the dispersion in all cells. By the second day, the drifters “feel” the decorrelation from their initial velocity (i.e. the lag is a significant fraction of the integral time scale) and the dispersion drops below the short-time curve.

In order to compare the long-time rms displacement to (5.7), curves of the form  $x_{rms} = a\sqrt{t}$ ,  $y_{rms} = b\sqrt{t}$  have been least-squares fitted to the final 80 days of displacement in Fig. 84. The curves’ shape closely match the observed meridional spreading; on average, the regression coefficients  $b$  give Lagrangian time scales 6% smaller than the direct estimates of  $T_v$ . However, the zonal rms displacement increases approximately linearly through day 120. The regression coefficients  $a$  give time scales averaging 78%

larger than those of Table 5.1, but are of dubious value given the linear, rather than  $\sqrt{t}$ , growth.

#### 5.4 Lagrangian spectra

The spectra of drifter speed were calculated in order to examine the frequency distribution of mesoscale energy. For this analysis, the tracks were not subdivided into multiple overlapping segments (i.e. each segment was composed of independent data). The mean and trend of each segment was removed, then a 10% cosine window was applied, before taking the Fourier transform. The spectra of all segments in a cell were then averaged, with bootstrapping used to get standard error bars.

Fig. 86 shows the spectrum of zonal and meridional drifter speed in an energy-preserving plot. Fig. 87 shows the spectra parced into the cyclonic (i.e. counter-clockwise) and anticyclonic (i.e. clockwise) rotary components. In the northern four cells, the energy-containing band peaks at 6–40 days. The most dramatic spectra are in the island lee cell; sharp spectral peaks occur at 4–4.8, 6, and 12 days period. The rotary spectra show that the 4–4.8 day peak is almost entirely cyclonic, while the 6 and 12 day peaks are predominantly anticyclonic. The anticyclonic spectrum also has barely significant peaks at 3 and 22 days (Fig. 88). This discretization of eddy energy suggests that the motion is a resonant response to direct forcing, or that some process or combination of processes is quantizing the mesoscale variability within the energetic 5–40 day band (such as fixed-frequency eddy generation and downstream vortex merging; see Chapter 3). To the northeast of the islands, anticyclonic energy is significantly greater than cyclonic energy throughout most of the eddy band. Within the southern two cells, the spectra are considerably less energetic, with broad peaks from 15 to 90 days period (consistent with the low rms velocities and increased time scales found

here). A relatively sharp peak at 15 days is only found in the western cell. This peak is probably due to anticyclonic lee eddies propagating southwestward into the northwest corner of the cell; the peak only appears in the anticyclonic spectrum, and does not appear if segments centered north of  $15^\circ\text{N}$  are excluded from the average. The eastern cell contains significantly more cyclonic energy in the 7.5–32 day band, with a robust peak of unknown origin at 18.5 days and a weaker one at 9.5 days.

The log-log plots of the spectra for the zonal/meridional (Fig. 89) and anticyclonic/cyclonic (Fig. 90) motion generally show a  $-2$  slope within the eddy-containing band in the four northern cells. The slope is well-defined in the north, east and north-east cells; it is masked by the sharp spectral peaks in the island lee. This slope has been found in models of off-resonant oceanic motion driven by white-noise atmospheric forcing [Hasselmann, 1976; Frankignoul and Müller, 1979] and has been observed in both Eulerian and Lagrangian spectra of surface currents [Colin de Verdiere, 1983] (but is not ubiquitous [Freeland *et al.*, 1975; Krauss and Böning, 1987]). In the southern two cells, the slope lies somewhere between  $-1.5$  and  $-2$ ; it is difficult to resolve precisely, due to features such as the energy plateau from 3–6 days in the western cell. The source of this energy is not obvious; low-mode equatorial waves might propagate within the southern boundary of the cell, but empirical evidence suggests they should be inertial or slightly superinertial [Eriksen, 1980].<sup>1</sup>

## 5.5 Discussion

Within the main body of the NEC south of the islands, zonal dispersion of the Lagrangian drifters is dominated by low-frequency meanders. To the north, dispersion is dominated by higher-frequency eddies. Due to the increased rms velocities of the lee

---

<sup>1</sup> Which may account for the enhanced anticyclonic (clockwise) energy at periods less than three days in the southern cells of Fig. 90 [Müller and Siedler, 1976].

eddy field, the apparent eddy diffusivity west of the islands is 1.3–1.6 times greater than to the east. Eddy energy in this region is focused in relatively narrow spectral peaks. Throughout the Hawaiian region, zonal dispersion is considerably greater than meridional dispersion. This result is ubiquitous in open-ocean drifter studies, and has been attributed to topographic effects [Rossby *et al.*, 1975; Freeland *et al.*, 1975], spatial anisotropy of meanders [Colin de Verdiere, 1983; Krauss and Böning, 1987], the  $\beta$ -effect [Haidvogel and Keffer, 1984], and meridional shear in the mean zonal flow [Krauss and Böning, 1987] (these mechanisms are not necessarily independent; for example, planetary vorticity gradients greatly influence the aspect ratio of mean currents).

Is there a kinematic law independently relating the length and time scales of eddies to their velocity variance? This is currently an unresolved question, although two models have been proposed. For SOFAR floats (700 m and 1300 m depth) deployed in MODE and LDE, J. F. Price (in [McWilliams *et al.*, 1983]) concluded that the Lagrangian properties scaled as

$$L_u = T_x u_{rms}, \quad K_{xx} = u_{rms}^2 T_x, \quad T_x \text{ constant.} \quad (5.10)$$

This parameterization also describes eddy scales in the Southern California Current System [Poulain and Niiler, 1989]. However, Krauss and Böning [1987] found the empirical relationship

$$T_u = L_u / u_{rms}, \quad K_{xx} = u_{rms} L_u, \quad L_u \text{ constant} \quad (5.11)$$

in their North Atlantic drifter study, and Brink *et al.* [1991] demonstrated the same relationship in the California Coastal Transition Zone (north of the Poulain and Niiler study region, and closer to the coast). For the Hawaiian data, Fig. 83 shows the predicted eddy diffusivity vs. rms speed according to the two models. Model 5.10 does a far better job explaining the observed meridional diffusivities. However, model 5.11 better explains the zonal diffusivities. The rms error of model 5.10 in explaining the

zonal/meridional diffusivity is 3700, 960 m<sup>2</sup>/s; the error of model 5.11 is 1900, 1900 m<sup>2</sup>/s. Thus, neither model is quantitatively superior, although it should be noted that only model 5.10 is consistent with the combined diffusivities of this study and those of Colain de Verdier [1983] and Poulain and Niiler [1989].

Taylor's Theorem accurately describes the meridional dispersion of drifters for at least the first 120 days. The initial zonal dispersion is also consistent with classical theory; however, it is quite inconsistent at times much larger than the integral time scale. Due to the asymmetry of meridional and zonal length scales of the mean currents, the most likely cause of this is meridional shear in  $\langle u \rangle$  [Krauss and Böning, 1987]. Indeed, for times considerably greater than  $T_u$ , this shear can cause a linear increase in  $x_{rms}$  (see Appendix F).

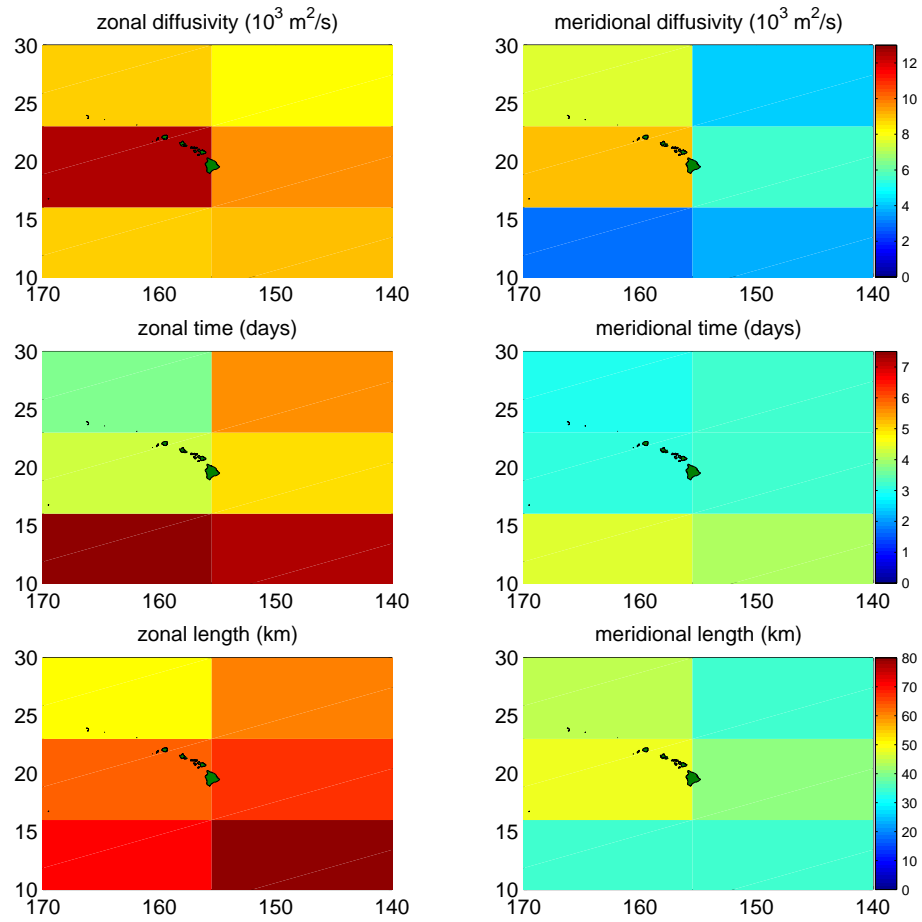


Figure 82: *Top:* Apparent zonal (left) and meridional (right) eddy diffusivities ( $10^3 \text{ m}^2/\text{s}$ ).

*Middle:* Lagrangian zonal (left) and meridional (right) time scales (days).

*Bottom:* Lagrangian zonal (left) and meridional (right) space scales (km).

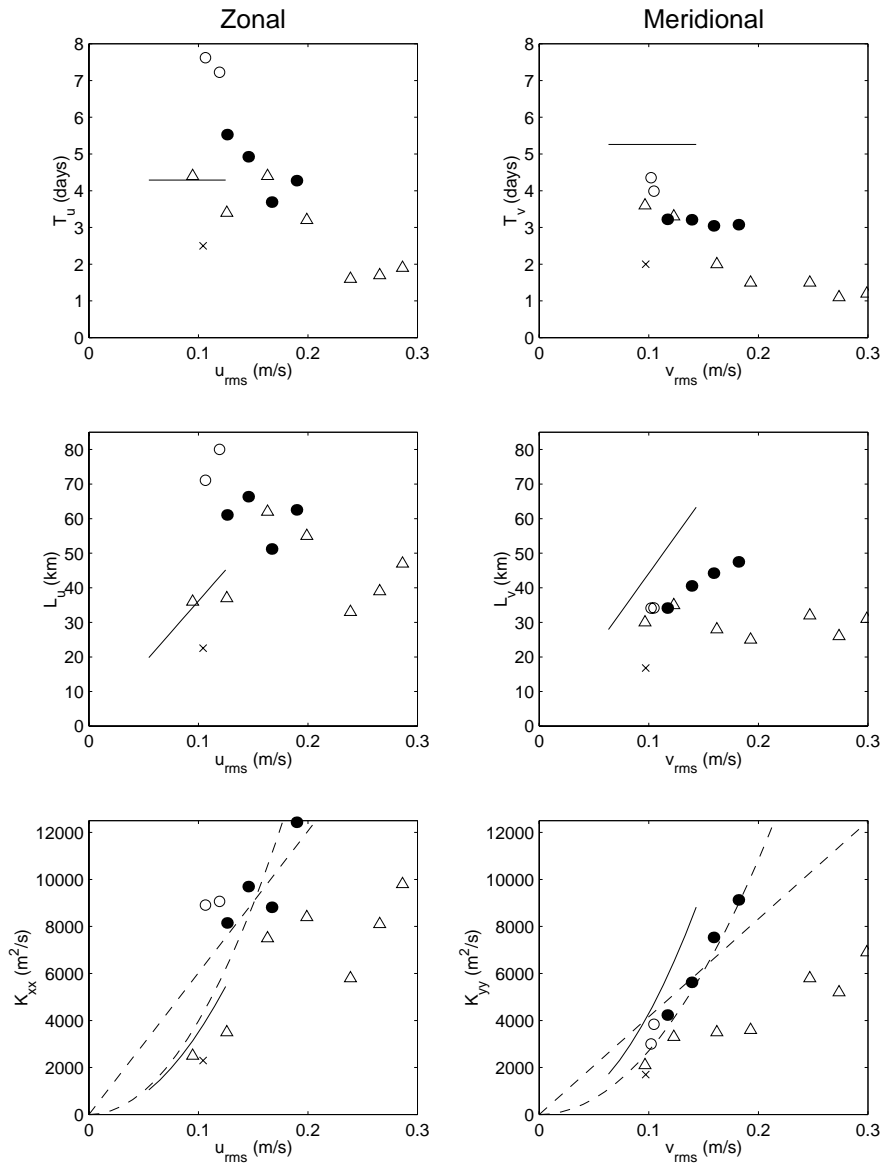


Figure 83: Lagrangian properties as a function of rms speed (left: zonal, right: meridional). Dots are Hawaiian values (open dots for the two southern cells, closed dots for the four northern cells). For comparison, triangles give values from Krauss and Böning [1987], crosses from Colin de Verdiere [1983], and solid lines from Poulain and Niiler [1989].

*Top:* integral time scale (vertical) vs. rms speed (horizontal).

*Middle:* length scale (vertical) vs. rms speed (horizontal).

*Bottom:* apparent eddy diffusivity (vertical) vs. rms speed (horizontal). The parabolic dashed curve is  $u_{rms}^2 \bar{T}_u$ , where  $\bar{T}_u$  is the mean integral time scale of the northern four cells. The straight dashed line is  $u_{rms} \bar{L}_u$ , where  $\bar{L}_u$  is the mean integral length scale of the northern four cells.

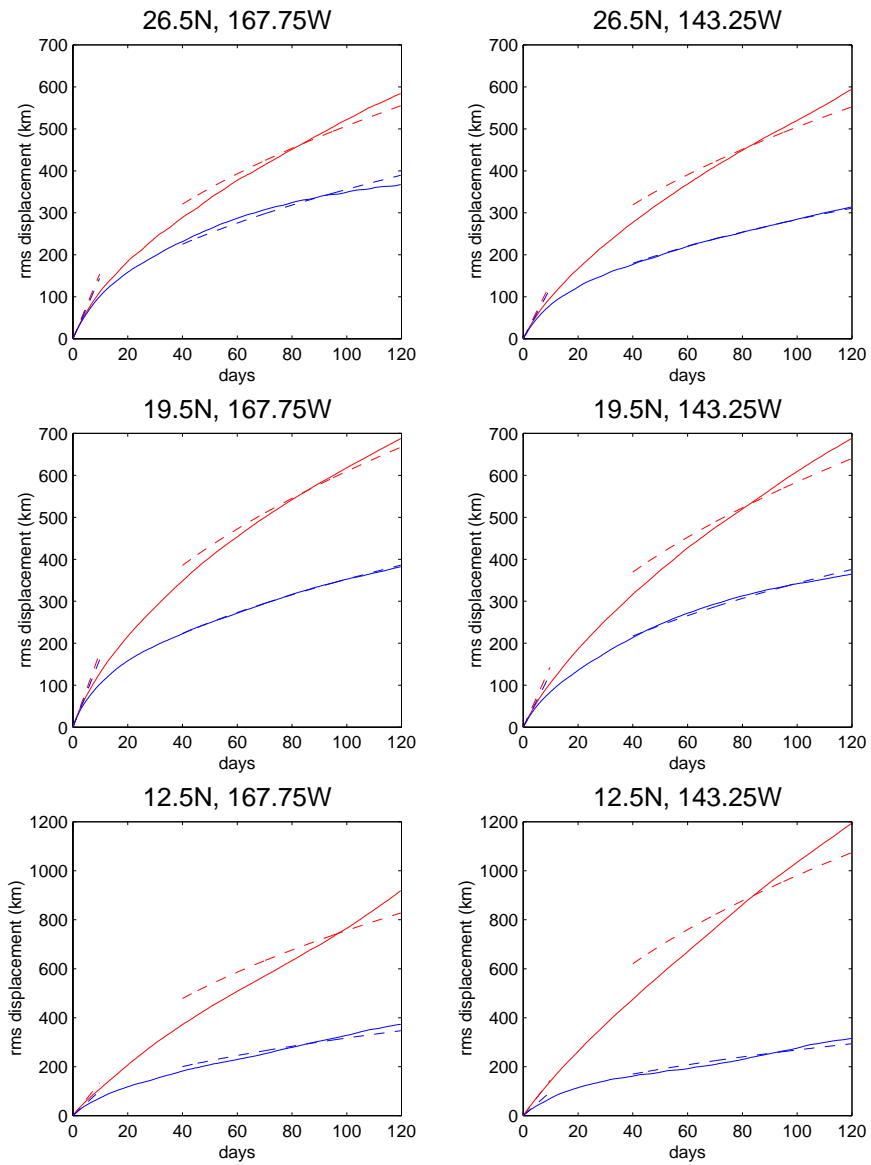


Figure 84: Rms displacement of drifters in the six cells. Titles indicate the cell center coordinates. In all cases, the upper curve is the zonal displacement and the lower curve is the meridional displacement. The dashed curves are parabolas fitted to the final 80 days of displacement.

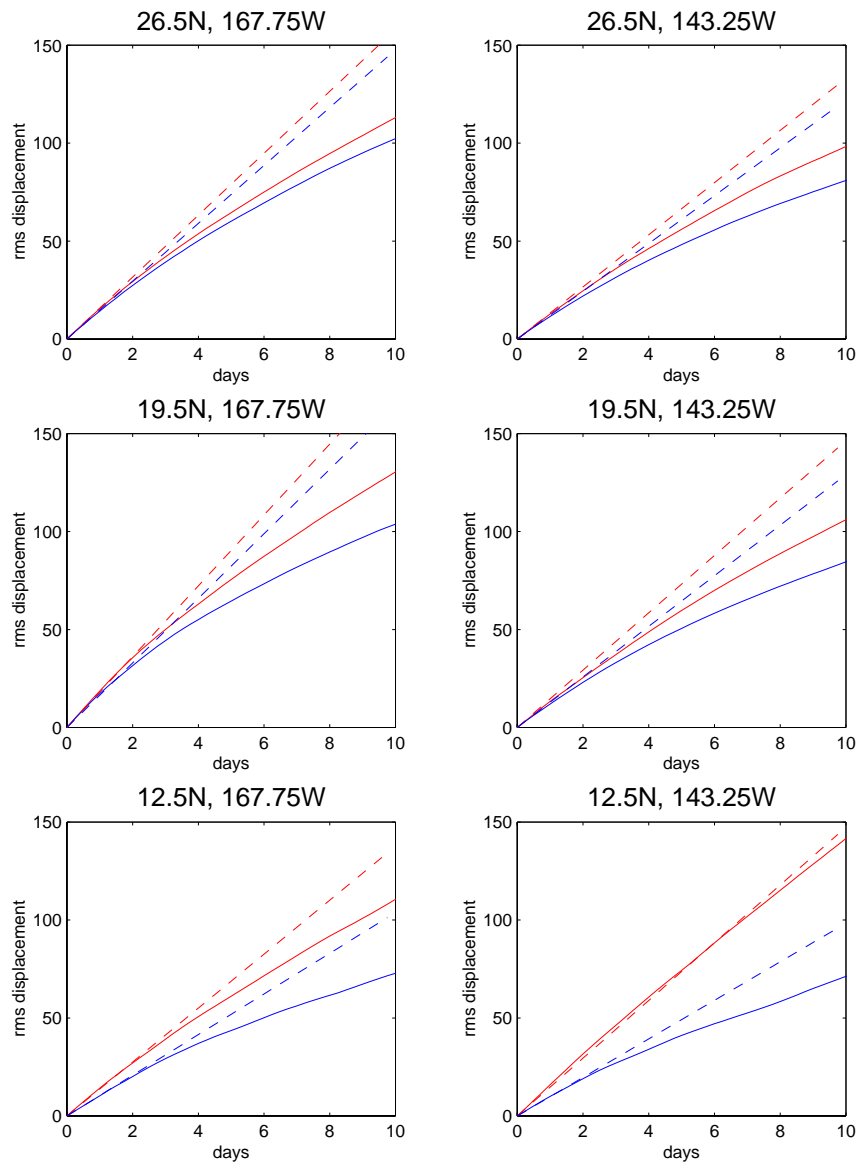


Figure 85: Closeup of Fig. 84 for days 1-10. Dashed lines indicate the short-time behavior predicted by Taylor's Theorem for homogeneous turbulence (top line zonal, bottom line meridional).

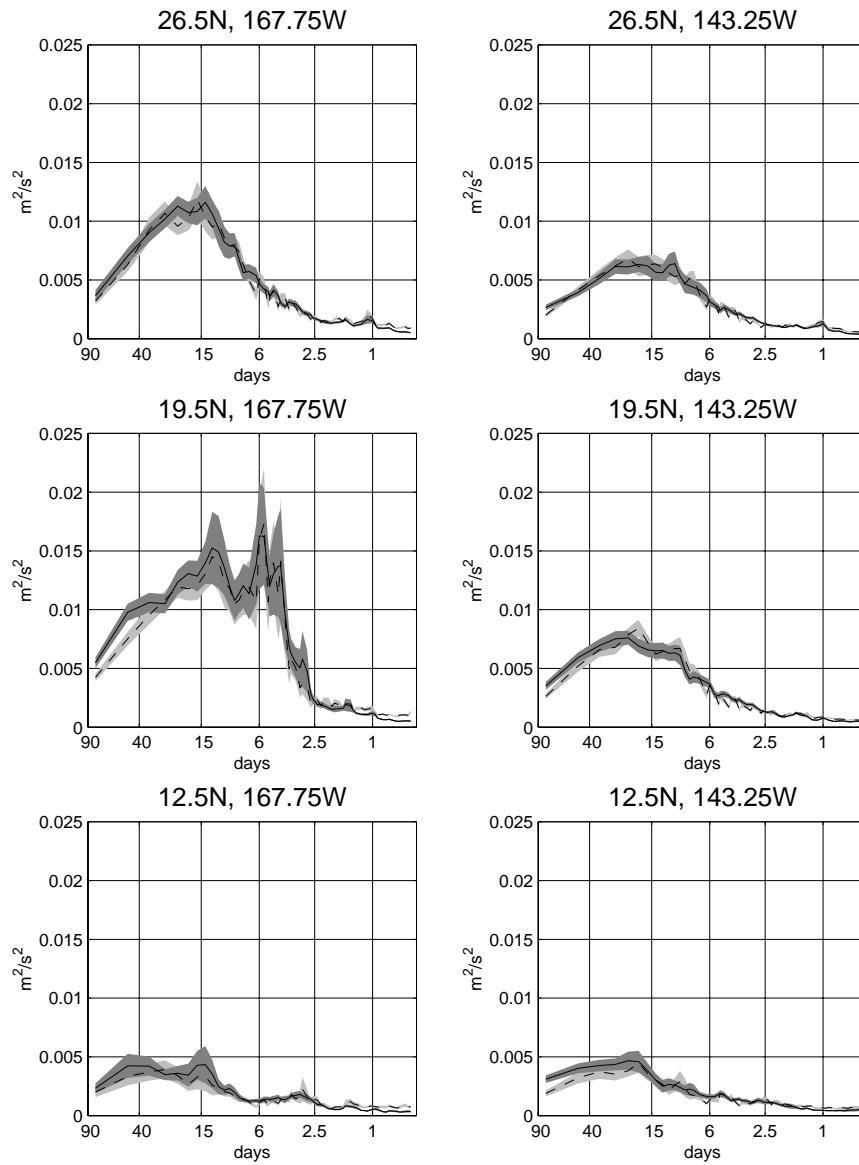


Figure 86: Energy-preserving plots of the Lagrangian spectra of  $u$  (solid) and  $v$  (dashed) in the six cells. The shading indicates the standard error bars.

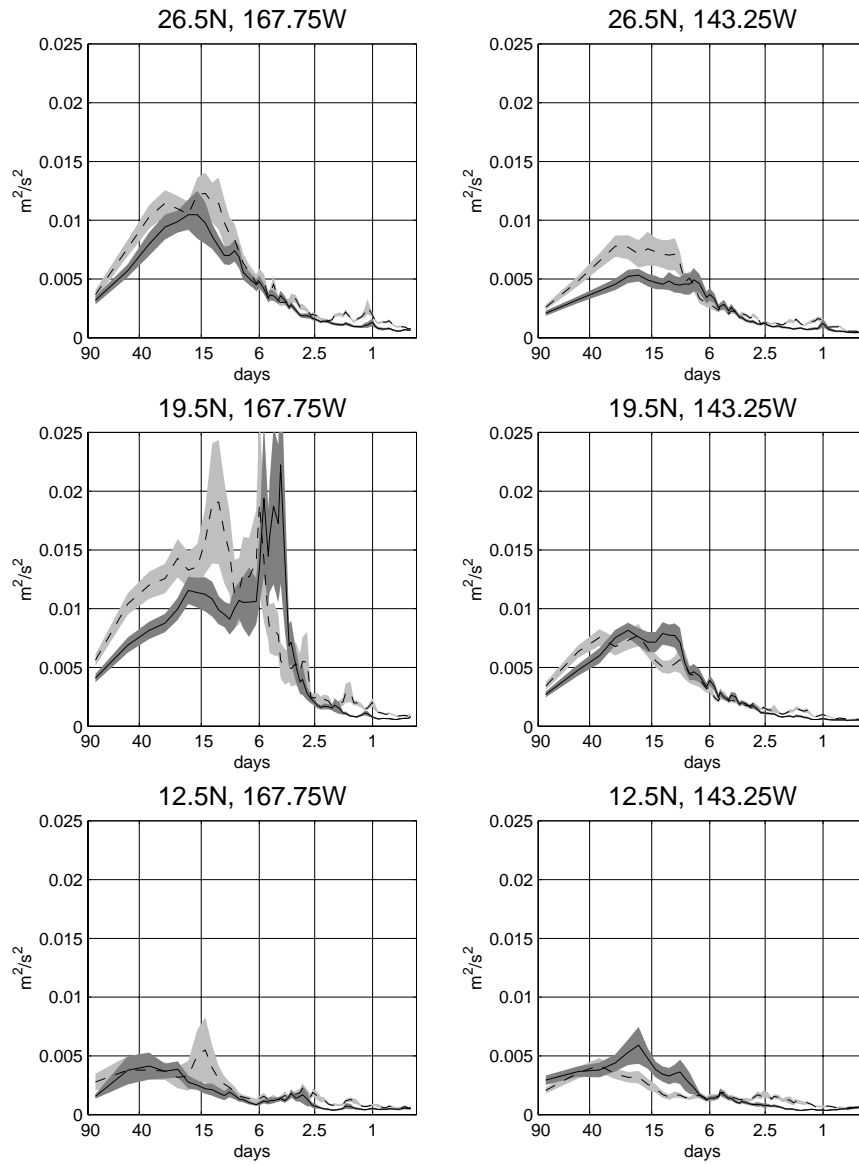


Figure 87: Energy-preserving plots of the Lagrangian cyclonic (solid) and anticyclonic (dashed) spectra in the six cells. The shading indicates the standard error bars.

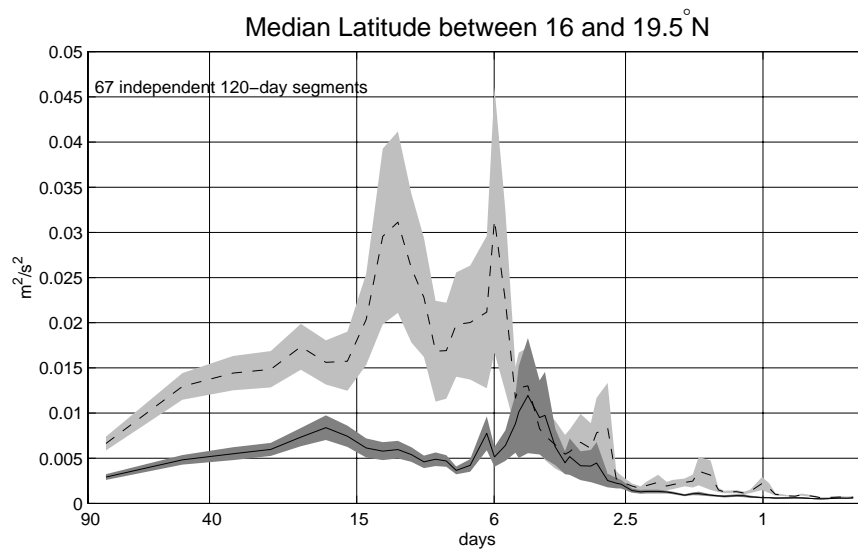
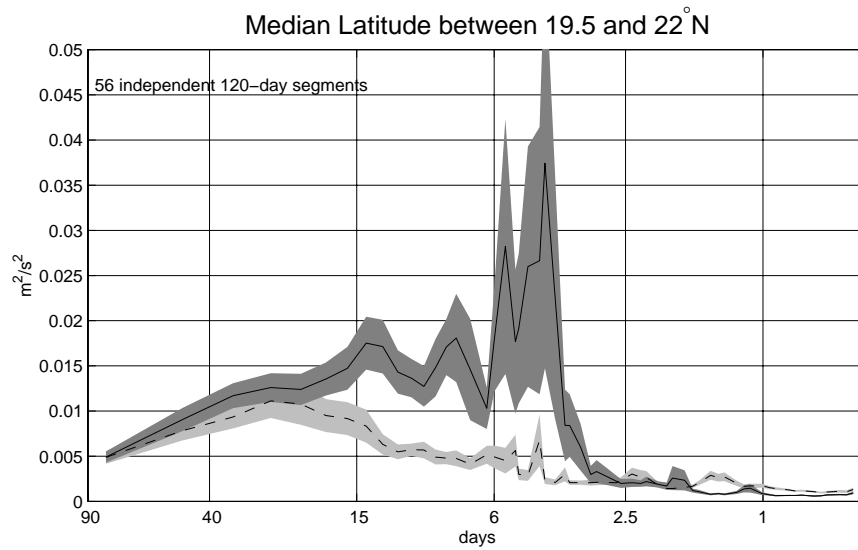


Figure 88: Energy-preserving plots of the Lagrangian cyclonic (solid) and anticyclonic (dashed) spectra west of the Hawaiian Islands. Shading indicates the standard error bars.

*Top:* All 120-day segments between 19.5 and 22°N and west of 156°W. Peaks in the cyclonic spectrum are at 4.3, 5.6, 7.8 and 13.6 days period.

*Bottom:* All 120-day segments between 16 and 19.5°N and west of 156°W. Subinertial peaks in the anticyclonic spectrum are at 3.0, 6.0, 11.6 and 21.6 days period.

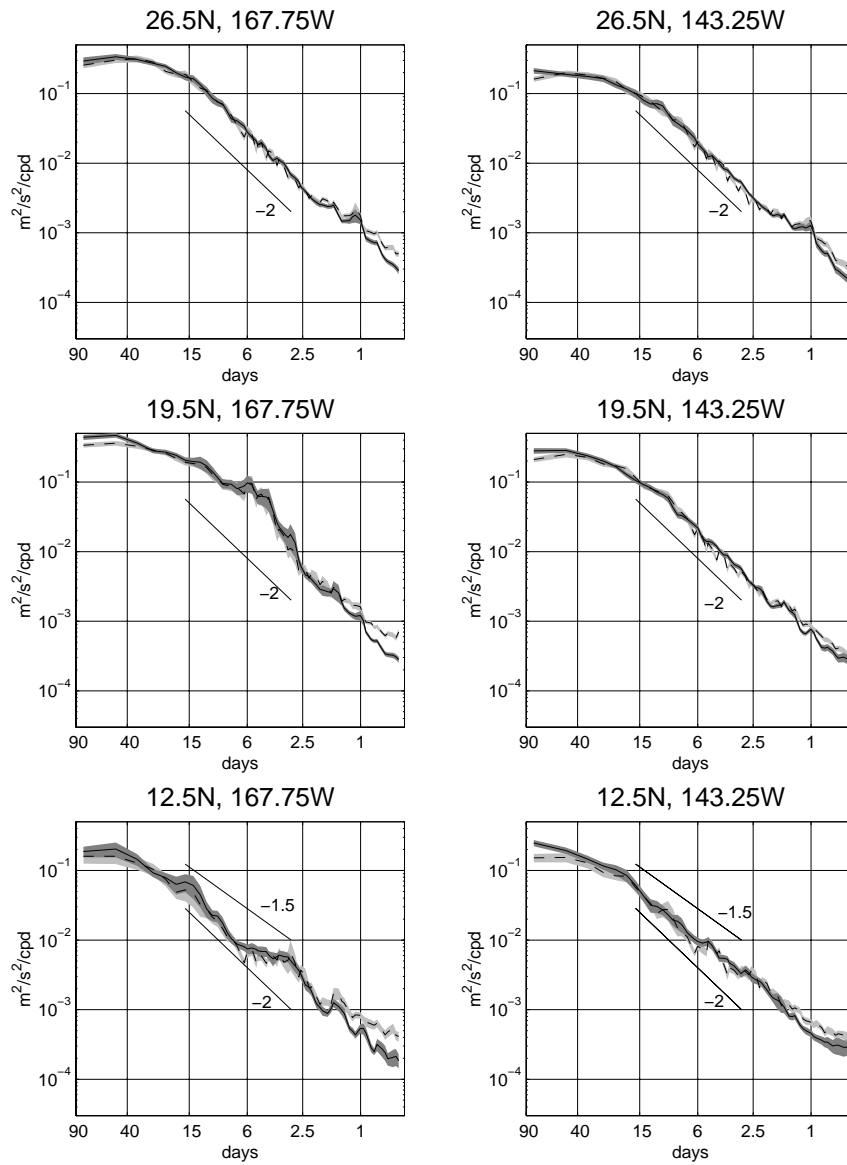


Figure 89: Log-log plots of the Lagrangian spectra of  $u$  (solid) and  $v$  (dashed) in the six cells. The shading indicates the standard error bars.

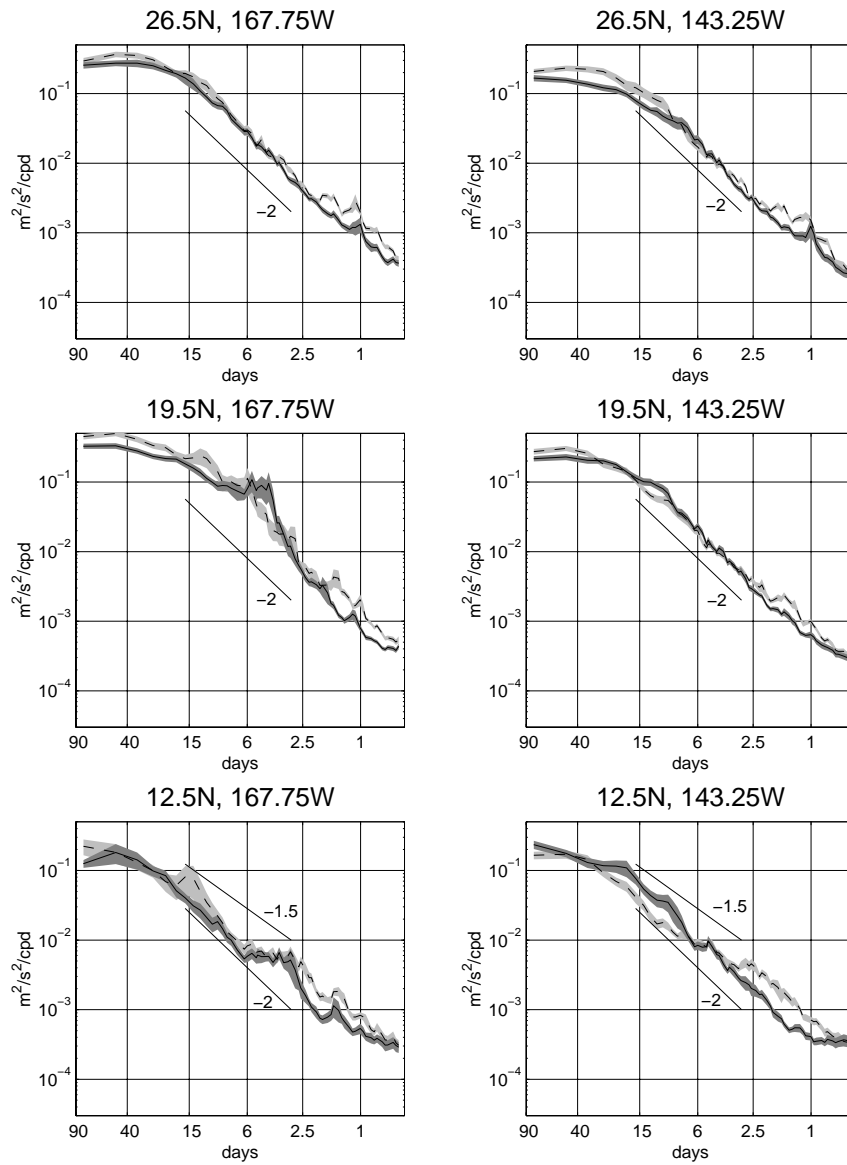


Figure 90: Log-log plots of the Lagrangian cyclonic (solid) and anticyclonic (dashed) spectra in the six cells. The shading indicates the standard error bars.

## CHAPTER 6

### DISCUSSION

The synthesis of drifter trajectories, ADCP measurements, in-situ sea level records, satellite altimetry and AVHRR imagery reveals a fascinating, rich picture of the circulation in the Hawaiian Island region. As portrayed in flowchart form (Fig. 91), the interaction of the island chain with the impinging gyre-scale oceanic and atmospheric circulation creates much finer-scale forcing fields, leading in turn to the formation of lee eddies. West of Keahole Point, Hawai‘i, a cyclonic shear line separates the island’s wind shadow from the trade wind jet funneled through the ‘Alenuihaha Channel. Along this line, Ekman pumping driven by surface divergence creates lee cyclones at intervals of 20 days (for relatively small cyclones) to 50–70 days (for large ones). The northern extent of the westward-flowing North Equatorial Current (NEC) impinges upon Hawai‘i, where it bifurcates into two branches: the North Hawaiian Ridge Current (NHRC), which flows along the northeast side of the archipelago to Kaua‘i, and the NEC jet, which flows along the southeast coast of Hawai‘i, separates from Hawai‘i’s South Point, and rejoins the main body of the NEC. Upon separation, this jet forms a strong anticyclonic shear layer in the ocean; instabilities in this layer may represent a significant source of energy for the generation of the anticyclonic eddies. In addition, as with the cyclones, wind forcing along the southern edge of Hawai‘i’s wind shadow may also play a role in their generation. In several cases noted in this study (and with at least one exception, AC94a), the growth of these anticyclones was limited by centrifugal instability, resulting in half-inertial eddies of core vorticity  $-f$  [Chew and Bushnell, 1990], Rossby number  $-1$ . One of the major new findings of this study is that the anticyclones are generated at a period of 50–70 days and tend to drift along a regular west-southwest

trajectory, consequently forming a train of anticyclones dominating the currents in the southern half of the island wake. This vortex train passes across Johnston Atoll, and individual eddies were tracked to the edge of the study region ( $180^\circ$ ). An extrapolation of the observed spin-down rate suggests that they persist for thousands of kilometers further to the west.

As predicted by Cushman-Roisin *et al.* [1990], the lee eddies propagate westward at a speed close to that of long baroclinic Rossby waves. Variations can be attributed to nonlinear effects, vortex interaction in the immediate lee of Hawai'i and advection of the anticyclones by the North Equatorial Current as they propagate south of  $\sim 18^\circ\text{N}$ . The eddies' meridional drift is due to drag from nonlinear effects [Chassignet and Cushman-Roisin, 1991], which causes cyclonic eddies to drift northward and anticyclonic eddies to drift southward. As a result of these propagation characteristics, the overall field of lee eddies is structured: anticyclones tend to be found south of  $19.5^\circ\text{N}$ , while cyclones are found north of that latitude. Exceptions (such as C96b) may happen when a weak eddy is advected by a stronger one, which overwhelms the drift which the weak eddy would experience in isolation.

As the eddies propagate westward, they grow larger and spin more slowly. In this study, this process was described by a spin-down model in which the eddies entrain surrounding water while conserving their angular momentum. Direct observations of one eddy (AC94b) suggest that an additional mechanism may play a significant role in the downstream evolution of anticyclones. The eddy's core vorticity abruptly decreased at least twice, on a time scale much shorter than the observed spin-down. This rapid change in the eddy's structure may have been caused by a merging with an adjacent eddy in the anticyclonic vortex train. Although there is an extensive literature dealing with vortex merging, surprisingly little attention has been paid to the characteristics of the merged

vortex. This gap has been addressed here, by using basic conservation laws as constraints determining the size and vorticity of a merged vortex, regardless of the specific details of the merging process itself. As a consequence of generation at a fixed core vorticity and downstream merging and spin-down, the Lagrangian periods of lee anticyclones may be “quantized” into bands at 3, 6, 12 (etc.) days. Evidence for this comes from observations of individual eddies (such as AC94b and AC94c) and from the Lagrangian spectra of all drifter trajectories in the island lee (see Fig. 88). While oceanic vortex merging has been observed in random eddy fields [Cresswell, 1982; Tokos *et al.*, 1994], the Hawaiian case has a special geometry reminiscent of the laboratory experiments of Brown and Roshko [1974] and Winant and Browand [1974]: the trajectory of the anticyclone train defines the southern edge of the island wake, so vortex merging within this train (along with the ambient spin-down of the eddies) may determine the growth rate of the oceanic shear between the wake and the NEC to the south.

For the first time, this study has produced a map of the upper-ocean wake of the Hawaiian Islands at the sub-gyre scale (a schematic picture appears as Fig. 92). Earlier studies, such as Wyrтки and Kilonsky [1984], hinted that the wake was complex in its structure; the two-dimensional picture presented here emerges with the synthesis of high spatial resolution current measurements. The wake is composed of two elongated, counter-rotating gyres extending over 1000 km west from Hawai‘i. The mean vorticity of the northern gyre is cyclonic, while the southern gyre is anticyclonic. The gyres are separated by a narrow countercurrent, called the Hawaiian Lee Countercurrent (HLCC), which runs along 19.5°N and reaches a peak mean eastward speed of  $\sim 10$  cm/s. At the northern edge of the cyclonic gyre, a previously undocumented current, the Hawaiian Lee Current (HLC), runs west-northwest along the leeward coasts of the major islands to Kaua‘i and Ni‘ihau. The HLC reaches peak speeds of  $\sim 25$  cm/s, and has year-to-year

variations similar to that of the HLCC. After passing Kaua'i and Ni'ihau, the HLC joins with the NHRC to form a westward HLC/NHRC extension which runs along 22°N to the edge of the study region.

Because of the propagation characteristics described earlier, cyclonic and anticyclonic lee eddies tend to be sorted on either side of 19.5°N. Averaged over time, their vorticity contributes to the vorticity of the wake gyres. The passage of anticyclones along a regular trajectory lifts the mean dynamic height along that path, presumably enhancing the sharpness of the North Equatorial Ridge first noted by Wyrski [1974]. The eddies converge eastward momentum at the latitude of the HLCC, which may be a significant driving mechanism for the countercurrent. The eddy-to-mean energy flux associated with eddy momentum advection reaches  $10\mu\text{W}/\text{m}^3$  in the vicinity of the HLCC, sufficient to spin up the 10 cm/s current from rest in  $\sim 10$  days.

Within the main body of the North Equatorial Current south of the islands, zonal dispersion of the Lagrangian drifters is dominated by low-frequency meanders. Everywhere else, dispersion is dominated by the mesoscale eddies. Passing east to west across the islands, the apparent eddy diffusivity increases by 1.3-1.6 times due to the increased rms velocities of the lee eddy field. Throughout the region, zonal dispersion is considerably greater than meridional dispersion, an ubiquitous result of open-ocean drifter studies which can be attributed to the observed meridional shear in the predominantly zonal currents of the region.

In the course of this study, many questions have been raised which remain to be answered in future investigations. Two subjects particularly lend themselves to study in the near-future are eddy generation and vortex merging:

*Eddy generation* – What is the relative significance of the relevant forcing mechanisms for Hawaiian lee eddies? Two mechanisms, wind forcing and instability in an oceanic

shear flow, have been discussed in this paper. For the cyclones, the only effective source of energy (given the observed spin-up time) is direct wind forcing [Patzert, 1968]. This conclusion is supported by existing direct and indirect current observations in the ‘Alenuihaha Channel, but should be reevaluated pending long-term observations of surface currents away from the immediate coasts of Hawai‘i and Maui. The anticyclones could be generated by both direct wind forcing and shear instabilities in the northern edge of the separated NEC jet. Much more work, both observational and numerical, is needed before their relative significance can be quantified. Perhaps the most promising method to address this issue is to create a high-resolution numerical model of eddy generation in Hawai‘i’s lee, with the wind and current forcing fields characterized by observations presented in this study. Within the framework of this model, the effects of the individual forcing mechanisms could be observed in isolation and while acting together. This study’s observations of lee eddies could serve to validate the model output with all forcing mechanisms present.

*Vortex merging* – What are the relevant conservation laws determining the characteristics of a merged vortex? Two possible merging scenarios (mass conserved and energy conserved) were examined in Appendix E, along with physical justifications for each. Which (if either) is correct? Is filamentation critical in the merging process, as hypothesized by Cushman-Roisin [1989], or does the process more strongly resemble the Rossby adjustment problem? This question could be answered with direct observations of vortex merging, either in the oceanic context or in a tank experiment. For small initial vortices (compared to the internal deformation radius), the two scenarios predict a measurably different merged vortex, allowing them to be tested against the observations.

On a grander scale, do Hawaiian lee anticyclones merge as they propagate down-

stream? Evidence has been presented in this study which suggests they do, but direct observations of the merging process are required to verify that this process is indeed occurring. Ideally, these observations could be made via repeat ADCP and hydrographic transects along the mean anticyclone trajectory. In lieu of this, remote observations such as coastal current-measuring radar could allow a significant advance in our understanding of both eddy generation and evolution in the immediate lee of the Hawaiian Islands.

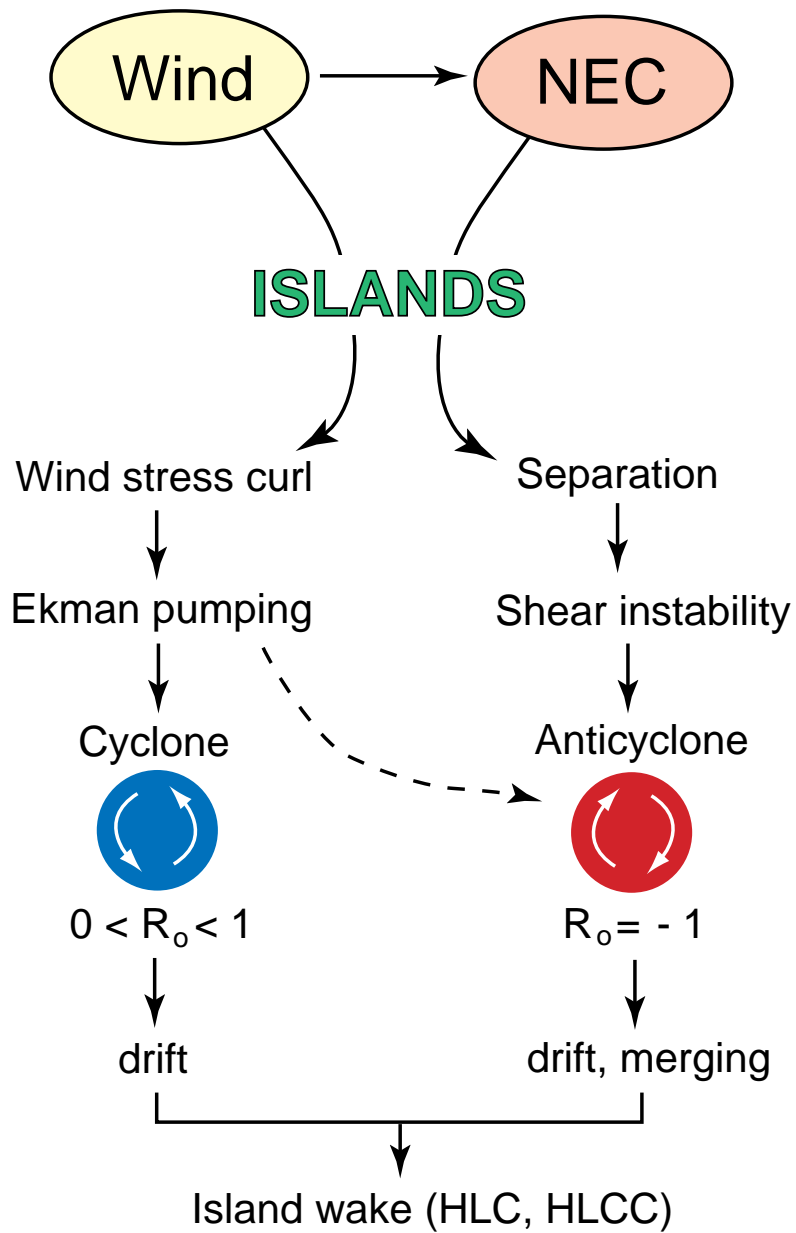


Figure 91: A flowchart of the dynamics impacting mesoscale and sub-gyre-scale circulation in the Hawaiian Island region.

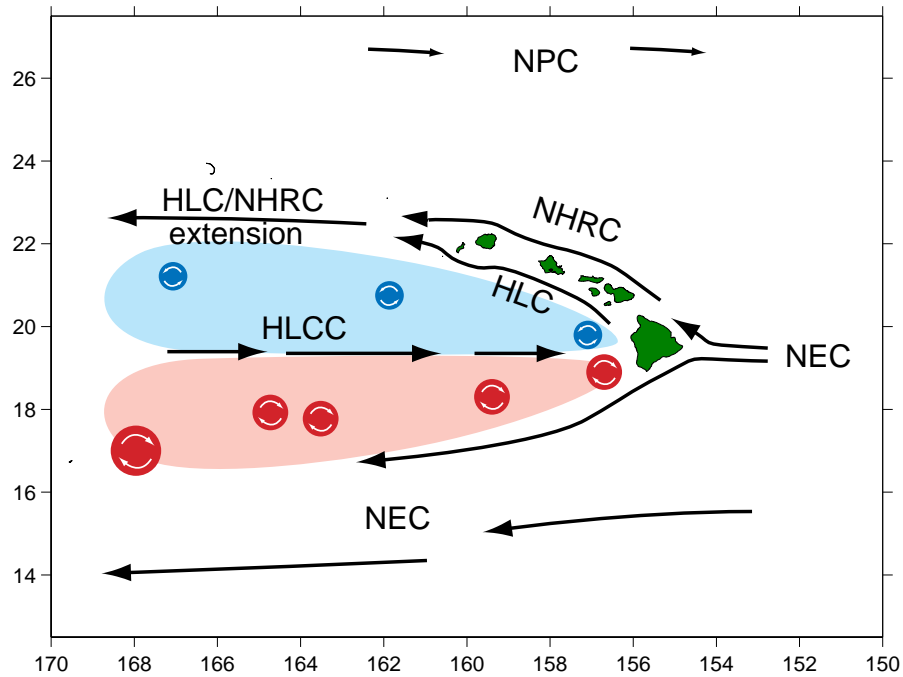


Figure 92: Schematic of the oceanic circulation in the Hawaiian Island region. The major currents are the North Pacific Current (NPC), North Equatorial Current (NEC), North Hawaiian Ridge Current (NHRC), Hawaiian Lee Current (HLC) and Hawaiian Lee Countercurrent (HLCC). Blue/red shading indicates the elongated lee cyclonic/anticyclonic gyres, with shaded circles representing the repeated passage of lee eddies.

## APPENDIX A

### KRIGING

*The interpolation method for the drifter data is described. This appendix originally appeared in Qiu et al. [1997].*

The irregularly-spaced satellite fixes of the drifting buoys were interpolated to 1/4 day intervals using the kriging method [Hansen and Herman, 1989]. In this method, the vector  $\mathbf{x}$  containing irregularly-sampled latitude or longitude fixes (treated independently) is considered to contain a true signal  $\hat{\mathbf{x}}$  plus measurement noise  $\epsilon$ :

$$x(t_i) = x_i = \hat{x}_i + \epsilon_i. \quad (\text{A.1})$$

The noise is assumed to be uncorrelated with itself and  $\hat{\mathbf{x}}$ , with a zero mean and fixed variance  $\langle e^2 \rangle$ :

$$\langle x_i \rangle = \langle \hat{x}_i \rangle, \text{ i.e. } \langle \epsilon_i \rangle = 0, \quad (\text{A.2})$$

$$\langle \epsilon_i \epsilon_j \rangle = \delta_{ij} \langle e^2 \rangle, \quad (\text{A.3})$$

$$\langle \epsilon_i \hat{x}_j \rangle = 0. \quad (\text{A.4})$$

An estimate  $\hat{x}_o^*$  of  $\hat{x}$  at time  $t_o$  is constructed as

$$\hat{x}_o^* = w_i x_i, \quad (\text{A.5})$$

where the repeated index implies a sum over  $i$  from 1 to  $n$  ( $n = 10$  in our interpolations), and the weights  $\mathbf{w}$  are chosen such that

$$\langle \hat{x}_o - \hat{x}_o^* \rangle = 0, \quad (\text{A.6})$$

$$\langle (\hat{x}_o - \hat{x}_o^*)^2 \rangle = \text{minimum}. \quad (\text{A.7})$$

Condition A.6 constrains the weights such that

$$\sum_{i=1}^n w_i = 1, \quad (\text{A.8})$$

while condition A.7 requires minimizing

$$\sigma_k^2 \equiv \langle (\hat{x}_o - \hat{x}_o^*)^2 \rangle = \langle \hat{x}_o^2 \rangle - 2w_i \langle \hat{x}_o \hat{x}_i \rangle + w_i w_j \langle \hat{x}_i \hat{x}_j \rangle + \langle e^2 \rangle w_i w_i. \quad (\text{A.9})$$

To do this, one needs the autocorrelation function  $\langle \hat{x}_i \hat{x}_j \rangle$ . The approach taken by Hansen and Herman (1989) is to assume knowledge of a structure function  $\hat{S}_{ij}$ ,

$$\hat{S}_{ij} = \frac{1}{2} \langle (\hat{x}_i - \hat{x}_j)^2 \rangle, \quad (\text{A.10})$$

$$\langle \hat{x}_i \hat{x}_j \rangle = \frac{1}{2} \langle x_i^2 \rangle + \frac{1}{2} \langle x_j^2 \rangle - S_{ij}. \quad (\text{A.11})$$

In terms of  $S_{ij}$ , the error  $\sigma_k^2$  is

$$\sigma_k^2 = 2w_i \hat{S}_{oi} - w_i w_j \hat{S}_{ij} + \langle e^2 \rangle w_i w_i. \quad (\text{A.12})$$

By minimizing  $\sigma_k^2$  with respect to the weights, one finds that

$$w_j \hat{S}_{ij} - w_i \langle e^2 \rangle + \lambda = \hat{S}_{oi} \quad (\text{A.13})$$

where  $\lambda$  is an unknown Lagrange multiplier introduced to incorporate constraint A.6.

This result may be multiplied by  $\sum_i w_i (=1)$  to find

$$\sigma_k^2 = w_i \hat{S}_{oi} + \lambda. \quad (\text{A.14})$$

Equation A.13 consists of  $n$  equations and  $n + 1$  unknowns (counting  $\lambda$ ). One may eliminate  $\lambda$  from this set of equations by subtracting each  $i^{\text{th}}$  equation from the  $(i - 1)^{\text{th}}$  equation. With inclusion of condition A.6, one is left with a set of  $n$  equations and  $n$  unknowns, and may solve for the interpolation weights.

After applying this interpolation technique to 6.5 years of drifter data from the tropical Pacific Ocean, Hansen and Poulain [1996] derived generic structure functions for the tropical Pacific Ocean. They used the fractional Brownian motion function

$$\hat{S}_{ij} = \alpha |t_i - t_j|^\beta, \quad (\text{A.15})$$

for which  $\beta = 1$  models pure Brownian motion and  $\beta = 2$  results in strictly linear motion. For the north tropical Pacific Ocean, Hansen and Poulain found optimal values for  $\alpha$  and  $\beta$  of

$$10^2\alpha = 1.152(^{\circ})^2, \beta = 1.604 \quad (\text{latitude}),$$

$$10^2\alpha = 1.912(^{\circ})^2, \beta = 1.846 \quad (\text{longitude}).$$

We used these first-guess values for  $\alpha$  and  $\beta$ , and adjusted them in a second iterative step which minimized the variance between observed and interpolated points [Hansen and Poulain, 1996]. Values for  $\langle e^2 \rangle$  were estimated from fixes of a stationary (grounded) drifter, as described in the text.

## APPENDIX B

### MODELS FOR THE RADIAL STRUCTURE OF REDUCED GRAVITY EDDIES

*Analytical models for the structure of an eddy are described, including a generalized core/shell model developed for this study*

#### B.1 Solid-body eddy

A solid-body eddy has an azimuthal velocity  $v(r) = \frac{\zeta}{2}r$  extending to radius  $r = r_o$ , where  $\zeta$  is the constant vorticity of the eddy.<sup>1</sup> The angular speed of the eddy is  $\omega = \zeta/2$ , and the rotational period is  $T = 2\pi/\omega$ . By imposing the boundary condition  $h = 0$  at  $r = r_o$ , cyclogeostrophy (3.3) may be integrated to yield

$$h(r) = -\frac{\zeta}{2} \left( f + \frac{\zeta}{2} \right) \frac{r_o^2 - r^2}{2g'}, \quad r \leq r_o. \quad (\text{B.1})$$

The total change in upper layer thickness from the eddy edge to the eddy center is  $h(r = 0)$ , which can be written as

$$\frac{h(r = 0)}{r_o} = -\frac{r_o H_1}{R_d^2} \frac{\zeta}{2f} \left( 1 + \frac{\zeta}{2f} \right), \quad (\text{B.2})$$

where  $R_d = \sqrt{g'H_1}/f$  is the Rossby deformation radius.

In the limit  $H_1 \rightarrow 0$ , the eddy becomes a lens-shaped bulge of light water surrounded by slightly denser water. This model is frequently invoked to describe warm-core rings (c.f. [Gill and Griffiths, 1981; Nof, 1981]). Lens-shaped eddies cannot be cyclonic, because in the absence of Coriolis forces the fluid would relax radially outward. This is also demonstrated by an inspection of (B.2), which gives geometrically-meaningful solutions ( $h > 0$ ) only if  $-2f < \zeta < 0$ .

When  $H_1 > 0$ , the eddy can be either cyclonic or anticyclonic. The requirement that the total thickness  $H_1 + h$  be greater than zero requires

$$2\frac{R_d^2}{r_o^2} > \frac{\zeta}{2f} \left( 1 + \frac{\zeta}{2f} \right). \quad (\text{B.3})$$

---

<sup>1</sup>In azimuthal coordinates, the vorticity is given by  $\zeta = \frac{1}{r}\partial_r (r\partial_r v)$ .

## B.2 Vortices with finite-shear edges

The solid-body cylindrical vortex model is a simple description of both anticyclonic and cyclonic eddies, but it has a major physical shortcoming. Once  $H_1 > 0$ , the eddy has an infinite-shear edge separating vortex fluid from surrounding upper-layer fluid of identical density. Without buoyancy forces to maintain the velocity discontinuity, one would expect turbulent mixing to rapidly smear the edge vorticity into a finite shell surrounding the solid-body core. Within this shell,  $v(r)$  diminishes with increasing  $r$ .

### B.2.1 Gaussian eddies

If the interface displacement  $h$  is modeled as a Gaussian,

$$h = h(0)e^{-r^2/2l^2}, \quad (\text{B.4})$$

then cyclogeostrophy (3.3) gives an azimuthal speed

$$v = \frac{fr}{2} \left( -1 \pm \sqrt{1 - 4 \frac{g'h(0)}{f^2 l^2} e^{-r^2/2l^2}} \right) \quad (\text{B.5})$$

[Patzert, 1968]. At small  $r$  (specifically,  $\exp(-r^2/2l^2) \approx 1$ ), the eddy is in solid-body rotation with vorticity  $\zeta$ ,

$$\zeta = \left( -1 \pm \sqrt{1 - 4 \frac{g'h(0)}{f^2 l^2}} \right) f. \quad (\text{B.6})$$

Of the two solutions, only the  $+$ -root gives  $v \rightarrow 0$  as  $r \rightarrow \infty$ , indicating that  $\zeta \geq -f$ . For quasigeostrophic eddies, the second term in the square root is much less than one; a Taylor's series expansion to second order in this term gives the velocity structure

$$v \approx -\frac{g'h(0)}{fl^2} r e^{-r^2/2l^2}. \quad (\text{B.7})$$

Beyond the inner solid-body core, the azimuthal speed smoothly peaks at  $r \sim l$ ; past this, it decays rapidly due to the exponential term.

### B.2.2 Rankine eddies

The Rankine vortex is another commonly-used model for the azimuthal velocity structure. It consists of a solid-body core surrounded by an irrotational shell:

$$v = \frac{\zeta}{2} \begin{cases} r, & r \leq r_o, \\ r_o^2/r, & r > r_o. \end{cases} \quad (\text{B.8})$$

Griffiths and Hopfinger [1987]) noted that vortices in their laboratory experiments were well-described by this structure out to  $r \sim 4r_o$ .

The Rankine model remains analytically simple even for strongly nonlinear vortices. However, because the azimuthal speed drops off as  $1/r$ , Rankine vortices have infinite energy on an infinite domain. In a finite oceanic eddy, azimuthal velocity must drop off more rapidly than  $1/r$ , although it does not necessarily decay as rapidly as in the Gaussian model.

### B.2.3 The core/shell eddy model

To combine the strengths of the Gaussian and Rankine model, a core/shell model was developed for this study. The azimuthal velocity is described by

$$v(r) = \frac{\zeta}{2} \begin{cases} r, & r \leq r_i, \\ -\left(\frac{r_i^2}{r_o^2 - r_i^2}\right) \left(r - \frac{r_o^2}{r}\right), & r_i < r \leq r_o, \\ 0, & r_o < r. \end{cases} \quad (\text{B.9})$$

The solid-body core of vorticity  $\zeta$  extends to  $r = r_i$ . Beyond this, a shell of constant vorticity

$$\zeta_o = -\zeta \frac{r_i^2}{r_o^2 - r_i^2} \quad (\text{B.10})$$

extends to radius  $r = r_o$ . In the limit  $r_o \rightarrow \infty$ , the shell vorticity vanishes and the model has a Rankine velocity profile. For  $r_o = \sqrt{2}r_i$ , the core and shell have opposite-signed vorticity of equal magnitude. The shell vorticity is greater in magnitude if  $r_o < \sqrt{2}r_i$ , and in the limit  $r_o \rightarrow r_i$  the velocity profile reverts to the solid-body model with an

infinite shear edge. The three independent parameters  $\zeta$ ,  $r_i$ , and  $r_o$  fully determine the eddy structure in this model. The added degree of freedom <sup>2</sup> allows the outer structure of the eddy to be fit to the data, instead of having it be determined by the vortex model and the observed core size. This flexibility is physically justified by the observed variations in laboratory vortex structure: as discussed by Kloosterziel and van Heijst [1991],

It was found in the experiments [of cyclonic eddy generation] that the vorticity distribution depends to some degree on the generation technique applied. For example, in some cases the outer ring of negative vorticity turned out to be rather narrow, with the negative vorticity having a relatively large magnitude. In other cases this ring appeared to be much wider, and the negative vorticity magnitude correspondingly weaker. Similar remarks apply to anticyclonic vortices, but with ‘cyclonic’ everywhere replaced by ‘anticyclonic,’ ‘negative’ by ‘positive,’ and so on.

As discussed in the section on centrifugal instability, the stability of cyclonic vortices is strongly dependent on the ratio of shell to core vorticity.

---

<sup>2</sup>Both the Gaussian and Rankine structures are determined by two parameters.

## APPENDIX C

### OBSERVATIONS OF LEE EDDIES, 1994–1996

*Drifter, ADCP, AVHRR and altimetric observations of Hawaiian lee eddies from mid-1994 to 1996 are presented.*

#### C.1 August and October 1994 cruises

On 15 August 1994, the R/V *Townsend Cromwell* left Honolulu, O‘ahu for cruise TC9407. A day later, it passed near the south point of Hawai‘i. Shipboard ADCP recorded the NEC jet (Fig. 25) and an anticyclonic eddy, hereby dubbed AC94c. A nearly concurrent AVHRR image (Fig 24) shows the clockwise rotation in the core of the eddy.

The least-squares analysis of the ADCP currents suggest that AC94c was centered at  $18.991^{\circ}\text{N}$ ,  $156.767^{\circ}\text{W}$ , 90 km off the coast of Hawai‘i (Fig. 93). Unfortunately, the ship did not pass close enough to the eddy to record azimuthal speed within its core. The available measurements show the core must have been less than 60 km in radius, with peak speeds greater than 80 cm/s. If it is assumed that the innermost measurements were on the edge of a solid-body core, it had a vorticity of  $-0.6f$ . Because the azimuthal speed may have climbed above 80 cm/s inside of 60 km, this is a lower estimate of the core vorticity’s magnitude. Azimuthal speed dropped off considerably more rapidly than  $1/r$  at 65–90 km from the eddy center; the eddy’s outer structure may have been strongly affected by its proximity to Hawai‘i, and could be reasonably well described by a shell of constant vorticity  $0.3f$ .

The *Townsend Cromwell* returned to O‘ahu in early September, passing near an anticyclonic eddy on 8 September 1994 (Fig. 94). The eddy was centered at  $18.5^{\circ}\text{N}$ ,  $157.25^{\circ}\text{W}$ . It is likely that this was again AC94c, which had propagated WSW at 3.5 cm/s. The ship came within 40 km of the eddy center. The profile of azimuthal

speed showed that the eddy may have had a core of radius  $\sim 50$  km, with a peak speed of 1.2 m/s and a vorticity of  $\sim -4.4 \times 10^{-5} \text{ s}^{-1}$  ( $-0.96f$ , rotational period 3.3 days). The transport through the vertical cross-section at the bottom of Fig. 94 is 12.5 Sv.

During TC9407, 13 drifters were deployed in Hawai'i's lee (Fig. 95). Five of the drifters began circling a cyclonic lee eddy (C94a), five more traveled south, advected between C94a and AC94c, and the remaining three passed north towards the Kaiwi Channel.

The five drifters captured by C94a completed 2–3 orbits before leaving it (Fig. 96); several were then captured by AC94c. The orbits around C94a reveal an elliptical vortex with a solid-body core of vorticity  $1.4 \times 10^{-5} \text{ s}^{-1}$  ( $0.29f$ , rotational period 10.4 days). A least-squares fit of the core/shell model's sea surface displacement was performed on the altimetry in the frame of reference moving with C94a, and showed a core of radius 90 km, vorticity  $1.3 \times 10^{-5} \text{ s}^{-1}$  with peak speeds of 60 cm/s. All but one of the drifter orbits were consistent with this structure; the outermost drifter had a radius of 76.5 km, but a longer period (14.2 days).

On 4 October 1994, the *Cromwell* traveled SW from O'ahu to equatorial waters on cruise TC9410. Nine additional drifters were deployed during this cruise. The *Cromwell* passed within 75 km of the center of an anticyclonic eddy at  $17.9^\circ\text{N}$ ,  $160.3^\circ\text{W}$ . As shown in Fig. 95, it seems reasonable to identify this eddy as (yet again) AC94c: a sea level anomaly high propagates WSW from the 8 September eddy center to the 4 October one; this is also visible in the  $18^\circ$  to  $19^\circ\text{N}$  band-averaged sea level anomaly (Fig. 30), in which a ridge smoothly connects the 8 September and 4 October eddy center longitudes. From 8 September to 4 October, AC94c had traveled westward at a mean speed of 14.4 cm/s, southward at 2.9 cm/s, anomalously rapid compared to other anticyclones at this latitude.

The ADCP profile (Fig. 97) shows that the ship did not penetrate the core of the eddy. To the north of the eddy center, the azimuthal speed decayed with distance more rapidly than irrotationally; to a distance of  $\sim 130$  km, the decay could be described by a shell of vorticity  $0.12f$ . To the south, the velocity dropped off similarly within  $\sim 110$  km, then nearly leveled out (perhaps due to the superposition of the NEC). The azimuthal speed was 76 cm/s at the closest approach radius of 72 km, so the vorticity in the core must have been greater in magnitude than  $-2.1 \times 10^{-5} \text{ s}^{-1}$  ( $-0.54f$ , rotational period 6.0 days). Drifters entrained within the eddy (described below) indicated a core of  $\sim 65$  km in radius; thus, this vorticity estimate may have been close to the actual core vorticity of the eddy. If so, the rotational period of the core roughly doubled between the 8 September and 4 October ADCP transects. The azimuthal transport through the vertical profile at the bottom of Fig. 97 is 10.8 Sv.

The trajectories of many drifters were strongly influenced by the presence of AC94c, marking its passage from  $160.5^\circ\text{W}$  to  $170.8^\circ\text{W}$  (Figs. 98, 99). Three drifters were deployed within the eddy and spent over 100 days orbiting it. Fig. 100 shows the rotational radii and periods of their orbits. Two of the drifters completed several orbits of 50–65 km and periods of  $\sim 6$  days, with a linearly-increasing speed vs. radius suggesting they were in the solid-body core of the eddy. One of the drifters moved to a radius of  $\sim 75$  km in late October, and completed six loops with a mean period of 12.4 days. It then made one very small orbit (40 km radius, 8.5 day period) before leaving AC94c in January 1995. A second drifter completed six orbits of mean radius 58.6 km, period 5.6 days, then slowly increased in both period and radius until its final orbit was 88.3 km, 16 days. It left the eddy at the end of December 1995. The third drifter stayed within the core until early December, making 10 loops of mean radius 56.6 km, period 6.19 days. It then jumped to three large ( $\sim 70$  km) orbits of period 12.9 days

before joining the first on a final loop of radius 33.4 km, period 8.1 days and leaving the eddy. AC94c propagated close to the mean anticyclone path at speeds well-described by (3.13, 3.14). It passed across Johnston Atoll on 10 January 1995, lifting sea level there by  $\sim 30$  cm (Fig. 32).

Fig. 101 shows the ERS-1 and TOPEX passes in the frame of reference moving with AC94c. Least-squares fits of the core/shell model give the values presented in Table C.1. The inferred core radius agrees reasonably well with the direct drifter observations (Fig. 100), but the fit gives a lower core vorticity.

Table C.1: Structure of AC94c from altimetry.

Dates	$r_i$ (km)	$r_o$ (km)	$\zeta$ ( $10^{-5} \text{ s}^{-1}$ )	$\zeta/f$	$4 \pi/\zeta$ (days)
8-31 Oct. 1994	61.4	416.0	-1.99	-0.44	7.3
1 Nov.-15 Dec. 1994	61.4	536.0	-2.03	-0.45	7.2
16 Dec. 1994-30 Jan. 1995	56.4	389.0	-1.94	-0.43	7.5

Anticyclone AC94d trailed AC94c, and was a particularly strong feature in the altimetry (Figs. 98, 99). AC94d forming off the south point of Hawai'i in early October (Fig. 22), approximately 56 days after AC94c had formed. AVHRR imagery on 9 October (Fig. 102) shows a jet of cold water passing the south point, and by 22 October the warm pool may have been rotating anticyclonically in the immediate lee of Hawai'i (unfortunately, this was somewhat obscured by clouds). The altimetry shows that AC94d had moved out of the immediate lee of the island by 14 November. Its influence on drifter trajectories can be seen in the subplots for 11/14/94, 11/24/94, 12/14/94, 2/2/95 and 2/12/95 of Figs. 98, 99. AC94d crossed Johnston Atoll on 20 March 1995, creating a pronounced sea level rise there (see Fig. 32). It also captured a drifter for a large half-orbit from 19 May–8 June 1995 (not shown).

Anticyclone AC94e can be seen in the altimetry NW of AC94b on 25 September 1994 (Fig. 98); it propagated westward at 6.75 cm/s, and AC94b passed it to the south

in December 1994. Another anticyclone, AC94f, was also well north of the mean path of anticyclones. It may have propagated into the study region from the north in early November. In mid-November, it captured a drifter; a second one joined it in early January 1995. AC94f propagated westward along  $20^{\circ}\text{N}$  at  $8.4\text{ cm/s}$ . Both AC94e and AC94f were near the latitude of Wake Island; if their position is extrapolated from their last appearance in the altimetry (at  $180^{\circ}$ ) to Wake's longitude, and their westward speed is assumed to have remained constant, they crossed Wake Island on 9 October 1995 and 1 November 1995.

Cyclone C94b was born in the lee of Hawai'i sometime before 22 October. A sequence of AVHRR images (Fig. 102) show that the eddy moved south along the west coast of Hawai'i for over half a month. It then began propagating WNW. On 12 December 1994, a drifter began orbiting C94b at  $20.3^{\circ}\text{N}$ ,  $158.1^{\circ}\text{W}$  (due south of O'ahu) (Fig. 103). The drifter made 8 complete orbits before leaving the eddy; the first four, of radii 32–42 km, all had periods of  $\sim 10.0$  days, suggesting a solid-body core of vorticity  $1.45 \times 10^{-5}\text{ s}^{-1}$  ( $0.29f$ ). The drifter jumped to larger orbits in February 1995, and another drifter joined it for one large and anomalously fast orbit. Eddy C94b moved WNW for 30 days at an impressive  $31.1\text{ cm/s}$ , then in early February 1995 it slowed and turned to the SE, propagating in that direction at  $10.8\text{ cm/s}$  for the remaining 50 days that the drifters tracked it.

Anticyclone AC94g formed in early December 1994 (see Fig. 22), southeast of C94b and 56 days after AC94d. The eddy can be seen trailing AC94d to at least  $175^{\circ}\text{W}$  in the altimetry (Fig. 30). Although it did not capture any drifters, AC94g is noteworthy because of its unusual prominence in several AVHRR images. The young eddy can be seen on 12 December (Fig. 102) in the immediate lee of Hawai'i. On 26 December, AC94g was a spectacular feature in the SST image. It is nearly circular, with a radius of

$\sim 100$  km. The eddy had swept away most of Hawai‘i’s warm pool, and remained visible through December due to the anticyclonic advection of this water. The altimetry shows that AC94g’s propagation was described fairly well by (3.13, 3.14); it passed C94b in early February 1995,<sup>1</sup> and crossed Johnston Atoll in late August/early September 1995. The Johnston sea level record has a  $\sim 20$  cm/s peak concurrent with the eddy’s passage (Fig. 32).

Another significant feature in the altimetry (Figs. 98, 99) and *in-situ* sea level at Johnston Atoll (Fig. 32) are the deep lows between and to the south of anticyclones AC94b, AC94c and AC94d. These lows drift WNW, with approximately the same westward speed as the anticyclones. The drifters clustered around the lee anticyclones, did not enter the lows for any appreciable span of time. These lows may be cyclonic eddies generated east of the Hawaiian Islands, which have been occasionally seen in hydrographic transects of the North Equatorial Current south of the latitude of Hawai‘i [Wyrтки, 1982].

## C.2 July–August 1995 cruise

On 27 July–5 August 1995, the R/V *Townsend Cromwell* conducted cruise TC9503 between Honolulu, O‘ahu and the lee of Hawai‘i (Fig. 104). Eight WOCE drifters were deployed on this cruise, and shipboard ADCP recorded upper-ocean currents.

While passing south of the Kaiwi Channel and SW of Moloka‘i, the *Cromwell* crossed a relatively small cyclone (eddy C95a; Fig. 105). The eddy had an inner core of radius  $\sim 30$  km, with an edge speed of  $\sim 65$  cm/s and a vorticity of  $4.4 \times 10^{-5} \text{ s}^{-1}$  ( $0.85 f$ , rotational period 3.3 days). Outside the core, the azimuthal speed dropped off with an anticyclonic vorticity of  $O(-1 \times 10^{-5} \text{ s}^{-1})$  ( $-0.2f$ ). C95a was shallow; core speeds

---

<sup>1</sup>It was during this time that C94b turned from WNW to SE propagation. This suggests that it was advected off the mean propagation path of lee cyclones by AC94g.

dropped rapidly below 40 m. The total transport through the vertical profile in Fig. 105 is 1.51 Sv. AVHRR images (Fig. 106) show that C95a formed south of the Kaiwi Channel in early July. By 29 July, it was a well-defined elliptical mass of cold water; the ADCP transect on 29 July passed across its semiminor axis, which was approximately half the length of its semimajor axis. The two drifters deployed south of O‘ahu completed one circuit around C95a before leaving it and becoming entrained in C95b.

Cyclone C95b formed shortly before 8 July in the immediate lee of Hawai‘i. AVHRR imagery from 6 July (not shown) show an undisturbed warm pool, but by 8 July cold water off Keahole Point had begun rotating cyclonically (Fig. 106). Over the next ten days, C95b drifted SW, but then turned to the east and propagated directly into the west coast of Hawai‘i. This eastward drift may have been advection from AC95a (to be discussed momentarily), which was south of C95b.<sup>2</sup> It was pressed tightly against the island during TC9503. The *Cromwell* made several back-and-forth transects through the eddy’s core, and deployed five drifters in it; the resulting data showed that C95b was comparable in size to the two largest cyclones presented in Patzert [1968] (c.f. his Figs. 29 and 59). From 29 July to 7 August, C95b is visible in the AVHRR images because of the cyclonic advection of warm (28°C) water. Presumably, diurnal warming in Hawai‘i’s wind shadow had created a thin layer of warm water overlying the upwelled cold water in C95b’s core. Fig. 108 shows the center of the eddy as determined by least-squares fit onto the ADCP data. The eddy was within 30 km of the leeward coast of Hawai‘i, resulting in  $\sim 1$  m/s northward currents along the shore. As a lowest-order attempt to address the eddy’s asymmetry while examining its structure, the eddy was divided into nearshore and farshore sides, each assumed to be azimuthally symmetric.

---

<sup>2</sup>The positions of these two eddies may have resembled the newly-formed cyclone and AC94b in Fig. 23; note the striking similarity between the 14 May 1994 image and the 1 August 1995 image of Fig. 106 as the cyclones press against Hawai‘i.

A least-squares fit of a Rankine vortex described the velocity structure of each side reasonably well (Fig. 108). At 50 m depth, the Rankine vortex fit to the nearshore data had a peak speed of 51 cm/s at 23.7 km from the eddy center, giving a core vorticity of  $4.10 \times 10^{-5} \text{ s}^{-1}$  ( $0.85 f$ ). At the same depth, the farshore velocity profile had a peak speed of 51 cm/s at a radius of 56.4 km, giving a core vorticity of  $2.06 \times 10^{-5} \text{ s}^{-1}$  ( $0.43 f$ ). While the core radius had tightened on the inshore side of the eddy, there was not strong evidence that the flow was accelerated. The northward transport across the inshore ADCP section of Fig. 108 is 3.0 Sv, while the southward transport across the farshore section is 8.4 Sv. As demonstrated by Nof [1988a], the interaction of a cyclonic eddy with a wall to its east will produce a southward- propagating squirt which bleeds fluid from the eddy. The ADCP data suggests this was indeed happening: a narrow ( $\sim 7.5$  km wide), 33.5 cm/s jet flowed SW towards the south point of Hawai'i. It is worth noting that the farshore radius was greater than the separation distance between the eddy and Hawai'i: the edge of the eddy may have been rotating onto the south point of the island, shearing off, and flowing NE along the SE coast. One would expect this mechanism to strip the eddy of all but the core fluid in a single rotation,  $\sim 3.4$  days. As suggested by the AVHRR images (Fig. 106), this cruise observed C95b in the process of colliding with the island.

If fluid was being sheared from the edge of the eddy, it may have produced an extremely sharp vorticity gradient at the eddy's edge. For a core radius of 24 km and vorticity of  $0.85f$ , the stability condition (3.12) shows that the eddy is unstable if the shell is less than 33 km in radius. There is some evidence for azimuthal-mode 2 instability in the AVHRR images (Fig. 106): on 1 August, what appears to be small anticyclonic satellite vortices lie north and south of AC95b. The northern feature had rotated a quarter-turn around the eddy by 7 August. The elongated S-shape of the eddy

on 1 August (also see the 14 May 1994 image of Fig. 23) resembles the tripolar vortex described by van Heijst *et al.* [1991]. Tripoles form when a cyclonic vortex becomes unstable and sheds the anticyclonic vorticity of its shell into two satellite anticyclones. Unfortunately, it is difficult to verify the presence of these satellite eddies in the data; the ADCP transects did not overlap them, and the drifter tracks are not affected by them. On 2 August, one of the drifters was deployed at 20.2°N, 157.0°W (immediately SW of Kaho’olawe), and completed four very tight (11-19 km radius) anticyclonic orbits before passing north through the Kaiwi Channel. The orbits had a mean period of  $4.6 \pm 0.6$  days (suggesting a core vorticity of  $-3.2 \times 10^{-5} \text{ s}^{-1}$ ,  $-0.6f$ ). However, as can be seen in Fig. 106 (e) and (f), these loops did not appear to coincide with the satellite-eddy-like features in the AVHRR. While it is possible that this was a small anticyclone shed from C95b, the anticyclone was first observed exactly where wind forcing could have produced it (see section 3.3). In addition, the AVHRR images on 1–14 August suggest that C95b was drawing a plume of cold water westward through the ‘Alenuihaha Channel. As this flow separated from Kaho’olawe and passed into the region of anticyclonic shear between C95a and C95b, it could have become unstable and formed the small vortex.

By 16 August, C95b had propagated to 157°W and reverted to a cold-core SST feature (Fig. 107). Presumably, once it moved out of Hawai’i’s lee, wind-driven mixing erased the thin ( $\sim 5$  m [Wenzel, 1992]) layer of warm water overlying the cold core. In addition, the eddy may have drawn cooler (26°C) water from the windward side of the islands through the ‘Alenuihaha Channel, as suggested by the 1–14 August images. On 3 September, the eddy was elongated along its N/S axis, and again showed some evidence of mode 2 instability (Fig. 107)<sup>3</sup>. Images on 11 and 12 September show that

---

<sup>3</sup>The 3 September AVHRR image also shows cold water passing the south point and forming an anticyclonic cusp, reminiscent of the AC94g spin-up image (Fig. 102); during this time, anticyclone

C95b became quite circular over the course of the intervening week.

The trajectories of the drifters deployed during the *Cromwell* cruise are presented in Figs. 109–111. Five drifters were deployed in C95b, and moved WNW with it as it propagated out of Hawai‘i’s lee (Fig. 112). The drifters were initially 10–30 km from the eddy center, with orbital periods averaging 3.6 days (suggesting a solid-body core of vorticity  $4.0 \times 10^{-5} \text{ s}^{-1}$ ,  $0.82f$ ). From mid-August to early October, the drifters moved outward in the eddy, with radii of 40–80 km and periods of 4–8 days. During this time, the azimuthal speeds of the drifters were no longer linearly increasing with distance, suggesting that they had moved outside the eddy’s core.

Three of the drifters remained in C95b for greater than 50 days, and three more drifters were temporarily captured by the eddy after 1 October (Fig. 113). One of the drifters remained in the eddy for a spectacular 237 days; from early December 1995 to late January 1996, it switched to small (10–20 km) orbits with a mean period of 6.0 days. The linear speed-vs.-distance during this interval indicated a solid-body core of vorticity  $2.4 \times 10^{-5} \text{ s}^{-1}$  ( $0.47f$ ). The core did not extend beyond  $\sim 30$  km, for in February 1995 the drifter made two  $\sim 40$  km loops with a 15 day period, then returned to two small ( $< 20$  km) orbits of period 6.3 days before leaving the eddy.

Anticyclone AC95a was born west of the south point of Hawai‘i in July 1995 (Fig. 22). Two drifters deployed during TC9503 orbited AC95a for nearly 50 days (Fig. 114), after which one left the eddy and the other abruptly stopped transmitting. A third drifter orbited AC95a for a single loop. The orbital characteristics of the drifters suggest an azimuthal structure very similar to that of AC94c seen on 8 October 1994 (see Fig. 97), which had a core of vorticity  $-2.4 \times 10^{-5} \text{ s}^{-1}$  ( $-0.5f$ , rotational period 6 days). Outside this core, azimuthal speed may have dropped off more rapidly in AC95a than in AC94c.

---

AC95b was born.

In mid-October 1995, two drifters began circling anticyclone AC95b at  $19.0^\circ\text{N}$ ,  $156.6^\circ\text{W}$  (just west of the south point of Hawai‘i), and remained in orbital motion for over two months (Fig. 115). AC95b was born in early September 1995 (Fig. 22); an AVHRR image on 3 September (Fig. 107) shows cold water passing the south point and forming an anticyclonic cusp, reminiscent of the AC94g spin-up image (Fig. 102). The drifter orbits show that AC95b had a solid-body core of radius 80 km, maximum speed 50 cm/s, and vorticity  $-1.4 \times 10^{-5} \text{ s}^{-1}$  ( $-0.31f$ , rotational period 10.4 days).

In December 1995 to early January 1996, two drifters began orbiting an anticyclone ahead of AC95b, which may have again been AC95a. The drifter tracks (Fig. 110) suggest that the two eddies may have begun rotating anticyclonically about their center of mass, and were possibly drawing together. Unfortunately, all four drifters left the anticyclones in early to mid-January 1996, leaving the fate of these anticyclones unknown.

### C.3 April 1996 cruise

On 5–8 April 1996, the R/V *Townsend Cromwell* sailed from O‘ahu to Maui to recover three current meters deployed near the latter island. Seven drifters were launched west of Lana‘i during this cruise. Two looped counter-clockwise around Lana‘i, passed around Moloka‘i to the north, and left the island lee region. A third drifter ran aground on the south shore of Moloka‘i. The remaining four drifters passed south of Lana‘i and into Hawai‘i’s lee (Figs. 116–118). These all made at least a partial clockwise loop around AC96c, which was centered near  $19.5^\circ\text{N}$ ,  $157.7^\circ\text{W}$ . Only two completed a full orbit, one of period 12.9 days, radius 79 km (mean speed 7.2 cm/s) and the other of period 16.2 days, radius 101 km (mean speed 7.1 cm/s). These drifters then left the vicinity of the eddy.

On 15 April, a small boat was used to deploy two additional drifters off the west coast of Hawai'i. They were placed within the core of lee cyclone C96b, which was immediately to the east of AC96a. One of the drifters orbited for 18 days (Fig. 119), then left to encounter C96a (described below). The other orbited for over 40 days, revealing a solid-body core greater than 30 km in radius, with core vorticity  $3.4 \times 10^{-5} \text{ s}^{-1}$  ( $0.7f$ , rotational period 4.3 days). C96b was initially stationary; in early May it began propagating almost due south at  $\sim 8 \text{ cm/s}$ . The drifter left C96b around  $18^\circ\text{N}$ ,  $156.5^\circ\text{W}$ . During most of May 1996, the drifter trajectories suggested that AC96a and C96b were very close to each other, and that AC96a was also moving southward. It is possible that these two eddies had paired, creating a dipole which was self-advecting southward; the May 1996 trajectories show the eddies were  $\sim 100 \text{ km}$  apart, so the observed C96b propagation speed of  $8 \text{ cm/s}$  is only slightly faster than the advection speed of  $\sim 7 \text{ cm/s}$  suggested by the drifters around AC96a.

The drifter which left C96b headed NW; in early May, it entered eddy C96a south of Maui (Fig. 120). The eddy drifted WNW until mid-May, then turned south. The orbits of the drifter suggest that the core was  $\sim 30\text{--}40 \text{ km}$  in radius, with a vorticity of  $4.9 \times 10^{-5} \text{ s}^{-1}$  ( $0.97f$ , rotational period 3.0 days). In late May, the drifter left C96a and traveled into the immediate lee of Hawai'i. There it made three clockwise orbits, each  $\sim 45 \text{ km}$  in radius with an orbital period of  $\sim 4.0$  days. If this was the solid-body core of a newly-formed anticyclone (AC96b), its vorticity was  $-3.64 \times 10^{-5} \text{ s}^{-1}$  ( $-0.78f$ ). A concurrent AVHRR image on 31 May (Fig. 118) shows a possible anticyclonic cusp west of Hawai'i's south point, although the feature is not particularly clear. After the third orbit, the drifter passed NE through the 'Alenuihaha Channel and out of the Hawaiian lee region.

In September 1996, a drifter which had run aground was redeployed in the immediate

lee of Hawai'i, very close to the core of anticyclonic eddy AC96c (Fig. 121). It tracked the eddy for nearly 120 days, leaving it on 17 January 1997 at  $18.4^{\circ}\text{N}$ ,  $162.8^{\circ}\text{W}$ . Initially, the drifter moved outward from 15 km orbits to 40 km orbits in a solid-body core of vorticity  $-5 \times 10^{-5} \text{ s}^{-1}$  ( $-1.0f$ , rotational period 2.9 days). In early October, the orbits slowly increased in size from 40 to 50 km, while the period rapidly increased from 3 days to 6–12 days. Throughout this time, the eddy drifted NW. Then, in late October, AC96c abruptly turned SW and the drifter spiraled into orbits 15–23 km in radius. These orbits again indicated a solid-body structure, but of a lower vorticity:  $-1.75 \times 10^{-5} \text{ s}^{-1}$  ( $-0.36f$ , rotational period 8.3 days). Finally, the eddy turned WSW as the drifter made three large ( $> 60 \text{ km}$ ) orbits, then left the eddy.

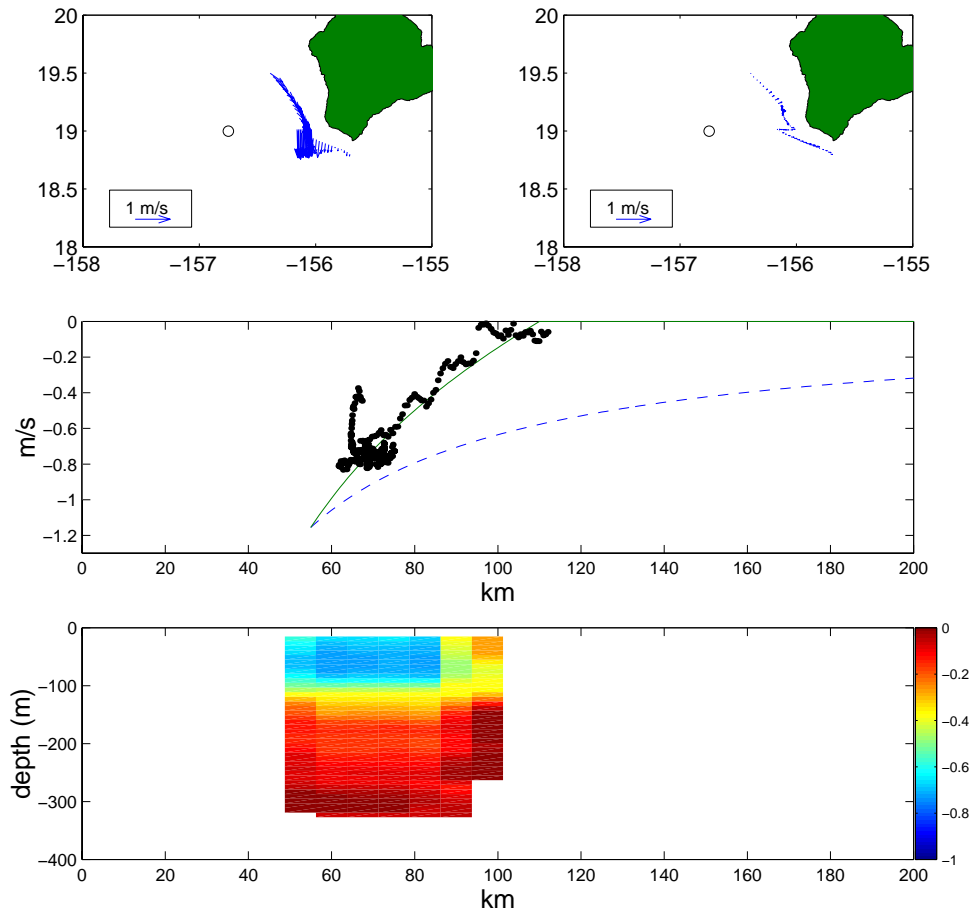


Figure 93: *Top*: A circle marks the center of anticyclonic eddy AC94c as seen on 16 August 1994. The azimuthal (left) and radial (right) components of velocity are shown. *Middle*: azimuthal speed vs. distance from eddy center. Negative values indicate clockwise rotation. The solid line is a curve of constant cyclonic vorticity  $0.3f$ . The dashed line is for the irrotational profile  $v \propto 1/r$ . *Bottom*: azimuthal speed (m/s) as a function of depth. Negative values are clockwise.

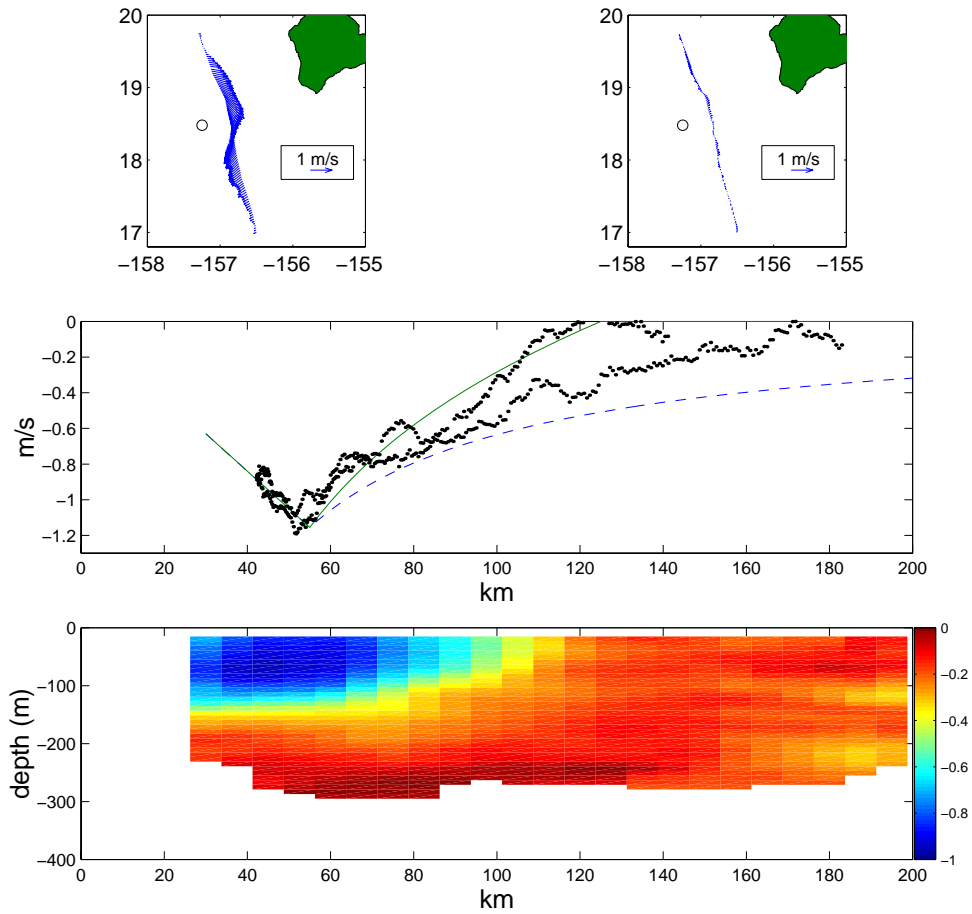


Figure 94: *Top*: A circle marks the center of anticyclonic eddy AC94c as seen on 8 September 1994. The azimuthal (left) and radial (right) components of velocity are shown.

*Middle*: azimuthal speed vs. distance from eddy center. Negative values indicate clockwise rotation. The solid line is for the shell/core model with core radius 55 km, vorticity  $-.91f$  and shell vorticity  $0.2f$ . The dashed line is a Rankine vortex with the same core radius.

*Bottom*: azimuthal speed (m/s) as a function of depth. Negative values are clockwise.

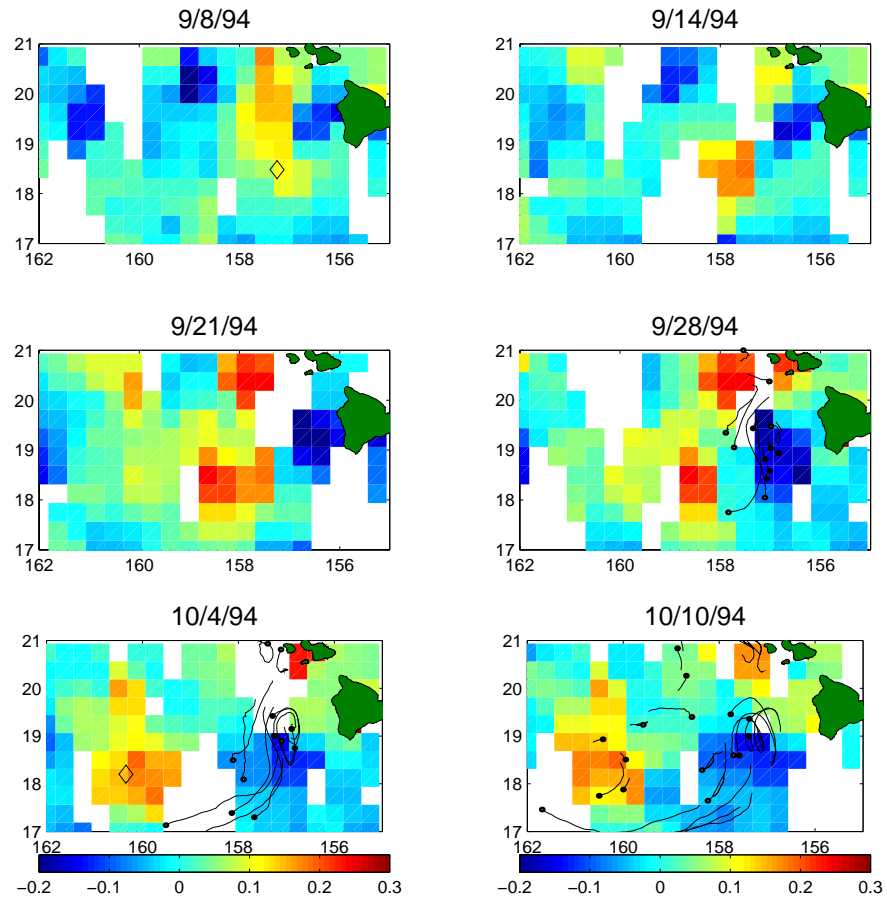


Figure 95: Snapshots of the median 10-day ERS-1/TOPEX sea level anomaly on a 0.75° square grid, in meters. Every other value on the grid is composed of independent data. Diamonds in the top-left and bottom-left panels show the center location of eddy AC94c as determined from the ADCP data (Figs. 94, 97) Dots show the location of drifters on the given date; tails shows the previous 10 days of the drifters' trajectories.

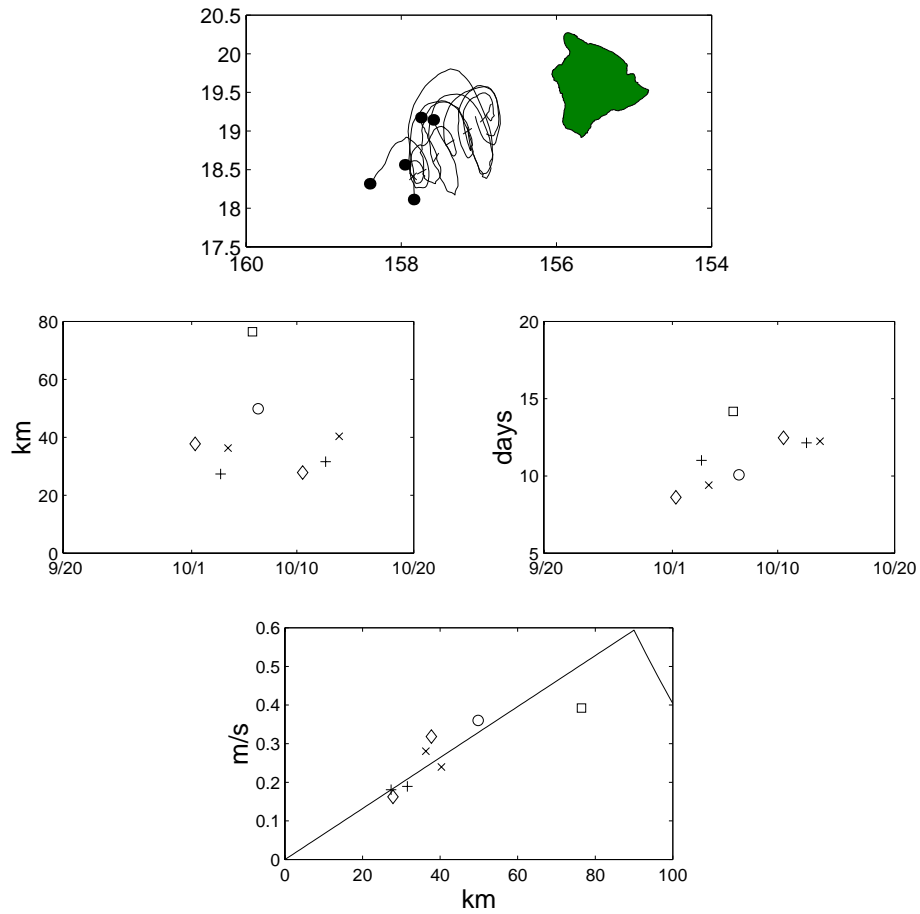


Figure 96: Orbital characteristics of drifters in C94a.

*Top:* trajectories of drifters around eddy (solid lines), with dots marking the location of the drifter when it left the eddy. The dashed line is the path of the eddy center, with an **x** marking its last known location.

*Middle, left:* orbital radius vs. time. Different symbols are used for different drifters.

*Middle, right:* orbital period vs. time.

*Bottom:* orbital speed vs. radius. The solid line is derived from a least-squares fit of the core/shell model to the altimetry.

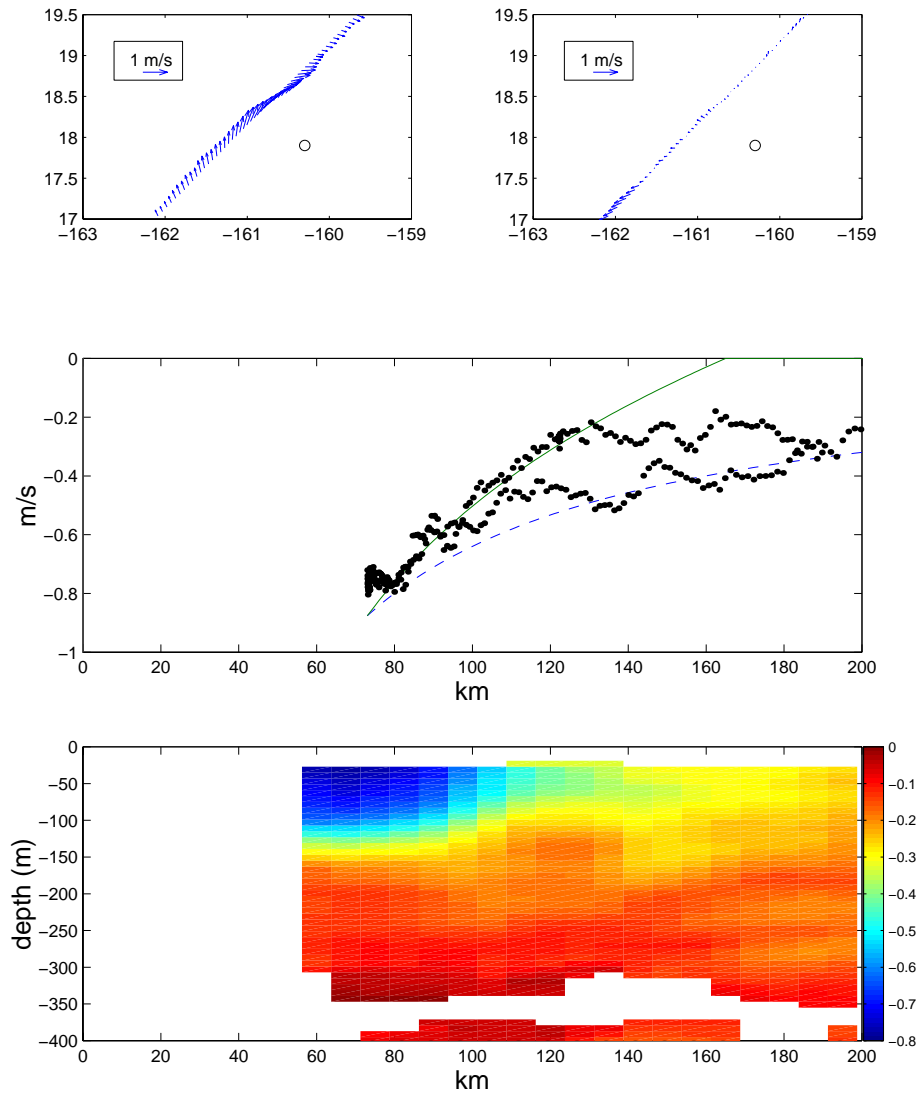


Figure 97: *Top*: A circle marks the center of anticyclonic eddy AC94c. The azimuthal (left) and radial (right) components of velocity are shown.

*Middle*: azimuthal speed vs. distance from eddy center. Negative values indicate clockwise rotation. The solid line is for a shell of constant cyclonic vorticity  $0.12f$ . The dashed line is for the irrotational profile  $v \propto 1/r$ .

*Bottom*: azimuthal speed (m/s) as a function of depth. Negative values are clockwise.

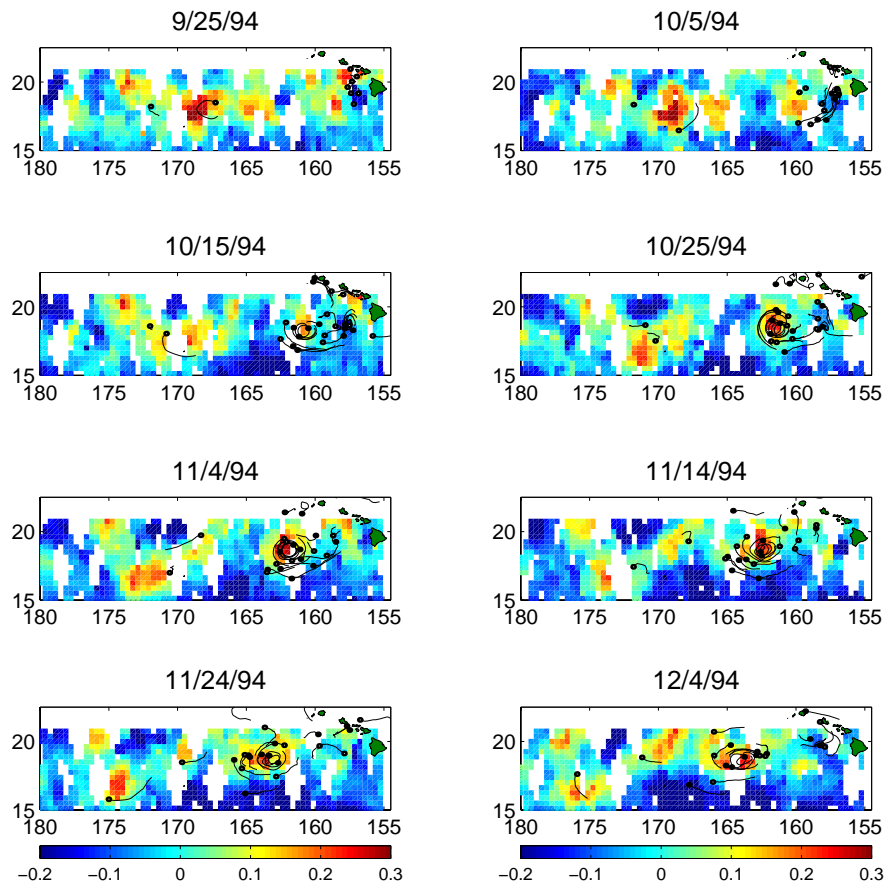


Figure 98: Ten-day snapshots of drifters. Dots show the location of the drifters on the given date; the tail shows the previous ten days of the drifters' trajectories. Background coloring is the median 20-day sea level anomaly on a  $0.75^\circ$  square grid, in meters. Every other grid is composed of independent data.

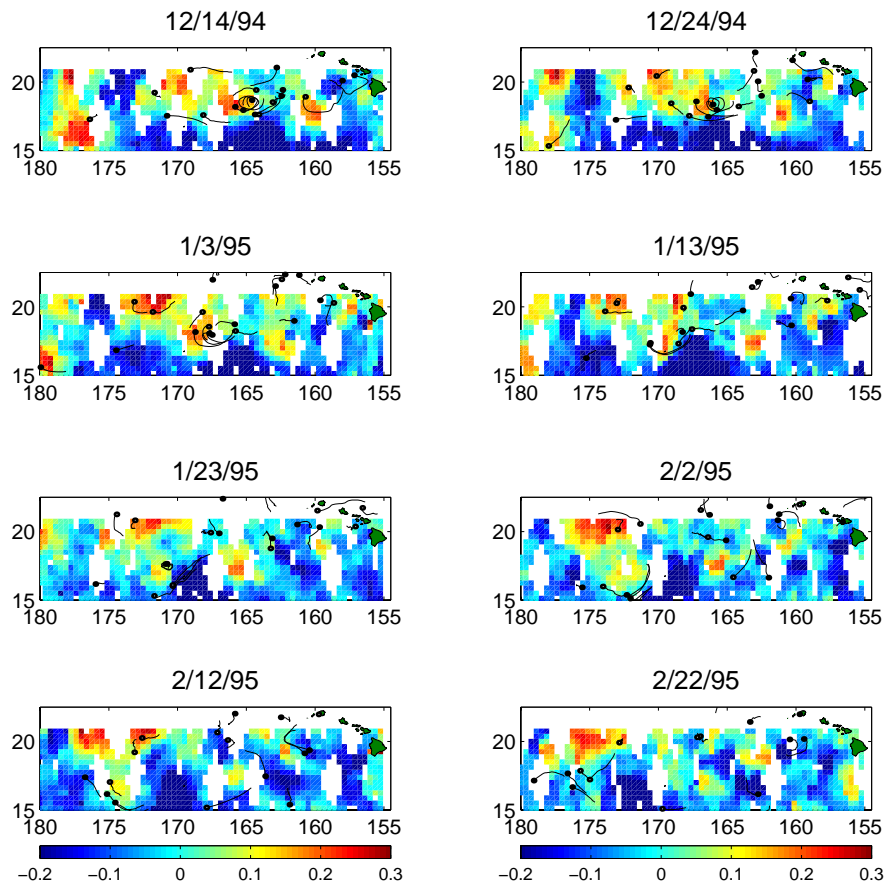


Figure 99: Ten-day snapshots of drifters. Dots show the location of the drifters on the given date; the tail shows the previous ten days of the drifters' trajectories. Background coloring is the median 20-day sea level anomaly on a  $0.75^\circ$  square grid, in meters. Every other grid is composed of independent data.

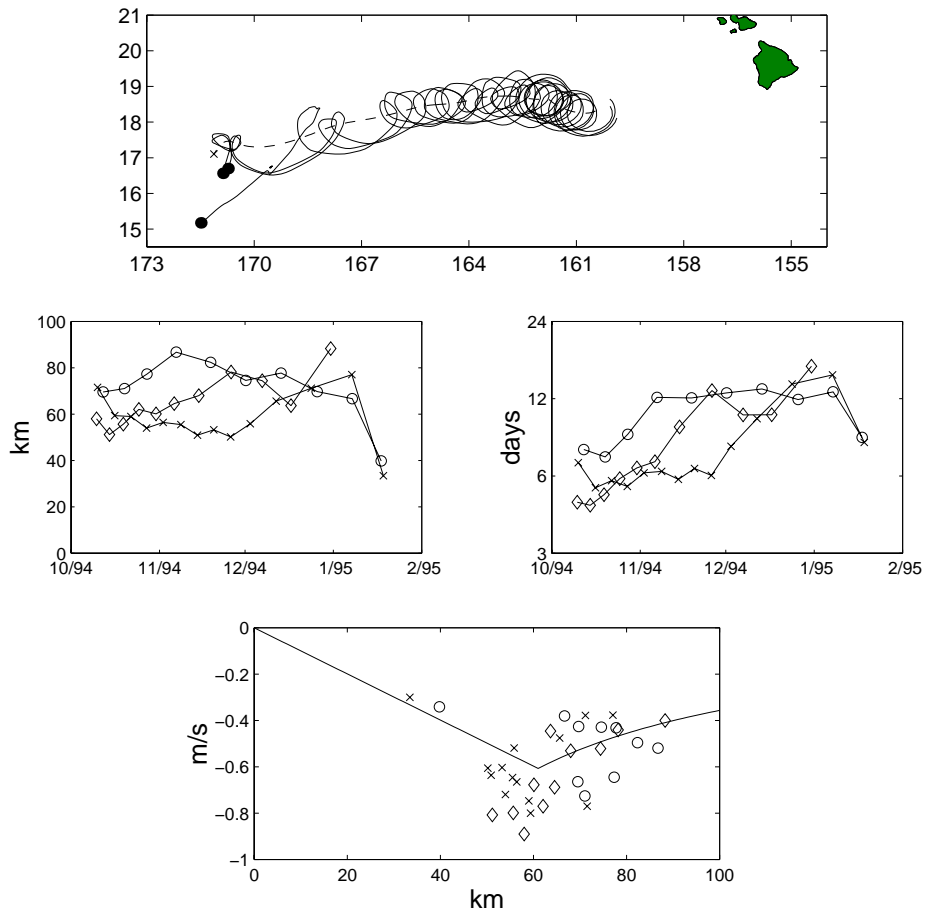


Figure 100: Orbital characteristics of drifters in AC94c.

*Top:* trajectories of drifters around eddy (solid lines), with dots marking the location of the drifter when it left the eddy. The dashed line is the path of the eddy center, with an **x** marking its last known location.

*Middle, left:* orbital radius vs. time. Different symbols are used for different drifters.

*Middle, right:* orbital period vs. time.

*Bottom:* orbital speed vs. radius. The solid line is derived from the altimetry for 8–31 October 1994 (see Fig. 101).

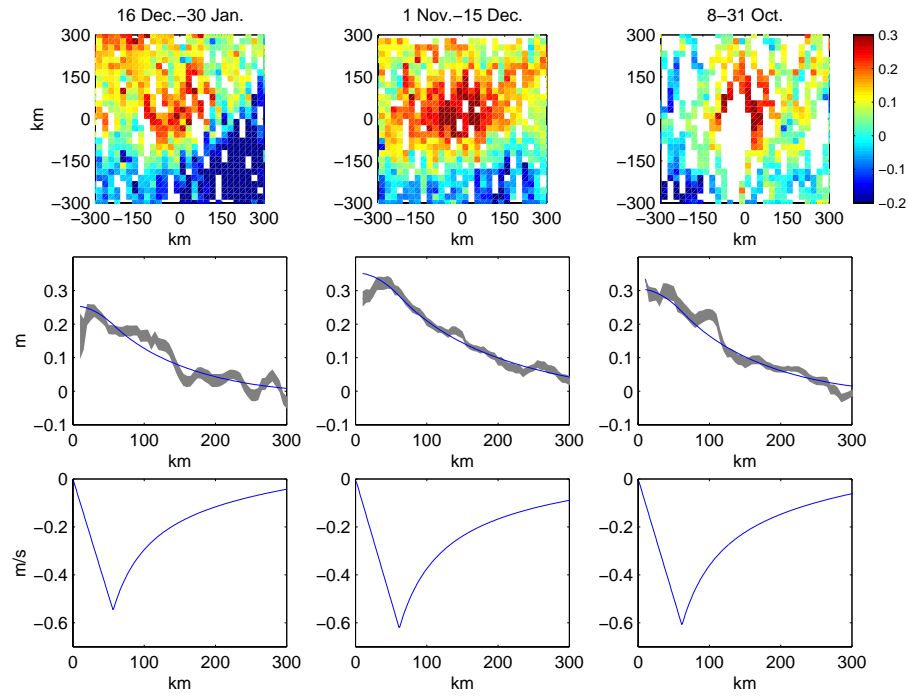


Figure 101: *Top*: ERS-1 and TOPEX altimetry in the frame of reference moving with eddy AC94c, broken into three time spans.

*Middle*: azimuthally-averaged sea level anomaly for each time span. Smooth lines are least-squares fits of the core/shell model sea surface displacement.

*Bottom*: corresponding velocity structure from the least-squares fits.

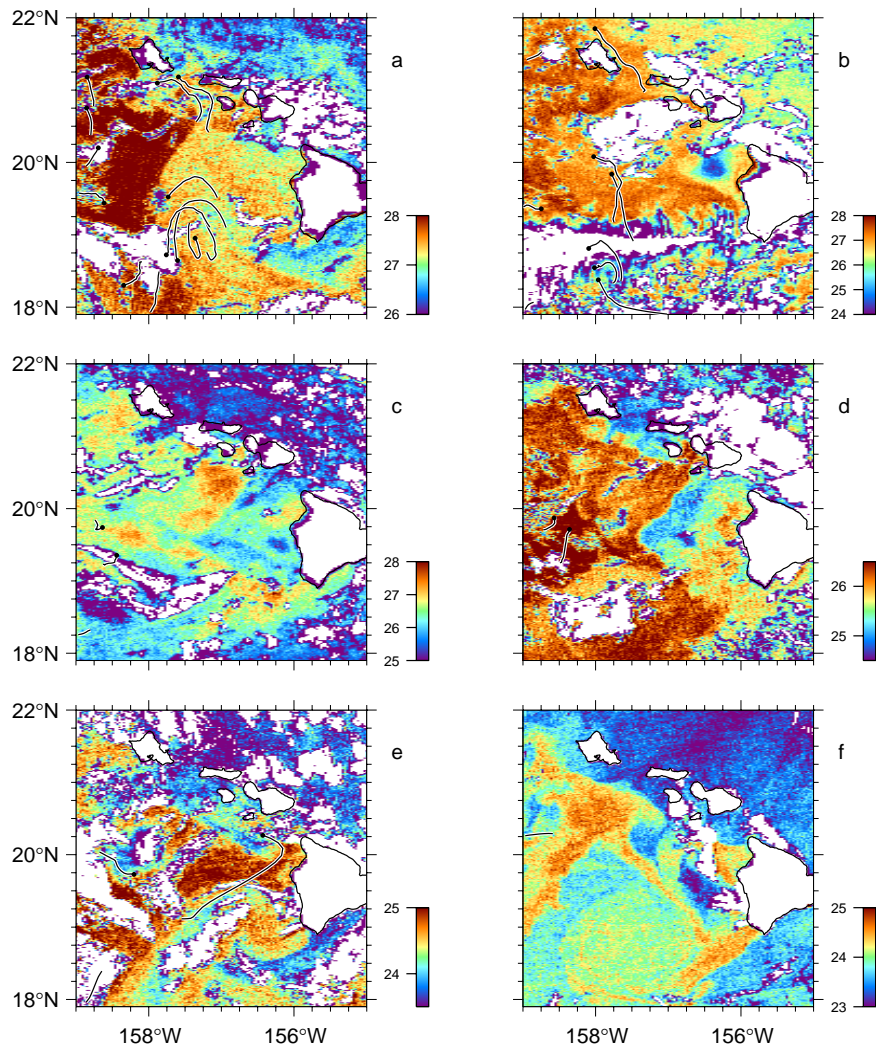


Figure 102: AVHRR SST images ( $^{\circ}\text{C}$ ), with concurrent drifter positions (points, with lines showing previous five days) overlaid. Temperatures colder than  $22^{\circ}\text{C}$  have been flagged as clouds (white). The images were taken on 9 October 1994 at 1746 UTC (a), 22 October at 1804 UTC (b), 6 November at 0511 UTC (c), 9 November at 0546 UTC (d), 12 December at 0531 UTC (e) and 26 December at 0528 UTC (f).

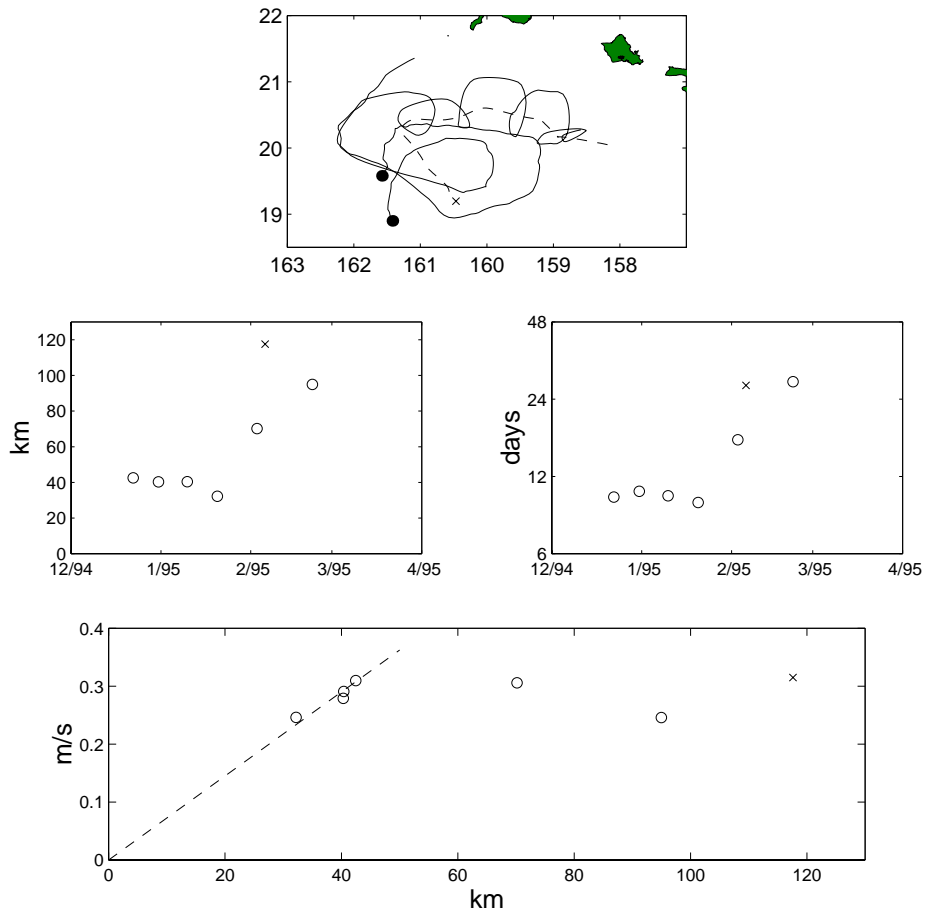


Figure 103: Orbital characteristics of drifters in C94b.

*Top:* trajectories of drifters around eddy (solid lines), with dots marking the location of the drifter when it left the eddy. The dashed line is the path of the eddy center, with an **x** marking its last known location.

*Middle, left:* orbital radius vs. time. Different symbols are used for the two drifters.

*Middle, right:* orbital period vs. time.

*Bottom:* orbital speed vs. radius. The dashed line is for solid-body rotation at a period of 10.0 days.

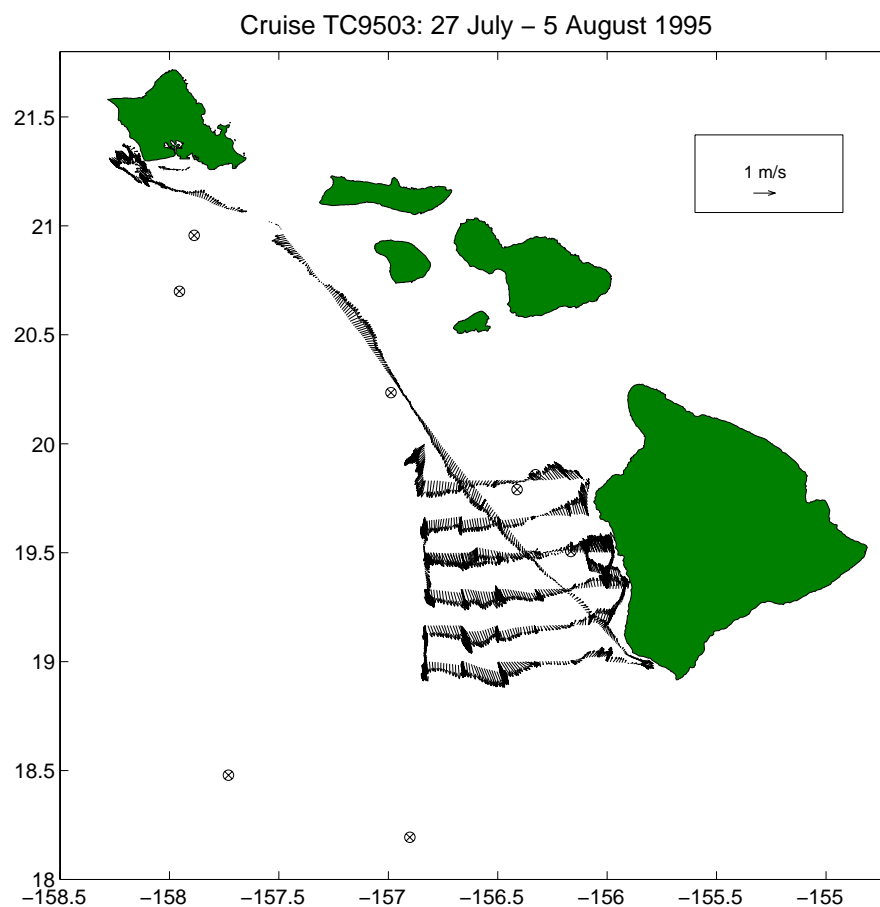


Figure 104: July–August 1995 cruise of R/V *Townsend Cromwell*. ADCP velocity at 47 m depth is shown. Circled  $x$ 's indicate the first satellite fixes on drifters deployed during the cruise.

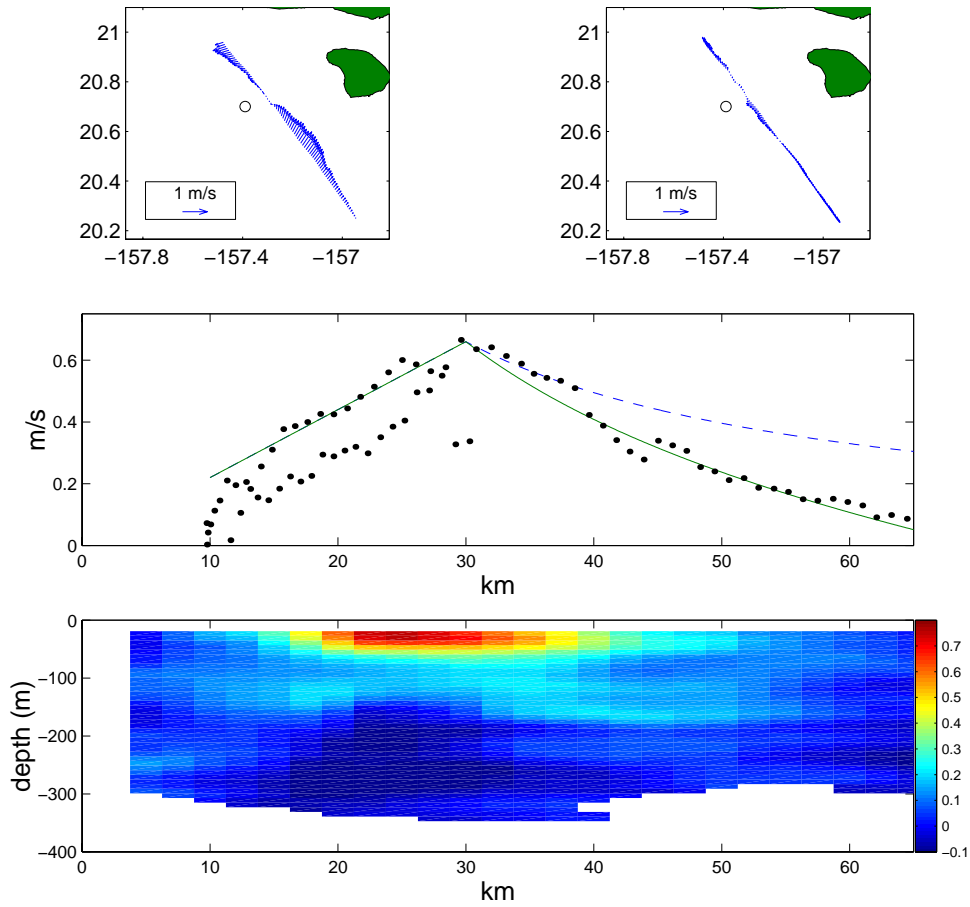


Figure 105: *Top*: A circle marks the center of cyclonic eddy C95a. The azimuthal (left) and radial (right) components of velocity are shown.

*Middle*: azimuthal speed vs. distance from eddy center. Positive values indicate counter-clockwise rotation. The dashed line is an estimated fit of a Rankine vortex structure, and the solid line is a fit of form (B.9) with core vorticity  $4.4 \times 10^{-5} \text{ s}^{-1}$ , radius 30 km and shell vorticity  $-1 \times 10^{-5} \text{ s}^{-1}$ .

*Bottom*: azimuthal speed (m/s) as a function of depth. Positive values are counter-clockwise.

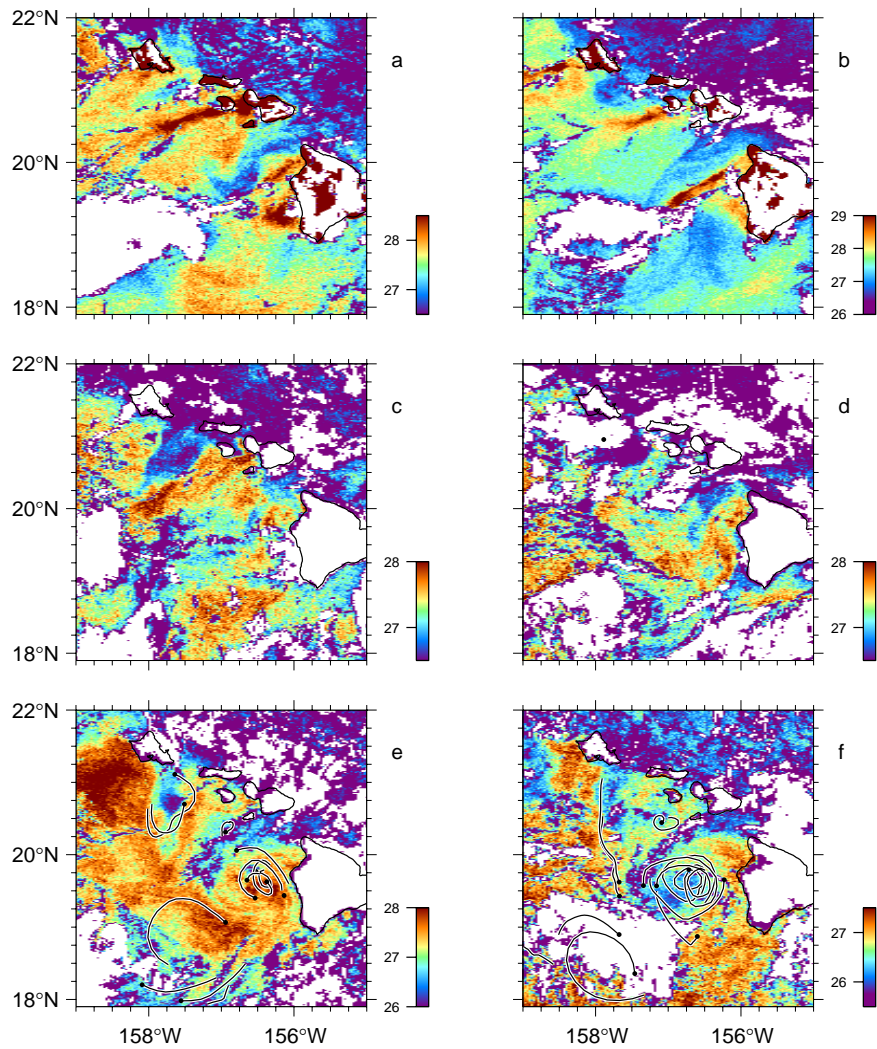


Figure 106: AVHRR SST images ( $^{\circ}\text{C}$ ), with concurrent drifter positions (points, with lines showing previous five days) overlaid. Temperatures colder than  $22^{\circ}\text{C}$  have been flagged as clouds (white). The images were taken on 8 July 1995 at 0021 UTC (a), 18 July at 0014 UTC (b), 29 July at 1230 UTC (c), 1 August at 1157 UTC (d), 7 August at 0226 UTC (e) and 14 August at 1742 UTC (f).

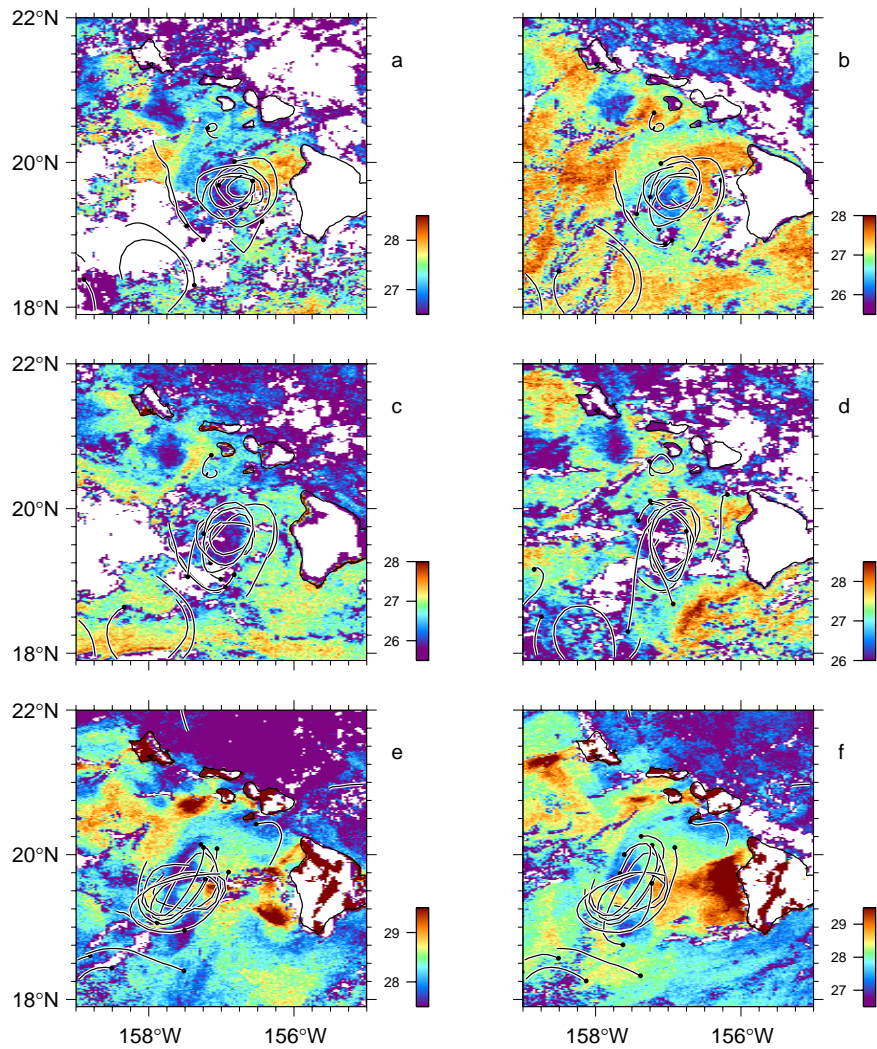


Figure 107: AVHRR SST images ( $^{\circ}\text{C}$ ), with concurrent drifter positions (points, with lines showing previous five days) overlaid. Temperatures colder than  $22^{\circ}\text{C}$  have been flagged as clouds (white). The images were taken on 16 August 1995 at 1236 UTC (a), 18 August at 0527 UTC (b), 18 August at 1755 UTC (c), 21 August at 1142 UTC (d), 3 September at 2358 UTC (e) and 4 September at 2347 UTC.

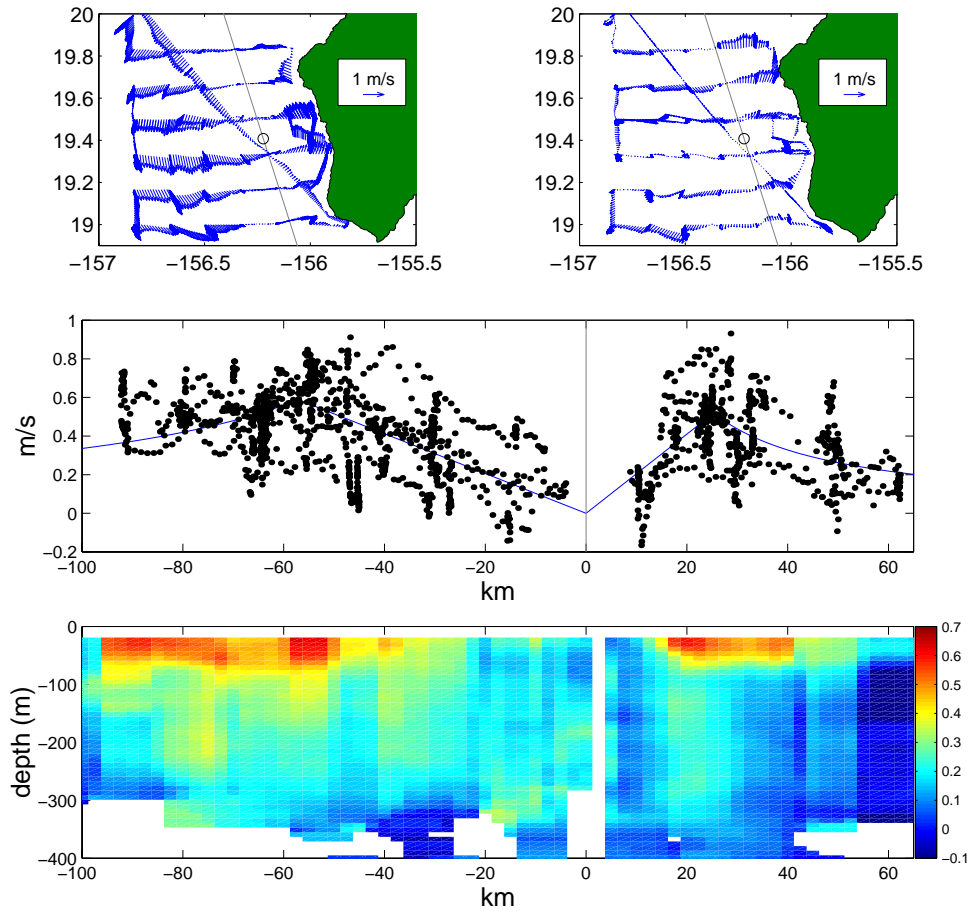


Figure 108: *Top*: A circle marks the center of the cyclonic lee eddy C95b. The azimuthal (left) and radial (right) components of velocity are shown. A gray line marks the division between the nearshore and farshore sides of the eddy.

*Middle*: azimuthal speed for the nearshore (right-hand side) and farshore (left-hand side) sides of the eddy, as a function of distance from eddy center. Positive values indicate counter-clockwise rotation. Solid lines indicate least-squares fit of a Rankine vortex onto the points.

*Bottom*: azimuthal speed (m/s) for the nearshore and farshore sides of the eddy as a function of depth. Positive values are counter-clockwise.

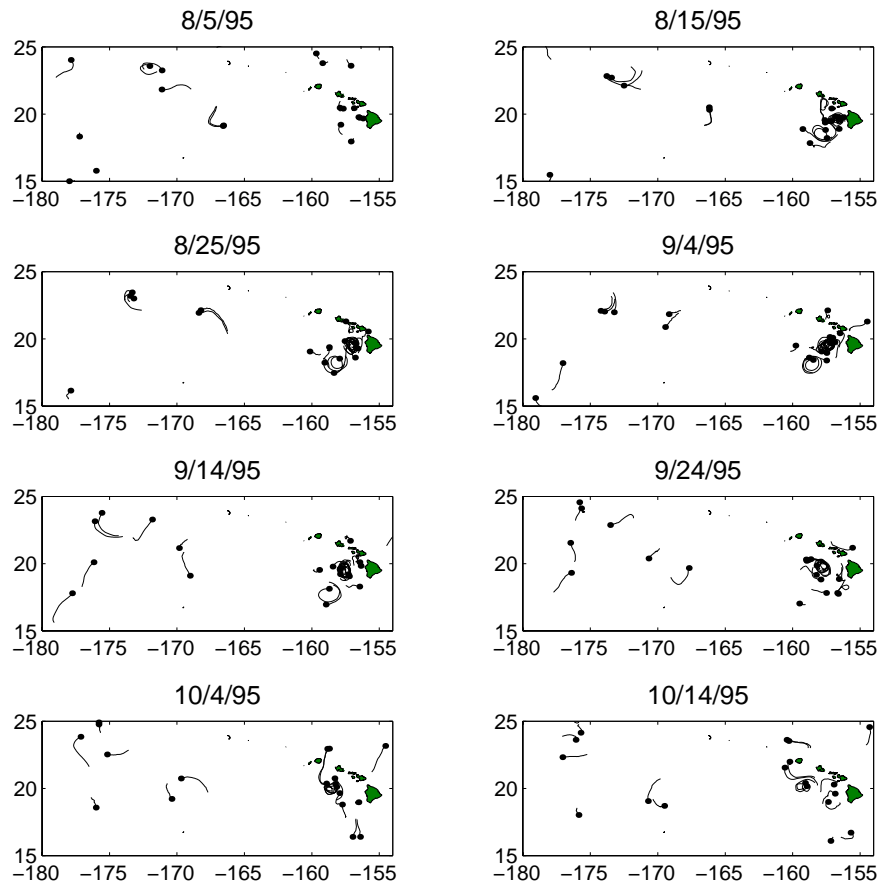


Figure 109: Ten-day snapshots of drifters. Dots show the location of the drifters on the given date; the tail shows the previous ten days of the drifters' trajectories.

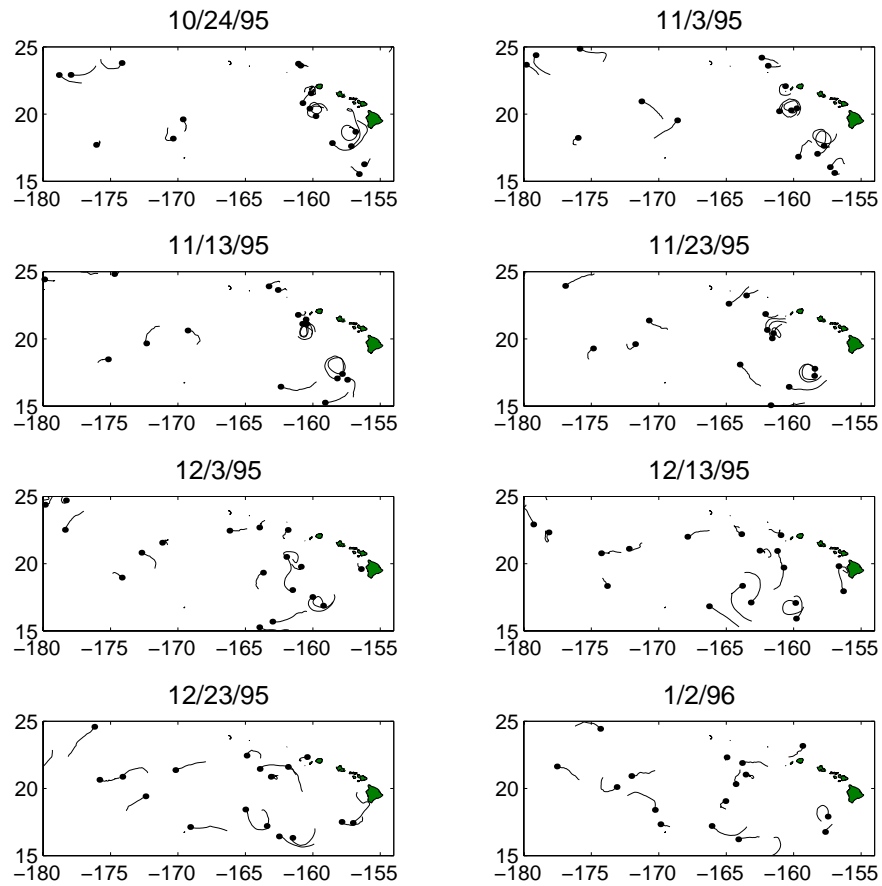


Figure 110: Ten-day snapshots of drifters. Dots show the location of the drifters on the given date; the tail shows the previous ten days of the drifters' trajectories.

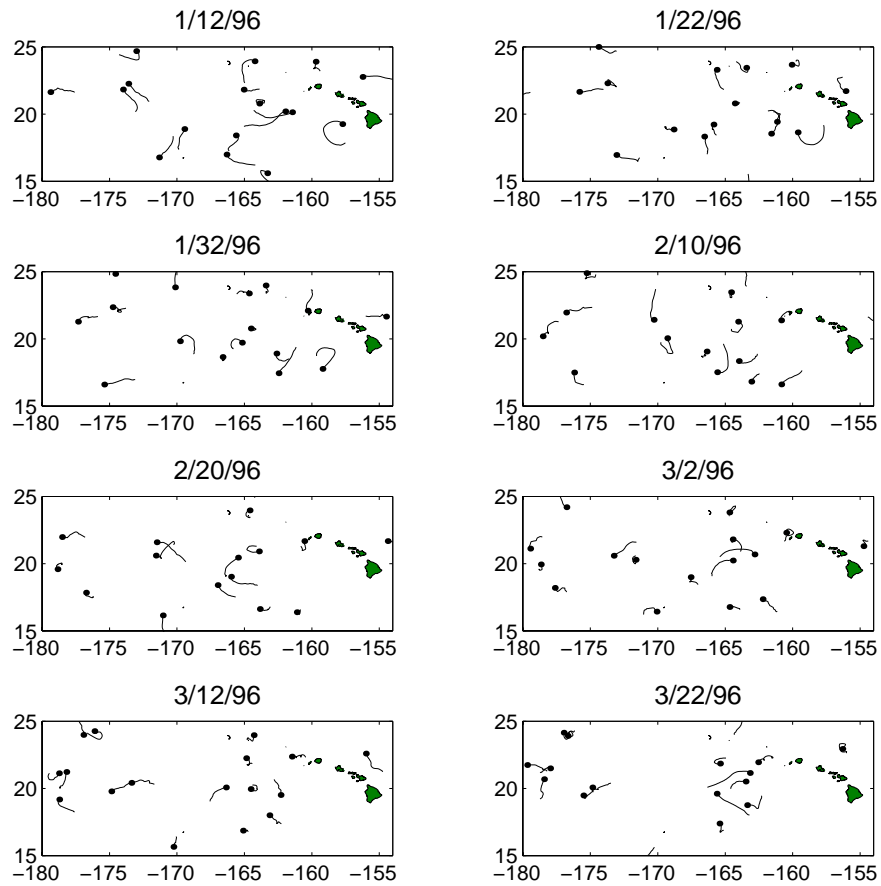


Figure 111: Ten-day snapshots of drifters. Dots show the location of the drifters on the given date; the tail shows the previous ten days of the drifters' trajectories.

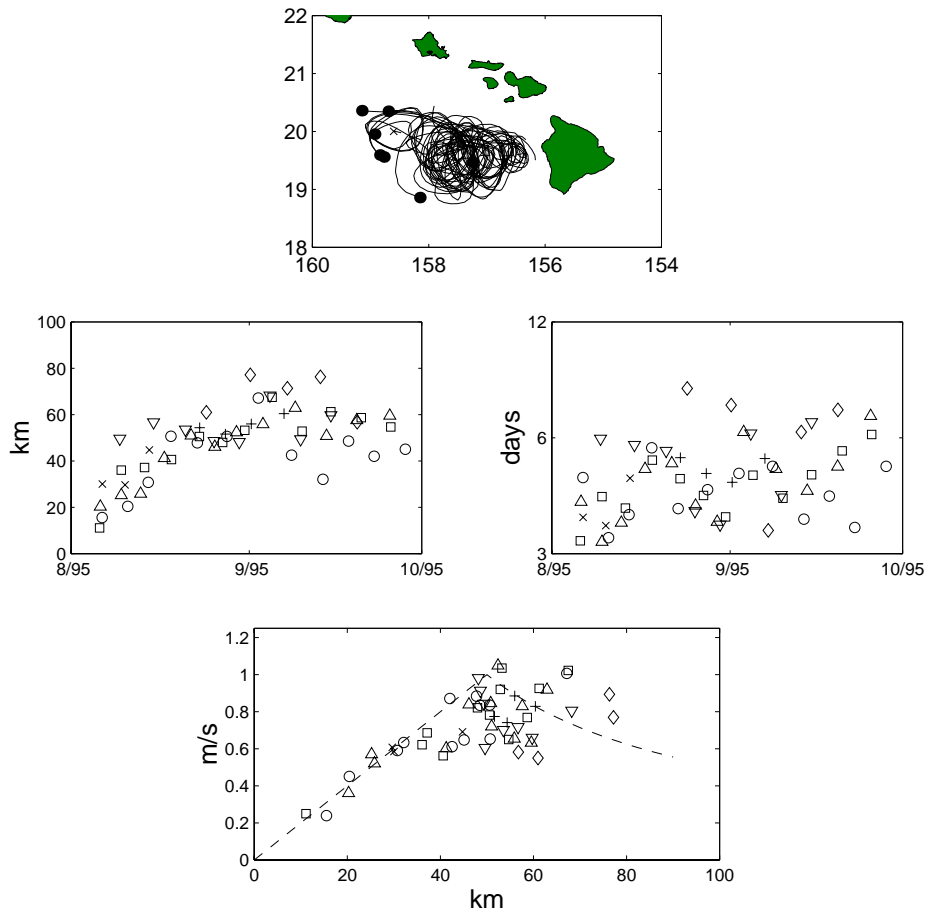


Figure 112: Orbital characteristics of drifters in C95b (6 August – 1 October 1995).  
*Top:* trajectories of drifters around eddy (solid lines), with dots marking the location of the drifter on 1 October. The dashed line is the path of the eddy center, with an  $x$  marking its location on 1 October.  
*Middle, left:* orbital radius vs. time. Different symbols are used for different drifters.  
*Middle, right:* orbital period vs. time.  
*Bottom:* orbital speed vs. radius. The dashed line is for solid-body rotation at a period of 3.6 days.

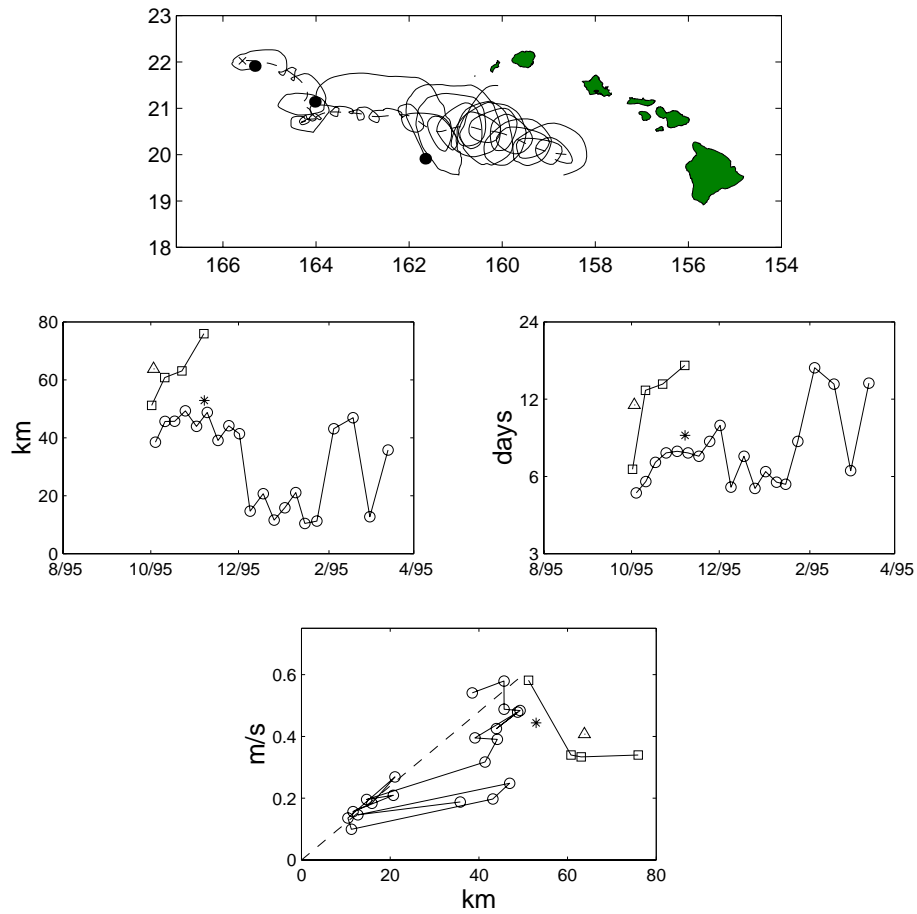


Figure 113: Orbital characteristics of drifters in C95b (1 October 1995 – 9 March 1996).  
*Top:* trajectories of drifters around eddy (solid lines), with dots marking the location of the drifter when it left the eddy. The dashed line is the path of the eddy center, with an **x** marking its last known location.  
*Middle, left:* orbital radius vs. time. Different symbols are used for different drifters.  
*Middle, right:* orbital period vs. time.  
*Bottom:* orbital speed vs. radius. The dashed line is for solid-body rotation at a period of 6.1 days.

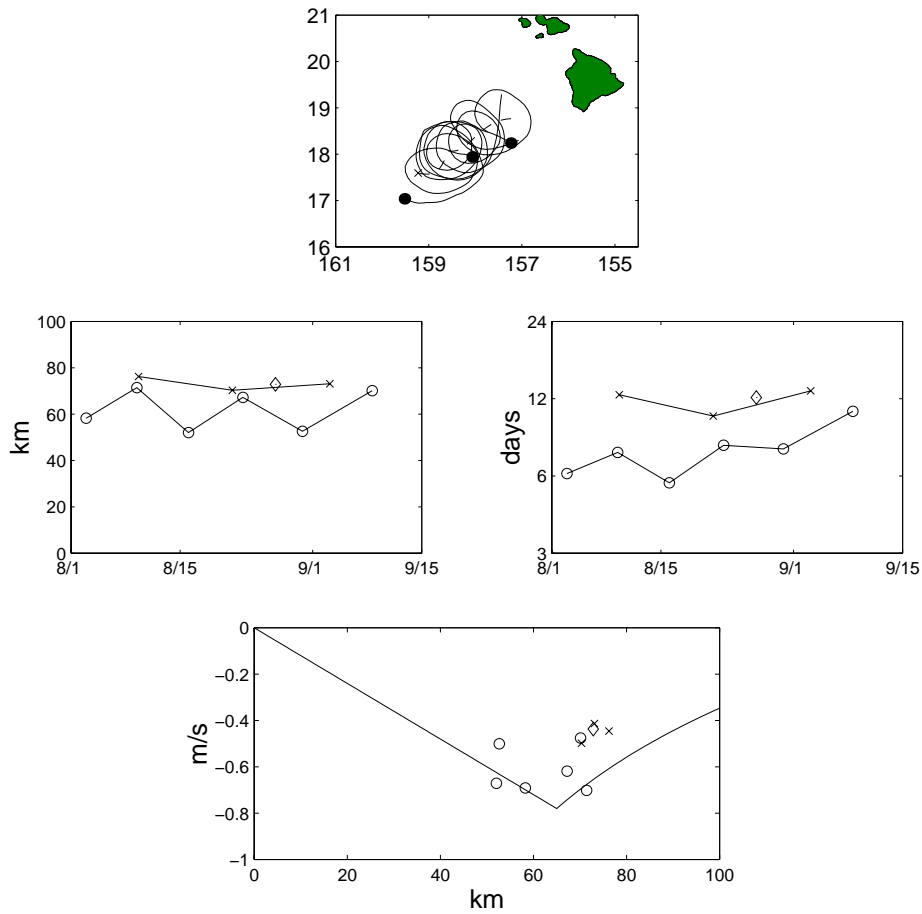


Figure 114: Orbital characteristics of drifters in AC95a.

*Top:* trajectories of drifters around eddy (solid lines), with dots marking the location of the drifter when it left the eddy. The dashed line is the path of the eddy center, with an **x** marking its last known location.

*Middle, left:* orbital radius vs. time. Different symbols are used for different drifters.

*Middle, right:* orbital period vs. time.

*Bottom:* orbital speed vs. radius. The solid line is the fit to the ADCP observations of eddy AC94c, which was at the same position the previous year (see Fig. 97).

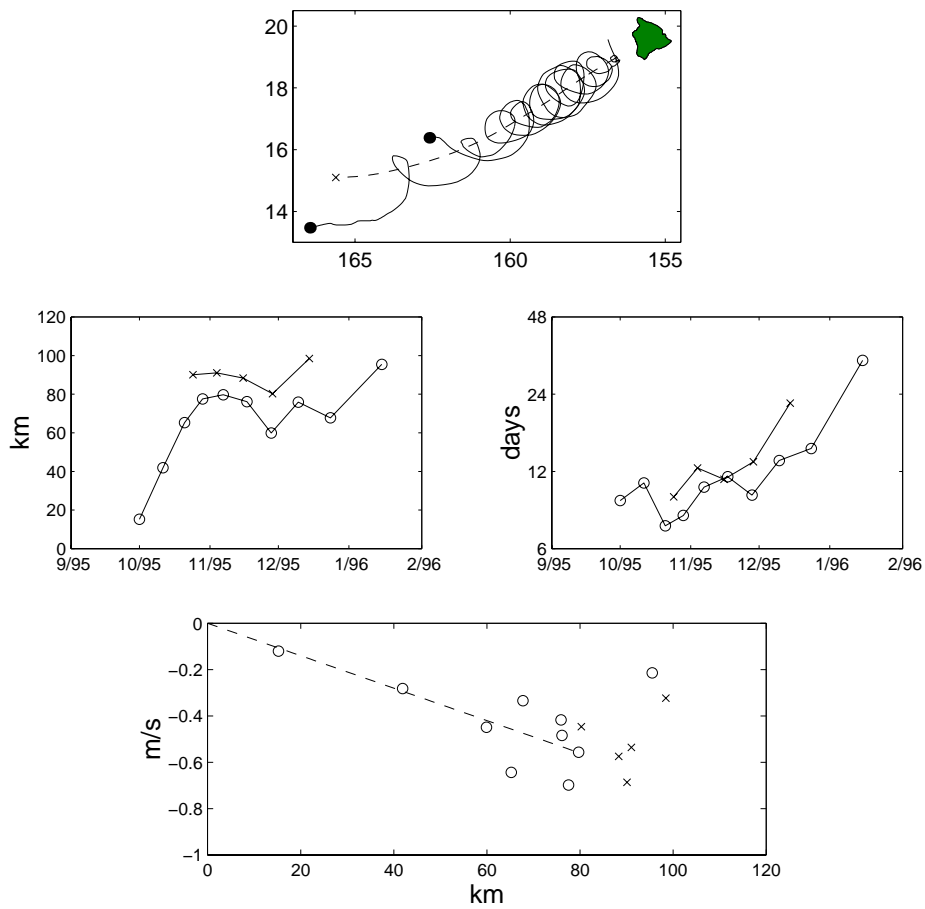


Figure 115: Orbital characteristics of drifters in AC95b.

*Top:* trajectories of drifters around eddy (solid lines), with dots marking the location of the drifter when it left the eddy. The dashed line is the path of the eddy center, with an **x** marking its last known location.

*Middle, left:* orbital radius vs. time. Different symbols are used for different drifters.

*Middle, right:* orbital period vs. time.

*Bottom:* orbital speed vs. radius. The dashed line is for solid-body rotation at a period of 10.4 days.

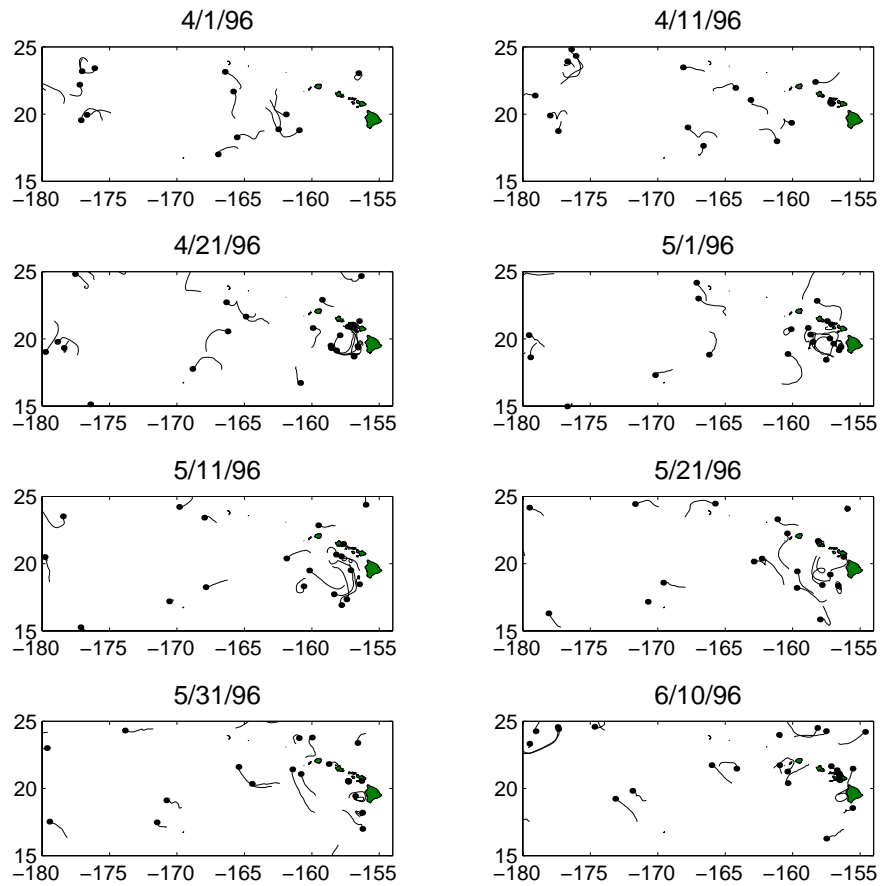


Figure 116: Ten-day snapshots of drifters. Dots show the location of the drifters on the given date; the tail shows the previous ten days of the drifters' trajectories.

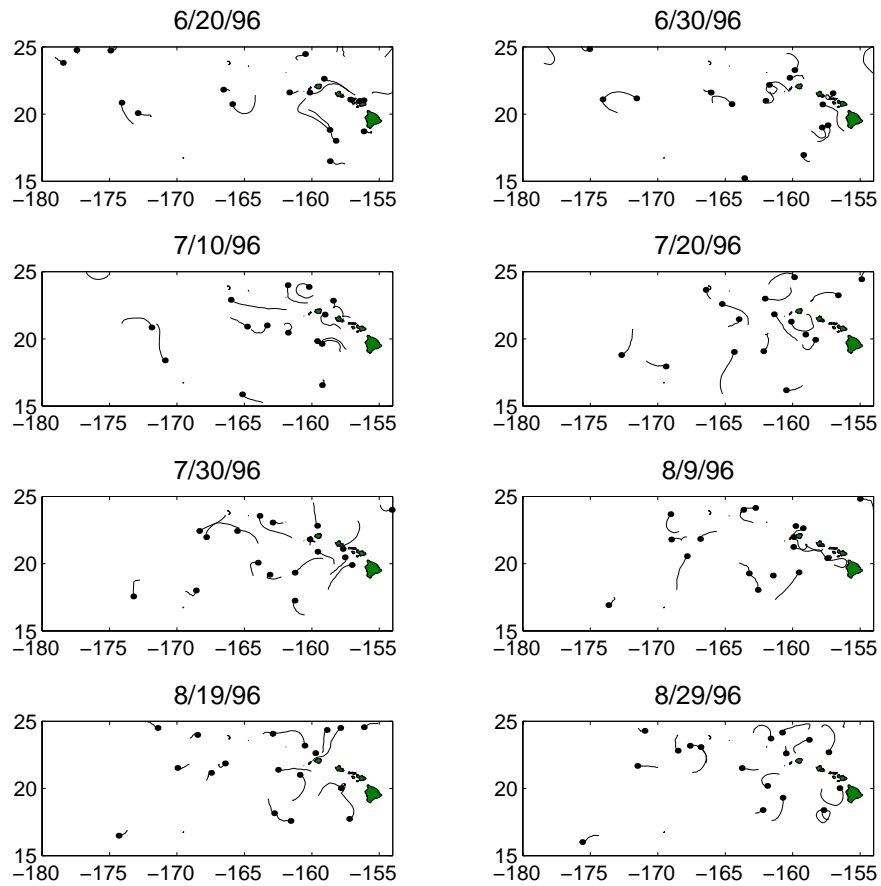


Figure 117: Ten-day snapshots of drifters. Dots show the location of the drifters on the given date; the tail shows the previous ten days of the drifters' trajectories.

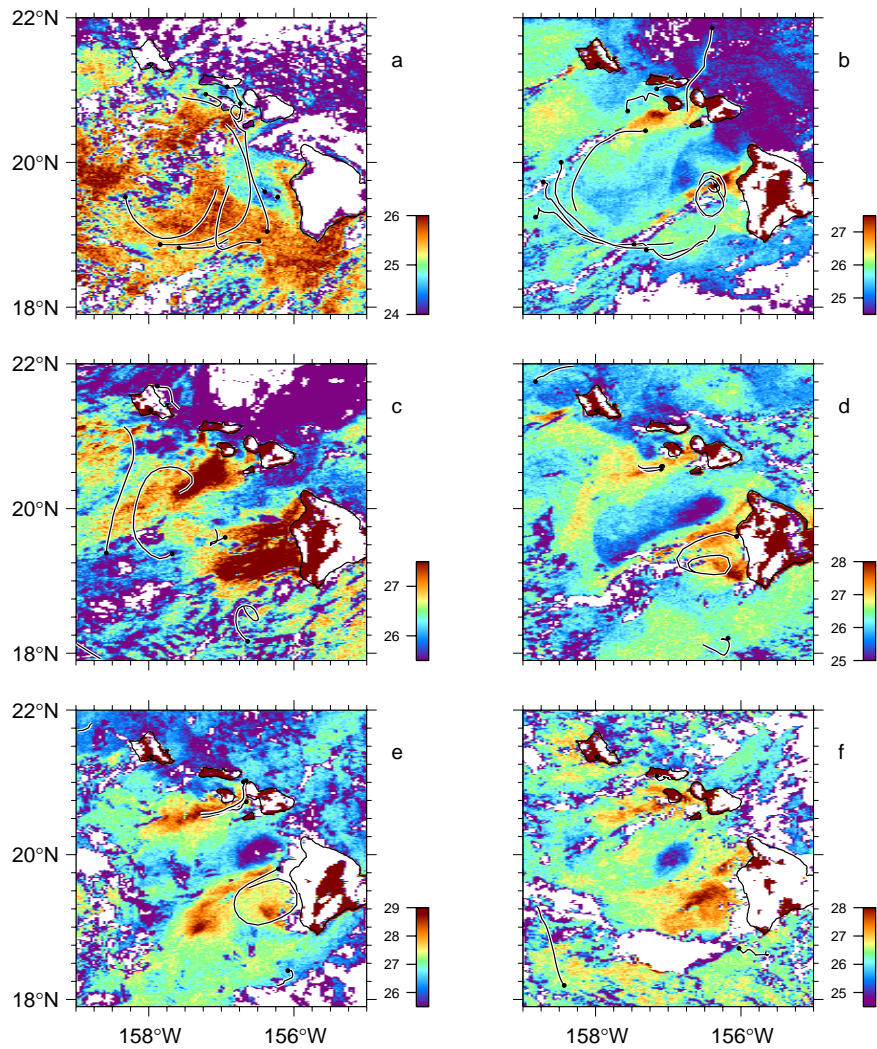


Figure 118: AVHRR SST images ( $^{\circ}\text{C}$ ), with concurrent drifter positions (points, with lines showing previous five days) overlaid. Temperatures colder than  $22^{\circ}\text{C}$  have been flagged as clouds (white). The images were taken on 18 April 1996 at 1736 UTC (a), 22 April at 2353 UTC (b), 13 May at 2327 UTC (c), 31 May at 2332 UTC (d), 5 June at 0029 UTC (e) and 18 June at 2338 UTC (f).

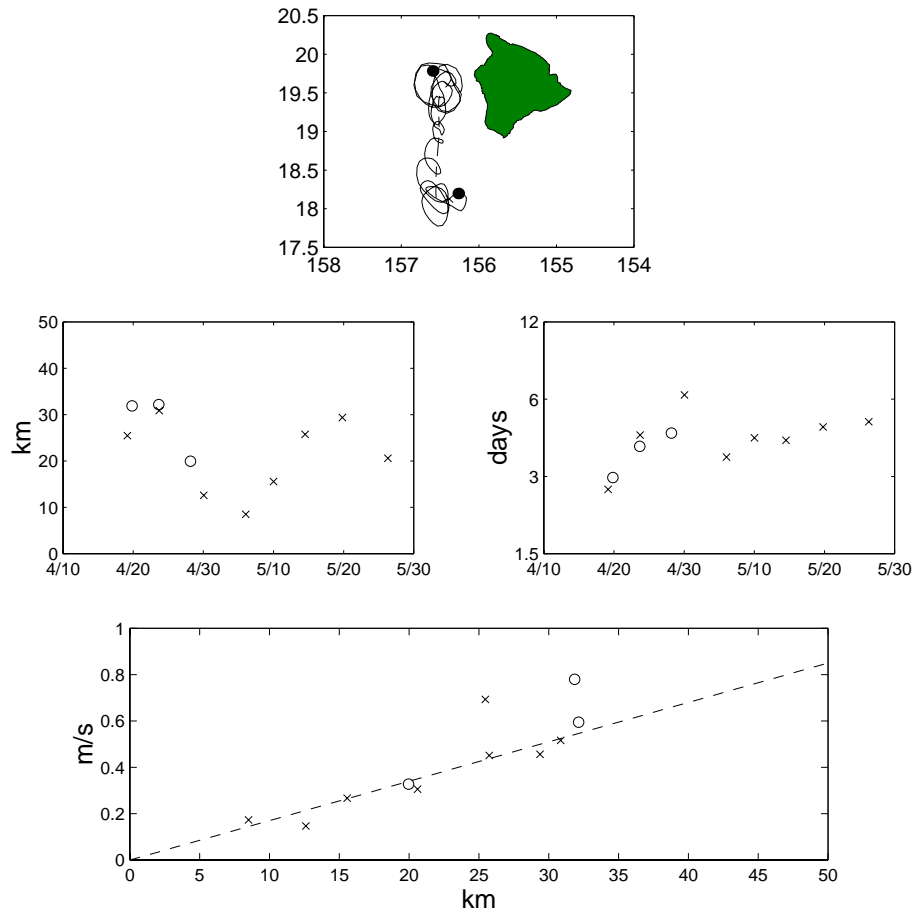


Figure 119: Orbital characteristics of drifters in C96b.

*Top:* trajectories of drifters around eddy (solid lines), with dots marking the location of the drifter when it left the eddy. The dashed line is the path of the eddy center, with an **x** marking its last known location.

*Middle, left:* orbital radius vs. time. Different symbols are used for different drifters.

*Middle, right:* orbital period vs. time.

*Bottom:* orbital speed vs. radius. The dashed line is for solid-body rotation at a period of 4.28 days.

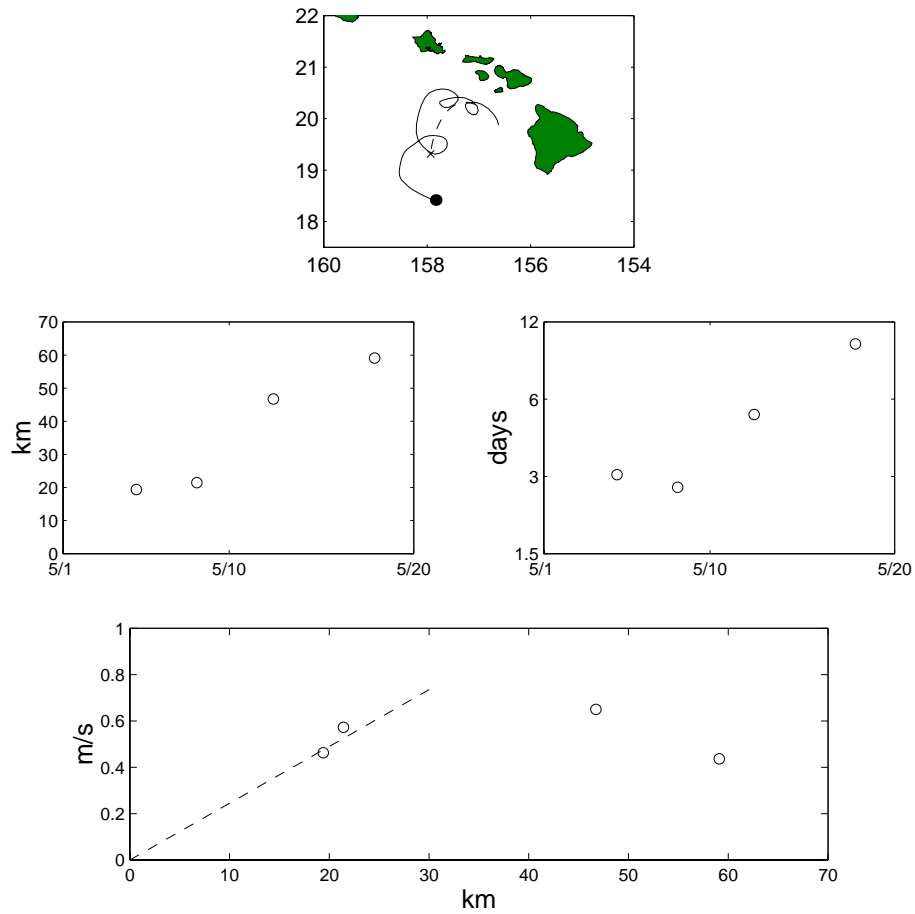


Figure 120: Orbital characteristics of a drifter in C96a.

*Top:* trajectory of drifter around eddy (solid lines), with a dot marking the location of the drifter when it left the eddy. The dashed line is the path of the eddy center, with an **x** marking its last known location.

*Middle, left:* orbital radius vs. time.

*Middle, right:* orbital period vs. time.

*Bottom:* orbital speed vs. radius. The dashed line is for solid-body rotation at a period of 2.97 days.

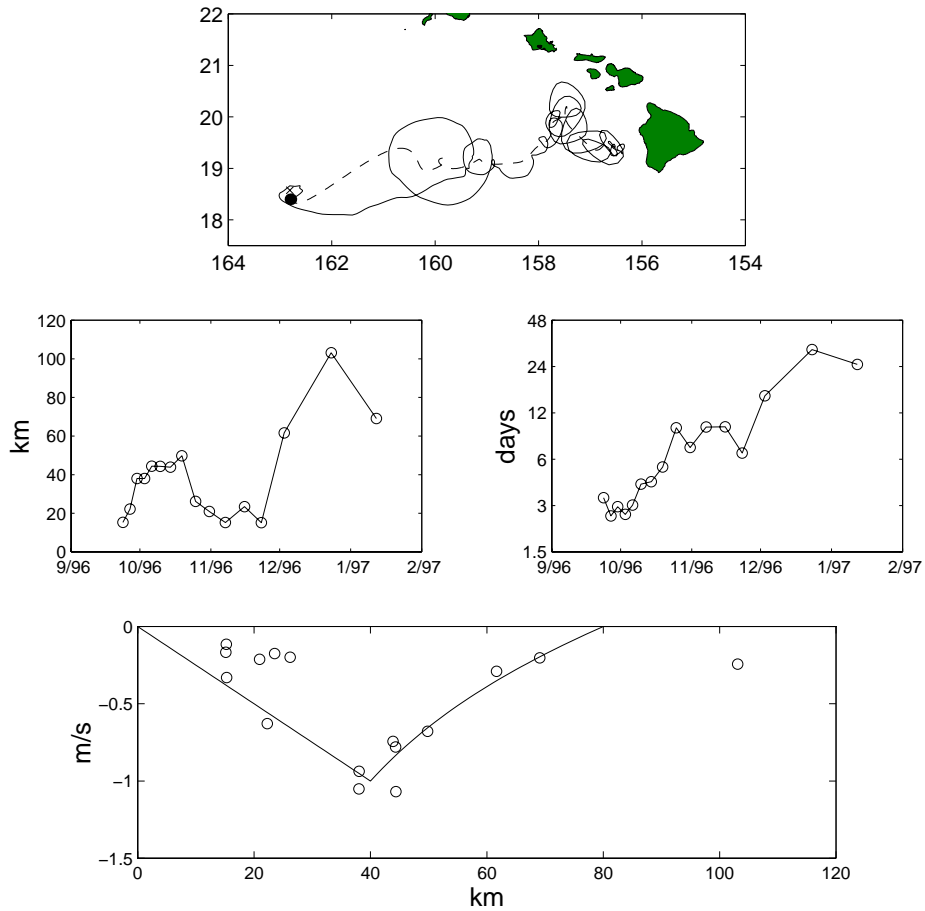


Figure 121: Orbital characteristics of a drifter in AC96c.

*Top:* trajectory of drifter around eddy (solid line), with a dot marking the location of the drifter when it left the eddy. The dashed line is the path of the eddy center, with an **x** marking its last known location.

*Middle, left:* orbital radius vs. time.

*Middle, right:* orbital period vs. time.

*Bottom:* orbital speed vs. radius. The lower dashed line is for solid-body rotation at a period of 2.9 days. The upper dashed line is for solid-body rotation at a period of 8.3 days.

APPENDIX D  
EDDY DISSIPATION

*A simple model for eddy spin-down, paramaterized in terms of entrainment, is presented.*

The core/shell model of an eddy's azimuthal velocity structure is given by (B.9). With the explicit inclusion of a momentum flux, the vorticity discontinuities would rapidly smooth, and on a longer time scale the eddy would spin down as shell vorticity diffuses outward, the peak azimuthal speed drops, and the core vorticity lowers in magnitude. In this appendix, a spin-down model is described which was designed to implicitly simulate this process, while retaining the analytically simple core/shell structure. This was done by formulating vorticity diffusion in terms of an entrainment rate. As the core gains mass, angular momentum conservation requires its vorticity to approach zero.

The shell radius  $r_o$  is assumed to expand at a rate set by the magnitude of the shell's vorticity:

$$\frac{d}{dt}r_o = \sqrt{|\zeta_o|A}, \quad (\text{D.1})$$

where  $A$  is a viscosity constant. This formulation assumes that the more irrotational the shell is, the slower its vorticity will diffuse outward. The entrainment rate into the shell from outside is then

$$\frac{d}{dt}M(r = r_o) = 2\pi\rho r_o H_1 \sqrt{|\zeta_o|A}, \quad (\text{D.2})$$

i.e. the side area of the eddy at  $r = r_o$  times the density, times  $dr_o/dt$ . The shell vorticity  $\zeta_o$  is related to the core vorticity  $\zeta$  by

$$\zeta_o = -\frac{r_i^2}{r_o^2 - r_i^2}\zeta. \quad (\text{D.3})$$

Substitution gives an entrainment rate

$$\frac{d}{dt}M(r = r_o) = 2\pi\rho r_i H_1 \sqrt{\frac{|\zeta|A}{1 - r_i^2/r_o^2}}. \quad (\text{D.4})$$

Similarly, the core radius  $r_i$  is assumed to expand at a rate set by the magnitude of the vorticity jump across  $r = r_i$ :

$$\frac{d}{dt}r_i = \sqrt{|\zeta - \zeta_o|A}. \quad (\text{D.5})$$

The entrainment rate into the core is then

$$\frac{d}{dt}M_i = 2\pi\rho r_i [H_1 + h(r = r_i)] \sqrt{\frac{|\zeta|A}{1 - r_i^2/r_o^2}}. \quad (\text{D.6})$$

This fluid must come from the surrounding shell of opposite-signed vorticity. Thus, the net change in the shell's mass is (D.4 minus (D.6):

$$\frac{d}{dt}M_o = -2\pi\rho r_i h(r = r_i) \sqrt{\frac{|\zeta(t)|A}{1 - r_i^2/r_o^2}}. \quad (\text{D.7})$$

The assumptions of the model lead to an asymmetry between cyclonic and anticyclonic eddies. For cyclones ( $h < 0$  at  $r = r_i$ ), the side area of the core is relatively small; the shell gains fluid from the outside more rapidly than the core gains fluid from the shell. However, anticyclones ( $h > 0$  at  $r = r_i$ ) have a relatively large side area, so the shell loses fluid to the core more rapidly than it is replaced from the outside. Consequently, the core of an anticyclone spins down more quickly than that of a cyclone.

For a given viscosity  $A$ , the entrainment rates were numerically evaluated in incremental steps. After each step, conservation of net angular momentum was used to determine the new core vorticity. The shell vorticity was set by  $\zeta$ ,  $r_i$  and  $r_o$ . The value of  $A$  was tuned to match the observed decrease in a drifter within eddy AC94b.

## APPENDIX E

### VORTEX MERGING IN A $1\frac{1}{2}$ -LAYER FLUID ON AN $f$ -PLANE

*An analytical model of eddy merging is presented, with the accompanying mathematical development focused upon the appropriate conservation laws for merging and the characteristics of the merged vortex. This appendix is a slightly modified form of a paper by Rick Lumpkin, Pierre Flament, Rudolf Kloosterziel and Laurence Armi submitted to J. Phys. Ocean. Notes and Correspondences.*

#### E.1 Introduction

Liked-sign vortices spontaneously merge in rotating tanks [Nof and Simon, 1987; Griffiths and Hopfinger, 1987] and in the ocean [Cresswell, 1982; Tokos *et al.*, 1994]. Merging has been numerically modeled in a wide range of settings [Melander *et al.*, 1988; Verron and Valcke, 1994; Carton and Bertrand, 1994; Valcke and Verron, 1997]. However, because most of these experiments have focused on quantifying the space and time scales in which merging occurs, less progress has been made in understanding the kinematics of merging. How do the basic conservation laws govern the characteristics of the merged vortex? Existing analytical models which conserve mass and angular momentum find that the merged vortex has more energy than the initial vortices [Gill and Griffiths, 1981]. These results have lead some researchers to conclude that the complete, unforced merging of reduced gravity vortices is not energetically possible [Cushman-Roisin, 1989; Dewar and Killworth, 1990; Pavia and Cushman-Roisin, 1990].

In this paper, the mass, angular momentum and energy budgets of merging vortices are examined with a simple analytical model. It is shown that the absolute angular momentum of vortices and surrounding fluid is equal to the background angular momentum (the angular momentum in the absence of vortices), plus the sum of the vortices' relative angular momentum (the angular momentum seen in the rotating reference frame). Consequently, conservation of the absolute angular momentum requires conservation

of the relative momentum of the vortices. It is concluded that free vortex merging is not energetically prohibited; two possible merging scenarios are suggested based on the conservation budgets.

## E.2 Development of the model

The model has two layers: the upper layer (density  $\rho$ ) extends from  $z = 0$  to  $z = -H_1$ , and the lower layer (density  $\rho + \delta\rho$ ) extends from  $z = -H_1$  to  $z = -H_2$  (Fig. 122). The system is rotating at angular speed  $\Omega$  (Fig. 123). Before merging, there are two identical, azimuthally-symmetric vortices in the upper layer, touching at a single point. It is assumed that the fluid is reorganized into quiescent fluid surrounding a single vortex, and that the final vortex has the same velocity structure as its parents; for example, vortices in solid-body rotation merge to produce a vortex also in solid-body rotation (though not necessarily rotating at the same rate).

### E.2.1 Mass and angular momentum of an isolated vortex

Consider a vortex in the upper layer with radius  $r_o$ , extending vertically from the surface  $z = \eta(r)$  to  $z = -H_1 - h(r)$  (Fig. 122). The surface deflection  $\eta$  is related to the azimuthal speed  $v$  by cyclogeostrophy:

$$\frac{v^2}{r} + 2\Omega v = g\partial_r\eta, \quad (\text{E.1})$$

where  $r$  is the radial distance from the vortex center and  $g$  is gravity. Since there are no horizontal pressure gradients in the lower layer,

$$h = \frac{g}{g'}\eta, \quad (\text{E.2})$$

where the reduced gravity  $g'$  is  $g'/g = \delta\rho/\rho$ . The total mass of the vortex is

$$M = m_H + m_h + m_\eta, \quad (\text{E.3})$$

where

$$m_H = \pi \rho r_o^2 H_1, \quad m_h = 2\pi \rho \int_0^{r_o} dr r h(r), \quad m_\eta = 2\pi \rho \int_0^{r_o} dr r \eta(r). \quad (\text{E.4})$$

With (E.2), it follows that

$$m_\eta = \frac{\delta \rho}{\rho} m_h. \quad (\text{E.5})$$

In the rotating frame, the relative angular momentum <sup>1</sup> of the vortex is

$$L = 2\pi \rho \int_0^{r_o} dr r^2 [H_1 + h(r) + \eta(r)] v(r). \quad (\text{E.6})$$

In the inertial frame, the vortex is centered at  $\mathbf{R} = \mathbf{R}_o$  (the position of  $\mathbf{R} = 0$ , the axis of rotation, does not affect the solutions). Its absolute angular momentum is

$$\tilde{L} = L + M R_o^2 \Omega + (I_H + I_h + I_\eta) \Omega \quad (\text{E.7})$$

(the tilde indicating absolute quantities expressed in the inertial frame), where the moments of inertia are

$$I_H = 2\pi \rho \int_0^{r_o} dr r^3 H_1 = \frac{1}{2} m_H r_o^2, \quad I_h = 2\pi \rho \int_0^{r_o} dr r^3 h(r), \quad I_\eta = 2\pi \rho \int_0^{r_o} dr r^3 \eta(r). \quad (\text{E.8})$$

Using (E.2), it follows that

$$I_\eta = \frac{\delta \rho}{\rho} I_h. \quad (\text{E.9})$$

### E.2.2 Angular momentum of vortices immersed in quiescent fluid

In the absence of vortices, the absolute angular momentum of the quiescent background state would be

$$\tilde{L}_{back} = [H_1 \rho + (H_2 - H_1)(\rho + \delta \rho)] \int_A dA R^2 \Omega \quad (\text{E.10})$$

---

<sup>1</sup>Specifically, the vertical component of the angular momentum vector

where the integral is taken over an arbitrary finite domain  $A$ .

In the presence of  $N$  vortices (denoted by the subscript  $\alpha = 1 \dots N$ ), the absolute angular momentum of the quiescent surrounding fluid is

$$\tilde{L}_* = \tilde{L}_{back} - \sum_{\alpha=1}^N \left\{ \left[ m_{H,\alpha} + \frac{\rho + \delta\rho}{\rho} m_{h,\alpha} \right] R_\alpha^2 + \left[ I_{H,\alpha} + \frac{\rho + \delta\rho}{\rho} I_{h,\alpha} \right] \right\} \Omega. \quad (\text{E.11})$$

This is less than  $\tilde{L}_{back}$  because the vortices occupy volume below  $z = 0$ .

The absolute angular momentum of the total system (with  $N$  vortices) is obtained by combining (E.7) and (E.11):

$$\tilde{L}_{tot} = \tilde{L}_* + \sum_{\alpha} \tilde{L}_{\alpha} = \tilde{L}_{back} + \sum_{\alpha=1}^N \left\{ L_{\alpha} + \left[ \left( m_{\eta,\alpha} - \frac{\delta\rho}{\rho} m_{h,\alpha} \right) R_{\alpha}^2 + \left( I_{\eta,\alpha} - \frac{\delta\rho}{\rho} I_{h,\alpha} \right) \right] \Omega \right\}. \quad (\text{E.12})$$

Vortices extend to height  $\eta$  above  $z = 0$ ; revolution and rotation of this mass at speed  $\Omega$  adds angular momentum to the background state. Similarly, vortices extend a distance  $h_{\alpha}$  into the lower layer; because this fluid is lower in density, it subtracts angular momentum from the background state. Using (E.5) and (E.9), (E.12) simplifies to

$$\tilde{L}_{tot} = \tilde{L}_* + \sum_{\alpha} \tilde{L}_{\alpha} = \tilde{L}_{back} + \sum_{\alpha} L_{\alpha}. \quad (\text{E.13})$$

Angular momentum added by surface bulges is equal to angular momentum subtracted by layer interface bulges, and they cancel. The absolute angular momentum of the entire system differs from the angular momentum of the background state only by the sum of the relative angular momentum of the vortices.

### *E.2.3 Energy of vortices*

The kinetic energy of a vortex is

$$KE = 2\pi\rho \int_0^{r_o} dr r [H_1 + h(r) + \eta(r)] \frac{1}{2} v^2, \quad (\text{E.14})$$

and the potential energy is

$$PE = 2\pi\rho \int_0^{r_o} dr r [h(r) + \eta(r)] \frac{1}{2} g\eta. \quad (\text{E.15})$$

The net energy  $E = KE + PE$  may be related to the relative angular momentum as follows. The relative angular momentum  $L$  is given by (E.6). From cyclogeostrophy (E.1),

$$v = -\frac{1}{2\Omega} \left( \frac{v^2}{r} - g\partial_r\eta \right). \quad (\text{E.16})$$

Substitution yields

$$-\Omega L = 2\pi\rho \int_0^{r_o} dr r (H_1 + h + \eta) \left( \frac{1}{2}v^2 - \frac{1}{2}rg\partial_r\eta \right). \quad (\text{E.17})$$

The term containing  $\partial_r\eta$  may be integrated by parts, yielding

$$-\Omega L = 2\pi\rho \int_0^{r_o} dr r \left[ (H_1 + h + \eta) \frac{1}{2}v^2 + (2H_1 + h + \eta) \frac{1}{2}g\eta \right]. \quad (\text{E.18})$$

Using (E.4), (E.14) and (E.15), this becomes

$$E = -\Omega L - gH_1 m_\eta. \quad (\text{E.19})$$

The total energy of  $N$  vortices is then

$$E_{tot} = - \sum_{\alpha=1}^N (\Omega L_\alpha + gH_1 m_{\eta,\alpha}). \quad (\text{E.20})$$

### E.3 Vortex merging

When two vortices (denoted by subscripts  $a$  and  $b$ ) merge to produce a single vortex ( $c$ ), mass conservation requires

$$M_c = M_a + M_b \quad (\text{E.21})$$

where the mass is given by (E.3).

By definition, the background angular momentum  $\tilde{L}_{back}$  remains unchanged. Thus, from (E.13), conservation of angular momentum requires

$$L_c = L_a + L_b. \quad (\text{E.22})$$

Conservation of the absolute angular momentum reduces to conservation of the relative angular momentum of the vortices.

Energy conservation requires  $E_c = E_a + E_b$ . Using (E.20), this becomes

$$\Omega L_c + gH_1 m_{\eta,c} = \Omega L_a + gH_1 m_{\eta,a} + \Omega L_b + gH_1 m_{\eta,b}. \quad (\text{E.23})$$

From (E.22), it follows that angular momentum and energy can be simultaneously conserved when either

$$m_{\eta,c} = m_{\eta,a} + m_{\eta,b} \quad (\text{E.24})$$

or  $H_1 = 0$ .

### *E.3.1 Solid-body vortices*

A solid-body vortex has the velocity structure  $v(r) = \omega r$ , where  $\omega$  is constant. By imposing  $\eta = 0$  at  $r = r_o$ , cyclogeostrophy (E.1) may be integrated to yield

$$\eta(r) = -\frac{1}{2g}\omega(2\Omega + \omega)(r_o^2 - r^2), \quad r \leq r_o. \quad (\text{E.25})$$

The relative angular momentum is

$$L = (I_H + I_h + I_\eta)\omega. \quad (\text{E.26})$$

Consider two solid-body vortices ( $a$  and  $b$ ) merging to produce vortex  $c$ , assumed to be in solid-body rotation. Given  $\omega_a$ ,  $\omega_b$ ,  $r_a$  and  $r_b$ , two independent constraints determine  $\omega_c$  and  $r_c$ . This leads us to the dilemma which faced Pavia and Cushman-Roisin [1990]: which of the three constraints (mass, angular momentum and energy conservation) should be applied? Following Pavia and Cushman-Roisin, two separate merging scenarios are considered; in each, two of these properties are conserved, and the budget of the third is examined. Physical interpretations of the results will be discussed in the final section. This development is specifically restricted to the particular case of identical merging vortices ( $\omega_a = \omega_b$ ,  $r_a = r_b$ )

### *Conserving mass and angular momentum*

Fig. 124 shows the values of  $\omega_c$  and  $r_c$  which conserve mass and angular momentum. Several curves are shown, each corresponding to a fixed ratio of  $r_a$  to the internal Rossby radius  $R_d$ :

$$R_d = \frac{1}{2\Omega} \sqrt{\frac{g'H_1}{1 + g'/g}}. \quad (\text{E.27})$$

In the limit  $r_a/R_d \rightarrow \infty$ , the vortices are anticyclonic lenses ( $H_1 \ll h_{a,c}$ ); in particular, zero PV lenses ( $\omega_1 = -\Omega$ ) merge such that

$$\omega_c = \frac{2}{3}\omega_a, \quad r_c = \sqrt{\frac{3}{2}}r_a. \quad (\text{E.28})$$

The bottom panel of Fig. 124 shows the ratio of final energy  $E_c$  to initial energy  $2E_a$ . For lens-shaped vortices, energy is conserved. However, for finite  $r_a/R_d$ , energy is lost in the merging; this approaches 50% in the limit  $r_a/R_d \rightarrow 0$  (in this limit, the vortices are cylinders).

### *Conserving angular momentum and energy*

Fig. 125 shows the values of  $\omega_c$  and  $r_c$  which conserve angular momentum and energy. Compared to the mass-conserving scenario (Fig. 124), the change in period ( $\omega_a/\omega_c$ ) is smaller for a given  $r_a/R_d$ , and decreases with decreasing  $r_a/R_d$ . The final radius is smaller than in the mass-conserving scenario; in the limit  $r_a/R_d \rightarrow 0$ ,  $r_c/r_a \rightarrow 2^{1/4} (\approx 1.19)$ .

For finite  $r_a/R_d$ , the final vortex has less mass than the initial two vortices. In the limit  $r_a/R_d \rightarrow 0$ , the mass loss is  $M_c/2M_a = 1/\sqrt{2} (\approx 0.71)$ . Mass is conserved in the lens-shaped limit  $r_a/R_d = \infty$ .

### E.3.2 Vortices with finite-shear edges

When  $H_1 > 0$  in the solid-body model, the vortex has an infinite-shear edge separating vortex fluid from upper-layer fluid of identical density. This is not a stable configuration: turbulent mixing will rapidly smear the edge vorticity into a shell surrounding the solid-body core. Within this shell,  $v(r)$  diminishes with increasing  $r$  (c.f. Fig. 3 of Griffiths and Hopfinger [1987]). If this shell is included in the vortices' structure, how does it affect the characteristics of the final vortex? To address this question, vortices are considered with the velocity structure

$$v(r) = \begin{cases} \omega r, & r \leq r_i, \\ -\left(\frac{r_i^2}{r_o^2 - r_i^2}\right) \omega \left(r - \frac{r_o^2}{r}\right), & r_i < r \leq r_o, \\ 0, & r_o < r. \end{cases} \quad (\text{E.29})$$

The azimuthal speed  $v$  is continuous at  $r = r_i, r_o$  (Fig. 126). The solid-body core extends to  $r = r_i$ , and is surrounded by a constant-vorticity shell extending to  $r = r_o$ . The ratio of shell vorticity  $\zeta_o$  to core vorticity  $\zeta_i$  is

$$\frac{\zeta_o}{\zeta_i} = -\frac{r_i^2}{r_o^2 - r_i^2}. \quad (\text{E.30})$$

In the limit  $r_o \gg r_i$ , the outer shell is nearly irrotational and the vortex becomes Rankine-like. If  $r_o < \sqrt{2}r_i$ , the shell vorticity is greater in magnitude than the core vorticity. In the limit  $r_o \rightarrow r_i$ , the velocity profile reverts to the solid-body model.

Initially, I had planned to use conservation of mass, angular momentum and energy to determine  $\omega_c$ ,  $r_{i,c}$  and  $r_{o,c}$ . However, except in a particular limit (described below), all constraints could not be simultaneously satisfied, presumably due to their nonlinearity. Paralleling the solid-body case, two merging scenarios are considered: one in which mass is conserved, and the other in which energy is conserved. In both scenarios, it is assumed that the mass  $M_i$  of the solid-body core is conserved:

$$M_i = 2\pi\rho \int_0^{r_i} dr r [H_1 + h_i(r) + \eta_i(r)]. \quad (\text{E.31})$$

This additional constraint demands that fluid parcels retain the sign of their vorticity, i.e. the core of the merged vortex is the fused cores of the initial vortices. In the energy-conserved scenario, it demands that mass changes occur for shell fluid. Unlike total mass, (E.31) can be conserved simultaneously with energy; in this scenario, mass changes are associated with shell fluid.

### *Conserving mass and angular momentum*

If net mass and angular momentum are conserved, the initial vortices are identical, and  $r_{o,a}/r_{i,a} = 10$ , Fig. 127 shows  $\omega_c$ ,  $r_{i,c}$  and  $r_{o,c}$  as functions of  $\omega_a/\Omega$ . The curves closely resemble those of Fig. 124; they converge for  $r_{i,a}/R_d \rightarrow 0$  (in this limit, the vortices are cylinders). Due to the presence of the opposite-vorticity shell, the period jump  $\omega_a/\omega_c$  is always closer to 2 and the radius jump  $r_{i,c}/r_{i,a}$  is always closer to  $\sqrt{2}$  than for the solid-body counterpart to this scenario.

The bottom panel of Fig. 127 shows the ratio of final energy  $E_c$  to initial energy  $2E_a$ . Energy is lost for small  $r_{i,a}/R_d$ ; this loss approaches 0 for  $r_{i,a} \gg R_d$ . The energy loss is nearly independent of  $\omega_a/\Omega$ . If  $r_{i,a}/R_d \geq 8$ , energy is conserved within 0.1 % for all values of  $\omega_a/\Omega$ .

Fig. 128 shows how the characteristics of the merged vortex vary as a function of  $r_{o,a}/r_{i,a}$ , for  $\omega_a/\Omega = -1$ . For vortices with nearly irrotational shells ( $r_{o,a} \gg r_{i,a}$ ), the merged vortex has a core period nearly double that of the original vortices ( $\omega_a/\omega_c \sim 2$ ) and inner and outer radii larger by  $\sim \sqrt{2}$ . The dependence of the solutions on  $r_{i,a}/R_d$  becomes increasingly significant as  $r_{o,a} \rightarrow r_{i,a}$  (the solid-body limit), and energy is lost (particularly for small  $r_{i,a}/R_d$ ).

### *Conserving angular momentum and energy*

Fig. 129 shows the characteristics of the merged vortex if angular momentum and energy are conserved. As in the previous scenario, the initial vortices are assumed to be identical and  $r_{o,a}/r_{i,a} = 10$ . Compared to the solid-body counterpart of this scenario (Fig. 125),  $\omega_a/\omega_c$  is closer to 2. The increase in the shell radius  $r_{o,c}/r_{o,a}$  is closer to  $\sqrt{2}$  than in the solid-body case, and is only weakly a function of  $\omega_a/\Omega$ .

Mass is conserved for large vortices ( $r_{i,a} \gg R_d$ ), but for smaller vortices the final state has less mass. This loss is approximately independent of  $\omega_a/\Omega$ ; for  $r_{i,a} = R_d$ , 7.6% of the mass is lost in the merging.

Fig. 130 shows the characteristics of the merged vortex as a function of  $r_{o,a}/r_{i,a}$ , for  $\omega_a/\Omega = -1$ . For vortices with nearly irrotational shells, mass is conserved and the solutions are identical to those of the previous scenario. The mass loss exceeds 10% for shell radius smaller than  $r_{o,a}/R_d \sim 10$ .

## **E.4 Discussion**

In this model of vortex merging, potential vorticity conservation has been replaced by the constraints that the integrated angular momentum of the system is conserved, and the vortices preserve a particular velocity structure. These assumptions require that some physical process alters the PV of individual fluid parcels during merging. Nof [1986; 1988b] has suggested this is done by turbulent mixing at the vortices' contact point, where strong opposite-signed vorticity is entrained as the vortices enmesh each other. In numerical models, the sharp vorticity gradients are rapidly smoothed by diffusion [Melander *et al.*, 1988]. Laboratory observations [Nof and Simon, 1987] support Nof's [1986] hypothesis that PV alteration is an essential feature of vortex merging.

Although the surrounding fluid is assumed to remain quiescent, fluid columns un-

derlying the vortices may be compressed or stretched in the merging. A column of quiescent fluid beneath a vortex bears potential vorticity  $2\Omega/(H_2 - H_1 - h)$ , where  $h$  is the downward displacement of the layer interface induced by the vortex. If the merging causes  $h$  to increase by  $\Delta h$ , the underlying column must gain anticyclonic vorticity  $\zeta$ ,

$$\frac{\zeta}{2\Omega} = -\frac{\Delta h}{H_2 - H_1 - h}, \quad (\text{E.32})$$

in order to conserve its angular momentum. Thus, our assumption of quiescence is valid in the limit  $H_2 - H_1 - h \gg \Delta h$ , and exact in the  $1\frac{1}{2}$ -layer limit  $H_2 \rightarrow \infty$ . While this limit is appropriate for many oceanic applications, it does not apply to lens-shaped vortices created by the collapse of fluid cylinders (such as those of Nof and Simon’s [1987] experiment). For these vortices, motion within the surrounding fluid may significantly affect the energy budget [Dewar and Killworth, 1990].

In their examination of lens-shaped vortex merging, Pavia and Cushman-Roisin [1990] conserved the mass and energy of the initial vortices, and showed that the absolute angular momentum of the vortices is not conserved. However, in this derivation the absolute angular momentum of the entire system was conserved, including the fluid which is quiescent in the rotating frame. This surrounding fluid plays a significant role in angular momentum conservation, which leads us to conclude that there is no “energy paradox” [Cushman-Roisin, 1989] inherent in lens-shaped vortex merging. To highlight the surrounding fluid’s role, consider the following thought experiment: a pair of two-dimensional cylinders of density  $\rho$ , mass  $m_a$  and radius  $r_a$  in solid-body rotation at rate  $\omega_a$  touch at the center of a tank which is rotating at rate  $\Omega$ . The cylinders are surrounded by fluid of density  $\rho_*$ . Some time later, they have merged to produce a single cylinder of the same density, with mass  $m_c = 2m_a$ , radius  $r_c$  and rotation rate  $\omega_c$ . It is centered on the contact point of its parents (the tank center). Conservation of

mass requires  $r_c = \sqrt{2}r_a$ , and angular momentum conservation requires

$$\omega_c = \frac{1}{2} \left[ \left( 1 - \frac{\rho_*}{\rho} \right) \Omega + \omega_a \right]. \quad (\text{E.33})$$

In the absence of surrounding fluid,  $\rho_* = 0$ , and (E.33) becomes

$$\omega_c = \frac{1}{2} (\Omega + \omega_a). \quad (\text{E.34})$$

This expression is analogous to the formulation of angular momentum conservation in Cushman-Roisin [1989] and Pavia and Cushman-Roisin [1990]. When  $\rho_* = 0$ , the thought experiment is describing coalescing fixed-height disks on a rotating table. To an observer in the rotating frame, the rotation rate of the resulting disk is more positive (for positive  $\Omega$ ) than it would be in the absence of rotation, due to Coriolis deflection applying a net torque on the coalescing fluid parcels (c.f. Feynman *et al.* [1987], pg. 19-8). However, if  $\rho_* = \rho$ , (E.33) simplifies to

$$\omega_c = \frac{1}{2} \omega_a, \quad (\text{E.35})$$

i.e. the period doubles and relative angular momentum is conserved. As the cylinders coalesce, they lose the absolute angular momentum associated with revolution about their joint center of mass, but this is balanced by the angular momentum gained by the displaced quiescent fluid. In the rotating frame, Coriolis deflection of the coalescing parcels is balanced by a pressure gradient in the surrounding quiescent fluid [Rossby, 1936; Rossby, 1948].

As shown in section E.3.1, solid-body vortices can conserve mass, angular momentum and energy only if the upper-layer depth  $H_1 = 0$ . If  $H_1$  is nonzero, energy conservation is independent from mass and angular momentum conservation. The three constraints cannot then be simultaneously satisfied. Two merging scenarios were considered, one in which mass is conserved, and the other in which energy is conserved (with angular

momentum conserved in both). If mass is conserved, the final vortex has less total energy than the initial vortices. These solutions are thus “energetically allowable” [Dewar and Killworth, 1990] in the sense that an external energy source is not required. Essentially, these solutions are analogous to the classical Rossby adjustment problem, for which the steady-state solution contains only 1/3 of the initial energy (c.f. Gill [1982], pp. 191–203). For the adjustment problem, and presumably for this merging scenario, the remaining energy is removed via Poincaré wave radiation. In the alternative merging scenario, it was assumed that energy is conserved; as a result, the final vortex has less mass than its parents. Cushman-Roisin [Cushman-Roisin, 1989] has proposed a physical interpretation to this: merging vortices often eject fluid in narrow filaments as they axisymmetrize [Griffiths and Hopfinger, 1987; Melander *et al.*, 1988]. Because the filaments bear negligible energy and relative angular momentum but a significant fraction of the mass [Cushman-Roisin, 1989], they are implicitly modeled by relaxing the mass conservation constraint as done in this scenario [Pavia and Cushman-Roisin, 1990]. It should be noted for completeness that a third scenario was considered in which mass and energy are conserved; the final state contained more angular momentum than the initial state (132% more for  $r_a = R_d$ ), and thus did not represent a physically meaningful free merging scenario.

The two merging scenarios predict similar results for large vortices ( $r_a \gg R_d$ ); their predictions diverge as the vortex size is decreased relative to the Rossby radius. However, while the solid-body model may accurately simulate the structure of a frontal oceanic eddy [Gill and Griffiths, 1981], it does not describe the structure of typical  $1\frac{1}{2}$ -layer vortices. By including a nearly irrotational shell, mass, angular momentum and energy can be conserved in the merged vortex (see section E.3.2). However, if the shell is a narrow ring of relatively strong vorticity, solutions do not exist which simultaneously

conserve all three. In numerical experiments, narrow rings of this form oppose vortex merging, and can halt merging completely if the internal Rossby radius is large compared to the radius of the vortex core [Valcke and Verron, 1997]. Alternatively, merging may require energy or mass loss, as was the case with solid-body vortices. This loss rapidly becomes negligible if the outer core is large compared to the Rossby radius, especially if the inner core is also large.

It can be concluded that in two physically significant limits, vortices can conserve mass, angular momentum and energy when they merge. Processes such as Poincaré wave radiation, filamentation [Cushman-Roisin, 1989] or shielding [Valcke and Verron, 1997] may explain why all three cannot be simultaneously conserved over the full range of sizes considered here. By quantifying the characteristics of initial and merged vortices, future laboratory experiments could determine which merging scenario best describes the actual process, and add significant insight into the kinematics of vortex merging.

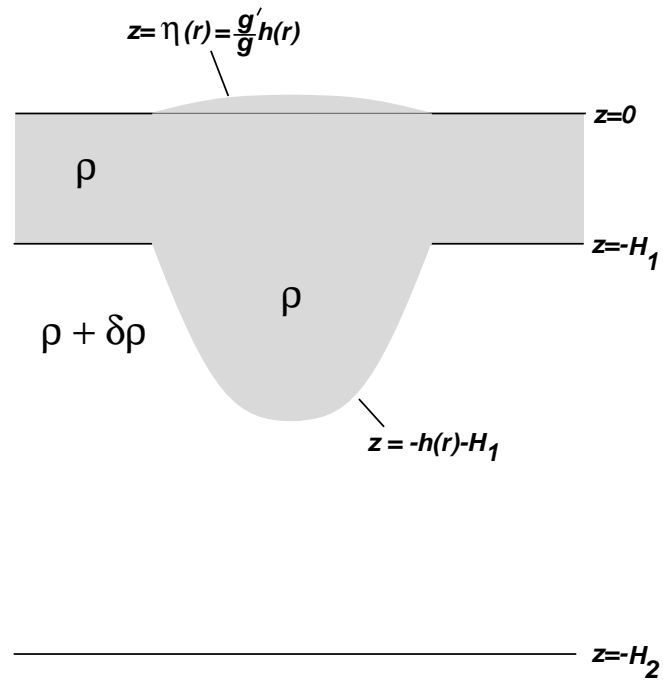


Figure 122: Side view of a vortex and surrounding quiescent fluid in the 2-layer model. For a vortex in solid-body rotation, the surface and interface displacements are parabolic, as sketched here.

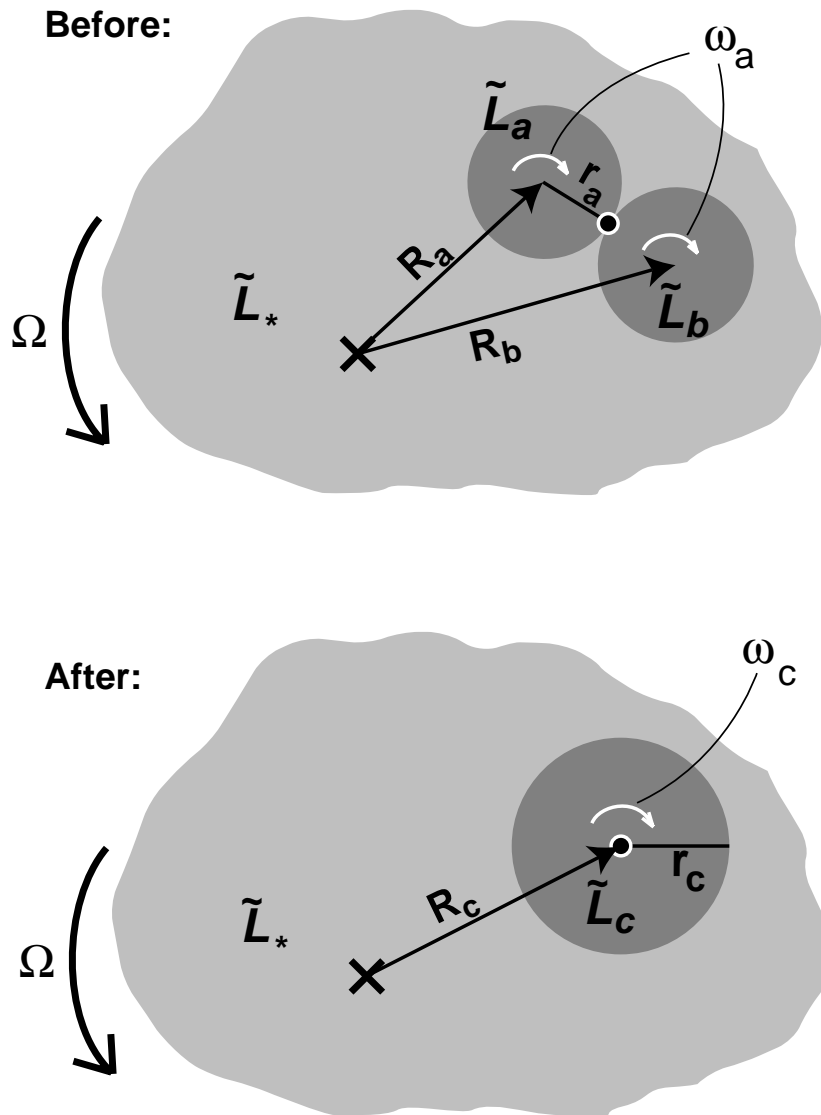


Figure 123: Top view of the merging model. The center of rotation of the system is at the black  $x$ .

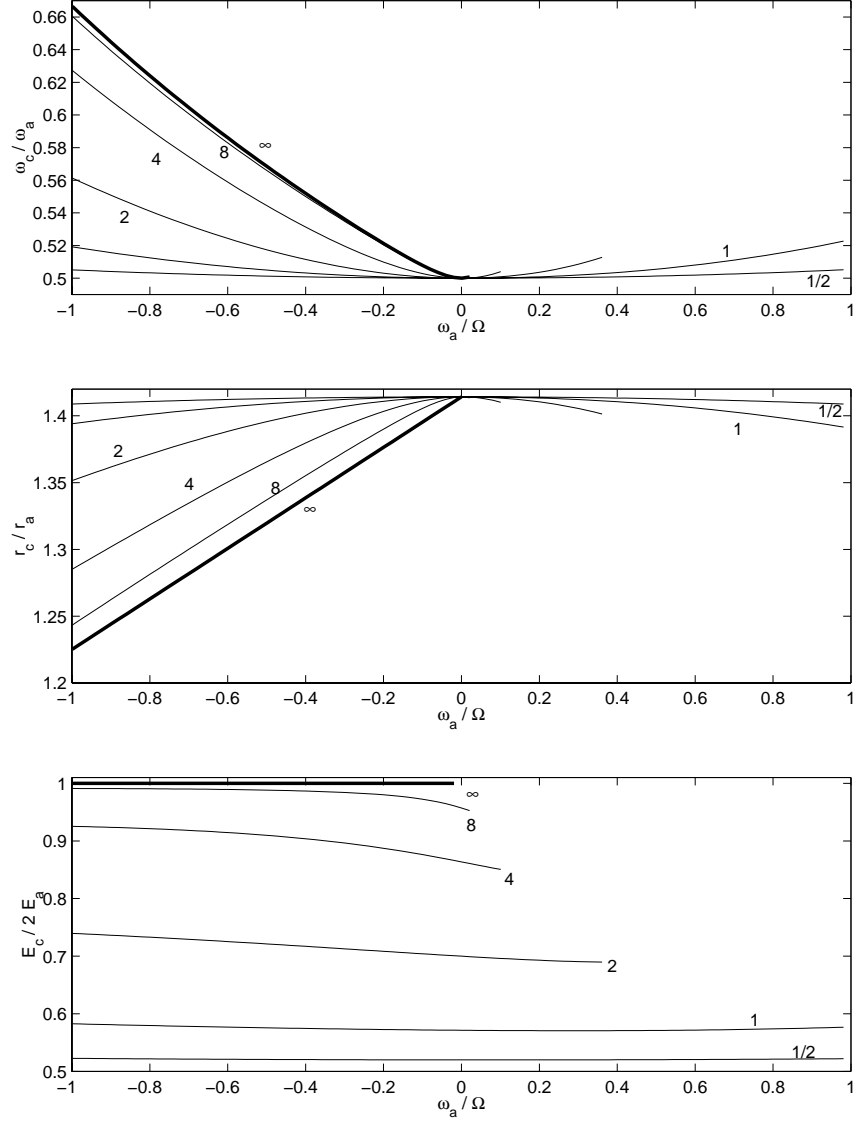


Figure 124: *Top:* ratio of final rotational frequency  $\omega_c$  to initial frequency  $\omega_a$  as a function of  $\omega_a/\Omega$ , for solid-body vortices which conserve mass and angular momentum when they merge. The label for each curve indicates the value of  $r_a/R_d$ . The heavy line gives the solution for a lens-shaped vortex ( $R_d = H_1 = 0$ ). Some curves end before reaching  $\omega_a = \Omega$ ; at greater values of  $\omega_a$ , the vortex has negative thickness  $H_1 + h + \eta$  at its center and is thus not geometrically valid.

*Middle:* ratio of final radius  $r_c$  to initial radius  $r_a$  as a function of  $\omega_a/\Omega$ .

*Bottom:* ratio of final energy  $E_c$  to initial energy  $2E_a$ . Except in the lens-shaped case, the merged vortex has less energy.

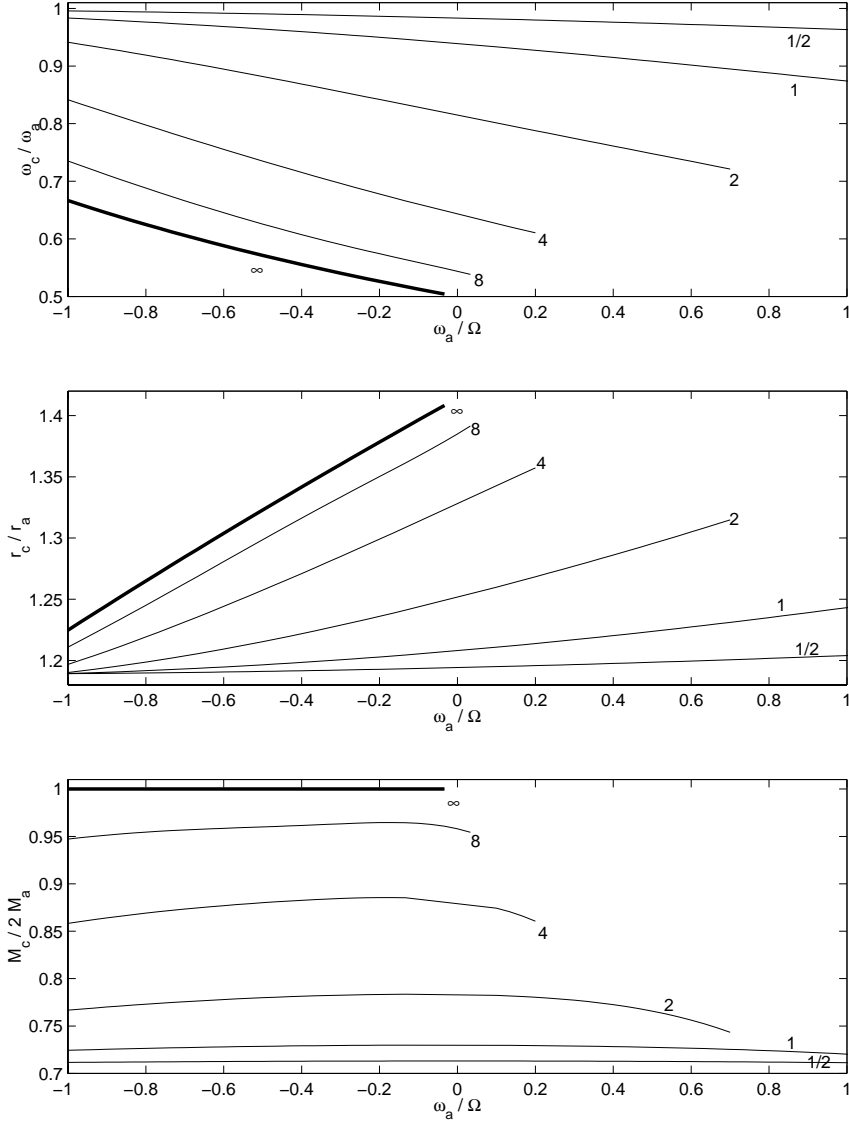


Figure 125: *Top:* ratio of final rotational frequency  $\omega_c$  to initial frequency  $\omega_a$  as a function of  $\omega_a/\Omega$ , for solid-body vortices which conserve angular momentum and energy when they merge. The label for each curve indicates the value of  $r_a/R_d$ . The heavy line gives the solution for a lens-shaped vortex ( $R_d = H_1 = 0$ ). Some curves end before reaching  $\omega_a = \Omega$ ; at greater values of  $\omega_a$ , the vortex has negative thickness  $H_1 + h + \eta$  at its center and is thus not geometrically valid.

*Middle:* ratio of final radius  $r_c$  to initial radius  $r_a$  as a function of  $\omega_a/\Omega$ .

*Bottom:* ratio of final mass  $M_c$  to initial mass  $2M_a$ . Except in the lens-shaped case, the merged vortex has less mass.

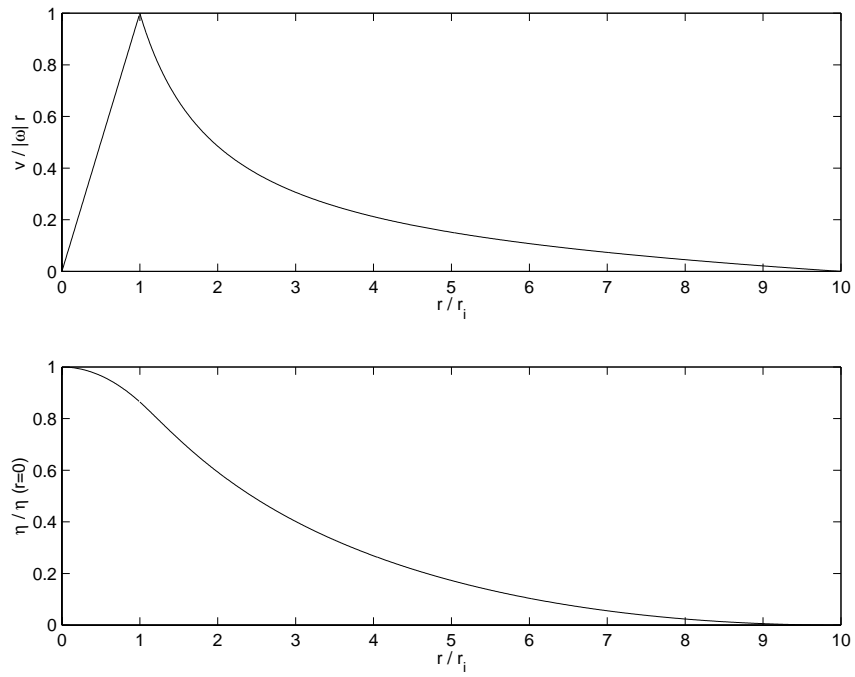


Figure 126: *Top*: azimuthal velocity  $v(r)$  vs. radial distance for a vortex with a finite-shear shell surrounding a solid body core. For this vortex,  $\omega = -\Omega$ . *Bottom*: sea surface displacement  $\eta$  vs. radial distance, calculated by integrating the cyclogeostrophic relation

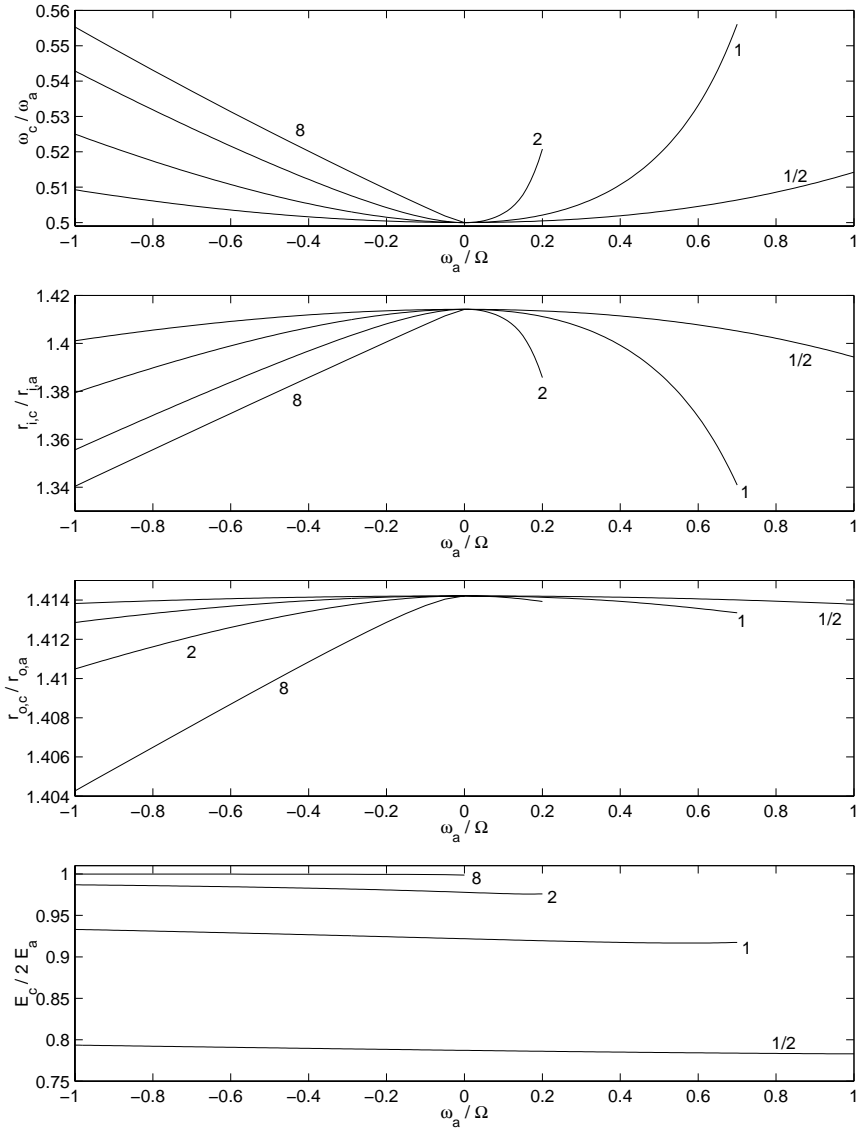


Figure 127: *Top:* ratio of final rotational frequency  $\omega_c$  to initial frequency  $\omega_a$  as a function of  $\omega_a/\Omega$ , for finite-shear vortices which conserve mass and angular momentum when they merge ( $r_{o,a} = 10r_{i,a}$ ). The label for each curve indicate the value of  $r_{i,a}/R_d$ . Some curves end before reaching  $\omega_a = \Omega$ ; at greater values of  $\omega_a$ , the vortex has negative thickness  $H_1 + h + \eta$  at its center and is thus not geometrically valid. *Middle, upper:* ratio of final core radius  $r_{i,c}$  to initial core radius  $r_{i,a}$ . *Middle, lower:* ratio of final shell radius  $r_{o,c}$  to initial shell radius  $r_{o,a}$ . *Bottom:* ratio of final energy  $E_c$  to initial energy  $2E_a$ .

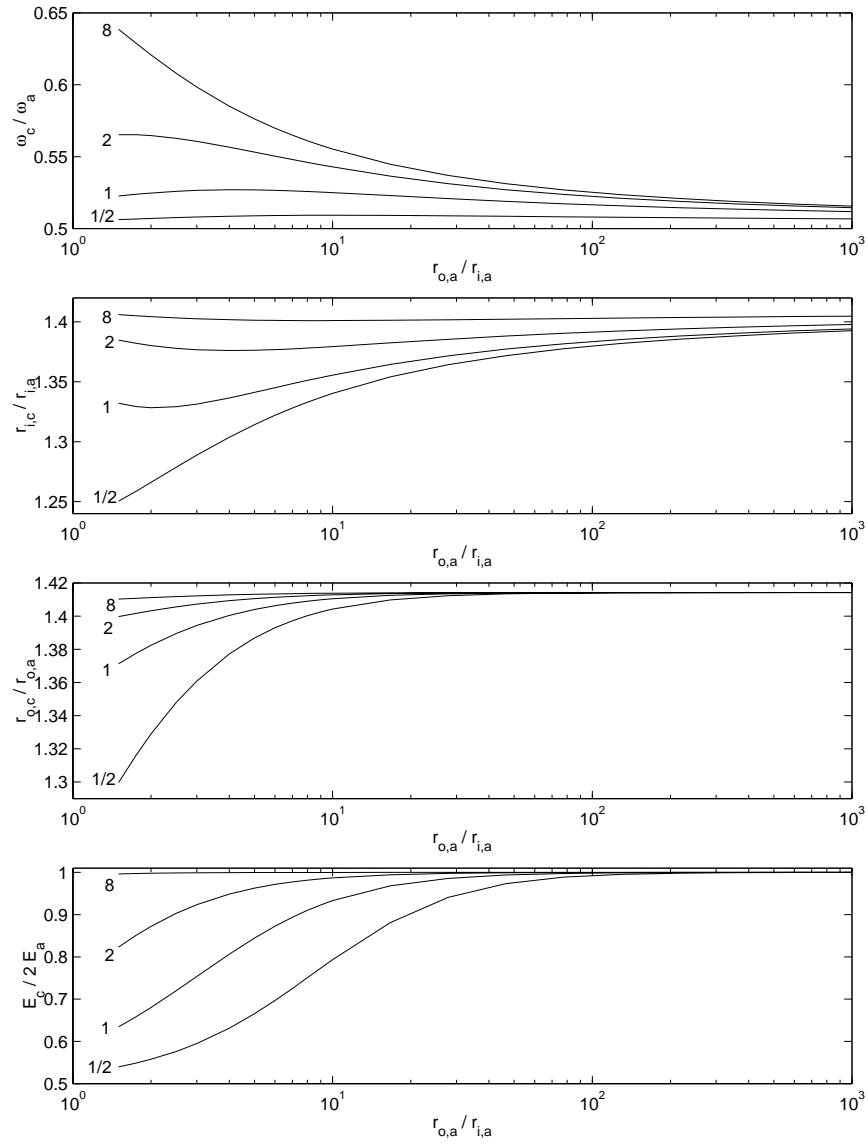


Figure 128: *Top*: ratio of final rotational frequency  $\omega_c$  to initial frequency  $\omega_a$  as a function of  $r_{o,a}/r_{i,a}$ , for finite-shear vortices which conserve mass and angular momentum when they merge ( $\omega_a/\Omega = -1$ ). The label for each curve indicate the value of  $r_{i,a}/R_d$ . *Middle, upper*: ratio of final core radius  $r_{i,c}$  to initial core radius  $r_{i,a}$ . *Middle, lower*: ratio of final shell radius  $r_{o,c}$  to initial shell radius  $r_{o,a}$ . *Bottom*: ratio of final energy  $E_c$  to initial energy  $2E_a$ .

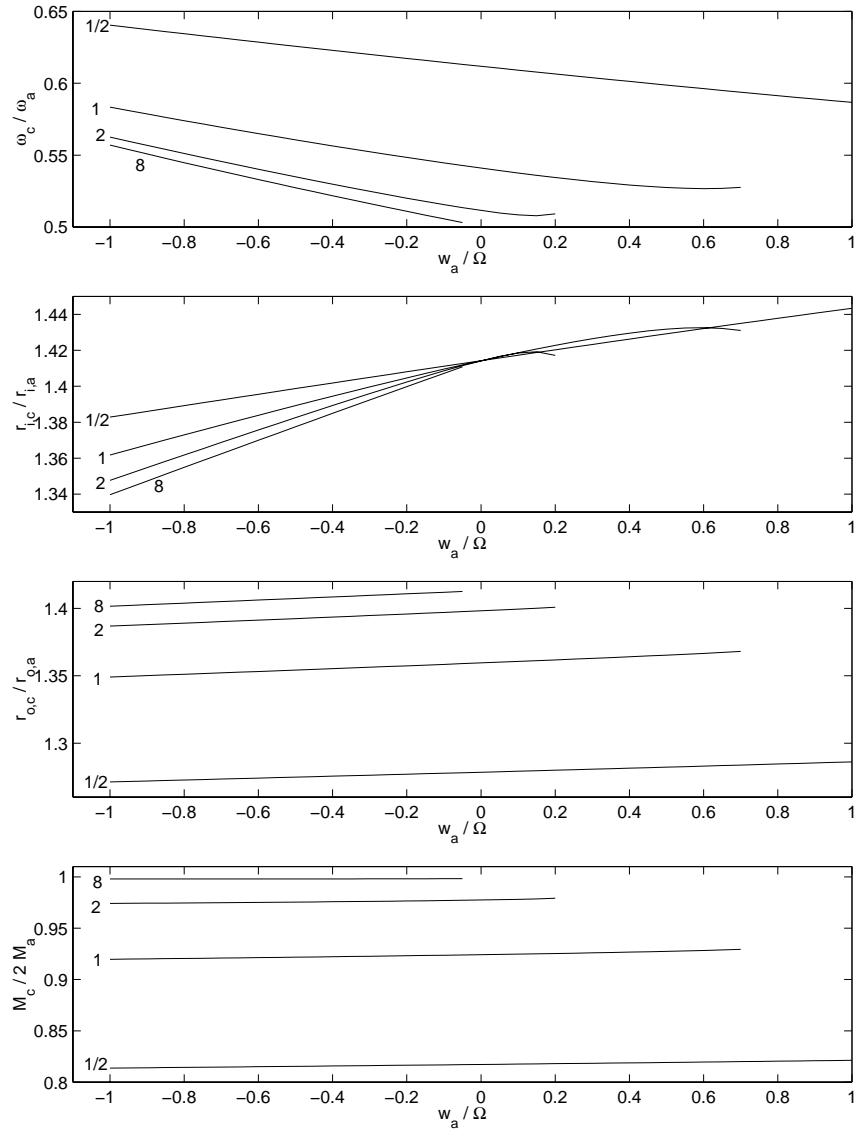


Figure 129: *Top*: ratio of final rotational frequency  $\omega_c$  to initial frequency  $\omega_a$  as a function of  $\omega_a/\Omega$ , for finite-shear vortices which conserve angular momentum and energy when they merge ( $r_{o,a} = 10r_{i,a}$ ). The label for each curve indicate the value of  $r_{i,a}/R_d$ . Some curves end before reaching  $\omega_a = \Omega$ ; at greater values of  $\omega_a$ , the vortex has negative thickness  $H_1 + h + \eta$  at its center and is thus not geometrically valid. *Middle, upper*: ratio of final core radius  $r_{i,c}$  to initial core radius  $r_{i,a}$ . *Middle, lower*: ratio of final shell radius  $r_{o,c}$  to initial shell radius  $r_{o,a}$ . *Bottom*: ratio of final mass  $M_c$  to initial mass  $2M_a$ .

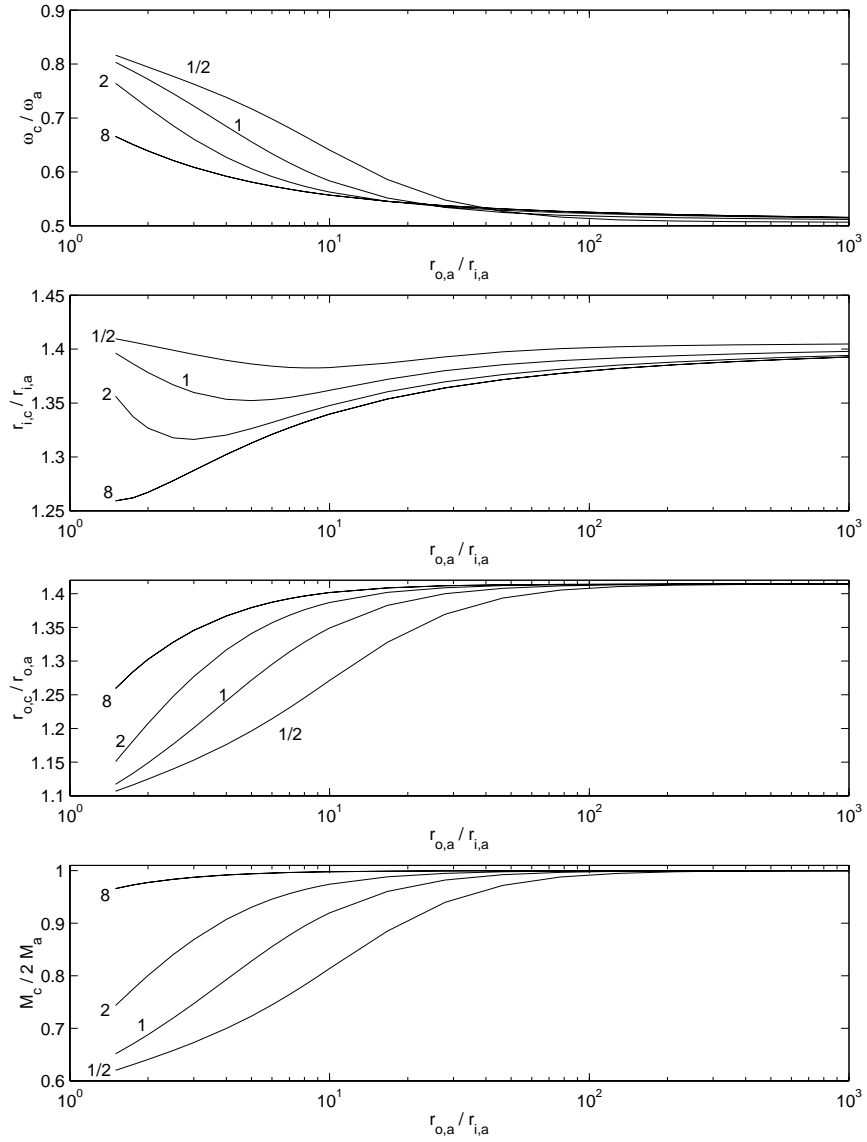


Figure 130: *Top*: ratio of final rotational frequency  $\omega_c$  to initial frequency  $\omega_a$  as a function of  $r_{o,a}/r_{i,a}$ , for finite-shear vortices which conserve angular momentum and energy when they merge ( $\omega_a/\Omega = -1$ ). The label for each curve indicate the value of  $r_{i,a}/R_d$ .

*Middle, upper*: ratio of final core radius  $r_{i,c}$  to initial core radius  $r_{i,a}$ .

*Middle, lower*: ratio of final shell radius  $r_{o,c}$  to initial shell radius  $r_{o,a}$ .

*Bottom*: ratio of final mass  $M_c$  to initial mass  $2M_a$ .

## APPENDIX F

### DISPERSION MAGNIFICATION BY THE MEAN CURRENT SHEAR

*The effect of a mean meridional shear on zonal dispersion is calculated and compared to the observations.*

Krauss and Böning [1987] noted that meridional shear in the mean zonal current could artificially magnify the zonal dispersion. This derivation is inspired by theirs, but differs by treating the meridional position of a drifter as a function of time, and assuming that the ensemble average of this quantity is zero. This approach produces an estimate of the zonal dispersion as a function of the mean meridional shear, which can be compared to direct measurements.

Consider mean currents of the form

$$\langle u \rangle = u_o + \alpha y', \quad \langle v \rangle = 0. \quad (\text{F.1})$$

By introducing a meridional shear in the mean zonal current, the assumption of homogeneity is violated. How will this affect the long-time zonal dispersion?

A spatially-homogeneous estimate of  $\langle u \rangle$  will be averaged over a meridional scale  $B$  (the maximum meridional size of the tracer cloud). This estimate (which I denote with a hat) is

$$\langle \hat{u} \rangle = \frac{1}{B} \int_{-B/2}^{B/2} dy' u = \langle u \rangle - \alpha y'. \quad (\text{F.2})$$

The estimate of  $u'$  is thus contaminated by the meridional shear of the mean current:

$$\hat{u}' = u - \langle \hat{u} \rangle = u' + \alpha y'. \quad (\text{F.3})$$

Then

$$\langle \hat{u}'^2 \rangle = \langle u'^2 \rangle + 2\alpha \langle u'y' \rangle + \alpha^2 \langle y'^2 \rangle. \quad (\text{F.4})$$

If  $u'$  and  $y'$  are nearly uncorrelated, the first and third terms dominate the right-hand

side of (F.4) and

$$\langle \hat{u}^2 \rangle \approx \langle u'^2 \rangle + 2\alpha^2 \langle v'^2 \rangle T_v t, \quad t \gg T_v, \quad (\text{F.5})$$

where (5.7) has been used. Assuming that the EKE is roughly homogeneous ( $\langle u'^2 \rangle \sim \langle v'^2 \rangle$ ), then

$$\langle \hat{u}^2 \rangle \approx \langle u'^2 \rangle \quad (\text{F.6})$$

for  $t \ll (2\alpha^2 T_v)^{-1}$ . This time scale can be estimated as follows: east of the Hawaiian Islands, the zonal current goes from 0 m/s at 26°N to -0.2 m/s at 14°N (see Fig. 52), giving  $|\alpha| \sim 1.5 \times 10^{-7} \text{ s}^{-1}$ . Using this value and  $T_v \sim 3.2$  days,  $(2\alpha^2 T_v)^{-1} \sim 930$  days. Because I am interested in dispersion for  $t \leq 120$  days, I proceed under the assumption that (F.6) applies and restrict this derivation to the “long-time limit” defined as

$$T_u \ll t \ll (2\alpha^2 T_v)^{-1}. \quad (\text{F.7})$$

The estimated autocorrelation of  $u'$  is

$$\begin{aligned} \hat{R}_u &= \frac{1}{\langle u'^2 \rangle T_m} \int_0^{T_m} d\tau [u'(t) + \alpha y'(t)] [u'(t + \tau) + \alpha y'(t + \tau)] \\ &\approx R_u + 2 \frac{\langle v'^2 \rangle}{\langle u'^2 \rangle} \alpha^2 T_v t R_y, \end{aligned} \quad (\text{F.8})$$

where  $R_y$  is the integral time scale of  $y'$ , a function which decays considerably more slowly than  $R_v$ . Because  $R_y \leq 1$ ,  $t \ll 1/2\alpha^2 T_v$ , and  $\langle u'^2 \rangle \sim \langle v'^2 \rangle$ ,

$$\hat{R}_u \approx R_u. \quad (\text{F.9})$$

The estimated autocorrelation function is not significantly contaminated by the meridional shear in  $\langle u \rangle$ , so direct estimates of the integral scales should not be either.

In the long-time limit, the dispersion is

$$\begin{aligned} \langle \hat{x}^2 \rangle &= 2 \langle u'^2 \rangle \int_0^t d\tau (t - \tau) \hat{R}_u(\tau) \\ &\approx 2 \langle u'^2 \rangle t \int_0^t d\tau \left[ R_u + 2 \frac{\langle v'^2 \rangle}{\langle u'^2 \rangle} \alpha^2 T_v t R_y \right] \\ &= 2 \langle u'^2 \rangle T_u t + 4 \langle v'^2 \rangle \alpha^2 T_v T_y t^2, \end{aligned} \quad (\text{F.10})$$

where  $T_y$  is the integral time scale of  $y'$  (for all 90-day independent drifter segments in the Hawaiian region, the mean value of  $T_y$  is 11 days). The second term on the right-hand side of (F.10) scales to the first term as

$$\frac{4 \langle v'^2 \rangle \alpha^2 T_v T_y t}{\langle u'^2 \rangle T_u} \sim 4 \alpha^2 T_y t. \quad (\text{F.11})$$

Thus, for  $t > 1/4\alpha^2 T_y \sim 100$  days,  $x_{rms}$  grows linearly due to the meridional shear of the mean zonal current.

According to (F.10), the mean shear scales as

$$|\alpha| \sim \frac{dx_{rms}/dt}{2\sqrt{\langle v'^2 \rangle T_v T_y}}. \quad (\text{F.12})$$

Thus, an estimate of  $|\alpha|$  can be derived from the observed long-time dispersion. From Fig. 84,  $\Delta x_{rms}/\Delta t$  east of the islands between days 100 and 120 is  $\sim .05$  m/s. Using this value,  $v_{rms} \sim .15$  m/s,  $T_v \sim 3.2$  days and  $T_y \sim 11$  days, (F.12) gives  $|\alpha| \sim 3.3 \times 10^{-7} \text{ s}^{-1}$ , approximately twice the direct measurement ( $|\alpha| \approx 1.5 \times 10^{-7} \text{ s}^{-1}$ ). This discrepancy may be due to the first term in the right-hand side of (F.10) playing a non-negligible role. Nevertheless, given the crude scaling arguments involved, this order-of-magnitude agreement suggests that Krauss and Böning's [1987] hypothesis is consistent with the observed long-time zonal dispersion.

## REFERENCES

- A. D. Kirwan, J., McNally, G. J., and Pazan, S., (1978). Wind drag and relative separations of undrogued drifters. *J. Phys. Oceanogr.*, **8**, 1146–1150.
- Allen, C. B., Kanda, J., and Laws, E. A., (1996). New production and photosynthetic rates within and outside a cyclonic mesoscale eddy in the North Pacific subtropical gyre. *Deep-Sea Res.*, **43**, 917–936.
- Argos, (1996). *Argos User Manual 1.0*. CLS, 18 avenue Edouard-Belin, 31055 Toulouse Cedex, France.
- Batchelor, G. K., (1949). Diffusion in a field of homogeneous turbulence. I. Eulerian analysis. *Aus. J. Sci. Res.*, **A2**, 437–450.
- Bendat, J. S. and Piersol, A. G., (1986). *Random Data, Analysis and Measurement Procedures*. John Wiley and Sons.
- Bennett, A. F. and Denman, K. L., (1985). Phytoplankton patchiness: inferences from particle statistics. *J. Marine Res.*, **43**, 307–335.
- Bernstein, R. and White, W., (1974). Time and length scales of baroclinic eddies in the central North Pacific Ocean. *J. Phys. Oceanogr.*, **4**, 613–624.
- Bingham, F. M., (1998). Evidence for the existence of a North Hawaiian Ridge Current. *J. Phys. Oceanogr.*, **28**, 991–998.
- Brink, K. H., Beardsley, R. C., Niiler, P. P., Abbott, M., Huyer, A., Ramp, S., Stanton, T., and Stuart, D., (1991). Statistical properties of near-surface flow in the California coastal transition zone. *J. Geophys. Res.*, **96**, 14693–14706.
- Brown, G. L. and Roshko, A., (1974). On density effects and large structure in turbulent mixing layer. *J. Fluid Mech.*, **64**, 775–816.

- Burks, J. B., (1967). The flow of water through the Molokai Channel. Master's thesis, School of Ocean and Earth Sciences and Technology, University of Hawaii at Manoa.
- Carton, X. and Bertrand, C., (1994). The influence of environmental parameters on two-dimensional vortex merger. In Heijst, G. J. F.v., editor, *Modelling of Oceanic Vortices*, pages 125–134. North-Holland.
- Chassignet, E. P. and Cushman-Roisin, B., (1991). On the influence of a lower layer on the propagation of nonlinear oceanic eddies. *J. Phys. Oceanogr.*, **21**, 939–957.
- Chew, F. and Bushnell, M. H., (1990). The half-inertial flow in the eastern equatorial Pacific: a case study. *J. Phys. Oceanogr.*, **20**, 1124–1133.
- Colin de Verdiere, A., (1983). Lagrangian eddy statistics from surface drifters in the eastern North Atlantic. *J. Marine Res.*, **41**, 375–398.
- Cresswell, G. R., (1982). The coalescence of two East Australian current warm-core eddies. *Science*, **215**, 161–164.
- Cushman-Roisin, B., Chassignet, E., and Tang, B., (1990). Westward motion of isolated eddies. *J. Phys. Oceanogr.*, **20**, 758–768.
- Cushman-Roisin, B., (1984). On the maintenance of the Subtropical Front and its associated countercurrent. *J. Phys. Oceanogr.*, **14**, 1179–1190.
- Cushman-Roisin, B., (1989). On the role of filamentation in the merging of anticyclonic lenses. *J. Phys. Oceanogr.*, **19**, 253–258.
- Davis, R. E., (1985). Drifter observations of coastal surface currents during CODE: The method and descriptive view. *J. Geophys. Res.*, **90**, 4741–4755.
- Davis, R. E., (1985). Drifter observations of coastal surface currents during CODE: The statistical and dynamical views. *J. Geophys. Res.*, **90**, 4756–4772.

- Dewar, W. K. and Killworth, P. D., (1990). On the cylinder collapse problem, mixing, and the merger of isolated eddies. *J. Phys. Oceanogr.*, **20**, 1563–1575.
- Dousset, B. and Flament, P., (1995). Satellite sea surface temperature images around the Hawaiian Islands, June 1990 to November 1994. Technical Report 94-02, School of Ocean and Earth Science and Technology, University of Hawaii at Manoa.
- Emery, W. J., Lee, W. G., and Magaard, L., (1984). Geographic and seasonal distributions of Brunt-Vaisala frequency and Rossby radii in the North Pacific and North Atlantic. *J. Phys. Oceanogr.*, **14**, 294–317.
- Emery, W. J., (1975). Dynamic height from temperature profiles. *J. Phys. Oceanogr.*, **5**, 369–375.
- Eriksen, C. C., (1980). Evidence for a continuous spectrum of equatorial waves in the Indian Ocean. *J. Geophys. Res.*, **85**, 3285–3303.
- Feynman, R. P., Leighton, R. B., and Sands, M. L., (1987). *The Feynman Lectures on Physics: Commemorative Edition*. Addison-Wesley.
- Firing, E., Qiu, B., and Miao, W., (1998). Time-dependent island rule and its application to the time-varying North Hawaiian Ridge Current. *J. Phys. Oceanogr.* (submitted).
- Firing, E., (1996). Currents observed north of Oahu during the first five years of HOT. *Deep-Sea Res.*, **43**, 89–112.
- Flierl, G. R., (1984). Rossby wave radiation from a strongly nonlinear warm eddy. *J. Phys. Oceanogr.*, **14**, 47–58.
- Frankignoul, C. and Müller, P., (1979). Quasi-geostrophic response of an infinite  $\beta$ -plane ocean to stochastic forcing by the atmosphere. *J. Phys. Oceanogr.*, **9**, 104–127.

- Freeland, H. J., Rhines, P. B., and Rossby, T., (1975). Statistical observations of the trajectories of neutrally buoyant floats in the North Atlantic. *J. Marine Res.*, **33**, 383–404.
- Geyer, W. R., (1989). Field calibration of mixed-layer drifters. *J. Atmos. Oceanogr. Tech.*, **6**, 333–342.
- Gill, A. E. and Griffiths, R. W., (1981). Why should two anticyclonic eddies merge? *Ocean Modelling*, **41**, 10–16.
- Gill, A. E., (1982). *Atmosphere-Ocean Dynamics*, volume 30 of *International Geophysics Series*. Academic Press.
- Godfrey, J., (1989). A Sverdrup model of the depth-integrated flow for the world ocean allowing for island circulations. *Geophys. Astrophys. Fluid Dynamics*, **45**, 89–112.
- Godin, G., (1972). *The Analysis of Tides*. University of Toronto Press.
- Graber, H., Ebuchi, N., and Vakkayil, R., (1996). Evaluation of ERS-1 scatterometer winds with wind and wave ocean buoy observations. Technical report, Jet Propulsion Laboratory, National Aeronautics and Space Administration, and National Space Agency of Japan.
- Griffiths, R. W. and Hopfinger, E. J., (1987). Coalescing of geostrophic vortices. *J. Fluid Mech.*, **178**, 73–97.
- Haidvogel, D. B. and Keffer, T., (1984). Tracer dispersal by mid-ocean eddies. *Dyn. Atmos. Oceans*, **8**, 1–40.
- Hansen, D. V. and Herman, A., (1989). Temporal sampling requirements for surface drifting buoys in the tropical Pacific. *J. Atmos. Oceanogr. Tech.*, **6**, 599–607.
- Hansen, D. V. and Paul, C. A., (1984). Genesis and effects of long waves in the equatorial Pacific. *J. Geophys. Res.*, **89**, 10431–10440.

- Hansen, D. V. and Poulain, P.-M., (1996). Quality control and interpolations of WOCE-TOGA drifter data. *J. Atmos. Oceanogr. Tech.*, **13**, 900–909.
- Hasselmann, K., (1976). Stochastic climate models. Part I. Theory. *Tellus*, **28**, 473–485.
- Holton, J. R., (1979). *An Introduction to Dynamic Meteorology*, volume 23 of *International Geophysics Series*. Academic Press, second edition.
- Johnson, G. C. and Toole, J. M., (1991). Flow of deep and bottom waters in the Pacific at 10°N. *Deep-Sea Res.*, ?, ?
- Kampé de Fériët, (1939). Le fonctions aleatoires stationnaires et la theorie de la turbulence homogene. *An. Soc. Sci., Bruxelles*, **59**, 145–194.
- Kessler, W. S., (1990). Observations of long Rossby waves in the northern tropical Pacific. *J. Geophys. Res.*, **95**, 5183–5217.
- Kloosterziel, R. C. and Heijst, G. J. F.v., (1991). An experimental study of unstable barotropic vortices in a rotating fluid. *J. Fluid Mech.*, **223**, 1–24.
- Krauss, W. and Böning, C. W., (1987). Lagrangian properties of eddy fields in the northern North Atlantic as deduced from satellite-tracked buoys. *J. Marine Res.*, **45**, 259–291.
- Kundu, P. K., (1990). *Fluid Mechanics*. Academic Press, Inc.
- Latham, R. C., (1967). Kauai Channel currents. Master’s thesis, School of Ocean and Earth Sciences and Technology, University of Hawaii at Manoa.
- Leonardi, A. P., Hurlburt, H. E., and O’Brien, J. J., (1998). The circulation in the lee of the Hawaiian Archipelago. In Staniforth, A., editor, *Research activities in atmospheric and oceanic modelling*, pages 8.27–8.28. WMO/ICSU/IOC World Climate Research Programme and WMO Weather Prediction Research Programmes.

- Leonardi, A. P., (1998). Dynamics of the North Hawaiian Ridge Current. Master's thesis, College of Arts and Sciences, Florida State University.
- Lobel, P. and Robinson, A., (1986). Transport and entrainment of fish larvae by ocean mesoscale eddies and currents in Hawaiian waters. *Deep-Sea Res.*, **33**, 483–500.
- Lumpkin, C., (1995). Resonant coastal waves and superinertial oscillations. Master's thesis, School of Ocean and Earth Sciences and Technology, University of Hawaii at Manoa.
- Luther, D. S. and Johnson, E. S., (1990). Eddy energetics in the upper equatorial Pacific during Hawaii-to-Tahiti Shuttle Experiment. *J. Phys. Oceanogr.*, **7**, 913–944.
- Luther, D. S., (1985). Trapped waves around the Hawaiian Islands. In *'Aha Huliko'a Proceedings*, pages 261–301. Hawaiian Institute of Geophysics.
- Mantyla, A. and Reid, J. L., (1983). Abyssal characteristics of the world ocean waters. *Deep-Sea Res.*, **30**, 805–883.
- McCreary, J. P., Lee, H. S., and Enfield, D. B., (1989). The response of the coastal ocean to strong offshore winds: With application to circulations in the Gulfs of Tehuantepec and Papagayo. *J. Marine Res.*, **47**, 81–109.
- McGary, J. W., (1955). Mid-Pacific Oceanography, part VI, Hawaiian offshore waters, December 1949–November 1951. Technical Report 152, U.S. Fish and Wildlife Service, Special Science Report.
- McNally, G. and White, W., (1985). Wind driven flow in the mixed layer observed by drifting buoys during autumn-winter in the mid-latitude North Pacific. *J. Phys. Oceanogr.*, **15**, 684–694.
- McNally, G., Patzert, W., Jr., A. K., and Vastano, A., (1983). The near-surface

- circulation of the North Pacific using satellite-tracked drifting buoys. *J. Geophys. Res.*, **88**, 7505–7518.
- McWilliams, J., Brown, E., Bryden, H., Ebbesmeyer, C., Elliot, B., Heinmiller, R., Hua, B. L., Leaman, K., Lindstrom, E., Luyten, J., McDowell, S., Owens, W. B., Perkins, H., Price, J., Regier, L., Riser, S., Rossby, H., Sanford, T., Shien, C., Taft, B., and Leer, J. V., (1983). The local dynamics of eddies in the western North Atlantic. In Robinson, A., editor, *Eddies in Marine Science*, pages 92–113. Springer-Verlag, Berlin.
- Melander, M. V., Zabusky, N. J., and McWilliams, J. C., (1988). Symmetric vortex merger in two dimensions: causes and conditions. *J. Fluid Mech.*, **195**, 303–340.
- Mitchum, G. T., (1995). The source of 90-day oscillations at Wake Island. *J. Geophys. Res.*, **100**, 2459–2475.
- Müller, P. and Siedler, G., (1976). Consistency relations for internal waves. *Deep-Sea Res.*, **23**, 613–628.
- Munch, C., (1996). The effect of the Hawaiian Ridge on mesoscale variability: results from TOPEX/POSEIDON. Master’s thesis, School of Ocean and Earth Sciences and Technology, University of Hawaii at Manoa.
- Mysak, L. and Magaard, L., (1983). Rossby wave driven Eulerian mean flows along non-zonal barriers, with application to the Hawaiian Ridge. *J. Phys. Oceanogr.*, **13**, 1716–1725.
- Nath, J. H., (1977). Wind tunnel tests on drogues. Technical report, NOAA Data Buoy Office.
- Niiler, P. P. and Paduan, J. D., (1995). Wind-driven motions in the northeast Pacific as measured by Lagrangian drifters. *J. Phys. Oceanogr.*, **25**, 2819–2830.

- Niiler, P. P., Davis, R. E., and White, H. J., (1987). Water-following characteristics of a mixed-layer drifter. *Deep-Sea Res.*, **34**, 1867–1882.
- Niiler, P. P., Sybrandy, A. S., Bi, K., Poulain, P. M., and Bitterman, D., (1995). Measurements of the water-following capability of holey-sock and TRISTAR drifters. *Deep-Sea Res.*, **42**, 1951–1964.
- Nof, D. and Simon, L. M., (1987). Laboratory experiments on the merging of nonlinear anticyclonic eddies. *J. Phys. Oceanogr.*, **17**, 343–357.
- Nof, D., (1981). On the  $\beta$ -induced movement of isolated baroclinic eddies. *J. Phys. Oceanogr.*, **11**, 1662–1672.
- Nof, D., (1986). The merging of isolated lenses. Technical Report DN-86-4, Florida State University.
- Nof, D., (1988). Eddy-wall interactions. *J. Marine Res.*, **46**, 527–555.
- Nof, D., (1988). The fusion of isolated nonlinear eddies. *J. Phys. Oceanogr.*, **18**, 887–905.
- Paduan, J. D. and Niiler, P. P., (1993). Structure of velocity and temperature in the northeast Pacific as measured with Lagrangian drifters in Fall 1987. *J. Phys. Oceanogr.*, **23**, 585–600.
- Patzert, W. C. and Wyrski, K., (1974). Anticyclonic flow around the Hawaiian Islands indicated by current meter data. *J. Phys. Oceanogr.*, **4**, 673–676.
- Patzert, W. C., (1968). Eddies in Hawaiian waters. Technical Report 69-8, Hawaiian Institute of Geophysics, University of Hawaii at Manoa.
- Pavia, E. G. and Cushman-Roisin, B., (1990). Merging of frontal eddies. *J. Phys. Oceanogr.*, **20**, 1886–1906.

- Poulain, P.-M. and Niiler, P. P., (1989). Statistical analysis of the surface circulation in the California current system using satellite-tracked drifters. *J. Phys. Oceanogr.*, **19**, 1588–1603.
- Price, J. F. and Rossby, H., (1982). Observations of a barotropic planetary wave in the western North Atlantic. *J. Marine Res.*, **40 (supplement)**, 543–558.
- Price, J., Woert, M. L. V., and Vitousek, M., (1994). On the possibility of a ridge current along the Hawaiian Islands. *J. Geophys. Res.*, **99**, 14101–14112.
- Qiu, B., Koh, D. A., Lumpkin, C., and Flament, P., (1997). Existence and formation mechanism for the North Hawaii Ridge Current. *J. Phys. Oceanogr.*, **27**, 431–444.
- Qiu, B., (1998). Seasonal eddy field modulation of the North Pacific Subtropical Countercurrent: TOPEX/POSEIDON observations and theory. *J. Phys. Oceanogr.* (submitted).
- Reid, J. L., (1965). Intermediate waters of the Pacific Ocean. Technical Report 2, Johns Hopkins Oceanographic Studies, Baltimore, Maryland.
- Roden, G. I., (1991). Effects of the Hawaiian ridge upon oceanic flow and thermohaline structure. *Deep-Sea Res.*, **38**, .
- Rossby, T., Voorhis, A. D., and Webb, D., (1975). A quasi-Lagrangian study of mid-ocean variability using long range SOFAR floats. *J. Marine Res.*, **33**, 355–382.
- Rossby, C.-G., (1936). Dynamics of steady ocean currents in the light of experimental fluid mechanics. *Papers in Phys. Oceanogr. and Meteorol.*, **V**, 1–43.
- Rossby, C.-G., (1948). On displacements and intensity changes of atmospheric vortices. *J. Fluid Mech.*, **7**, 175–187.
- SeaSpace, (1992). *TeraScan Reference Manual*.

- Smith, R. B. and Grubisić, V., (1993). Aerial observations of Hawaii's Wake. *J. Atmos. Sci.*, **50**, 3728–3750.
- Smith, S., (1988). Coefficients for sea surface wind stress, heat flux and wind profile as a function of wind speed and temperature. *J. Geophys. Res.*, **93**, 15467–15472.
- Stumpf, H. G. and Legeckis, R. V., (1977). Satellite observations of mesoscale eddy dynamics in the eastern tropical Pacific Ocean. *J. Phys. Oceanogr.*, **7**, 648–658.
- Sun, C., Price, J., Magaard, L., and Roden, G., (1998). The North Hawaiian Ridge Current: a comparison between an analytical theory and some prior observations. *J. Phys. Oceanogr.*, **18**, 384–388.
- Sybrandy, A. L. and Niiler, P. P., (1991). WOCE/TOGA Lagrangian drifter construction manual. Technical Report SIO Reference 91/6, WOCE Report Number 63, University of California, San Diego.
- Taylor, G. I., (1921). Diffusion by continuous movements. *Proc. Lond. Math. Soc.*, **20**, 196–212.
- Tennekes, H. and Lumley, J. L., (1972). *A First Course in Turbulence*. MIT Press.
- Tokos, K. L. S., Hinrichsen, H.-H., and Zenk, W., (1994). Merging and migration of two meddies. *J. Phys. Oceanogr.*, **24**, 2129–2141.
- Traon, P. L., Gaspar, P., Bouyssel, F., and Makhmara, H., (1995). Using TOPEX/Poseidon data to enhance ERS-1 orbit. *J. Atmos. Oceanogr. Tech.*, **12**, 161–170.
- Tsuchiya, M., (1968). Upper waters of the intertropical Pacific Ocean. Technical Report 4, The John Hopkins University.
- Tung, A. C., Rodman, M. R., Wei, C., Olson, E. J., Feely, R. A., and Gendron, J. F.,

- (1986). Carbonate chemistry of the North Pacific Ocean. Technical report, Office of Energy Research, Carbon Dioxide Research Division, Washington, D.C.
- UNESCO, (1981). Tenth report of the joint panel on oceanographic tables and standards. Technical Report 36, UNESCO Technical Papers in Marine Science.
- Valcke, S. and Verron, J., (1997). Interactions of baroclinic isolated vortices: The dominant effect of shielding. *J. Phys. Oceanogr.*, **27**, 524–541.
- Heijst, G. J. F.v., Kloosterziel, R. C., and Williams, C., (1991). Laboratory experiments on the tripolar vortex in a rotating fluid. *J. Fluid Mech.*, **225**, 301–331.
- Verron, J. and Valcke, S., (1994). Scale-dependent merging of baroclinic vortices. *J. Fluid Mech.*, **264**, 81–106.
- Kármán, T.v., (1954). *Aerodynamics, Selected Topics in Light of Their Historical Development*. Cornell University Press.
- Wenzel, D. B., (1992). Sea surface warming in the lee of Hawaii: extent and variability. Master's thesis, School of Ocean and Earth Sciences and Technology, University of Hawaii at Manoa.
- White, W. B. and Hasunuma, K., (1982). Quasi-stationary banded structure in the mean zonal geostrophic current regimes of the western North Pacific. *J. Marine Res.*, **40**, 1035–1046.
- White, W. B. and Walker, A. E., (1985). The influence of the Hawaiian Archipelago upon the wind-driven subtropical gyre of the western North Pacific. *J. Geophys. Res.*, **90**, 7061–7074.
- White, W., (1983). A narrow boundary current along the eastern side of the Hawaiian Ridge; the North Hawaiian Ridge Current. *J. Phys. Oceanogr.*, **13**, 1726–1731.

- White, W. B., (1986). Vertical Reynolds stress divergence in the upper ocean associated with linear wind-driven, near-inertial waves of finite amplitude. *J. Phys. Oceanogr.*, **16**, 1190–1203.
- Winant, C. D. and Browand, F. K., (1974). Vortex pairing: the mechanism of turbulent mixing layer growth at moderate Reynolds numbers. *J. Fluid Mech.*, **63**, 237–255.
- Wyrтки, K. and Kilonsky, B., (1984). Mean water and current structure during the Hawaii–Tahiti Shuttle Experiment. *J. Phys. Oceanogr.*, **14**, 242–254.
- Wyrтки, K., Burks, J., Latham, R., and Patzert, W., (1967). Oceanographic observations during 1965–1967 in the Hawaiian Archipelago. Technical Report 67-15, Hawaiian Institute of Geophysics, University of Hawaii at Manoa.
- Wyrтки, K., Graefe, V., and Patzert, W., (1969). Current observations in the Hawaiian Archipelago. Technical Report 69-15, Hawaiian Institute of Geophysics, University of Hawaii at Manoa.
- Wyrтки, K., (1974). The dynamic topography of the Pacific Ocean and its fluctuations. Technical Report 74-5, Hawaiian Institute of Geophysics, University of Hawaii at Manoa.
- Wyrтки, K., (1975). Fluctuations of the dynamic topography in the Pacific Ocean. *J. Phys. Oceanogr.*, **5**, 450–459.
- Wyrтки, K., (1977). *Water Masses in the Oceans and Adjacent Seas*. International Dictionary of Geophysics. Pergamon Press.
- Wyrтки, K., (1982). Eddies in the Pacific North Equatorial Current. *J. Phys. Oceanogr.*, **12**, 746–749.